Underwater Ultrasonic Transducer Technology. Construction, Characterization and Finite-Element Modelling.

Master thesis in Ocean Technology
Acoustics

Celine Prøytz

Department of Physics and Technology,
University of Bergen

March 2022

Preface

The work in this thesis is conducted at the Department of Physics and Technology at the University of Bergen. The work is a part of the ongoing research on Guided Waves at the Acoustics group at UoB. The work conducted in this thesis is based on the piezoelectric construction work, and experimental setup from the PhD thesis by Magne Aanes [1]. The work has been very instructive, both theoretical and practical. Especially the experimental work has been a big challenge.

I want to give a special thanks to my supervisors, Per Lunde, and my co-supervisors Magne Vestrheim and Mathias Sæther for giving me good guidance and support through the challenges I have met, and for taking time for discussions whenever necessary. In addition, they have given me a good follow up with beneficial advice and interesting talks along the way.

I also want to give a special thanks to Magne Aanes for sharing his experiences regarding the transducer construction and the simulation setup when obstacles have occurred.

The staff members at the Mechanical workshop at the Department of Physics and Technology have always been helpful. A special thanks to Roald Langøen for making the casings and cutting out all the front layers in the correct dimensions.

As well, I want to thank the staff engineers Bilal Hasan Qureshi and Werner Olsen for their patience and help with the soldering of wires to the piezoelectric disks used in the current thesis, and Børre Andreas Opedal Lunde for using your free time to give the last attempt at soldering the wires to the piezoelectric disks. It has been a challenging process with a lot of tries.

I also want to thank fellow students at the Acoustics group for interesting discussions throughout these years and for sharing tips and tricks in MATLAB and experimental setups.

At last, thanks to my family for their support and encouragement throughout these years at the University of Bergen.

March 2022

Celine Prøytz

Contents

Abstract **iv**

1 Introduction **1**
1.1 Background and motivation . . . 1
1.2 Objectives . . . 2
1.3 Literature . . . 2
1.4 Outline of the thesis . . . 3

2 Theory **4**
2.1 Introduction . . . 4
2.2 The piezoelectric disk . . . 4
2.3 Piezoelectric effect . . . 5
2.4 Finite Element Method . . . 5
2.5 Material constants . . . 7
2.6 Impedance matching . . . 7
2.7 Source sensitivity . . . 8
2.8 Rayleigh distance . . . 8
2.9 Beam pattern . . . 8

3 Transducer construction methods and design **9**
3.1 Introduction . . . 9
3.2 Transducer design . . . 9
3.3 Soldering . . . 11
3.4 Attaching the front layer to the Pz27 disk . . . 12
3.5 Attaching the steel casing . . . 15
3.6 Making the backing layer . . . 15
3.7 Attaching the back casing and the connector . . . 17

4 Measurements and experimental methods **19**
4.1 Introduction . . . 19
4.2 Dimension measurements of the piezoelectric disks . . . 19
4.3 Admittance measurements of the piezoelectric disks . . . 20
4.3.1 Deviations in the admittance measurements . . . 24
4.3.2 Admittance measurements of disk with front layer . . . 24
4.3.3 Admittance measurements with disk, front layer and steel casing . . . 25
4.3.4 Admittance measurements for the piezoelectric transducer in air . . . 25
4.3.5 Admittance measurements for the piezoelectric transducer in water . . . 26
4.4 Acoustic measurement setup in the water tank . . . 27
4.4.1 Rayleigh distance . . . 31

5 Simulation setup **32**
5.1 Introduction . . . 32
5.2 Admittance simulations of the piezoelectric disks . . . 32
5.3 Verification of the simulation setup . . . 34
5.4 Adjusted simulation setup . . . 37
5.5 Simulations of different backing layers . . . 38

5.6 Simulations of the transducer constructions . . . 41
5.7 Simulations with solder and vacuum gap . . . 43

6 Results and discussions **46**
6.1 Introduction . . . 46
6.2 The results from the preliminary construction and development . . . 46
6.2.1 Results from the soldering process . . . 46
6.2.2 How the heat from the oven and soldering iron affects the disk . . . 52
6.2.3 The results after attaching front layers to the piezoelectric disks . . . 53
6.2.4 The results after casings are attached to the front layers . . . 70
6.2.5 The results after pouring the backing layer in the construction . . . 78
6.3 Final construction results . . . 87
6.3.1 Transducer 1 . . . 87
6.3.2 Transducer 2 . . . 89
6.3.3 Transducer 3 . . . 92
6.3.4 Transducer 4 . . . 95
6.3.5 Transducer 5 . . . 99
6.3.6 Transducer 6 . . . 101

7 Conclusion and outlook **105**
7.1 Conclusion and overall findings . . . 105
7.2 Further work . . . 106

A Appendices **109**
A.1 FEMP files used for the simulation setup . . . 109
A.1.1 Read in project file with fluid . . . 109
A.1.2 Material file . . . 116
A.1.3 Inn-file . . . 120
A.2 MATLAB Scripts used for electrical measurements . . . 121
A.2.1 Impanal.m . . . 121
A.3 MATLAB Scripts used for acoustical measurements . . . 123
A.3.1 Main program for the source sensitivity measurements . . . 123
A.3.2 Calculation of the source sensitivity . . . 124
A.3.3 Directivity measurements . . . 125
A.3.4 Micosstep.m . . . 127
A.3.5 Parkerstep.m . . . 128
A.3.6 Frequency response of the hydrophone . . . 129

Abstract

The main objective of this thesis is to construct and characterize ultrasonic transducers. The transducers are constructed to get the information needed for finite element simulations with the wanted accuracy since commercial transducers do not provide sufficient information regarding the material data, dimensions and materials involved. The goal is to get a reasonable agreement between the measurements and simulations. These transducers are constructed for use in guided ultrasonic waves studies at 300 to 1000 kHz.

In this work, ultrasonic piezoelectric transducers with ka numbers of 17 and 46 with a thickness mode f_{TE1}, at 500 kHz is constructed and characterized. These transducers are constructed for being used in studies for ultrasonic beam transmission through solid steel plates, to see how the leaky lamb waves are induced in the steel plate with different ka numbers. Pz27 disks is used with dimensions (D_p x T_p) of 44 x 4 mm and 16 x 4 mm. Three transducers with a ka number of 17 and three with a ka number of 46 are made with one front layer, a backing layer, a steel casing and a UHF connector at the back. A thorough and detailed description of each of the steps in the transducer construction process is given. After each step, electrical measurements are conducted and simulated using finite element modelling. As well, acoustic measurements in water have been conducted for two of the constructed transducers.

The results have shown that the most critical part of the construction process has been soldering a wire to the piezoelectric disks back electrode, and attaching the disk to a front layer using conductive adhesive. Multiple disks have been soldered to get enough reasonable results. As well, it has been shown that it is harder to solder the disks with (D_p x T_p) of 16 x 4 mm than the disks with (D_p x T_p) of 44 x 4 mm. The conductance measurements after the disk with (D_p x T_p) of 16 x 4 mm are soldered have deviated more from the conductance measurements conducted before the disk have been soldered than the disks with (D_p x T_p) of 44 x 4 mm. More deviations are also seen between the measurements and simulations after front layers are attached to disks with (D_p x T_p) of 16 x 4 mm, than to disks with (D_p x T_p) of 44 x 4 mm.

Thirteen disks have been attached to a front layer. Different methods have been tried to finally find a method that has given a reasonable agreement between the measurements and simulations.

A tungsten epoxy backing layer has been used, where the mixture has been dried inside the casing, and an air cone is made in the back. This method of attaching the backing layer inside the casing has given little control over the material parameters of the backing layer. Even though the same mass ratio has been used for mixing the tungsten epoxy backing layers, by comparing the measurements to the simulations, it has been shown that the impedance of the backing layer has not been the same in the transducers.

The finished prototype transducers have achieved a reasonable agreement between the electrical and acoustic measurements and simulations. The source sensitivity has been measured for one transducer with a piezoelectric disk with (D_p x T_p) of 44 x 4 mm and one transducer with a piezoelectric disk with (D_p x T_p) of 16 x 4 mm from 200 to 1000 kHz. In addition, the directivity pattern at 575 kHz has been measured, but a steady-state region was not obtained.

Chapter 1

Introduction

1.1 Background and motivation

For decades, the Acoustics group at the University of Bergen has been working on Guided ultrasonic waves (GUW) [1]–[3], and studied guided ultrasonic waves measurements within a steel plate. The Guided ultrasonic wave measurements have been compared to finite element modelling with the use of the simulation software FEMP [4]. However, since commercial transducers do not provide sufficient information regarding the material data, dimensions and materials involved, transducers need to be built in-house to get the information needed for FEM simulations to compare with the measurements with the wanted accuracy. With the use of in-house constructed transducers, it is proven that simulations are possible with a large degree of accuracy [1], [5], [6], this is because the materials and dimensions of the transducer are known in detail, and reasonable values for the material constants are obtained.

At the University of Bergen, transducers with a ka number of 26 have been made for Guided Ultrasonic Waves research. Magne Aanes built three transducers for use in GUW measurements where the beam transmission through a fluid embedded steel plate and leaky lamb waves was studied, where measurements were compared to simulations [1]. Aanes achieved good agreements between measurements and simulations in FEMP for two transdcuers, where the piezoelectric material, Pz27, was used with a D/T-ratio of 6.25 and $ka = 26$ [1], where k is the wavenumber where the center frequency of the thickness mode f_{TE1} = 500 kHz is used, and a is the radius of the piezoelectric disk used. The transducers were used for studying Guided Ultrasonic waves in the frequency range 350-1000 kHz. The transducers was characterized in water, where the admittance $Y_t(f)$, source sensitivity $S_v(f)$, beam pattern $D(\theta, f)$ and the -3 dB angle of the incident beam exciting the plate, $\theta_{-3dB}(f_b)$, evaluated at the frequency f_b was measured. These transducers have been used in numerous GUW-studies [3], [5], [6].

The Acoustic group wants to study ultrasonic beam transmission through solid steel plates for other ka numbers within the same frequency area to see how the leaky lamb waves are induced in the steel plate with different ka numbers. It is only done some simulations with different ka numbers, but it is wanted to compare these simulations with measurements. The Acoustics group at the University of Bergen studied the changes of the first symmetrical and anti-symmetrical modes in the leaky lamb waves through a steel plate where simulations of the behaviours with three different ka numbers were made [7]. Aanes et al. investigated the changes in the S_1 mode by varying $\theta_{-3dB}(f_b)/\theta_{ZGV}$ by varying d, and implicit vary the radius, a, of the source [7]. θ_{ZGV} is the in-fluid plane-wave angle at which the group velocity of the S_1 Lamb mode of a free plate is zero [7]. The effects was investigated for $ka = 14$, 20 and 42 with simulations, and it was found that a low $\theta_{-3dB}(f_b)/\theta_{ZGV}$ indicated that $f_b \to f_c$ [7]. Aanes et al. saw that $ka = 42$ was closer to the plane wave theory than a lower ka number was [7]. Therefore, transducers with ka numbers of 17 and 46, with a thickness mode T_{E1} and center frequency at 500 kHz, lower and higher than those earlier constructed at the University of Bergen, are made for future use in the GUW study.

Therefore the goal is to construct and characterize transducers with a center frequency of 500 kHz but with different ka-numbers, below and above 26, which can be used further for equivalent studies for Guided Ultrasonic waves in water. These transducers are constructed equivalent to the method Aanes used with the same piezoelectric material, Pz27 with a f_{TE1}=500 kHz, but with other diameters than Aanes used [1]. It is also wanted to look at another type of backing layer than Aanes to change the bandwidth. For these transducers, measurements need to agree well with the simulations, so it is also a goal to see how well these transducers can agree with the

FE-modeling. The goal is to get the simulations in close agreement with the measurements for each step in the transducer construction. Every step of the construction process is described for establishing a transducer construction method.

1.2 Objectives

This work aims to build piezoelectric transducers with two different ka-numbers of 17 and 46 with $f_{TE1} = 500$ kHz, and compare the results with the results in [1]. Pz27 elements from Meggitt Ferroperm [8] is used with standard dimensions with (D_p x T_p) of 44 x 4 mm and 16 x 4 mm. The goal is to construct the piezoelectric transducers step by step and show measurements and simulations of every step. In addition, a detailed explanation of the construction processes is given. Three conventional piezoelectric transducers with a ka number of 17 and three with a ka number of 46 are made with one front layer, a backing layer, a steel casing and a UHF connector at the back.

Electrical measurements in air are conducted after every construction step, and simulations are made. Adjusted simulations have been made to give better agreement between the measurements and the simulations and to find out the problem with the construction when the measurements have not been in close agreement with the simulations. In addition, simulations of solder on the back electrode of the Pz27 disk have been made to see if the solder affects the electrical response. Vacuum gaps in the conductive adhesive layer have also been simulated to see if the difference between the measurements and simulations could be due to some air in the conductive adhesive layer.

Methods for attaching the front layers to the piezoelectric disks on both dimensions have been found and verified after multiple tries. Tungsten epoxy mixture has been used as the backing layer, where a cone is made in the back. Some adjustments in the simulation setup from [1] has been made. Simulations of small steps to create a cone are made to simulate the cone in the backing layer. The front layer has been simulated into the hatch in the casing as it is made.

The source sensitivity has been measured for one transducer with a disk with (D_p x T_p) of 44 x 4 mm and one transducer with a disk with (D_p x T_p) of 16 x 4 mm, and of the prototype transducer no. 3 in [1]. In addition, the beam pattern has been measured at 575 kHz.

1.3 Literature

Typical ultrasonic transducers use a piezoelectric disk to convert between electrical and mechanical energy. On this piezoelectric disk, acoustic matching and backing layers are bonded on and surrounded by a casing for protection like the method used by Aanes [1]. Besides these conventional transducers construction methods, other various techniques are used to construct piezoelectric transducers for measuring guided waves through steel plates. Gachagan et al. made in 2005 a transducer array for this purpose for efficient generation and detection of ultrasonic symmetric Lamb waves [9]. A piezoplatelet transducer was made by an array of small piezoceramic plates embedded within a soft polymer matrix [9]. The piezoceramic materials they used were modified lead titanate and lead metaniobate [9]. For measurements, the transducer was bonded onto the surface of the steel plate with a thin layer of epoxy. The transducer was shown to operate in the thickness mode and efficiently generate and receive antisymmetrical and symmetrical Lamb wave modes in metallic and fibre-reinforced polymer composite plates [9].

Castaings et al. made in 1999 a flexible interdigital PVDF Lamb wave transducer for use in the frequency range $0.5-4$ MHz [10]. The transducer had a rectangular, typical, apodised electrode pattern. Castaings stated that a benefit of such design was a reduction of side lobes in the transducer angular aperture for making the generation and reception of a pure Lamb mode easier [10].

Hidayat et al. made a conventional transducer with a tungsten epoxy backing layer [11]. A 1 MHz piezoelectric disk (PZT-8) was used as the active element with two wires attached to each side of the disk. An epoxy layer was applied on the front side of the disk and worked as a matching layer [11]. The disk with the front layer and backing layer was fastened inside an aluminium housing with an RG58 coaxial cable on one of the side surfaces. A high purity non-spherical tungsten powder ($99,99\%$) with a distribution of $1\mu m$ was mixed in epoxy at a weight ratio of 4:1. A shaker milling was used for obtaining a homogenous distribution of the tungsten powder in the epoxy, before the mixture was vacuum cured. The theoretical density was calculated as 3819 g/cm^3 while the measured density was 3156 g/cm^3 [11]. It was seen that the tungsten particles were homogeneously distributed in the

composite and that some air bubbles were trapped despite the use of vacuum-curing. However, the measurements showed that the mixing ratio of 4:1 was sufficient for the composite to work as a backing material [11].

In 2019 Bolstad et al. investigated intermetallic bonding as an alternative to polymeric bonding in ultrasound transducers [12]. Bolstad et al. [12] looked at the use of SLID (Solid-liquid interdiffusion) bonding which consisted of gold and tin, and compared this with a common polymeric epoxy material. They saw that the SLID bonding with a higher characteristic impedance was less influenced by a thickness variation than a soft epoxy bond. As well, a slight increase in the soft epoxy bond thickness gave a bigger reduction in the bandwidth compared to a higher thickness increase of the SLID bond [12].

In 2010 Abas et al. looked at the mix ratio of tungsten powder for obtaining a homogeneous mixture [13]. Different mixing ratios between 1:1 and 8:1 was used. It was stated that a bigger ratio than 8:1 failed because of saturation. The highest ratio made a backing layer with an acoustic impedance of 7.5 MRayls. However, it was seen that it was not a big difference between ratios of 4:1 and 8:1 in terms of the bandwidth and that despite ratios, it did not match the impedance of the PZT element used [13]. Another study from 2005 by Sugawara et al. [14] concluded that it was impossible to form a composite as a solid when the concentration of the tungsten powder was over 90% despite the particle size [14].

1.4 Outline of the thesis

In **Chapter 2** the theoretical basis used in this thesis is presented regarding the theory behind the simulation setup and the calculations done in the present work. The construction methods of the different transducers are presented in **Chapter 3**. In **Chapter 4** all the measurement methods and setup are presented. In **Chapter 5** the simulation setup is presented. The simulation setup are first verified with transducer no. 2 from [1], and the simulation setup for this thesis is given, with the changes done for adjusting the simulations to the measurements shown in Chap. 6. In **Chapter 6**, all the results are shown. First, the preliminary construction work results are presented, with results after the soldering process, after the disks are attached to the front layers, and after attaching the casings and making the backing layer with all the discussions, problems, and choices on the way. At the end of this chapter, all the simulations and measurement results for the finished transducers are presented. **Chapter 7** takes up the overall findings, conclusion and discussion for improvements and further work. The **Appendices** gives all the source codes used for the simulations and measurements.

Chapter 2

Theory

2.1 Introduction

This chapter presents the theory behind this thesis's simulations, measurements, and calculations. First, an explanation behind the piezoelectric disk and the piezoelectric effect is given in Sec. 2.2 and 2.3. In Sec. 2.4, an explanation behind the theory of the Finite Element simulations is explained with the most important equations. Then a brief description of how the material constants are calculated is given in Sec. 2.5. In Sec. 2.6, the method for calculating the thickness of the front layer and the characteristic acoustic impedance is shown. Then the most important equations used for making the measurements are given, the Source Sensitivity in Sec. 2.7, Rayleigh distance in Sec. 2.8 and the Beam pattern in Sec. 2.9.

2.2 The piezoelectric disk

The piezoelectric disks used in this thesis is Pz27 from Meggitt Ferroperm [8]. The Pz27 material is a soft lead zirconate titanate material with several qualities, like reliable coupling factors and charges coefficients, high Curie temperature, low mechanical quality-factor, low-temperature coefficients and low ageing rates [8].

The ka number of the piezoelectric disks is calculated as [15]

$$ka = \frac{2\pi f_{T_{E1}} a}{c_f} = \frac{\omega a}{c_f} \tag{2.1}$$

where f is the frequency of the thickness mode, T_{E1}, a is the radius of the piezoelectric disk, c_f is the sound velocity in water [15], and

$$k = \frac{\omega}{c_f} \tag{2.2}$$

is the wavenumber, where ω is the angular frequency [15].

The wavelength of the material is defined as [15]

$$\lambda = \frac{2\pi}{k} \tag{2.3}$$

and the characteristic impedance of the material is defined as [15]

$$Z = \rho_0 c_p \tag{2.4}$$

where ρ_0 is the density of the material and c_p is the phase speed of the material [15].

2.3 Piezoelectric effect

The transducers constructed in this work is based on the piezoelectric effect. The material used, Pz27 [8], has to be polarized for the piezoelectric qualities to be present. In an unpolarized condition, electrical dipoles linked to the domains in the material are randomly orientated [16]. Microscopically, a net dipole moment is obtained for the material equal to zero. After the polarization, a partly alignment of the dipoles is obtained, with a net dipole moment as a result [16]. By polarization, an extent in the polarization direction and a contraction in the direction normally on the polarization direction is achieved [16]. The electrode that has been connected to the positive part is marked and is on the backside of the material used in this thesis.

After the polarization, the material generates an electric potential when it is exposed to a mechanical force [16]. If the material is exposed to an electrical potential, it will generate a mechanical force, which is called the inverse piezoelectric effect [16].

When the material is polarized, it is used a strong electrical field. It is common to put the z-axis in the same direction as the direction the polarization in the material is given, which gives cylindrical symmetrical properties about this axis [17]. The movement is assumed to be in the thickness direction, z-direction [16].

The polarization of the piezoelectric materials gives a strong mechanical voltage to the material. This voltage will be trigged gradually over time, providing ageing effects in the material properties' [17]. Different additives can be used to get a lower voltage inside the material and better ageing effects. This ageing effect varies logarithmically over time [17].

With ageing, the piezoelectric properties, the dielectric constants, dielectric loss, and coupling factor will decrease [17]. In contrast, the elasticity properties, loss, mechanical C-factor, elastic stiffness, and frequency constant will increase [17].

2.4 Finite Element Method

The simulations in this thesis are all conducted with the software Finite Element Modeling of piezoelectric structures (FEMP) 5.0 and 6.1B [4]. FEMP 6.1B was available after the start of this work. FEMP is a software developed for simulating piezoelectric elements/transducers in both vacuum and fluids. The software has been developed by the Acoustic Group of the University of Bergen in cooperation with Christian Michelsen Research (CMR) [4]. All the theory behind the software is given in [4]. Among all the existing versions, the same equations are used [4]. A few of the essential equations will be presented here. FEMP is used in this thesis to simulate the admittance, source sensitivity and beam pattern.

The simulations in the software are modelled as an axis-symmetric problem, where the piezoelectric disk is assumed to be polarized in the thickness direction [4]. The simulated region is divided into a finite number of smaller volumes/elements, separated between finite and infinite elements. Within these elements, several nodes are defined, where the unknown quantities are determined [4].

The simulations made in this thesis for comparing with the measurements conducted in air are simulated in a vacuum since the fluid load of air is assumed to be small. The finite element equation in a vacuum is given as [4]

$$-\omega^2 \begin{bmatrix} M_{uu} & 0 \\ 0 & 0 \end{bmatrix} \begin{Bmatrix} \hat{u} \\ \hat{\phi} \end{Bmatrix} + \begin{bmatrix} K_{uu} & K_{u\phi} \\ K_{\phi u} & K_{\phi\phi} \end{bmatrix} \begin{Bmatrix} \hat{u} \\ \hat{\phi} \end{Bmatrix} = \begin{Bmatrix} F \\ -Q \end{Bmatrix} \tag{2.5}$$

where $[\,]$ indicates a matrix and $\{\}$ indicates a vector. A time-harmonic solution with $e^{i\omega t}$ is used, where ω is the angular frequency [4]. $[M_{uu}]$ is the global mass matrix, $\{\hat{u}\}$ is the global displacement vector, $\{\hat{\phi}\}$ is the global electrical potential vector, $\{Q\}$ is the global charge vector, $\{F\}$ is the surface traction vector, $[K_{uu}]$ is the global stiffness matrix, $[K_{u\phi}]$ is the global piezoelectric stiffness matrix, where $[K_{\phi u}]$ is the transposed matrix of $[K_{u\phi}]$, $[K_{\phi u}] = [K_{u\phi}]^T$, and $[K_{\phi\phi}]$ is the global dielectric stiffness matrix [4].

For the simulation calculations in this thesis, Direct Harmonic Analysis is used. In the Direct Harmonic Analysis, the transducers response function is calculated directly from manipulations of the matrices equations [4].

From the first equation in Eq. 2.5 the Direct harmonic analysis $[D]$ can be calculated [4]

$$[D]\{\hat{u}_0\} = -[H_{u\phi}]V \tag{2.6}$$

which is defined as [4]

$$[D] = [H_{uu}] - \omega^2 [M_{uu}] \tag{2.7}$$

Next, the displacement $\{\hat{u}_0\}$ is given as [4]

$$\{\hat{u}_0\} = -[D]^{-1}[H_{u\phi}]V = ([H_{uu}] - \omega^2[M_{uu}])^{-1}[H_{u\phi}]V \tag{2.8}$$

When inserting Eq. 2.8 in the second equation in Eq. 2.5 the admittance is found [4]

$$Y(\omega) = \frac{I}{V} = i\omega \left\{ [H_{u\phi}]^T [D]^{-1} [H_{u\phi}] - [H_{\phi\phi}] \right\} \tag{2.9}$$

The simulations made for comparing the measurements conducted in water are conducted with an infinite fluid loading of water around the transducer. The finite element equations for a piezoelectric disk immersed in an infinite fluid medium is given as [4],

$$-\omega^2 \begin{bmatrix} M_{uu} & 0 & 0 \\ 0 & 0 & 0 \\ 0 & 0 & -M_{\psi\psi} \end{bmatrix} + i\omega \begin{Bmatrix} \hat{u} \\ \hat{\phi} \\ \hat{\psi} \end{Bmatrix} + \begin{bmatrix} 0 & 0 & C_{u\psi} \\ 0 & 0 & 0 \\ C_{\psi u} & 0 & 0 \end{bmatrix} \begin{Bmatrix} \hat{u} \\ \hat{\phi} \\ \hat{\psi} \end{Bmatrix} + \begin{bmatrix} K_{uu} & K_{u\phi} & 0 \\ K_{\phi u} & K_{\phi\phi} & 0 \\ 0 & 0 & -K_{\psi\psi} \end{bmatrix} \begin{Bmatrix} \hat{u} \\ \hat{\phi} \\ \hat{\psi} \end{Bmatrix} = \begin{Bmatrix} 0 \\ -Q \\ 0 \end{Bmatrix} \tag{2.10}$$

where $[M_{\psi\psi}]$ is the global fluid mass matrix, $[K_{\psi\psi}]$ is the global fluid stiffness matrix, $[\hat{\psi}]$ is the global fluid velocity potential vector, $[C_{u\psi}]$ is the global fluid/structure coupling matrix, where $[C_{\psi u}]$ is the transposed matrix of $[C_{u\psi}]$, $[C_{\psi u}] = [C_{u\psi}]^T$ [4].

The finite element equations are transformed to H-form to simplify the calculation of the response function of the piezoelectric disk [4]. The potential difference between the two electrodes of the piezoelectric disk, V, and the current going to the non-grounded electrode, $I = \frac{dq}{dt} = i\omega Q$ are introduced when converting Eq. 2.10 to H-form [4]. Which gives the equation for the finite element equations for a piezoelectric disk immersed in an infinite fluid medium on H-form [4]

$$-\omega^2 \begin{bmatrix} M_{uu} & 0 & 0 \\ 0 & 0 & 0 \\ 0 & 0 & -M_{\psi\psi} \end{bmatrix} \begin{Bmatrix} \hat{u} \\ V \\ \hat{\psi} \end{Bmatrix} + i\omega \begin{bmatrix} 0 & 0 & C_{u\psi} \\ 0 & 0 & 0 \\ C_{\psi u} & 0 & 0 \end{bmatrix} \begin{Bmatrix} \hat{u} \\ V \\ \hat{\psi} \end{Bmatrix} + \begin{bmatrix} H_{uu} & H_{u\phi} & 0 \\ H_{\phi u} & H_{\phi\phi} & 0 \\ 0 & 0 & -K_{\psi\psi} \end{bmatrix} \begin{Bmatrix} \hat{u} \\ V \\ \hat{\psi} \end{Bmatrix} = \begin{Bmatrix} 0 \\ -I/i\omega \\ 0 \end{Bmatrix} \tag{2.11}$$

where V is the electrical potential between the electrodes of the piezoelectric disk [4]. The matrix $[H_{uu}]$ is defined in Eq. 3.190 in [4], the matrix $[H_{u\phi}]$ is defined in Eq. 3.191 in [4] and the matrix $[H_{\phi\phi}]$ is defined in Eq. 3.192 [4].

From equation three in Eq. 2.11 the velocity potential is calculated as [4]

$$\{\hat{\psi}\} = -i\omega(-[K_{\psi\psi}] + \omega^2[M_{\psi\psi}])^{-1}[C_{\psi u}]\{\hat{u}\} \tag{2.12}$$

The direct harmonic analysis is found by putting Eq. 2.12 in the first equation in Eq. 2.11

$$[D]\{\hat{u}\} = -\{H_{u\phi}\}V \tag{2.13}$$

where the Direct Harmonic Analysis is calculated as [4]

$$[D] = \left\{ [H_{uu}] - \omega^2[M_{uu}] + \omega^2[C_{u\psi}](-[K_{\psi\psi}] + \omega^2[M_{\psi\psi}])^{-1}[C_{\psi u}] \right\} \tag{2.14}$$

From Eq. 2.13 the displacement is found [4]

$$\{\hat{u}\} = -[D]^{-1}\{H_{u\phi}\}V \tag{2.15}$$

The admittance is given as [4],

$$Y = i\omega[\{H_{u\phi}\}^T [D]^{-1} \{H_{u\phi}\} - H_{\phi\phi}] \tag{2.16}$$

and the pressure is given as [4]

$$p = -i\omega\rho_f \{\hat{\psi}\} \tag{2.17}$$

2.5 Material constants

The equations used for calculating the material constants for the backing layers is given as [17]

$$c_{11} = c_p^2 \rho \tag{2.18}$$

where c_p is the compression velocity for transverse waves [17],

$$c_{44} = c_s^2 \rho \tag{2.19}$$

where c_s is the shear wave velocity for longitudinal waves [17], and

$$c_{12} = c_{11} - 2c_{44} \tag{2.20}$$

For isotropic materials, the material properties will not be dependent on the direction in the materials. The stiffness matrix c_{pq} are given on the form [17]

$$[c] = \begin{bmatrix} c_{11} & c_{12} & c_{12} & 0 & 0 & 0 \\ c_{12} & c_{11} & c_{12} & 0 & 0 & 0 \\ c_{12} & c_{12} & c_{11} & 0 & 0 & 0 \\ 0 & 0 & 0 & c_{44} & 0 & 0 \\ 0 & 0 & 0 & 0 & c_{44} & 0 \\ 0 & 0 & 0 & 0 & 0 & c_{44} \end{bmatrix} \tag{2.21}$$

In FEMP, the material constants are calculated with real and imaginary numbers when complex losses are calculated. The imaginary numbers contain a loss factor, Q., e.g. the stiffness matrix in Eq. 2.21 is calculated as

$$c = c^{'}(1 + i\frac{1}{Q_c}) \tag{2.22}$$

where the Q value is the loss value [4].

2.6 Impedance matching

For using a front layer in front of the transducer to increase the bandwidth, it is important to use a front layer that matches the impedance of the piezoelectric disk and the fluid it is radiating in. One method that is used for impedance matching is the method of quarter-wave matching to find the right thickness of the front layer l_m, which is given as [16]

$$l_m = \frac{\lambda_{m,l}}{4} = \frac{c_{m,l}}{4 f_{TE1}} \tag{2.23}$$

where $c_{m,l}$ are the compressional sound velocity of the front layer and $\lambda_{m,l}$ are the corresponding wavelength in the front layer. f_{TE1} is the frequency of the thickness mode of the piezoelectric disk [16].

The ideal characteristic impedance of the front layer is [17]

$$z_m = \rho_m c_{m,l} \tag{2.24}$$

where ρ_m is the density of the front layer. The ideal characteristic impedance of the front layer should be equal to the impedance between the piezoelectric disk and the fluid the transducer radiates into [17]

$$z_m = \sqrt{z_p z_f} \tag{2.25}$$

where $z_p = \rho_p c_p$ and $z_f = \rho_f c_f$ is the characteristic acoustic impedance of the piezoelectric disk and fluid, respectively [17].

2.7 Source sensitivity

The source sensitivity, measured for transducer no. 3 and 4 in Sec. 6.3 is defined as [17]

$$S_v(f) = \frac{P(z = d_0 = 1m, \theta = 0)}{V(f)} \tag{2.26}$$

where $V(f)$ is the input voltage to the transducer as a function of frequency, $P(z = d_0 = 1m, \theta = 0)$ is the free-field on-axis sound pressure at a distance $d_0 = 1m$, assuming far-field conditions at this distance [17]. If the distance is not $d_0 = 1m$, P will then represent an extrapolation of the pressure value in the far-field condition for the sound pressure amplitude at the sound field from the measurement with a distance d_0 on the sound-field in the far-field into the distance is $d_0 = 1$ m [17].

2.8 Rayleigh distance

The far-field distance is achieved when the distance from the source is greater than the Rayleigh distance [17],

$$r > r_r = \frac{A}{\lambda} = \frac{\pi a^2}{\lambda} \tag{2.27}$$

where r is the distance from the source, r_r is the Rayleigh distance for a circular source with radius a, A is the area of the source and λ is the wavelength of the source [17].

2.9 Beam pattern

The beam pattern, measured for the transducer no. 3 and 4 presented in Sec. 6.3 is defined as [15]

$$D(f, \phi) = \frac{P(d_o, f, \phi)}{P(d, f, 0)} \tag{2.28}$$

where $P(d_0, f, \phi)$ is the axial sound pressure amplitude at a distance d_0, assuming far-field conditions at this distance, with an angle ϕ from the acoustic-axis at a given frequency, f [15].

Chapter 3

Transducer construction methods and design

3.1 Introduction

This chapter explains the construction methods used for making the transducers. In Sec. 3.2, the design of the different transducers is shown, with a short explanation of the materials and methods used. The soldering process is described in Sec. 3.3, where the different methods and techniques used is explained. The procedure for attaching the front layers to the piezoelectric disks is explained in Sec. 3.4. In Sec. 3.5, how the casing is attached to the front layer is explained. The procedure of how the backing layer is made and attached inside the casings is described in Sec. 3.6, with the methods used for making a cone back in the backing layer. Finally, how the back casing and connector is attached to the different transducers is described in Sec. 3.7.

3.2 Transducer design

Six transducers with two different dimensions are constructed. The piezoelectric material that is used is a lead zirconate titanate piezoceramic material, Pz27, manufactured by Meggitt Ferroperm Piezoceramics [8]. The Pz27 disks have a standard diameter of 16 mm and 44 mm, and a standard thickness of 4 mm. The measured dimensions of the Pz27 disks are presented in Sec. 4.2. Since the diameters on the piezoelectric disks are different, the other materials' dimensions are adjusted regarding the piezoelectric disks. Regarding the different dimensions, it is also some minor difference in how the connector is attached since the connector has a broader diameter than the transducer made of a Pz27 disk with a diameter of 16 mm. The piezoelectric disks are named with the diameter and a number afterwards to separate the disks, e.g. 16-8 and 44-2. The mechanical workshop at the Department of Physics and Technology made the casings and cut out the front layers in the correct dimensions. A sketch of the two transducers with nominal dimensions is shown in Figs. 3.1a and 3.1b.

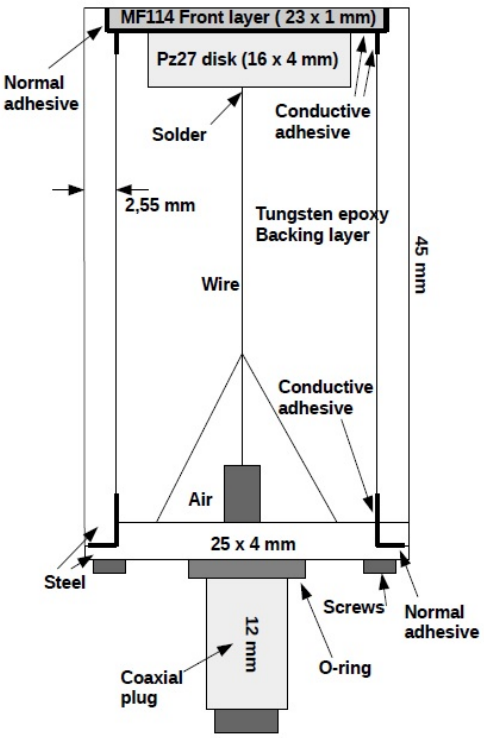

(a)

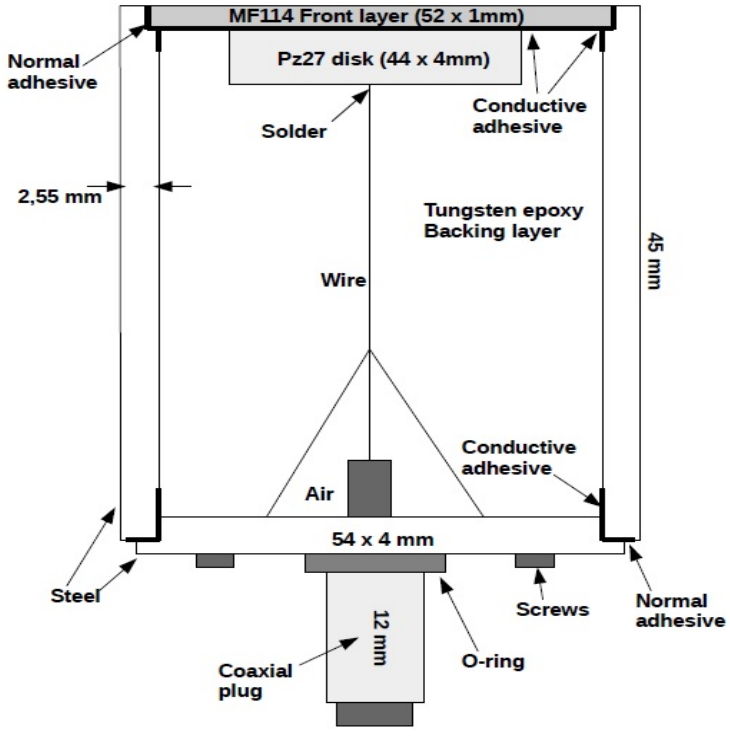

(b)

Figure 3.1: A sketch of the constructed transducers, with the dimensions and materials used. (a) The constructed transducer with a 16 mm diameter disk. (b) The constructed transducer with a 44 mm diameter disk.

In Fig. 3.1 a sketch of the transducers with the materials involved are shown, the different dimensions of the materials are approximated. The correct dimension measurements for the materials used in all the transducers are presented in Sec. 6.3. First, a wire is soldered on the back electrode in the middle of the Pz27 disk. Next, the Pz27 disk is attached to a front layer using conductive adhesive to connect the front electrode at the disk to the casing.

The front layer is then placed in a hatch on top of the steel casing using normal adhesive. For better contact, the conductive adhesive is placed from the back of the front layer to the side of the steel casing. The backing layer is then mixed and poured into the casing. Then, some conductive adhesive is placed on the back end of the steel casing to assure electrical connection through the normal adhesive between the side casing and back casing for getting electrical contact with the coaxial plug. The back casing is then attached to the steel casing using normal adhesive. The coaxial plug is then attached to the back casing after soldering to the wire with normal adhesive, and screws are used for getting electric contact from the steel casing to the coaxial plug. The screws are only fastened inside the back casing and not through the backing layer or the side casing. For the transducer with a piezoelectric disk with (D_p x T_p) of 16 x 4 mm, the screws are fastened at the end of the back casing over the connection to the side casing since the diameter of the connector is close to the diameter of the transducer. For the transducer with a piezoelectric disk with (D_p x T_p) of 44 x 4 mm, the screws are fastened closer to the middle of the transducer since the diameter of this transducer is larger than the connector. The plug inside the cone with air seen in Fig. 3.1 is the connector where the wires are soldered on into the plug. The material constants to the materials used in the construction process are taken from Aanes [1] and Sæther [18] and is given in Chap. 5 together with the simulation setup.

3.3 Soldering

Several methods were used for soldering the wires on the back electrode of the disks. For all the attempts, solder Sn63Pb37 from Elsold [19] was used with wires with three different thicknesses (0.6 mm single strain wire and 0.4 mm and 0.22 mm multiple strains wires). The results from the different methods are presented in Sec. 6.2.1.

The first tries were made by engineer Bilal Hasan Qureshi at the Department of Physics and Technology, UoB. The process met some obstacles, especially for the disks with (D_p x T_p) of 16 x 4 mm, where too much solder often got stuck along the wire. For the first try, the Pz27 disks were first preheated and then soldered at 250°C, at the recommended working range, below the curie temperature at 350°C [8]. This approach did not give satisfying results, especially for the disks with (D_p x T_p) of 16 x 4 mm. The result was better for the disks with (D_p x T_p) of 44 x 4 mm, but there were some deviations around the first thickness mode.

Another try was made where the disks were heated in a controlled environment in an oven (Techno HA-02 forced air convection reflow oven [20]). The disks were first preheated to 160°C for three minutes before a reflow mode was started, where a temperature of 220°C was held for two minutes before the disks were taken out of the oven and soldered. Unfortunately, the disks got some charge from the heating, so gloves had to be used, making it hard to solder properly. The disks got soldered at 225°C, which seemed too low since it was hard to fasten the wires. On the third try, the disk was soldered at 250 °C without preheating with a thinner wire (0.22 mm) to see if this achieved better results. The measured conductance conducted after the disks were soldered without preheating compared to the measurements before the disks were soldered deviated as much as those soldered after preheating, as seen in Sec. 6.2.1.

Other attempts were made by Werner Olsen at the Department of Physics and Technology, UoB, with the same thin wire. First, a machine that blew warm air was used to preheat the disks. Then the disks were soldered right below 250 °C, which gave satisfying results for the first tries. Next, six new disks with the same procedure were soldered, but the result on the disk with (D_p x T_p) of 16 x 4 mm was not satisfying. Some of the disks with (D_p x T_p) of 44 x 4 mm can be used if necessary, but it wasn't as good as the first soldered disks done this way.

Børre Andreas Opedal Lunde soldered more disks under more controlled conditions than in the past tries. The disks were first preheated to around 175 °C (same oven used as before with different settings), which took about three minutes, then the disk was in the oven at 175 °C for three minutes before it was taken out. The temperature in the oven varied between 171-176 °C, the setup and the oven is shown in Fig. 3.2 and 3.3.

(a) **(b)**

Figure 3.2: **(a)**The Techno HA-02 forced air convection reflow oven with the used temperature and time settings. **(b)** Shows how the disk is placed on a metal plate inside the oven.

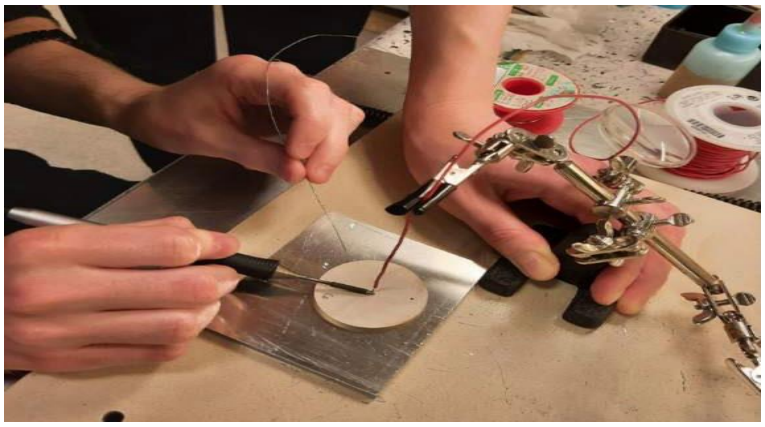

Figure 3.3: The soldering setup with the holder is used to hold the wire in the middle of the disk when soldering the wire to the preheated disk.

The soldering iron was heated up to 270 °C. The wire (0.40 mm) was bent a few millimetres to get better contact with the disks. The wire was attached to a holder, so it was more easily pointed in the middle of the disk. When taking the disk out of the oven, it was necessary to wait about 15 seconds before touching the disk with the soldering iron to avoid electrical shocks. Some time was also used to attach the wire correctly in the holder in the middle of the disk, so the disk possible had lost some heat when soldering. The disks were put on a metal plate (see Fig. 3.2b) in the oven. When taking the disk out, tools were used to carry the metal plate with the disk onto the soldering station seen in Fig. 3.3.

Some of the disks had to be soldered again since some of the wires jumped away after the soldering iron was removed. Also, the disk got cooled down fast, so when this happened, it was necessary to keep the soldering iron a bit longer on the solder to attach it to the disk. Based on the result from the measurements, it did not seem like the extra heat affected the disks since the deviations between the measurements conducted before and after the disks were soldered with this method were similar (see Sec. 6.2.1). The wire from the firsts tries was a thicker wire (0.6 mm) that was soldered vertically. However, this wire fell off on most of the disk. The other wires were thinner and soldered horizontally, which did not fall off.

3.4 Attaching the front layer to the Pz27 disk

The front layer MF114 [21] was attached to the front of the Pz27 disk using a two-component epoxy conductive adhesive from MG Chemicals [22], three different conductive adhesives were used, 8331, 8331S and 8330D [22]–[24]. The conductive adhesive was used to get an electric connection between the front electrode on the disk and the steel casing.

The front layer MF114 was chosen since it has a characteristic impedance of 6.4 MRayl, close to the ideal characteristic impedance of 7 MRayl between the Pz27 disk and water, calculated based on values given in Tab.

5.1 and a sound speed of water of 1485 m/s and a density of 1000 kg/m^3 with Eq. 2.25. Based on the quarter-wave matching method described in Sec. 2.6 with Eq. 2.23, a thickness of approximately 1 mm is chosen.

The mechanical workshop made two plastic forms to easily attach the Pz27 disks in the centre of the front layers, as shown in Fig. 3.4. Several attempts were made to attach the front layers to the Pz27 disk with different techniques to get a good electric response. Eight front layers are attached to disks with dimensions (D_p x T_p) of 16 x 4 mm to get three acceptable results, and five front layers are attached to disks with dimensions (D_p x T_p) of 44 x 4 mm.

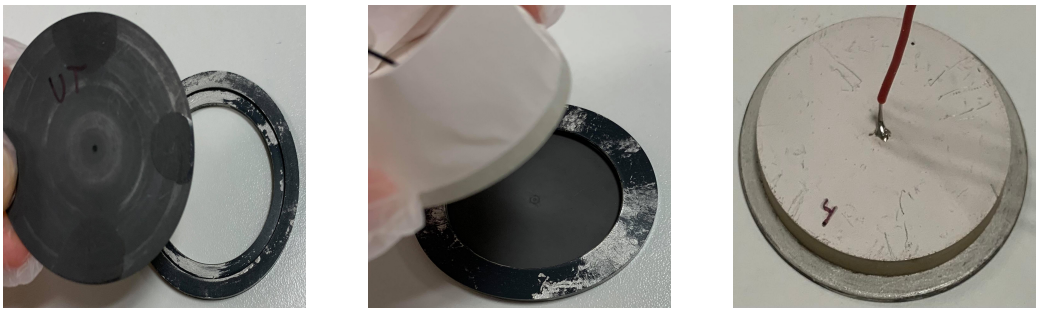

(a) **(b)** **(c)**

Figure 3.4: **(a)** Shows how the front layer is placed inside the plastic form. **(b)** Shows how the disk is placed in the middle of the plastic form for attaching the disk in the middle of the front layer. **(c)** Shows a finished result after a disk is attached to a front layer with conductive adhesive.

In Fig. 3.4a and 3.4b, one of the plastic forms made for attaching the disks in the middle of the front layer is shown. The front layer was placed in the middle ring, while the disk is placed in the inner circle. Fig. 3.4c shows the finished result where a disk is attached in the middle of the front layer with conductive adhesive on the whole back of the front layer. The disk in Fig. 3.4b is covered with tape for avoiding any conductive adhesive being attached to the side or top of the disk.

After the conductive adhesive was set for 24 hours, the thickness of the conductive adhesive was measured. The thickness of the conductive adhesive was measured by measuring the thickness of the front layer, conductive adhesive layer and the disk in ten different places, and then subtracting the thickness of the front layer and the disk from the mean value of these measurements, which then was used in the simulations.

First, it was discussed whether the front layer should be attached to the disk using both conductive adhesive and aluminium foil or only conductive adhesive. Aanes [1] attached the disk to the front layer with just the conductive adhesive. Still, it is expected that the electrical connection will be even better with aluminium foil as an alternative to SLID bonding described in Sec. 1.3.

A test was conducted to see if using aluminium foil between the disk and the front layer gave good results. First, the foil was attached to the front layer using Loctite epoxy extra time [25]. Then the disk (16-8) was attached on top of the foil using conductive epoxy adhesive, 8331 [23]. However, it was hard to avoid any bubbles when attaching the aluminium foil to the front layer, so some air was might trapped in the adhesive, which could be why the measured admittance was not close to the simulation.

A high and inconsistently resistance was first measured on the conductive adhesive on the front layer attached to disk 16-8. Therefore a thicker layer of the conductive adhesive was applied to the foil on the side of the disk to see if this gave better electrical contact. However, this didn't make the electrical contact better. The poor electrical response could be because the disk used during this test was a disk that got soldered, but the wire fell off afterwards. Therefore, disk 16-8 with the front layer was not used further. Based on these results, only conductive adhesive was used further to attach the front layers to the disks.

Disk 16-3 was applied to a front layer with only conductive adhesive. The different components of the conductive adhesive were first mixed, then it was applied to the front layer with a brush to get the layer as thin and even as possible, before the disk where put in the middle of the front layer with the help of the plastic form. However, this test with a thin conductive adhesive layer didn't make the electric contact better than the method described above. On the sides of the front layer, places that were not fully covered with the adhesive were spotted. Therefore it was applied some more conductive adhesive around and just near the disk with a thin brush to see if the contact got better. Using the Impedance Analyzer to check the contact, the admittance measurements fluctuated and were not close to the simulated values.

It was then tried to heat the glue beforehand instead of using it just after it was taken out of the fridge. The working temperature is up to 80 degrees [23]. The glue felt much easier to work with when it was just applied to a piece of the front layer. The two parts got mixed a lot easier. Therefore the conductive adhesive was taken out from the fridge 24 hours before using it to attach more disks to the front layers to achieve room temperature.

Adhesive, 8331S, from GM chemicals [24] was used for attaching disk 44-1, 44-2, 16-7 and 16-2 to front layers. 8331S were tried to see if this conductive adhesive gave better results. The test was done by first applying a fair amount of conductive adhesive with a small brush to cover the whole back of the front layer. The front layer was then taken on top of the disk and moved in circles over the disk. They were then taken apart from each other again. The excess conductive adhesive was wiped off before the disk and front layer was put back together and moved in circles again to avoid air bubbles and make the conductive adhesive uniformly. Next, the disk was centred in the middle of the front layer and pressed firmly together before removing the plastic form used to centre the disk in the middle of the front layer, as shown in Fig. 3.4b. The brush was then used to smooth over the ends of the front layer on the side of the disk where the adhesive was not uniformly. For disk 44-1, it was seen that some conductive adhesive was attached on the side and top of the disk, which could have affected the measurements shown in Fig. 6.7. Therefore, the next disks were covered with tape, as seen in Fig. 3.4b, before attaching them to a front layer. The same method for disk 44-1 was used for disks 44-2, 16-7 and 16-2, just that these disks were covered with tape. After the disks was centred in the middle of the front layer, the plastic form was removed. The brush was then used to smooth over the ends of the front layer on the side of the disk where the adhesive was not uniformly. Everything was then settled for a while before the tape was removed. First, a scissor was used to remove the tape on the back of the disk. Then a tweezer was used to gently remove the tape on the side without touching the disk or the front layer. The brush was then used again to smooth out the conductive adhesive on the side of the disk on the front layer. Before disk 16-2 was attached to a front layer, the conductive adhesive was just taken out from the fridge an hour before it was used. When attaching disk 16-2 to the front layer, it was seen that the adhesive didn't attach uniformly to the disk when they were moved in circles against each other. Also, spots on the front layer were seen without adhesive when they were taken apart again, and the brush was used to smooth out the adhesive. Finally, they were taken together again and moved in circles before they were pressed together.

For disk 44-4, 44-5, 44-7, 16-4, 16-5, 16-10 and 16-6, the conductive adhesive 8330D from MG Chemicals [22] was used to see if this conductive adhesive gave better results since the conductive adhesive 8331 and 8331S was several years old. First, the conductive adhesive was taken out of the fridge a day before to achieve room temperature. Then, the two parts got mixed in a small cup before the cup was held down in warm water at around 40 °C for two minutes [26]. After this, the adhesive was a bit smoother. For attaching disk 44-4 to a front layer, a clump of the conductive adhesive was placed in the middle of the front layer. Next, disk 44-4 was placed and pressed down at the front layer, smoothing out the mixture. The conductive adhesive didn't cover all of the surface of the disk, so the disk and front layer were taken apart again. Next, a small brush was used to cover the rest of the disk and front layer before the disk again were placed in the middle of the front layer, pressed firmly down and moved in some circles before they were pressed together to avoid air bubbles. A weight was placed on top of the disk for further pressing while the adhesive was dried for 24 hours. For disks 44-5 and 44-7, the same method as for disk 44-4 was used, but a bigger clump of the conductive adhesive was placed in the middle of the disk. A bigger clump of the conductive adhesive was used to make sure that all of the disk surfaces were covered with conductive adhesive before it was pressed against the front layer.

For disk 16-4, the conductive adhesive was again taken out from the fridge 24 hours prior. The adhesive was mixed in a plastic cup before being heated up in a box with warm water for about two minutes. A tape was placed around the disk. Then a clump of the conductive adhesive was placed in the middle of the front layer, then the disk got pushed down in the middle of the front layer and moved a bit in circular movements to place it just right in the middle. After the holder was removed, the adhesive that was pushed on the side got smoothed out with a brush, and some adhesive was removed. For disks 16-5, 16-10 and 16-6, the same method as for disk 16-4 was used, but a clump of the conductive adhesive was applied in the middle of the disk. While the front layer was on the table with the backside up, the disks were put in the middle and pressed down on the front layer. This way, it was easier to press the conductive adhesive down and outwards to the ends of the front layer. The excessive adhesive on the sides was taken away, and the parts around the disks that weren't covered were covered using a brush. The tape was then taken away. The sides were then smudged out with a brush, and some excessive adhesive outside the disk was removed.

From the results presented in Sec. 6.2.3, the method that was found to work best was to use the conductive adhesive 8330D from MG Chemicals [22], and take the conductive adhesive out at room temperature 24 hours prior. Then, after the different parts were mixed in a plastic cup, heat the conductive adhesive by holding the

plastic cup in warm water for about two minutes. As well, cover the disks with tape to avoid any conductive adhesive getting attached to the sides of the disks. For the disks with dimensions (D_p x T_p) of 16 x 4 mm, the best method was to apply a clump of the conductive adhesive in the middle of the disk, then press the disk down on the front layer and move it in circles against the front layer. For the disk with dimensions (D_p x T_p) of 44 x 4 mm, the same method was found to be the best, except that a bigger clump of the conductive adhesive had to be applied for assuring that the whole disk got covered with conductive adhesive when pressing it against the front layer.

3.5 Attaching the steel casing

For attaching the steel casing to the front layer, Loctite epoxy extra time [25] was used. It was decided to make a hatch in the casing, so the front layer with the conductive adhesive could be placed in the hatch on top of the casing. Fig. 3.5a shows the top of the casing with the hatch. Equally amount of both parts of the epoxy was mixed with a plastic pin. The glue was first applied with a thin pin on the inner side of the hatch, where the side of the front layer was placed. The front layer was put down with the disk on top, and the casing was then put downwards and pressed down around the front layer as seen in Fig. 3.5b. Then the whole construction was placed on top of a flat, with the front layer down. Then a weight was placed on top for making them stay tightly together while the glue was hardened and set for 24 hours. The measured admittance was not in close agreement with the simulation (see Sec. 6.2.4), so more conductive adhesive was applied around the inner side where the front layer meets the casing, as seen in Figs. 3.5b and 3.5c, which made the admittance measurement be in closer agreement to the simulation a seen in Fig. 6.23.

(a) **(b)** **(c)**

Figure 3.5: The process of attaching the front layer to the casing. **(a)** Shows the top of the casing with the hatch the front layer is put inside. **(b)** Shows the casing after it is placed around the front layer. **(c)** Shows the finished result after more conductive adhesive is applied around the inner side.

3.6 Making the backing layer

The backing layer used was a tungsten epoxy mixture made of SDS-Epofix-Hardener from Struers [27] together with tungsten grains. A tungsten epoxy backing layer was chosen to get a broader bandwidth than what Aanes achieved with an HCP70 backing layer [1]. The tungsten epoxy mixture was mixed with a mass ratio of ten of the tungsten powder, containing a mix of $50-250\ \mu m$ grains, mixed with a mass ratio of 25/3 for resin/hardener.

Before making the tungsten epoxy backing layer, a few tests were made to see how many air bubbles would appear in a construction. It was seen that air bubbles only occurred at the top of the test, and it was a lot fewer air bubbles when the mixture was mixed first and then poured over in another container without mixing it afterwards. The test made where the mixture was poured into another container after being mixed is seen in Fig. 3.6.

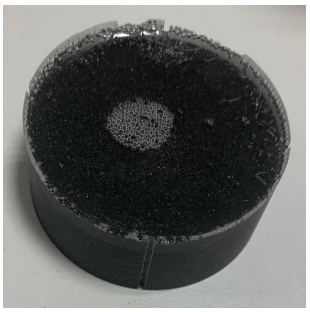

Figure 3.6: A test of a tungsten epoxy backing layer.

As seen in Fig. 3.6, most of the air bubbles are on the top edge of the tungsten epoxy mixture, and some air bubbles are in the middle on the top. No air bubbles were seen on the sides or the front.

A cone was made in the back of the backing layer to reduce reflections in the backing layer. Cones of paper was made with space in the middle for the wire. After the mixture was poured into the casings, the paper cone was placed on top with the wire in the middle, as seen in Figs. 3.7a and 3.8a.

(a) **(b)**

Figure 3.7: The process of making the cone in the tungsten epoxy backing layer inside the casing attached to a front layer with a disk with (D_p x T_p) of 44 x 4 mm. **(a)** The paper piece shaped as a cone is placed inside the tungsten epoxy backing layer for the first three hours after it is poured inside the casing. **(b)** Shows the backing layer with the cone after it is dried.

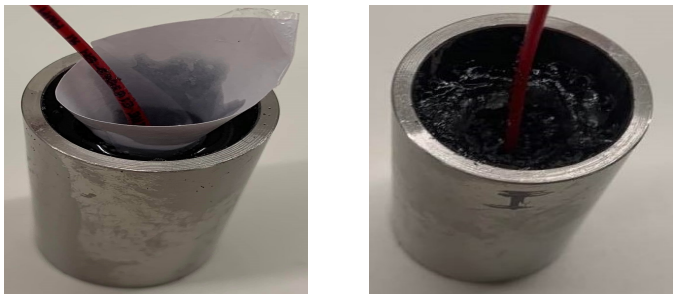

(a) **(b)**

Figure 3.8: The process of making the cone in the tungsten epoxy backing layer inside the casing attached to a front layer with a disk with (D_p x T_p) of 16 x 4 mm. **(a)** The paper piece shaped as a cone is placed inside the tungsten epoxy backing layer for the first three hours after it is poured inside the casing. **(b)** Shows the backing layer with the cone after it is dried.

For the first backing layer that was made inside the casing with disk 44-2, the paper cone was in the middle of the mixture until it dried, as shown in Fig. 3.7a. This resulted in very straight walls in the cone as seen in Fig. 3.9a, and the obtained result shown in Sec. 6.2.5 could be due to this. Therefore, the paper was taken out 3 hours after the mixture was poured inside the other casings. At this time, the mixture had dried enough to stay in place, but not too much, so some of it moved around when the paper was taken away. In this way, it was possible to obtain a more uneven cone. For the backing layer made inside the casing with disk 44-5, the paper cone was taken out a bit too late, so the walls got a bit straight, as seen in Fig. 3.9b, but less straight than for the 44-2. For the backing layer inside the casing with disk 44-7, the cone in the backing layer got more uneven, as seen in Fig. 3.9c. All

the backing layer inside casing with disks with (D_p x T_p) of 16 x 4 mm were as uneven as for the backing layer inside the casing with disk 44-7. It was also seen that fewer air bubbles was in the backing layers when the paper cone was removed before the mixture dried.

(a) **(b)** **(c)**

Figure 3.9: (a) The backing layer inside the casing with disk 44-2 with a cone with straight walls. **(b)** The backing layer inside the casing with disk 44-5 with a more uneven cone. **(c)** The backing layer inside the casing with disk 44-7 with the most uneven cone.

3.7 Attaching the back casing and the connector

For attaching the connector (UHF coaxial connector [28]), a hole in the back casings was made together with screw holes. A hole in the middle of the back casing and four holes for the screws, as seen in Fig. 3.10a, was made to attach the connector to the transducers with an disk (D_p x T_p) of 44 x 4 mm. However, the connector was too big for the transducer with a disk with (D_p x T_p) of 16 x 4 mm to be fastened with the screws holes on the connector, so two new holes were made, as seen in Fig. 3.11a. The back casing was first glued to the side casing using Loctite epoxy extra time [25]. Then the wire was soldered to the electrode at the connector. Then, for fastening the connector [28] to the back casing and making it waterproof, Loctite epoxy extra time [25] was used along with screws for better fastening and for getting electric contact between the steel casing and connector. Finally, an o-ring was placed around the connector to make the connection between the connector and the coaxial cable used for measurements waterproof, as seen in Figs. 3.10b and 3.11b. The result is presented in Sec. 6.3 for the finished transducers.

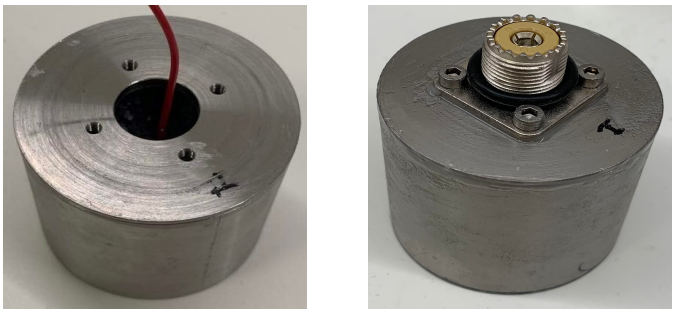

(a) **(b)**

Figure 3.10: The process of attaching the back casing and the connector to a transducer made with a disk with (D_p x T_p) of 44 x 4 mm. **(a)** The back casing with a hole for the connector and four screw holes after being attached to the casing. **(b)** The connector is fastened with four screws, and an o-ring is attached around the connector.

(a) **(b)**

Figure 3.11: The process of attaching the back casing and the connector to a transducer made with a disk with (D_p x T_p) of 16 x 4 mm. **(a)** The back casing with a hole for the connector and two screw holes after being attached to the casing. **(b)** The connector is fastened with two screws, and an o-ring is attached around the connector.

Chapter 4

Measurements and experimental methods

4.1 Introduction

Twenty Pz27 disks of each dimension were ordered from Meggitt Ferroperm AS [8], with standard dimensions (D_p x T_p) of 16 x 4 mm and 44 x 4 mm. The measured diameter and thickness of all the disks are presented in Sec. 4.2. In Sec. 4.3, the measurement setup for the admittance measurements for the different steps in the construction process is shown. Finally, the measurement setup in the water tank with an explanation of how the various measures are done is presented in Sec. 4.4.

4.2 Dimension measurements of the piezoelectric disks

The dimensions are measured by taking ten different measurements of each size and then calculating the mean value. The measurement uncertainty is calculated with the standard deviation and the uncertainty of the measurement instrument. A micrometre with a measurement uncertainty of $\pm 0.1 \mu$m [29] was used for measuring the diameter and thickness of the disks with (D_p x T_p) of 16 x 4 mm and the thickness of the disks with (D_p x T_p) of 44 x 4 mm.

For measuring the diameter of the disks with (D_p x T_p) of 44 x 4 mm, *Sylvac* S_{Cal} *Pro IP*67 electronic calliper [30] was used, with a measurement uncertainty of 20 μm in the measurement range of $0-100$ mm.

The uncertainty in Tab. 4.1 and 4.2 is found from

$$\Delta x_{total} = \sqrt{s^2 + \Delta x_{instrument}^2} \tag{4.1}$$

where $\Delta x_{instrument}$ is the uncertainty of the measurement instrument, and s is the standard deviation to the mean value of the measurements. All the results are presented in Tab. 4.1 and 4.2. The Pz27 disks is numbered with their dimensions. This numbering will be used further in this thesis and in the constructions with the given disks.

Table 4.1: Dimension measurements of the disks with (D_p x T_p) of 16 x 4 mm.

Disk	Diameter [mm]	Thickness [mm]	Disk	Diameter [mm]	Thickness [mm]
16-1	$16,184 \pm 0,003$	$3,974 \pm 0,001$	16-11	$16,187 \pm 0,005$	$3,980 \pm 0,001$
16-2	$16,201 \pm 0,003$	$3,978 \pm 0,002$	16-12	$16,224 \pm 0,016$	$3,978 \pm 0,001$
16-3	$16,184 \pm 0,003$	$3,973 \pm 0,002$	16-13	$16,210 \pm 0,004$	$3,971 \pm 0,001$
16-4	$16,173 \pm 0,004$	$3,968 \pm 0,002$	16-14	$16,189 \pm 0,006$	$3,976 \pm 0,002$
16-5	$16,171 \pm 0,003$	$3,973 \pm 0,001$	16-15	$16,192 \pm 0,004$	$3,977 \pm 0,001$
16-6	$16,206 \pm 0,004$	$3,974 \pm 0,002$	16-16	$16,209 \pm 0,005$	$3,980 \pm 0,016$
16-7	$16,203 \pm 0,002$	$3,988 \pm 0,001$	16-17	$16,227 \pm 0,003$	$3,984 \pm 0,002$
16-8	$16,184 \pm 0,003$	$3,977 \pm 0,003$	16-18	$16,211 \pm 0,003$	$3,990 \pm 0,001$
16-9	$16,186 \pm 0,003$	$3,984 \pm 0,004$	16-19	$16,225 \pm 0,003$	$3,990 \pm 0,001$
16-10	$16,196 \pm 0,003$	$3,974 \pm 0,001$	16-20	$16,234 \pm 0,003$	$3,996 \pm 0,001$

Table 4.2: Dimension measurements of the disks with (D_p x T_p) of 44 x 4 mm.

Disk	Diameter [mm]	Thickness [mm]	Disk	Diameter [mm]	Thickness [mm]
44-1	$44,06 \pm 0,02$	$3,981 \pm 0,002$	44-11	$44,03 \pm 0,01$	$3,984 \pm 0,001$
44-2	$43,93 \pm 0,01$	$3,978 \pm 0,002$	44-12	$44,07 \pm 0,01$	$3,978 \pm 0,001$
44-3	$43,94 \pm 0,01$	$3,980 \pm 0,001$	44-13	$44,08 \pm 0,01$	$3,987 \pm 0,001$
44-4	$44,09 \pm 0,01$	$3,989 \pm 0,002$	44-14	$44,10 \pm 0,01$	$3,996 \pm 0,002$
44-5	$44,02 \pm 0,01$	$4,004 \pm 0,001$	44-15	$44,08 \pm 0,01$	$3,993 \pm 0,001$
44-6	$43,91 \pm 0,01$	$3,989 \pm 0,002$	44-16	$44,08 \pm 0,02$	$4,009 \pm 0,001$
44-7	$44,03 \pm 0,01$	$4,017 \pm 0,002$	44-17	$44,07 \pm 0,04$	$4,021 \pm 0,002$
44-8	$44,12 \pm 0,01$	$3,994 \pm 0,004$	44-18	$43,98 \pm 0,02$	$4,000 \pm 0,002$
44-9	$44,05 \pm 0,03$	$3,993 \pm 0,002$	44-19	$44,03 \pm 0,02$	$3,996 \pm 0,001$
44-10	$43,95 \pm 0,01$	$3,997 \pm 0,001$	44-20	$44,05 \pm 0,02$	$3,983 \pm 0,001$

4.3 Admittance measurements of the piezoelectric disks

HP 4192A LF Impedance analyzer [31] in Fig. 4.1 is used for admittance measurements. The instrument is zero-calibrated at 1 MHz, with both open and short circuits. Then, the measurements are made from $1 - 1000$ kHz with 100 Hz steps with the use of the Matlab program, impanal.m, given in App. A.2. The disk is placed in a holder made of Styrofoam, as seen in Fig. 4.1. The wires on both sides are then pressed towards the disks on both sides. The wires are as short as possible to avoid effects from the wires. A voltage of 0.3V is used during the measurements.

The admittance analyzer has a frequency resolution of 1 mHz in the frequency range 5 Hz to 10 kHz, 10 mHz in the frequency range $10 - 100$ kHz, and 100 mHz in the frequency range $100 - 1000$ kHz [31]. When measuring the admittance with the Matlab program, the admittance analyzer changes the measuring area automatically.

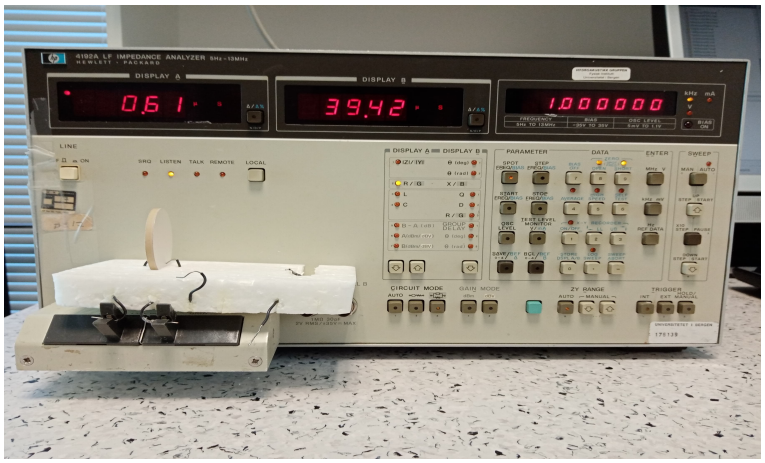

Figure 4.1: The HP 4192A LF Impedance Analyzer used for all the electric measurements.

The same measurement setup as used for measuring a disk without any wires solder onto is used for measuring the admittance for the disks after they are soldered as seen in Fig. 4.2.

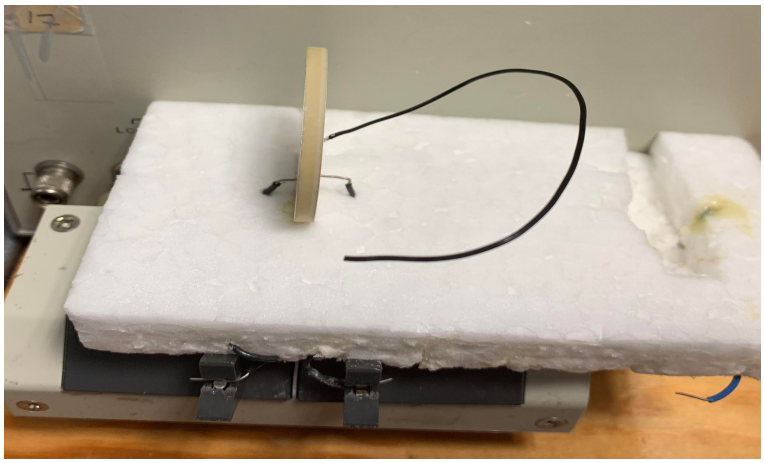

Figure 4.2: A disk with a soldered wire placed in the Styrofoam for electrical measurements with the Impedance Analyzer.

The disks are from different batches since disks with nos. $16-11$ to $16-20$ and $44-11$ to $44-20$ was ordered after the disks with nos. $16-1$ to $16-10$ and $44-1$ to $44-10$. The conductance measurements of all the disks from the different batches were plotted together to see if there were some discrepancies. In Fig. 4.3a the conductance measurements for the first batch, disks with nos. $16-1$ to $16-10$ are plotted together and in Fig. 4.3b the conductance measurements for the disks from the second batch, disks with nos. $16-11$ to $16-20$ are plotted together. In Fig. 4.3c the conductance measurements for two arbitrary disks from each batch are plotted together to see if it is any discrepancies between the two batches.

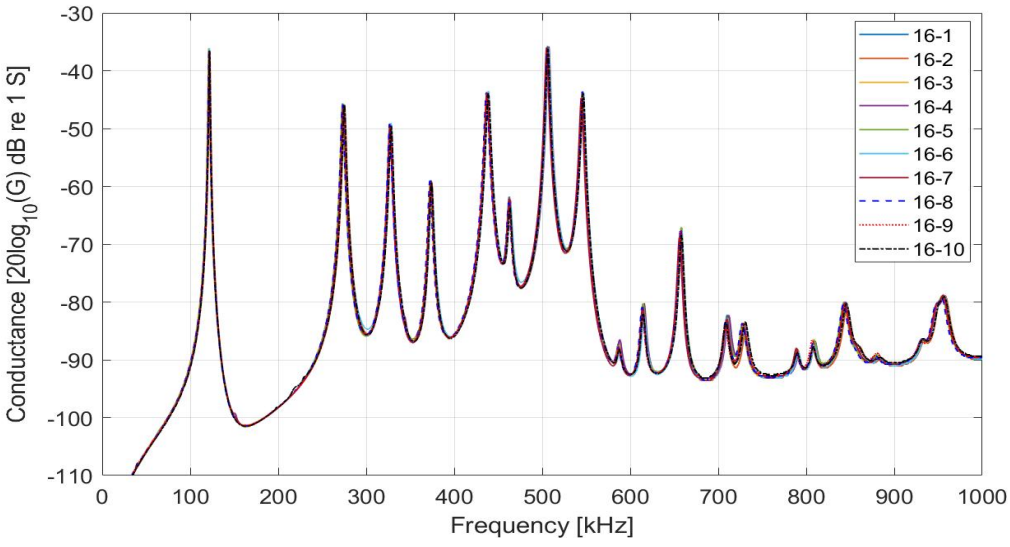

(a)

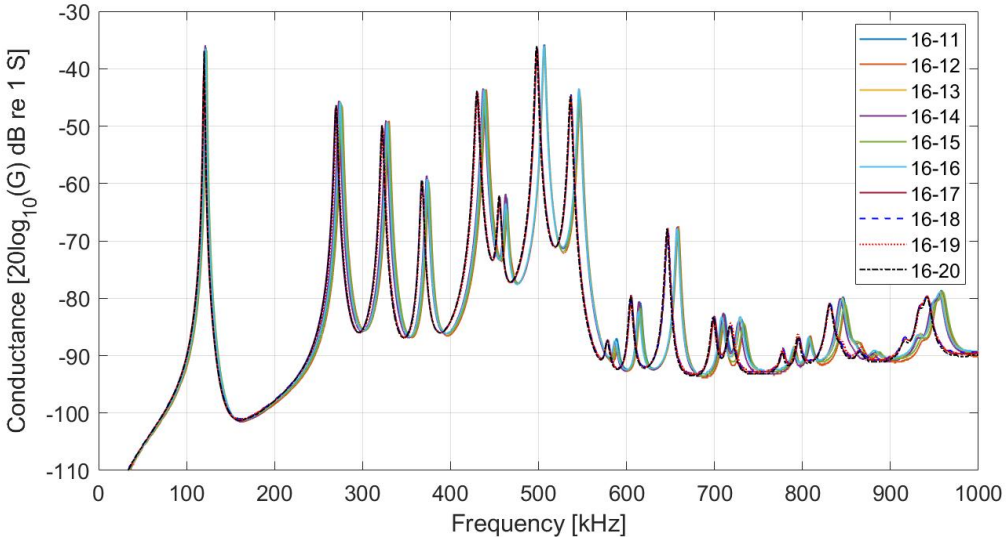

(b)

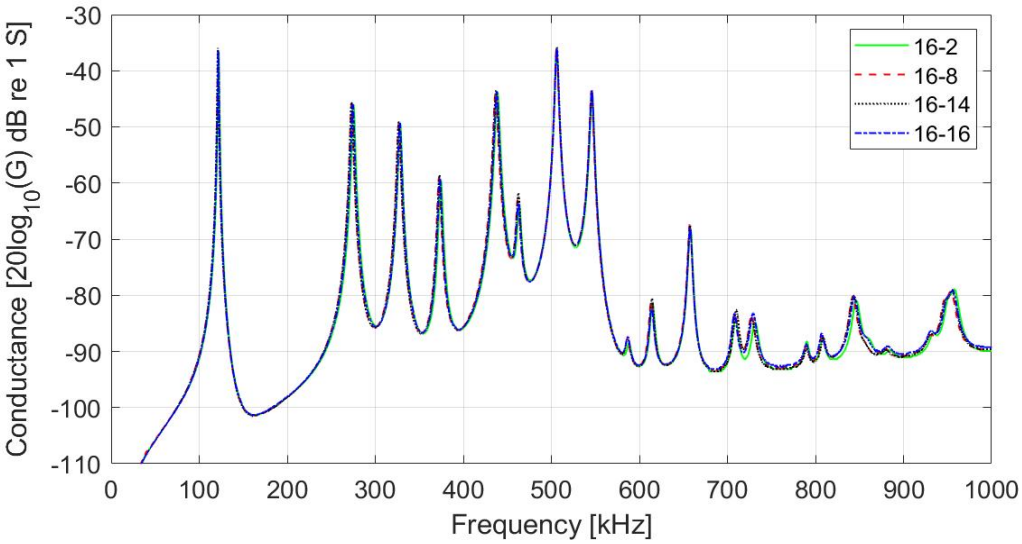

(c)

Figure 4.3: (a) Shows the conductance measurements of the disks from batch one, disks with nos. 16-1 to 16-10. (b) Shows the conductance measurements of the disks from batch two, disks with nos. 16-11 to 16-20. (c) Shows the conductance measurements from two arbitrary disks from each batch, disk 16-2,16-8,16-14 and 16-16.

As seen in Fig. 4.3a, batch one has no big discrepancies. There are minor differences between $600 - 1000$ kHz for the disks. The conductance measurements for disk 16-6 discrepants from the rest at 300 kHz and 475 kHz. More discrepancies are seen in batch two in Fig. 4.3b, where the resonances for disk 16-14,16-15 and 16-6 has a frequency shift after 350 kHz compared to the rest of the disks. In Fig. 4.3c where two arbitrary disks from each batch are plotted together, only minor differences are seen. Compared to Fig. 4.3b it is seen that the disk that has a frequency change from the rest are in close agreement with the disks from batch one.

In Fig. 4.4a the conductance measurements for the first batch, disks with nos. $44 - 1$ to $44 - 10$ are plotted together and in Fig. 4.4b the conductance measurements for the disk from the second batch, disks with nos. $44 - 11$ to $44 - 20$ are plotted together. In Fig. 4.4c the conductance measurements for two arbitrary disks from each batch are plotted together to see if it is any discrepancies between the two batches.

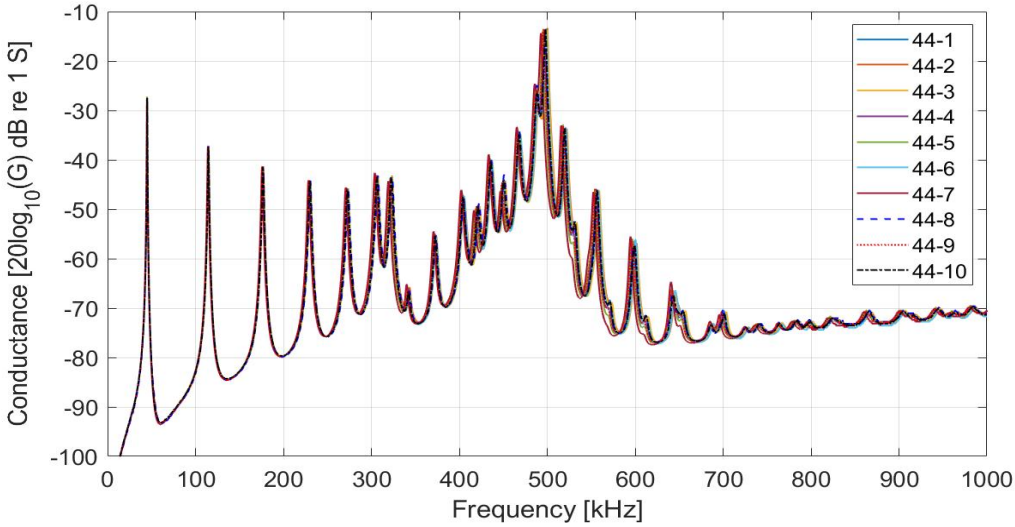

(a)

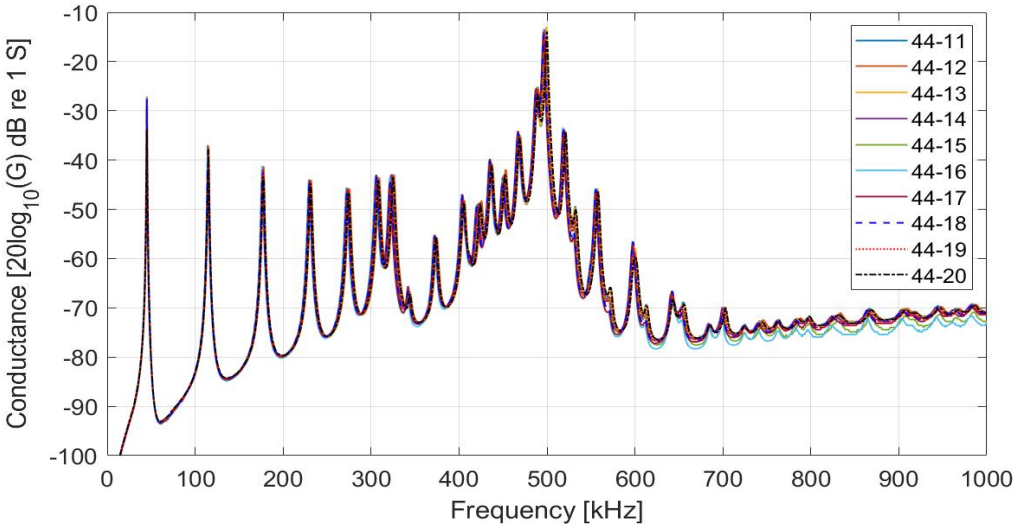

(b)

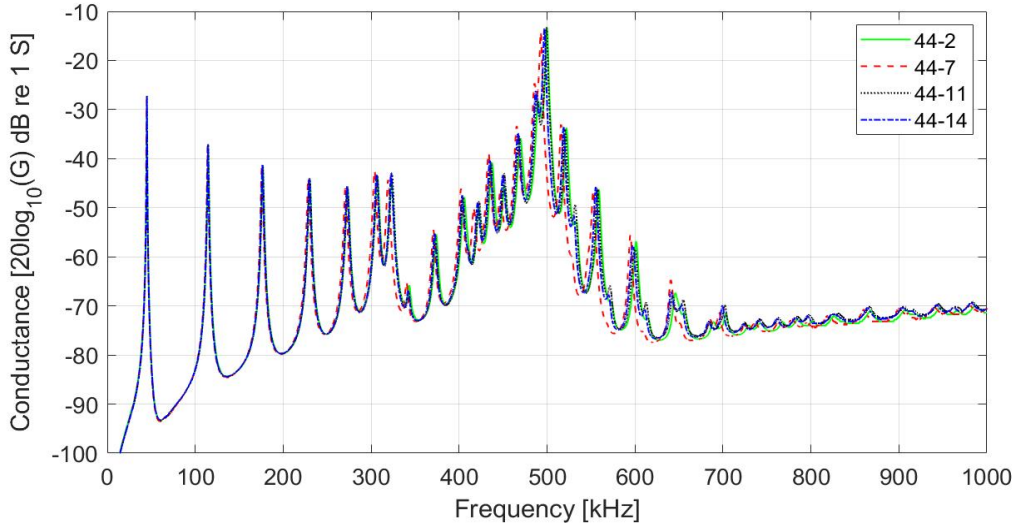

(c)

Figure 4.4: (a) Shows the conductance measurements of the disks from batch one, disks with nos. 44-1 to 44-10. (b) Shows the conductance measurements of the disk from batch two, disks with nos. 44-11 to 44-20. (c) Shows the conductance measurements from two arbitrary disks from each batch, disk 44-2,44-7,44-11 and 44-14.

Some discrepancies are seen around the thickness mode in batch one for the disks with nos. 44-1 to 44-10 in Fig. 4.4a. For batch two, the discrepancies around the thickness mode are minor between the disks, as seen in Fig. 4.4b, but the values for disk 44-15 and 44-16 after 600 kHz is lower than the rest of the disks. In Fig. 4.4c it is seen that the two disks from batch two are in close agreement with the measurement for disk 44-2 from batch one, but that disk 44-7 from batch one discrepant from the rest.

4.3.1 Deviations in the admittance measurements

When zooming in to the measurements shown in Fig. 5.1b, it was seen that the measurements varied by 0.40 dB in some regions, as shown in Fig. 4.5. Therefore it was checked if this variation was due to the measurement uncertainty in the Impedance Analyzer due to noise disturbance. The variances in the measurements were checked by measuring the admittance where the deviations occurred. Since the Impedance Analyzer takes the mean value of the measurements, it was checked if the variations corresponded to the values measured by the instrument by seeing how much the values changed on the same frequencies.

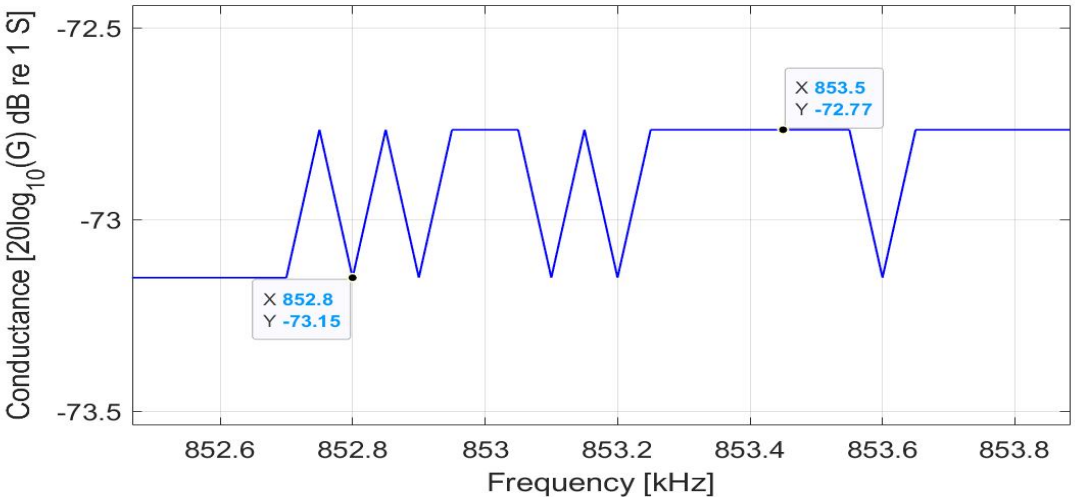

Figure 4.5: A zoomed-in plot for investigating the variances in the conductance measurement for disk 44-7.

With the instrument, it is seen that the measurements around the frequencies 852-854 kHz in Fig. 4.5 vary with 0.01 mS, which give a difference in 0.42 dB, by calculating the log of the measured values, $(20log_{10}(2.1x10^{-4}) - 20log_{10}(2x10^{-4}))$, which corresponds to the measurement variations seen in Fig. 4.5.

4.3.2 Admittance measurements of disk with front layer

The holder in Styrofoam in Fig. 4.6 is used for measuring the admittance when the front layer is attached to the disk. The construction is placed so the back of the front layer with the conductive adhesive is in contact with a wire attached outside the hole the disk lays inside in the Styrofoam seen in Fig. 4.6.

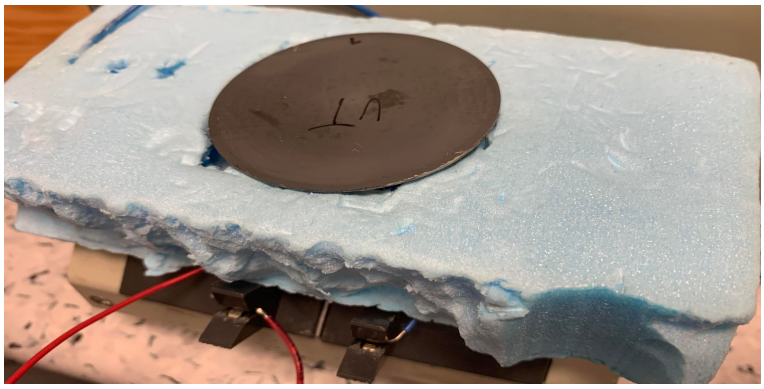

Figure 4.6: The holder in Styrofoam is used for measuring the admittance with the front layer attached to the disk.

4.3.3 Admittance measurements with disk, front layer and steel casing

For measuring the admittance on the structure consisting of a disk, front layer and steel casing, the setup shown in Fig. 4.7 is used. The same setup is also used for measuring the admittance when the backing layer is inside the steel casing.

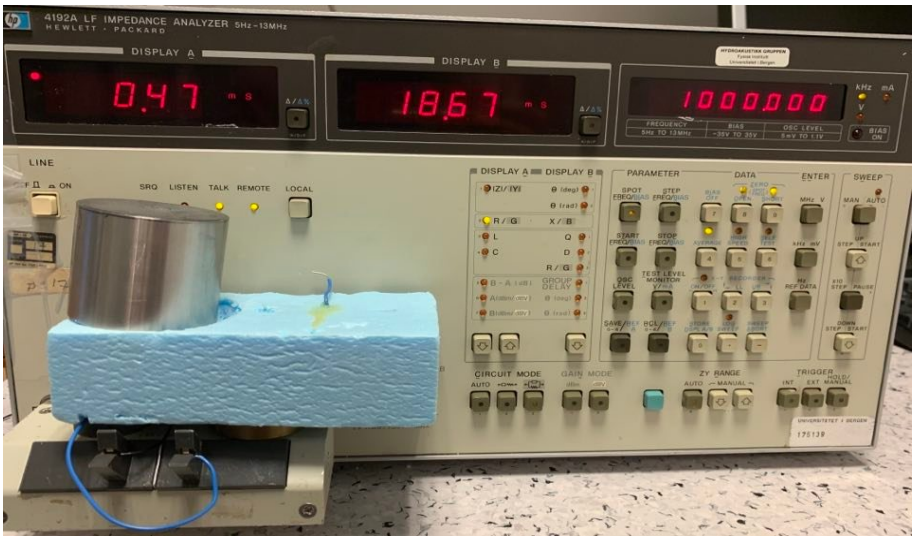

Figure 4.7: The setup used for measuring the admittance of an disk with front layer and steel casing.

As shown in Fig. 4.7, the casing is placed in a holder in Styrofoam. The casing is placed in the Styrofoam with an angle downwards to the right side. In this way, the wire on the inside, which is bent towards the steel casing on the left side, is pressed better towards the steel casing, giving better electric contact.

4.3.4 Admittance measurements for the piezoelectric transducer in air

For measuring the admittance on the transducer after the back casing and coaxial plug is attached, the setup shown in Fig. 4.8 is used. First, a coaxial cable is attached to the coaxial plug on the transducer. Next, a cable with two pinches is fastened to two short wires, which is again connected to the Impedance Analyzer's electrodes. Finally, the transducer is placed on a piece of Styrofoam to radiate freely. The Impedance Analyzer is zero-adjusted by placing another cable in the contact of one of the pinches, and then pressing the other into the connection of the coaxial cable.

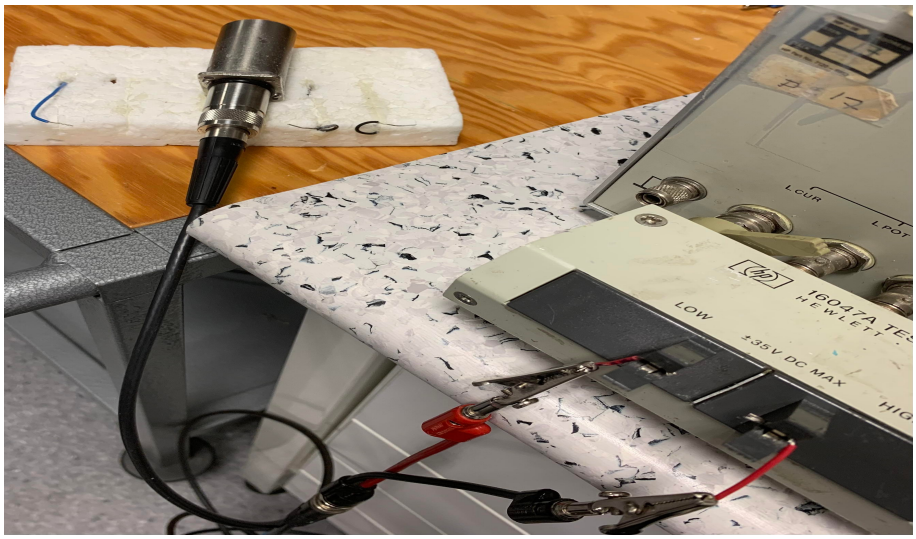

Figure 4.8: The setup used for measuring the admittance of the constructed transducers.

4.3.5 Admittance measurements for the piezoelectric transducer in water

For admittance measurements in water, a water tank, seen in Fig. 4.9 with dimensions $(102-105-401)$ cm³ $(height, y-width, x-length, z)$ is used.

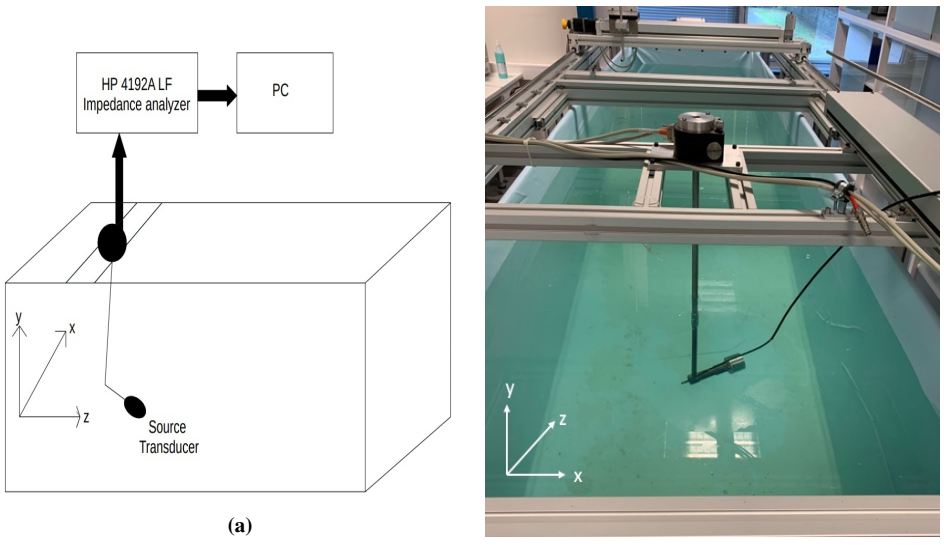

(a) **(b)**

Figure 4.9: The experimental measurement setup for measuring the admittance in water. (a) Sketch of the measurement setup. (b) Photograph of the measurement setup where the piezoelectric transducer are placed inside a metal rod which is fastened at the top of the water tank.

For measuring the admittance on the piezoelectric transducers in water, a waterproof coaxial cable with a length of 3.10 m is attached to the connector on the transducer, connected to the Impedance analyser and immersed in a water tank. The setup is shown in Fig. 4.9. For zero-adjusting, the same method as for air is used. The transducer is placed in and angle downwards in the water tank, towards the right sidewall in the tank. In this way, reflections are reduced since the sound waves are spread out in other directions than towards the transducer.

The admittance measurements in water are conducted from $4-1000$ kHz. For measuring lower than 4 kHz, the measured area on the Impedance analyzer had to be put on manual, making the values significantly changing. The values measured for frequencies below 4 kHz was also very high compared to the simulated values. The measured conductance of the prototype transducer no. 2 from [1] done by this author is compared to the measurement done by Aanes [1] in Fig. 4.10.

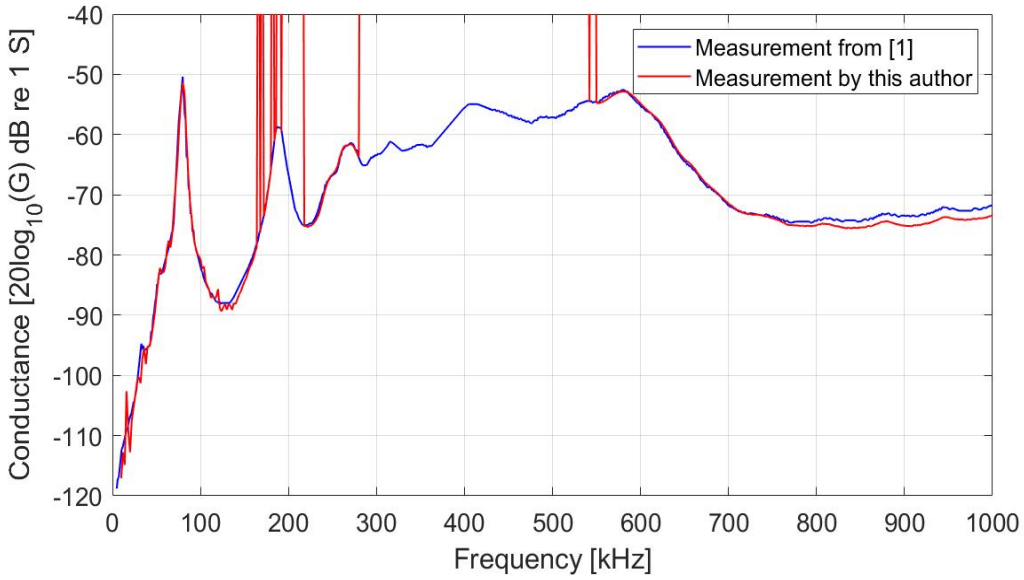

Figure 4.10: The results for the conductance measurements for prototype no.2 from [1] in water, the measurement taken from [1] (blue) compared to the measurement done by this author (red).

Another problem with measuring the admittance in water was spikes in the measurements, as seen in Fig. 4.10. As well, some more disturbance around $4-150$ kHz is seen in the measurement conducted by this author compared to the measurement from [1]. Because of the spikes, the admittance measurements in water presented in Sec. 6.3 is conducted with steps at 500 Hz for avoiding spikes in the measurements.

4.4 Acoustic measurement setup in the water tank

For acoustic measurements in water, a water tank shown in Fig. 4.11b with dimensions $(60-70-160)$ cm³ $(height, y-width, x-length, z)$ is used, the same water tank used by among [1]–[3] with the same instrumentation. A computer controls a HP 33120A [32] signal generator which is setting up a 10V peak-to-peak with a (130 μs duration) sine burst. The resulting waveform v(t) is transmitted to the piezoelectric transducer.

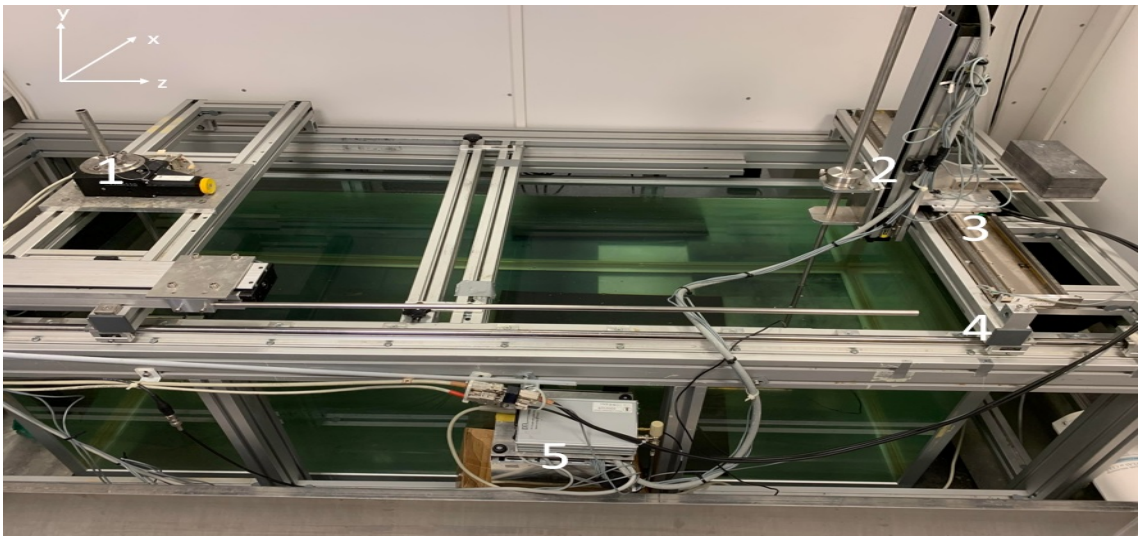

(a)

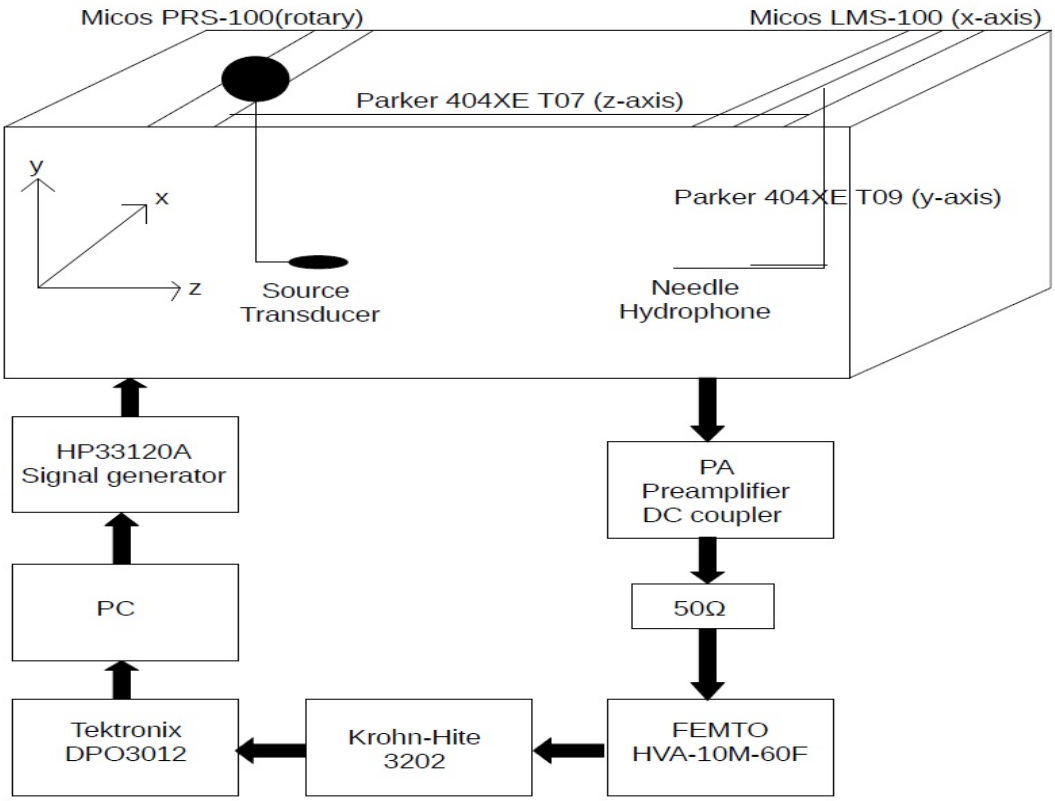

(b)

Figure 4.11: (a) Photograph of the acoustic measurement setup in the water tank with, (1) Micos PRS-100 rotary stage, (2) Parker 404XE T09 (y-axis), (3) Micos LMS-100 (x-axis), (4) Parker 404XE T07 (z-axis) and (5) the PA Preamplifier DC coupler. (b) Sketch of the acoustic measurement setup with the instrumentation.

A 1 mm PVDF needle hydrophone (serial no. 1820) with a 100 mm probe length and a measurement uncertainty of 9 % in the frequency range 0.1 - 1 MHz [33] is connected to a preamplifier (serial no. PA110078) and a DC coupler (serial no. DCPS223) [33] (marked with no. 5 in Fig. 4.11a) to detect the transmitted signal. The signal is terminated with a 50 Ohm loading parallel with the input of a high impedance (1 MOhm) FEMTO HVA-10M-60F amplifier [34] (operating in 40 dB mode) by an RG-58 coaxial cable from the DC coupler. Then the signal is filtered using two Krohn-Hite (type 3202) bandpass filters [35] in series (a 20 kHz Butterworth high pass filter and a 2 MHz Butterworth low pass filter) and digitized by a Tektronix DPO3012 oscilloscope [36]. The oscilloscope uses an 8-bit vertical resolution. Temporal settings are adjusted to 100 000 samples in the 400 μs window, with a sample rate of 250 MHz. An average of 256 bursts are used in the measurements presented. The hydrophone used has been calibrated in house using a 3-transducer reciprocity scheme by [1] in the frequency range $350 - 1000$ kHz, the Matlab program is given in App. A.3 together with the rest of the Matlab scripts used for the acoustic measurements.

Two different motor stages are used to align the piezoelectric source transducer and the needle Hydrophone in the water tank. A Micos rotary stage PRS-100 [37] (marked as no. 1 in Fig. 4.11a) with a max resolution of 0.0001 degrees is connected to a mounting rack where the piezoelectric source transducer is held so that the transducer can be rotated about its front surface in the x-direction. On the carriage where the needle hydrophone is placed, a Micos LMS-100 [38] (marked as no. 3 in Fig. 4.11a) with a max resolution of 0.015 μm makes the hydrophone move linear in the x-direction. A Parker 404XE T07 motor [39] with a positional accuracy of 90 μm is mounted on a carriage that can move in parallel to the z-direction from the rotary stage (marked as no. 4 in Fig. 4.11a). The needle hydrophone can move in the y-direction by a Parker 404XE T09 [40] linear stage motor (marked as no. 2 in Fig. 4.11a) with a positional accuracy of 106 μm.

A cross laser is used to align the needle hydrophone on-axis with the piezoelectric source transducer. Fine-tuning is done acoustically by finding the maximum sound pressure at 500 kHz. Aanes [1] measured the amplification factor of the FEMTO HVA-10M-60-F amplifier as a function of frequency, and saw that the amplification factor was relatively flat in the frequency range with a constant amplification factor of 45.74 dB, which is also used

when conducting the acoustic measurements in this thesis. Aanes also measured that the filter's response varied by up to 1 dB in the frequency range of 100 kHz to 1 MHz [1].

The measurements for transducer no. 3 in [1] is tried to verify as close as possible to know if the measurements for the transducers presented in Sec. 6.3 is done correctly. The source sensitivity measurements are made over the frequency range of $200-1000$ kHz. The result for the source sensitivity measurements conducted by this author of prototype no. 3 transducer from [1] compared to the measurements in [1] is shown in Fig. 4.12. The source sensitivity measurements in the water tank were measured with a distance of $d = 0.885$ m between the source transducer and the needle hydrophone. The measurements are extrapolated spherical out to one meter when calculating the source sensitivity.

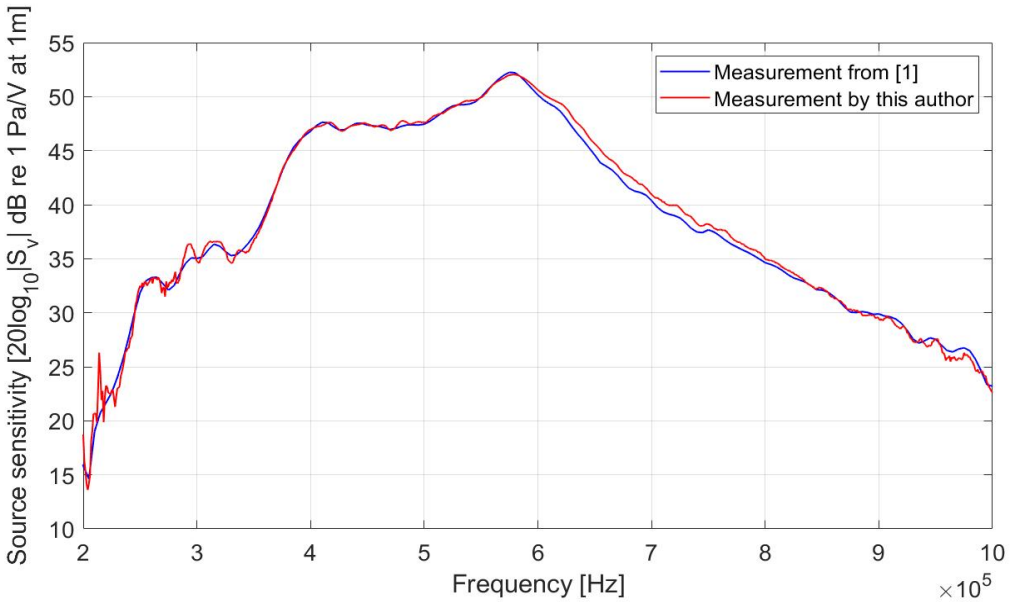

Figure 4.12: The results for the source sensitivity measurements with prototype no. 3 from [1] in water, the measurement from [1] (blue) compared to the measurement done by this author (red).

As seen in Fig. 4.12, the measurement conducted by this author is close to the measurements from [1], but has some more disturbance between 200-300 kHz. This is probably because the needle hydrophone is not perfectly aligned with the source transducer. As well, Aanes used a length of $d = 0.9065$ m [1] when conducting these measurements, which makes the source transducer closer to the far-field conditions, which could give less disturbance in the measurements. The bandwidth, which is measured by measuring the width between two points at the blue curve in Fig. 4.12 which is 3 dB down from the max value, is measured to be 83 kHz.

For measuring the beam pattern, the same distance of $d = 0.885$ m between the transducer and hydrophone is used. The beam pattern was measured at 575 kHz using the prototype transducer no. 3 from [1] and compared to the measurements in [1]. The results are shown in Fig. 4.13.

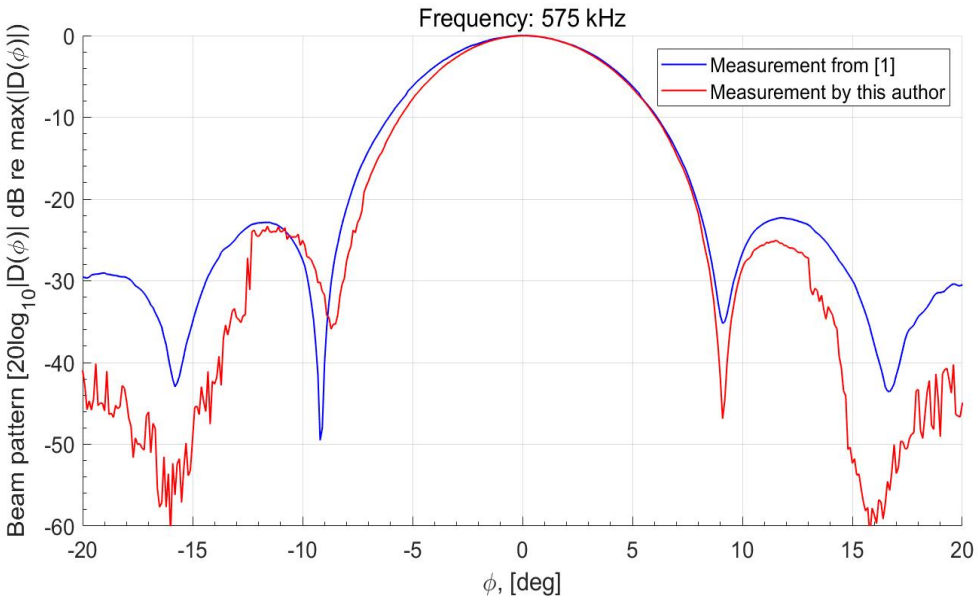

Figure 4.13: The results for the beam pattern measurements for prototype no. 3 from [1] in water, the measurement from [1] (blue) compared to the measurement done by this author (red).

It was a problem with finding a steady-state region in the signals for calculating the beam pattern. As seen in Fig. 4.13 a reasonable agreement between the measurements conducted by this author and the measurements conducted by [1] is seen between -10 to 10 degrees. It seems that the transducer has been slightly away from the on-axis compared to the measurement by [1], since the main lobe goes further down on the right side compared to the measurement by [1]. The beam radius, which is defined at the main lobe down 3 dB from the center [15] is 3.5 degrees for transducer no. 3 from [1].

Fig. 4.14 shows the signals at 15 and 40 degrees away from the on-axis. As seen in Fig. 4.14, no steady state region is obtained at 15 degrees, and at 40 degrees it is impossible to distinguish the signal from the noise.

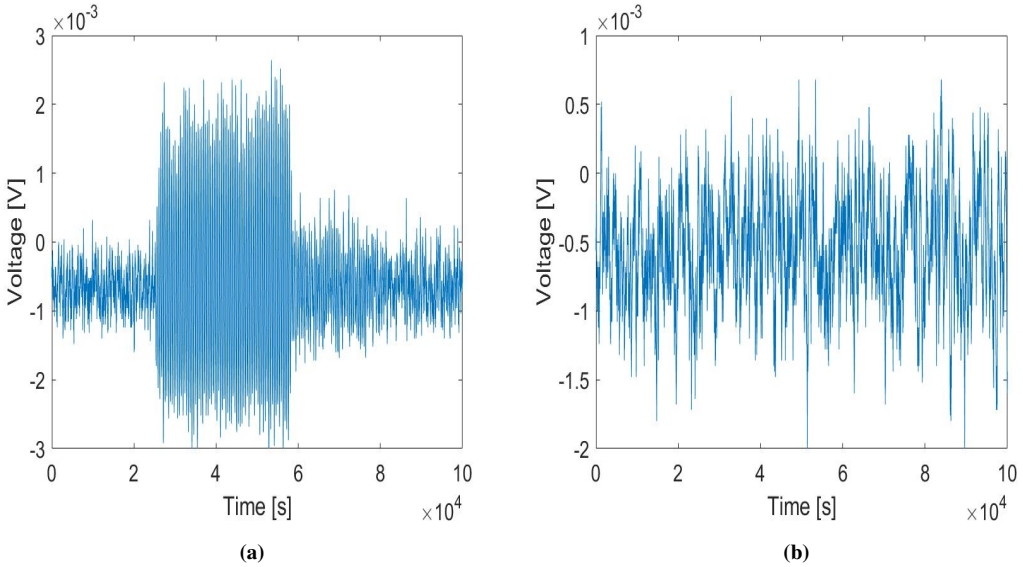

(a) **(b)**

Figure 4.14: (a) The signal obtained at 15 degrees away from the on axis. (b) the signal obtained at 40 degrees away from the on axis.

It could also be some ageing effects on the transducer or the hydrophone. As well, the hydrophone should be calibrated every, which has not been done since Aanes did it before conducted the measurements in [1]. Therefore it is likely that variations in the source sensitivity and beam pattern have varied since Magne Aanes made the measurements in [1].

4.4.1 Rayleigh distance

The Rayleigh distance for the piezoelectric disks with a standard dimension (D_p x T_p) of 16 x 4 mm and 44 x 4 mm is shown in Figs. 4.15a and 4.15b as a function of frequency from 1-1000 kHz.

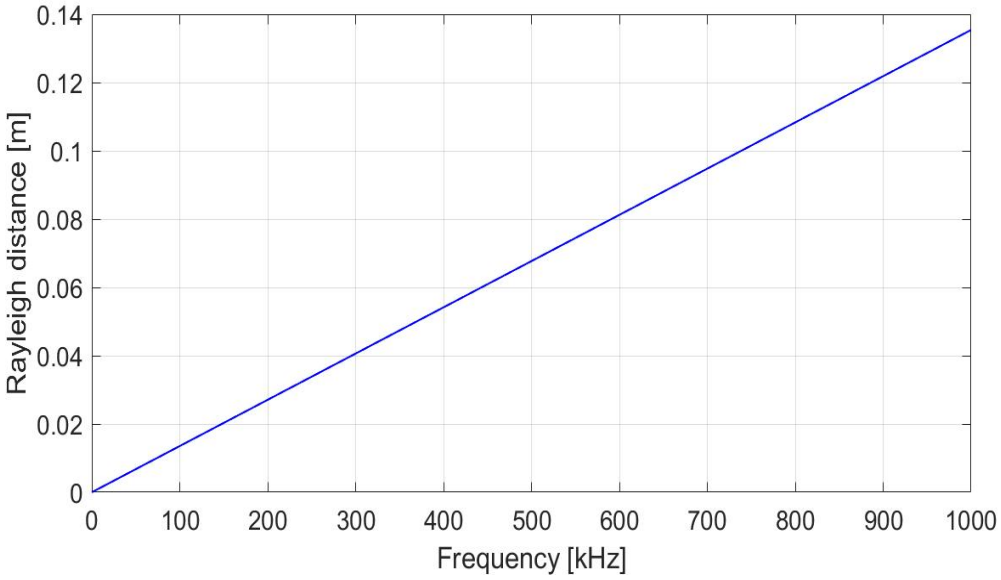

(a)

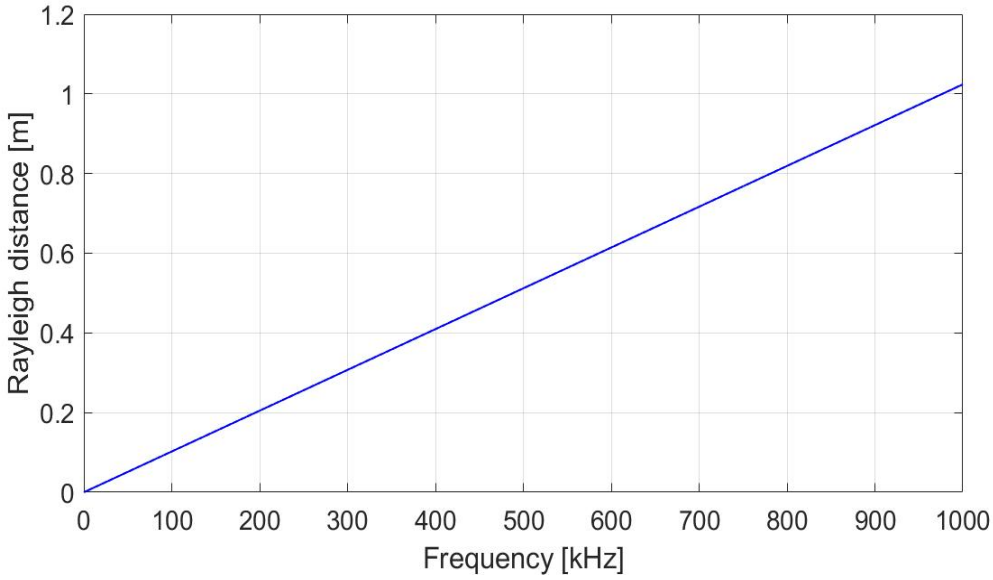

(b)

Figure 4.15: (a) The Rayleigh distance for an disk with standard dimensions (D_p x T_p) of 16 x 4 mm. (b) The Rayleigh distance for a disk with standard dimensions (D_p x T_p) of 44 x 4 mm.

Since the highest obtained distance between the transducer and the hydrophone is $d = 0.885$ m, the hydrophone will be in the far-field for all frequencies for the transducers with an disk with dimensions (D_p x T_p) of 16 x 4 mm. However, the water tank is not long enough for this to be the case for the transducers with a Pz27 disk with dimensions (D_p x T_p) of 44 x 4 mm, where the distance used in the measurements only apply for far-field condition up to around 800 kHz.

Chapter 5

Simulation setup

5.1 Introduction

The software FEMP 5.0 and 6.1b is used for the Finite Element simulations (FEMP 6.1 was released after this work began)[4]. In Sec. 5.2, the different piezoelectric constants used to simulate the piezoelectric disks is presented. In Sec. 5.3, verification of the simulation setup has been made. Then, an adjusted simulation setup made by this author is compared to the earlier simulation setup in Sec. 5.4. Next, simulations of different backing layers are presented in Sec. 5.5. Then, in Sec. 5.6, the complete transducer construction simulations are shown. Finally, the methods used for adjusting the simulations when the measurement and simulations have deviated from each other are explained in Sec. 5.7.

5.2 Admittance simulations of the piezoelectric disks

Admittance simulations of the piezoelectric disks were made with the use of both the piezoelectric constants by Lohne/Knappskog [41] and Lohne/Knappskog/Aanes [1] from Tab. 5.1, and with the use of Direct Harmonic Analysis with complex losses. The admittance of the disks is simulated with seven elements per wavelength in both the radial and thickness direction with an order of 2, at a step frequency of 100 Hz from 1 kHz to 1 MHz.

The piezoelectric constants from Lohne/Knappskog [41], Lohne/Knappskog/Aanes [1] and Meggitt Ferroperm [8] are shown in Tab. 5.1. The constants from Meggitt Ferroperm are the original constants for Pz27, and the constants from Lohne/Knappskog [41] and Lohne/Knappskog/Aanes [1] are adjusted from the constants from Meggitt Ferroperm [8].

Table 5.1: The different sets of piezoelectric constants for Pz27, the constants given by Meggitt Ferroperm [8], the adjusted piezoelectric constants made by Lohne/Knappskog [41] and the further adjusted piezoelectric constants made by Lohne/Knappskog/Aanes [1].

Piezoelectric constants	Ferroperm	Adjusted(Lohne/Knappskog)	Adjusted(Lohne/Knappskog/Aanes)
$c_{11}^E\ [10^{10}N/m^2]$	$14,70$	$11,875(1+i/95,75)$	$12,025(1+i/96)$
$c_{12}^E\ [10^{10}N/m^2]$	$10,50$	$7,430(1+i/71,24)$	$7,63(1+i/70)$
$c_{13}^E\ [10^{10}N/m^2]$	$9,370$	$7,425(1+i/120,19)$	$7,42(1+i/120)$
$c^E33\ [10^{10}N/m^2]$	$11,30$	$11,205(1+i/(177,99)$	$11,005(1+i/(190)$
$c_{44}^E\ [10^{10}N/m^2]$	$2,30$	$2,110(1+i/75)$	$2,11(1+i/75)$
$c_{66}^E\ [10^{10}N/m^2]$	$2,12$	$2,160(1+i/315,01)$	$2,160(1+i/315,01)$
$e_{31}\ [C/m^2]$	$-3,090$	$-5,4(1-i/166)$	$-5,4(1-i/166)$
$e_{33}\ [C/m^2]$	$16,00$	$16,0389(1-i/323,77)$	$17(1-i/324)$
$e_{15}\ [C/m^2]$	$11,60$	$11,20(1-i/200)$	$11,20(1-i/200)$
$\varepsilon_{11}^S/\varepsilon_0$	1130	$916(1-i/50)$	$916(1-i/50)$
$\varepsilon_{33}^S/\varepsilon_0$	914	$920(1-i/86,28)$	$920(1-i/86,28)$
$\rho\ [kg/m^3]$	7700	7700	7700

Both the Lohne/Knappskog [41] and Lohne/Knappskog/Aanes [1] constants were used for simulating the admittance

of the piezoelectric disks. Since the piezoelectric constants are dependent on the D/T ratio, the constant d_{33} depends on the disks volume [17], it was expected that the constants by Lohne/Knappskog/Aanes [1] made for D/T = 6.25 corresponded the best for D/T = 4, and Lohne/Knappskog [41] corresponded best for D/T = 11, since this is made for D/T = 10. In Fig. 5.1 the log of the conductance measurements of disk 16-5 and 44-7 is compared to the simulations with constants from [41] and [1].

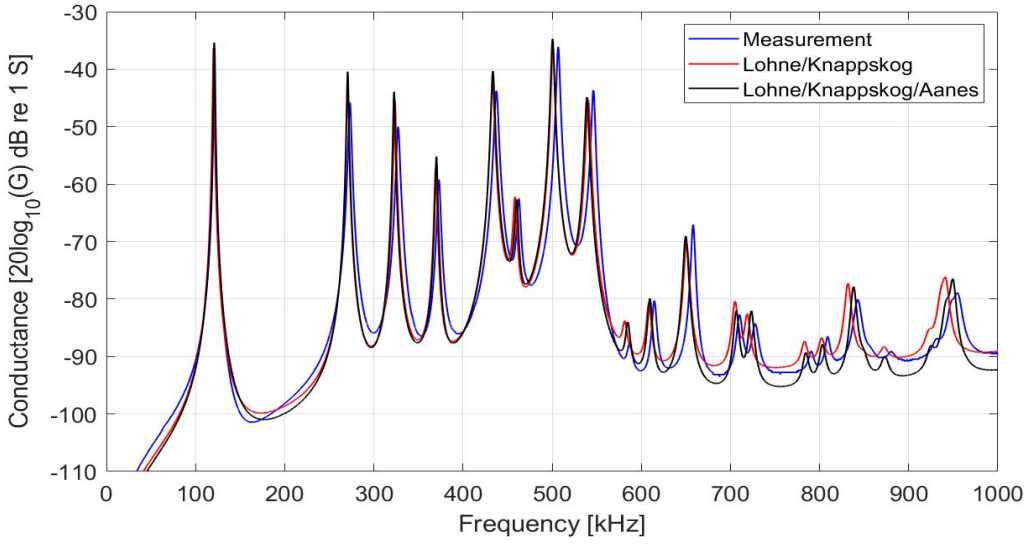

(a)

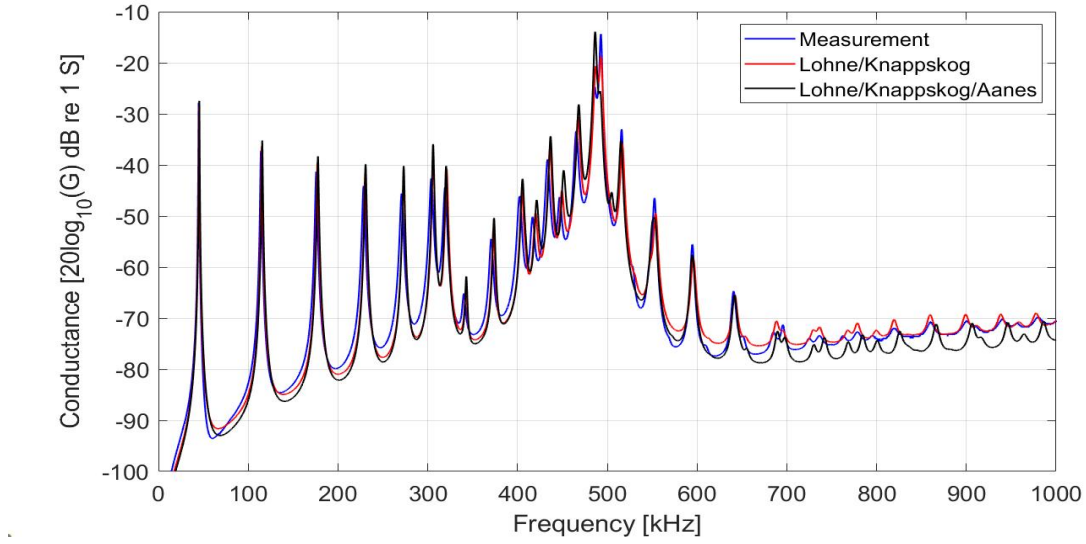

(b)

Figure 5.1: Comparison between the measurements and the simulations conducted with two different sets of piezoelectric constants, (a) for disk 16-5 and (b) for disk 44-7.

For both disks, as seen in Fig. 5.1a and 5.1b, the simulations with the piezoelectric constants from Lohne/Knappskog/Aanes [1] deviates more from the measurements and the simulations with the piezoelectric constants from Lohne/Knappskog [41], especially after 700 kHz for both the disks. In the thickness mode at 500 kHz in Fig. 5.1b, it is also seen that the simulations with the Lohne/Knappskog data set agrees better to the measurements than for Lohne/Knappskog/Aanes data set. In Fig. 5.1a, it is seen that the resonance tops after 700 kHz agrees better with the Lohne/Knappskog/Aanes data set. Still, since the simulation goes lower in amplitude than the measurements and the Lohne/Knappskog data set, the Lohne/Knappskog data set is used further in the simulations for all disks, for all the construction steps.

5.3 Verification of the simulation setup

Firstly, the simulation setup made by this author is used to simulate the same simulations of prototype no. 2 made by [1] to verify the simulation setup. The prototype transducer no. 2 is used since several measurement and simulation steps were shown. For comparing with the simulations done in this thesis, the program CurveSnap [42] is used to get the data from the figures Aanes gave in his thesis [1]. However, the program did not correctly separate the measurement and simulation plots in the figures. This author made the mesh used for the simulations with the use of the dimensions given in [1] for the prototype no. 2 transducer, and used the same material constants.

The dimensions of the material constants for the prototype no. 2 transducer by [1] is given in Tab. 5.2. The Pz27 disk has dimensions (D_p x T_p) of 24.894 x 3.936 mm, the front layer has (D_f x T_f) of 30.460 x 1.054 mm. Two pieces of the HCP70 backing layer has been used where the first backing layer has a thickness (T_{b1}) of 13.45 mm and the second a thickness of (T_{b2}) of 15.01 mm. The casing has a thickness (T_{c1}) of 2.64 mm, and the back casing has a thickness (T_{c2}) of 4.11 mm. The length of the casing (L_c) is 34.32 mm, and the thickness of the conductive adhesive (T_{ea}) is 0.074 mm. The cone in the backing layer has a thickness (T_{ac}) of 10.42 mm and a radius (R_{ac}) of 4.01 mm [1].

Table 5.2: The dimensions for the prototype transducer no. 2 in [1].

D_p [mm]	24.894	T_p [mm]	3.936
D_f [mm]	30.460	T_f [mm]	1.054
T_{b1} [mm]	13.45	T_{b2} [mm]	15.01
T_{c1} [mm]	2.64	T_{c2} [mm]	4.11
L_c [mm]	34.32	$T_{ea}[mm]$	0.074
T_{ac} [mm]	10.42	R_{ac} [mm]	4.01

The material constants used for the front layer are shown in Tab. 5.3, the constants for the conductive adhesive are given in Tab. 5.4, the constants for the HCP70 backing layer are given in Tab. 5.5 and the constants for the steel casing are given in Tab. 5.6. For water, a sound speed of 1485 m/s and a density of 1000 kg/m^3 is used in the simulations [1]. All the constants are taken from [1]. These material constants are also used for the simulations presented in Chap. 6.

The compressional sound velocity of the front layer (c_l) is 2250 m/s, the shear sound velocity (c_s) is 1000 m/s, the density of the front layer (ρ) is 2850 kg/m^3 and the loss factor Q is 20 [1].

Table 5.3: Material constant for the Eccosorb MF114 front layer [21] given by [1].

c_l $[m/s]$	2250
c_s $[m/s]$	1000
ρ $[kg/m^3]$	2850
Q	20

The compressional sound velocity of the conductive adhesive (c_l) is 1700 m/s, the shear sound velocity (c_s) is 1000 m/s, the density of the conductive adhesive (ρ) is 2340 kg/m^3 and the loss factor Q is 50 [1].

Table 5.4: The material constants for the electrically conductive adhesive 8331 [23] given by [1].

c_l $[m/s]$	1700
c_s $[m/s]$	1000
ρ $[kg/m^3]$	2340
Q	50

The compressional sound velocity of the HCP70 backing layer (c_l) is 1605.5 m/s, the shear sound velocity (c_s) is 826 m/s, the density of HCP70 (ρ) is 300 kg/m^3 and the loss factor Q is 25 [1].

Table 5.5: The material constants for the HCP70 backing layer [1].

c_l $[m/s]$	1605,5
c_s $[m/s]$	826
ρ $[kg/m^3]$	300
Q	25

The compressional sound velocity of the steel casing (c_l) is 5780 m/s, the shear sound velocity (c_s) is 3050 m/s, the density of the steel (ρ) is 8000 kg/m^3 and the loss factor Q is 1000 [1].

Table 5.6: The material constants for the steel casing [1].

c_l $[m/s]$	5780
c_s $[m/s]$	3050
ρ $[kg/m^3]$	8000
Q	1000

The simulation mesh made for transducer no. 2 from [1], made by this author is shown in Fig. 5.2.

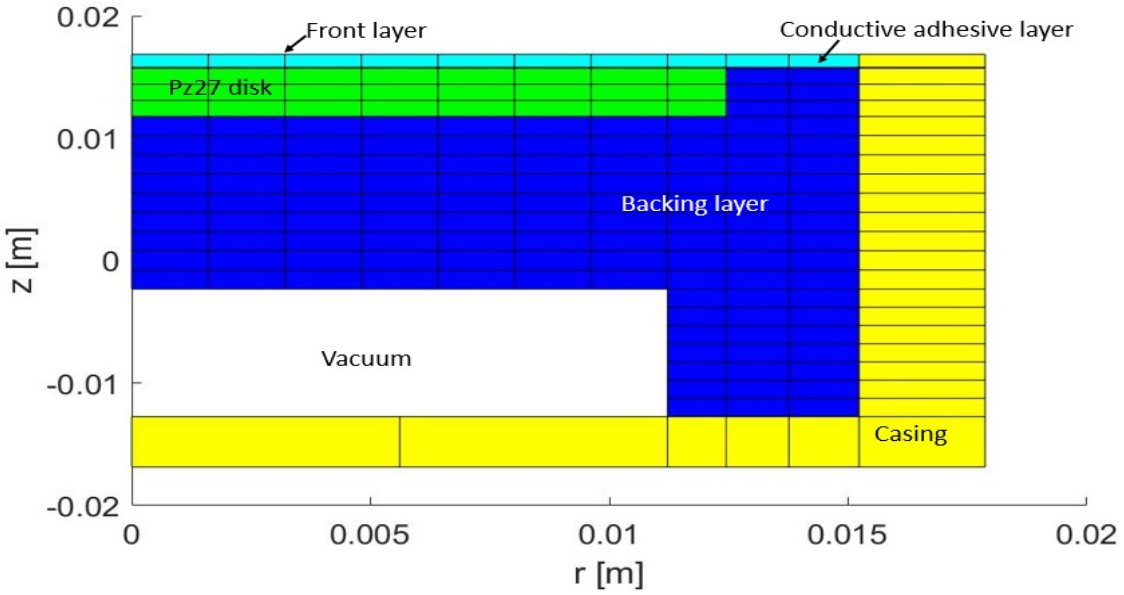

Figure 5.2: A mesh constructed of the prototype transducer no. 2 from [1] vibrating in a vacuum. The transducer consists of a piezoelectric disk (green region), a front layer (light blue region) with an adhesive layer in between the front layer and the piezoelectric disk, and the backing layer (dark blue region), with a casing (yellow region) enclosing the backing layer of the transducer.

For the simulations done to verify the simulations setup, simulations of the air gap were made as Aanes did [1], with a rectangle as seen in Fig. 5.2. The simulation was made with three elements per wavelength in both the radial and thickness direction as done in [1].

The simulation Aanes did with a disk and front layer was simulated, but the results were not the same as Aanes showed in his thesis [1]. However, the same result appeared when adding a layer of conductive adhesive with a thickness of 0.074 mm in the simulation setup, as seen in Fig. 5.3. It was, therefore, not made any effort to achieve the same results with only disk and front layer.

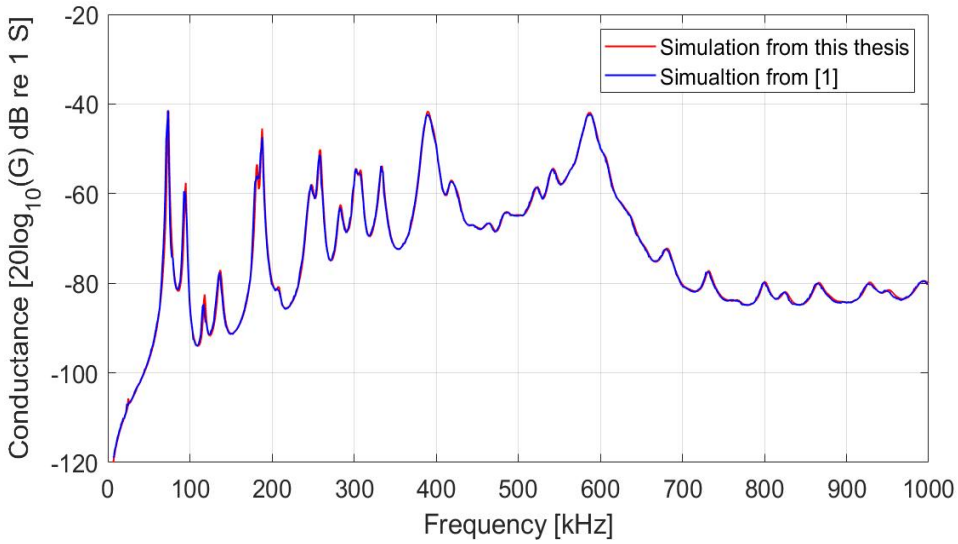

Figure 5.3: The simulated conductance in air by [1] (blue) compared to the simulation done by this author (red) of the piezoelectric disk with front layer and a conductive adhesive layer.

Fig. 5.3 shows the conductance simulations in red done by this author for the disk and front layer with the conductive adhesive in between, used in Aanes prototype no. 2 transducer [1]. The blue curve is the simulation done by Aanes, given by CurveSnap [42]. This program didn't catch all the tops on the curve, but otherwise, the curve is very alike and seen for the comparison in water in Fig. 5.5 where this setup has been taken further, the result from the simulations done by this author is the same as the simulation from [1]. The same accounts for Fig. 5.4.

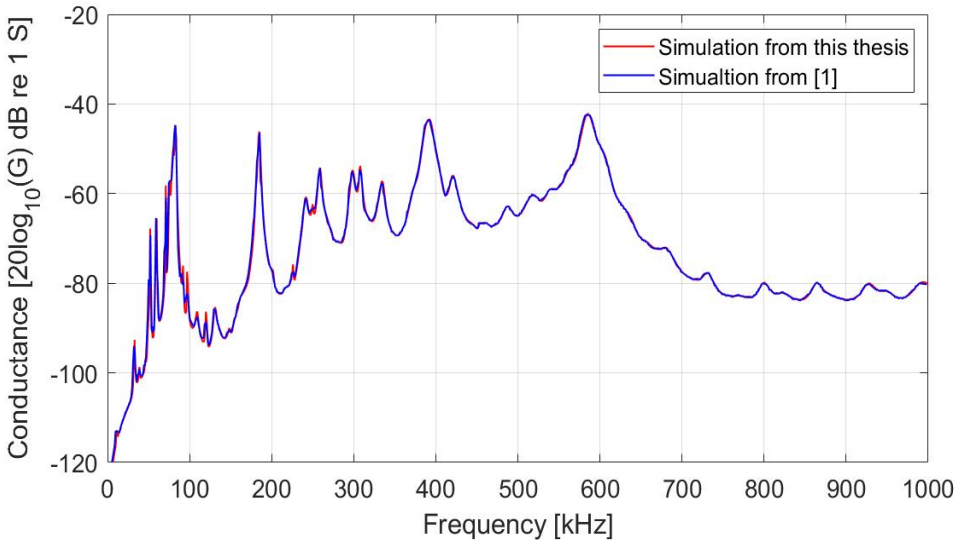

Figure 5.4: The simulated conductance in air by [1] (blue) compared to the simulation done by this author (red) of the prototype transducer no. 2 from [1].

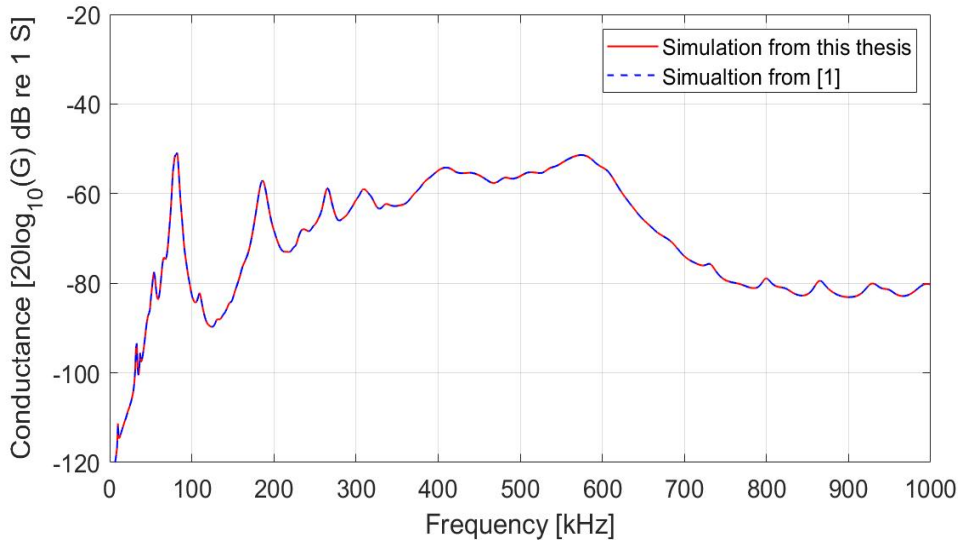

Figure 5.5: The simulated conductance in water by [1] (blue) compared to the simulation done by this author (red) of the prototype transducer no. 2 from [1].

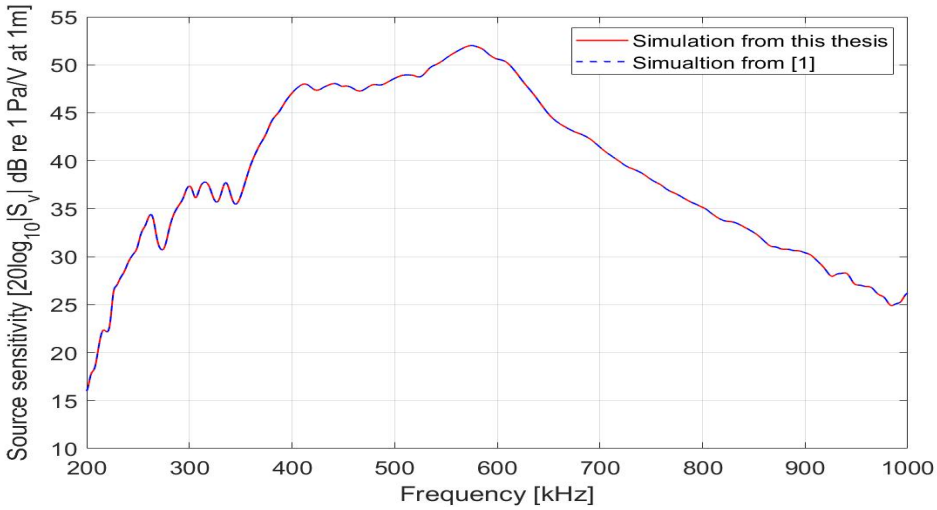

Figure 5.6: The simulated source sensitivity in water by [1] (blue) compared to the simulation done by this author (red) of the prototype transducer no. 2 from [1].

The simulations of transducer no. 2 in water are verified with access to Aanes results files. As seen in Fig. 5.5 and 5.6, the simulations done by this author agrees with the simulations conducted in [1].

5.4 Adjusted simulation setup

Adjustments in the simulation setup from Fig. 5.2 was made and compared to the simulations done with the mesh from Fig. 5.2 and with the measurements from [1]. As seen in the mesh for the transducer simulation in Fig. 5.2, the cone in the backing layer is simulated as a rectangle, and the front layer is not put in a hatch in the casing as it is made. This setup is adjusted by this author for prototype no. 2, and compared with the measurements done for this prototype to see if the modified simulations agrees better than the simulations conducted before. The measurements and the simulations from [1] used for comparing with the adjusted simulations is taken from [1] with CurveSnap [42]. First, the cone in the backing layer was made with steps instead of being simulated as a rectangle (see Fig. 5.7a). Next, simulations with the front layer in a hatch in the transducer were made (see Fig. 5.7b) together with the cone. These were compared to the measurements of transducer prototype no. 2 by [1] and

the simulations to see if the adjusted simulations done by this author made the simulations agrees better with the actual measurements.

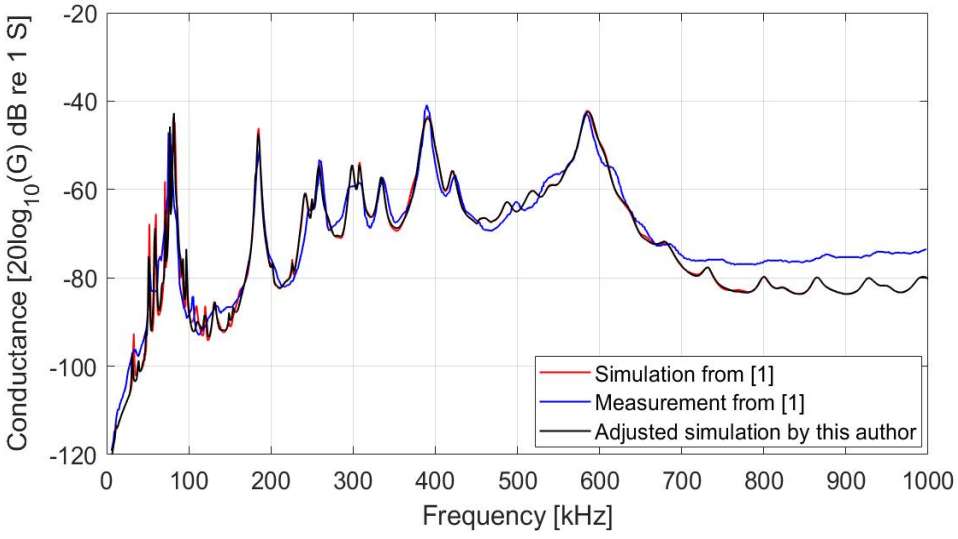

(a)

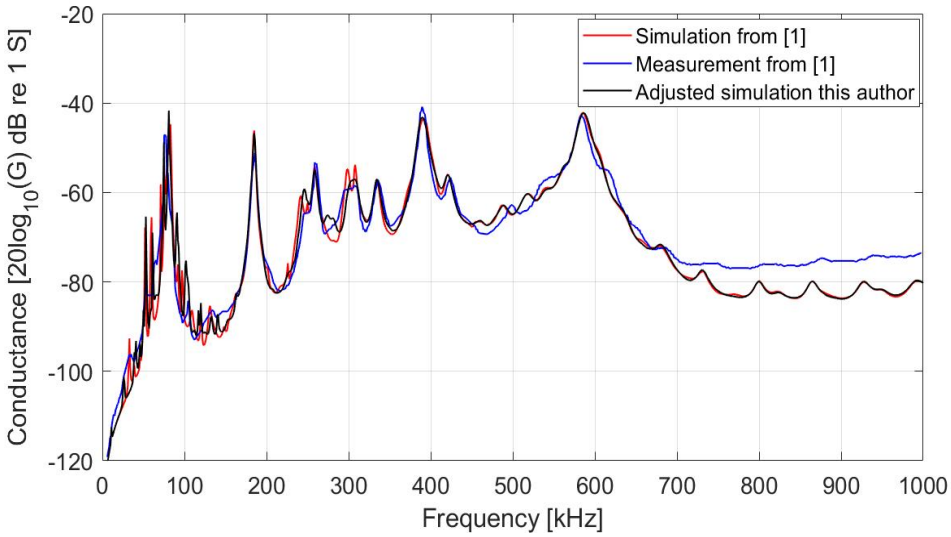

(b)

Figure 5.7: Comparison between the measurement (blue) and simulation (red) by [1] for transducer no. 2 from [1] in air, compared to an adjusted simulation by this author (black). (a) The vacuum is simulated with steps downwards instead of a rectangle. (b) The front layer is simulated in a hatch in the casing in addition.

As seen in Fig. 5.7b, putting the front layer in the hatch as it is built gives a better agreement between the simulation and measurement. Especially around 300 kHz, where the adjusted simulations don't split the resonance like the simulation done by [1] does. Therefore, the transducer simulations conducted in Chap. 6 are simulated with the front layer in a hatch in the casing, and the vacuum cone is simulated with steps, as shown in Sec. 5.6.

5.5 Simulations of different backing layers

Simulations of the transducer construction were made with different backing layers to see which backing layer was suitable for the transducers. Simulations of the source sensitivity of the transducer with HCP70, tungsten epoxy with $Z_p = 11.9$ MRayl and $Z_p = 16.8$ Mrayl were made, where material constants for HCP70 in Tab. 5.5 are taken from [1], and the material constants for the tungsten epoxies are taken from [18], [43]. The material constant for the tungsten epoxy backing layer with an impedance of 11.9 MRayls are presented in Tab. 5.7, and

the material constants for the tungsten epoxy backing layer with an impedance of 16.8 MRayl are presented in Tab. 5.8.

The compressional sound velocity of the tungsten epoxy backing layer with an impedance of 11.9 MRayl (c_l) is 1600 m/s, the shear sound velocity (c_s) is 800 m/s, the density (ρ) is 7470 kg/m^3 and the loss factor Q is 13.5.

Table 5.7: Material constant for tungsten-epoxy backing layer with $Z_p = 11.9$ MRayl [18].

c_l $[m/s]$	1600
c_s $[m/s]$	800
ρ $[kg/m^3]$	7470
Q	13.5

The compressional sound velocity of the tungsten epoxy backing layer with an impedance of 16.8 MRayl (c_l) is 1706 m/s, the shear sound velocity (c_s) is 900 m/s, the density (ρ) is 9820 kg/m^3 and the loss factor Q is 11.8.

Table 5.8: Material constants for tungsten-epoxy backing layer with $Z_p = 16.8$ MRayl [43].

c_l $[m/s]$	1706
c_s $[m/s]$	900
ρ $[kg/m^3]$	9820
Q	11.8

Fig. 5.8a shows the simulation of the source sensitivity for the different backing layers. The simulations where made with the same setup and dimensions made for prototype no. 2 in [1]. Since the simulations shown in Fig. 5.8a of the tungsten epoxy backing layers was uneven, a simulation of the same backing layers is made with a 10.5 mm longer backing layer, as well as the vacuum gap in the backing layer was simulated as a cone with steps in Fig. 5.8b.

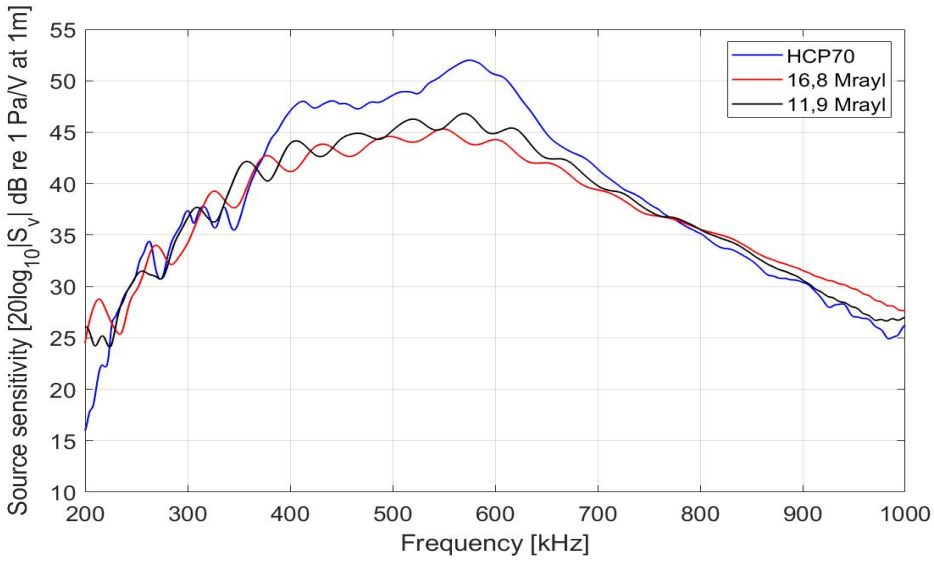

(a)

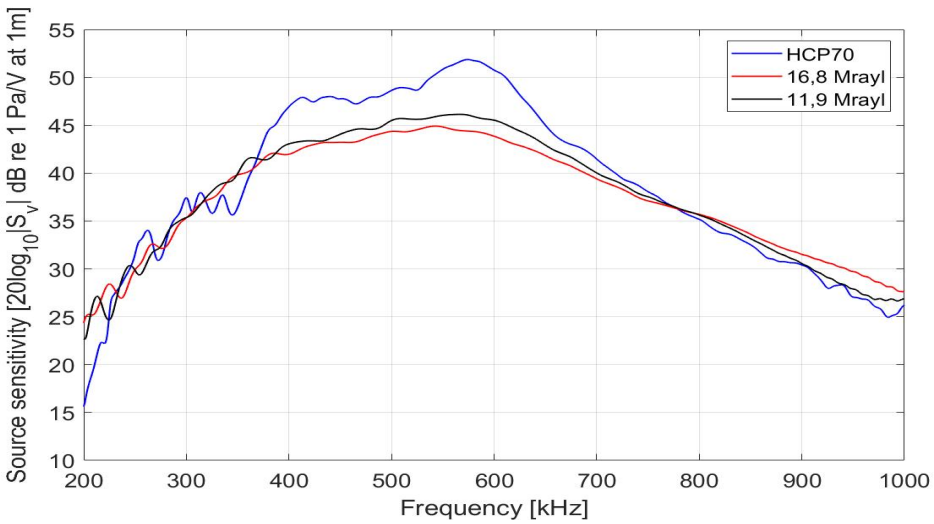

(b)

Figure 5.8: (a) Simulations of the transducer no. 2 from [1], with HCP70 backing layer (blue curve), tungsten epoxy backing layer with $Z_p = 16.8$ MRayl (red curve) and with tungsten epoxy backing layer with $Z_p = 11.9$ MRayl (black curve) with a thickness of 24.5 mm using the same simulation setup in Fig. 5.2. (b) Simulations of the transducer no. 2 from [1], with HCP70 backing layer (blue curve), tungsten epoxy backing layer with $Z_p = 16.8$ MRayl (red curve) and with tungsten epoxy backing layer with $Z_p = 11.9$ MRayl (black curve) with a thickness of 35 mm with simulations of an uneven cone in the backing layer.

As seen in Fig. 5.8, the tungsten epoxy backing layers gave a broader bandwidth than the HCP70 backing layer. With the same simulation setup as shown in Fig. 5.2, the simulations with tungsten epoxy backing layers in Fig. 5.8a had several ripples. By simulating an uneven cone and a longer backing layer as done in the simulations in Fig. 5.8b, the tungsten epoxy backing layers has fewer ripples. Tungsten epoxy was therefore chosen as the backing layer with a 35 mm long backing layer, and an uneven cone in the back to reduce backscattering as simulated in Fig. 5.8b When comparing the simulations of the tungsten epoxy backing layer with a thickness of 24.5 and 35 mm, the ripples seen in Fig. 5.8a is probably because of the effects of backscattering that a tungsten epoxy backing layer of 24.5 mm is not long enough to reduce.

Simulations of two of the backing layers made for the prototype transducers presented in Sec. 6.3 deviated with the measurements. Therefore the tungsten epoxy backing layer was simulated with $Z_p = 8.7$ MRayl for transducer no. 5 and with $Z_p = 10.1$ MRayl for transducer no. 6. The material constant used for simulating the tungsten epoxy backing layer with $Z_p = 8.7$ MRayl is given in Tab. 5.9

The compressional sound velocity of the tungsten epoxy backing layer with an impedance of 8.7 MRayl (c_l) is 1600 m/s, the shear sound velocity (c_s) is 800 m/s, the density (ρ) is 5470 kg/m^3 and a loss factor Q of 28.5 is used [1].

Table 5.9: Material constants for tungsten epoxy backing layer with $Z_p = 8.7$ MRayl [18].

c_l $[m/s]$	1600
c_s $[m/s]$	800
ρ $[kg/m^3]$	5470
Q	28.5

The material constant used for simulating the tungsten epoxy backing layer with $Z_p = 10.1$ MRayl is given in Tab. 5.10. The compressional sound velocity of the tungsten epoxy backing layer with an impedance of 10.1 MRayl (c_l) is 1560 m/s, the shear sound velocity (c_s) is 800 m/s, the density (ρ) is 6500 kg/m^3 and a loss factor Q, of 15 is used [43].

Table 5.10: Material constants for tungsten epoxy backing layer with $Z_p = 10.1$ MRayl [43].

c_l $[m/s]$	1560
c_s $[m/s]$	800
ρ $[kg/m^3]$	6500
Q	15

5.6 Simulations of the transducer constructions

The simulated mesh of transducer no. 3 presented in Sec. 6.3.3 with a piezoelectric disk with (D_p x T_p) of 44 x 4 mm (disk 44-7) in a vacuum made by this author is shown in Fig. 5.9. The dimensions used in the simulations are presented in Sec. 6.3.3 in Tab. 6.15. A simulated mesh of transducer no. 4 presented in Sec. 6.3.5 with a piezoelectric disk with (D_p x T_p) of 16 x 4 mm (disk 16-5) in a vacuum made by this author is shown in Fig. 5.10. The simulated mesh for transducer no. 4 in water is shown in Fig. 5.11. The dimensions of the materials used in the simulations of transducer no. 4 are presented in Sec. 6.3.4 in Tab. 6.16.

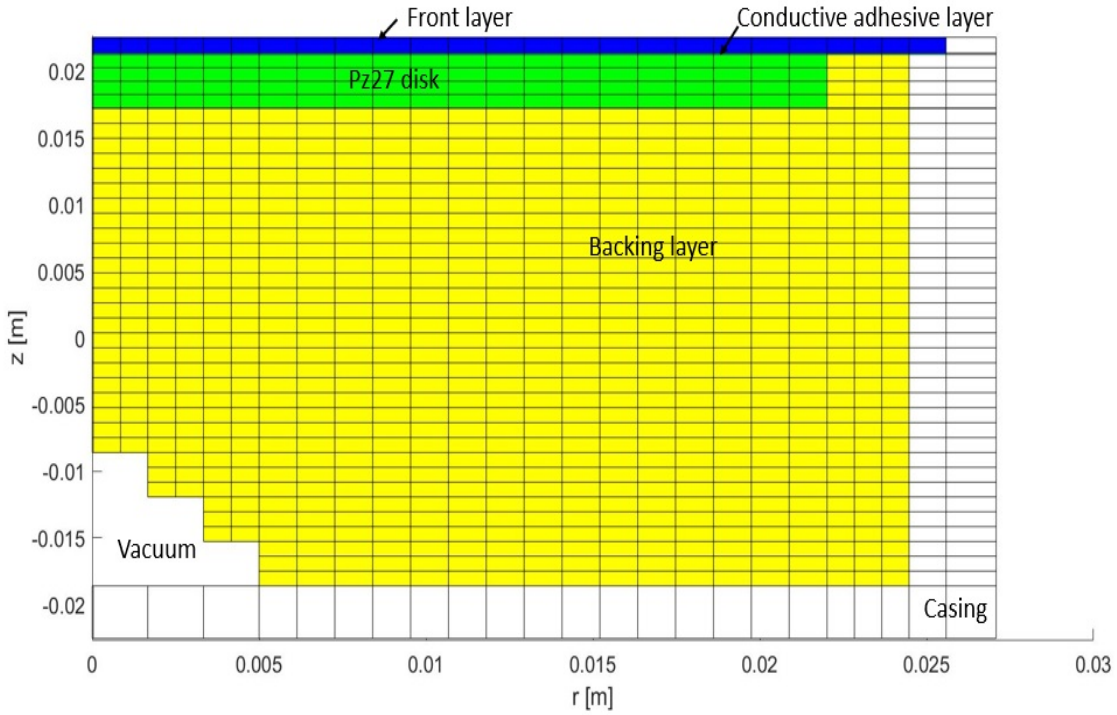

Figure 5.9: The simulated transducer mesh (transducer with disk 44-7 presented Sec. 6.3.3) in a vacuum, consisting of a piezoelectric disk (green region), front layer (blue region) with an adhesive layer in between the front layer and the piezoelectric disk, and the backing layer (yellow region), with a casing and back casing (white region) enclosing the backing layer of the transducer. In the backing layer, a vacuum cone is also made.

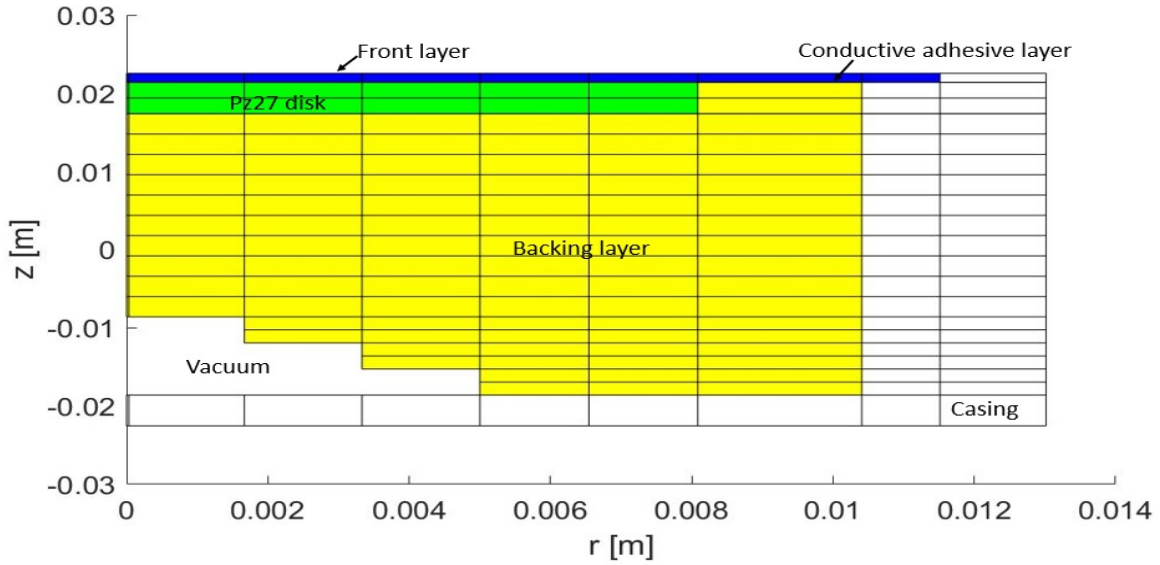

Figure 5.10: The simulated transducer mesh (transducer with disk 16-5 presented Sec. 6.3.4) in a vacuum, consisting of a piezoelectric disk (green region), front layer (blue region) with an adhesive layer in between the front layer and the piezoelectric disk, and the backing layer (yellow region), with a casing and back casing (white region) enclosing the backing layer of the transducer. In the backing layer, a vacuum cone is also made.

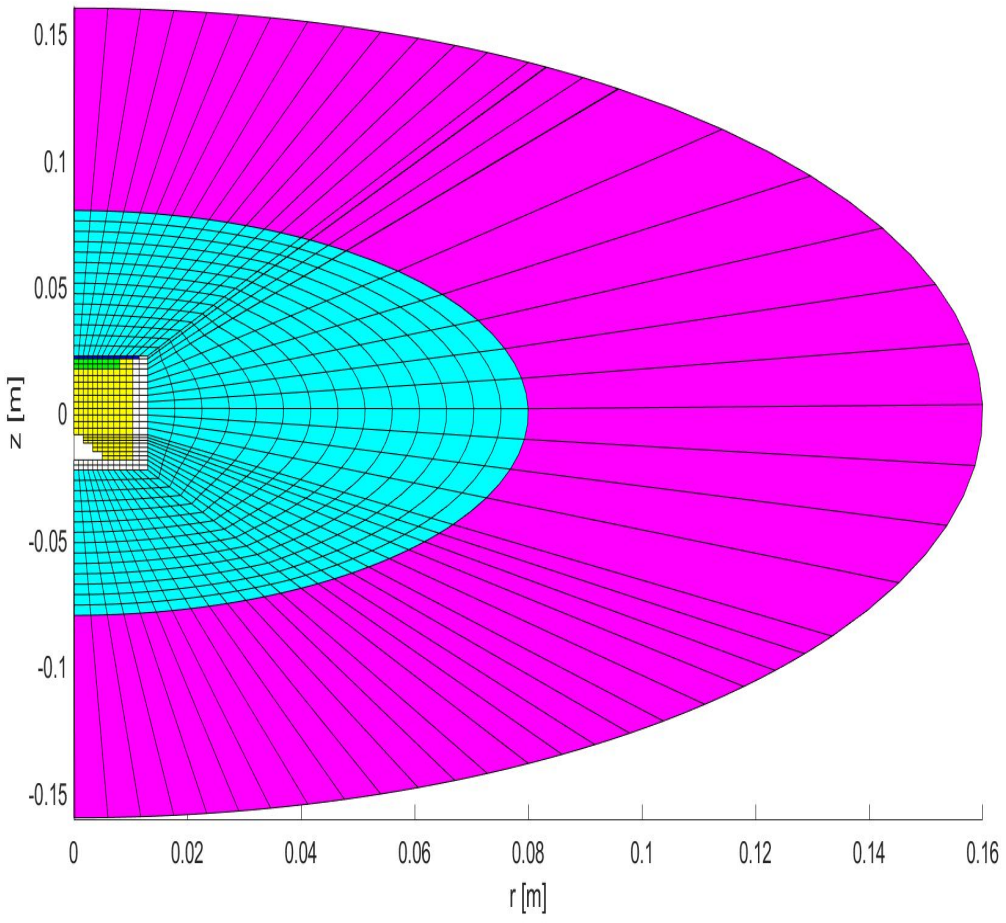

Figure 5.11: The simulated transducer mesh (transducer with disk 16-5 presented in Sec. 6.3.4) in fluid. The transducer is surrounded by finite fluid elements (light blue region) and infinite fluid elements (purple region).

Simulations of the transducer construction for this thesis in water were made with finite fluid elements with a radius of 80 mm and infinite fluid elements with a radius of 80 mm. The finite fluid elements were simulated with three elements per compressional wavelength and three elements per shear wavelength. The infinite fluid elements were simulated with three elements per compressional wavelength and one element per shear wavelength. For the transducer simulations in vacuum in Figs. 5.9 and 5.10, the simulations where conducted with three elements per wavelength at 1 MHz in both directions. A simulation of a transducer was simulated with seven elements per wavelength and compared to a simulation with three elements per wavelength to see if three elements per wavelength was sufficient, see Fig. 5.12.

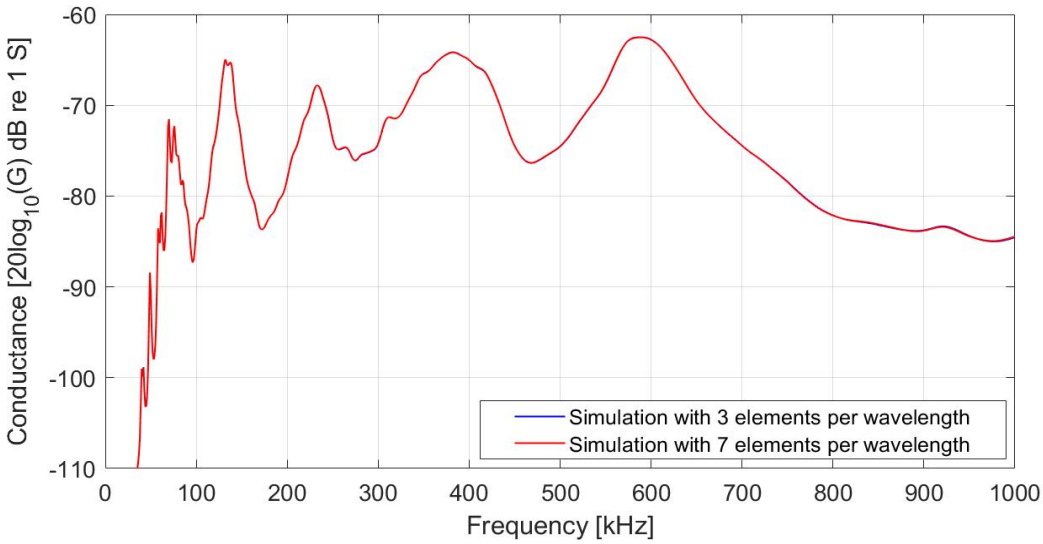

Figure 5.12: The simulated conductance of a transducer radiating in air. Simulation with 3 elements per wavelength (blue) compared to simulation with 7 elements per wavelength (red).

As seen in Fig. 5.12, it is only a slight difference between the two simulations after 800 kHz. Therefore three elements per wavelength seem sufficient for the simulations presented in this thesis, as well three elements per wavelength was also used in [1].

5.7 Simulations with solder and vacuum gap

Adjustments in the simulation setup were made to make the simulations agree better with the measurements when the simulation deviated too much from the measurements. The adjusted simulations were made by changing the conductive adhesive thickness and the dimensions of the solder. The radius used for the solder in the simulations were found by measuring the diameter of the solder on the disks and then adjusting it by seeing which radius gave the best correspondence to the measurements. The thickness of the solder was found by seeing what thickness in the simulations gave the best correspondence to the measurement. Small air gaps in the conductive adhesive layers were also simulated when this was not enough. The air gaps were placed between the disk and the front layer, with different sizes, with one or more air gaps to see if the simulations got more like the actual measurement. A mesh containing solder and a vacuum gap in the conductive adhesive layer is shown in Fig. 5.13. The mesh is with disk 16-7, with solder thickness of 0.03 mm and a radius of 3 mm. The vacuum gap has a radius of 0.85 mm. When solder or vacuum gaps are used in the simulations presented in Chap. 6, this is explicitly described.

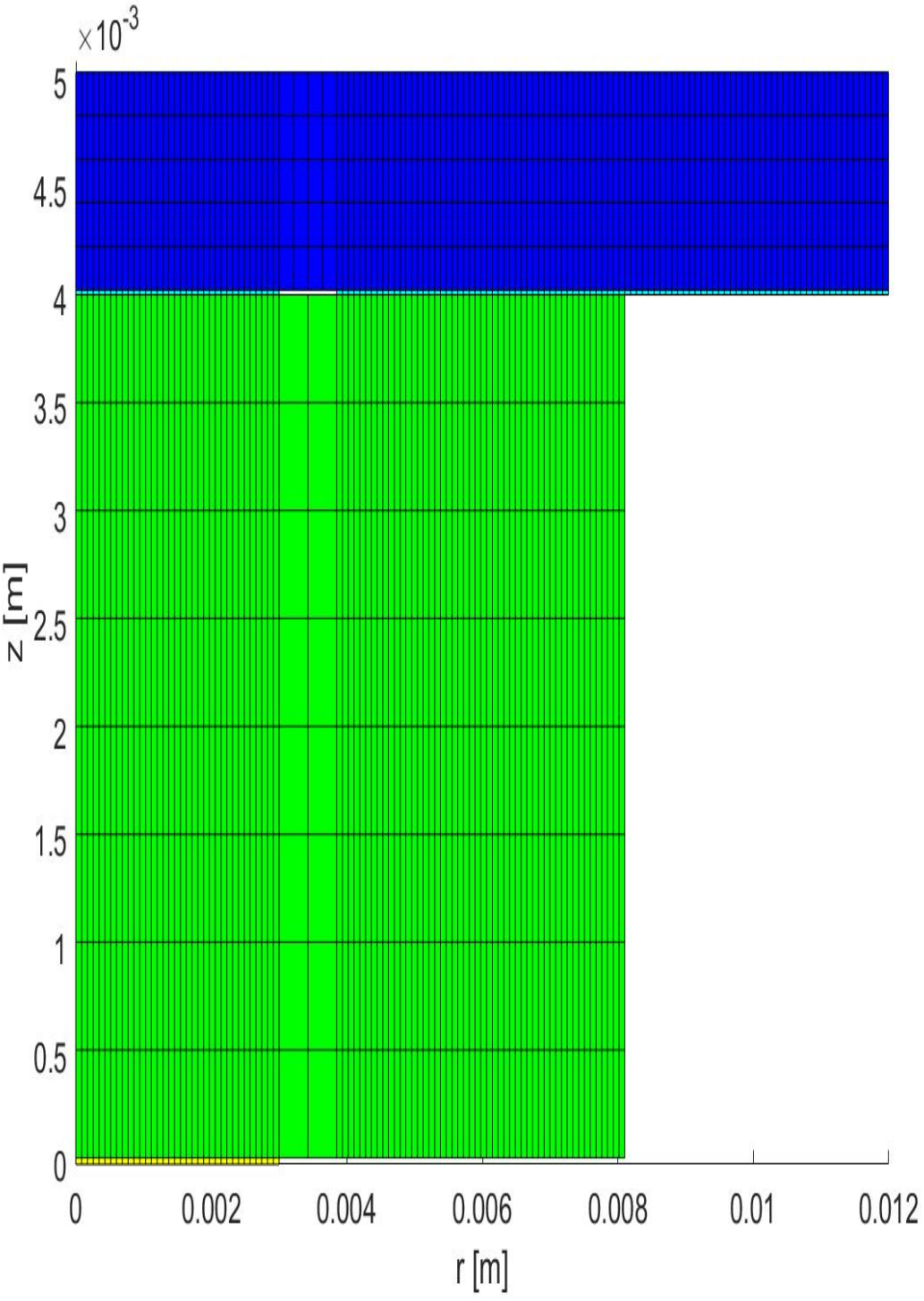

Figure 5.13: Mesh grid of the simulation that is done to adjust the simulation to the measurement. The solder (yellow region), the piezoelectric disk 16-7 (green region), the conductive adhesive (light blue region), where the white spot is vacuum, and the front layer (dark blue region).

The white spot between the disk and the front layer in Fig. 5.13 is the size and place that makes the best adjustment to the measurement, as seen in the results presented for disk 16-7 in Fig. 6.16, which has some of the same curves as the measurements, unlike the simulation without solder and a vacuum gap.

The material constants used for solder are only approximately since this is not measured in this thesis. The material constants in Tab. 5.11 and 5.12 is taken from [44]. Since the solder that is used consists of 63 % tin and 37 % lead [19], the material constants for solder is calculated by adding the constants for tin and lead from [44] by the relation 63:37. The calculated material constants used in the simulations are presented in Tab. 5.13

The compressional sound velocity of tin (c_l) is 3300 m/s, the shear sound velocity (c_s) is 1700 m/s, the density (ρ) is 7300 kg/m^3 [44]. The loss factor Q is not stated in [44], and are therefore put to infinity which means that FEMP is not using complex losses for calculating the material [4].

Table 5.11: The material constants for tin [44].

c_l $[m/s]$	3300
c_s $[m/s]$	1700
ρ $[kg/m^3]$	7300
Q	∞

The compressional sound velocity of the lead (c_l) is 2200 m/s, the shear sound velocity (c_s) is 700 m/s, the density (ρ) is 11200 kg/m^3 [44]. The loss factor Q is not stated in [44], and are therefore put to infinity which means that FEMP is not using complex losses for calculating the material [4].

Table 5.12: The material constants for lead [44].

c_l $[m/s]$	2200
c_s $[m/s]$	700
ρ $[kg/m^3]$	11200
Q	∞

The compressional sound velocity of the solder is calculated by taking $0.63 \times 3300 + 0.37 \times 22000$, which gives a compressional sound velocity (c_l) of 2893 m/s. The shear sound velocity (c_s) is calculated to 1330 m/s, the density (ρ) is calculated to 8743 kg/m^3, and the loss factor Q is put to infinity.

Table 5.13: The calculated material constants for solder (Sn63).

c_l $[m/s]$	2893
c_s $[m/s]$	1330
ρ $[kg/m^3]$	8743
Q	∞

Chapter 6

Results and discussions

6.1 Introduction

In this chapter, the results from the construction process explained in Chap. 3. is presented together with the results from the simulations. In Sec. 6.2, the result from the preliminary construction and development is presented with results achieved after the Pz27 disks are soldered and after attaching the front layers, attaching the casing and attaching the backing layer. Finally, in Sec. 6.3, the results from the finished prototype transducers are presented, with electrical measurements from air and water for the transducers after the back casing and connector are attached. In addition, acoustic measurements, the source sensitivity and beam pattern measurements are conducted for two of the finished prototype transducers.

6.2 The results from the preliminary construction and development

In this section, all the admittance results after soldering a wire to the disk, attaching the front layers to the disks, attaching the casings to the front layers and attaching the backing layers are shown with measurements and finite element simulations. In Sec. 6.2.1, the measured conductance of some of the disks before and after a wire is soldered on the back electrode is presented. How the heat from the soldering process affects the disk is investigated in Sec. 6.2.2. Next, the results from admittance measurements and simulation of a disk attached to a front layer are shown in Sec. 6.2.3. The measurements with the best correspondence with the simulations of the disks attached to the front layers are used further. The results after casings are applied to the front layers with these disks are presented in Sec. 6.2.4. Finally, the results after the backing layer are made inside the casing is presented in Sec. 6.2.5.

6.2.1 Results from the soldering process

Some of the results from the soldering process described in Sec. 3.3 is shown in this section. In Fig. 6.1 the best conductance measurement results obtained for each dimension before and after the disks are soldered is shown, where the log of the conductance is plotted against the frequency.

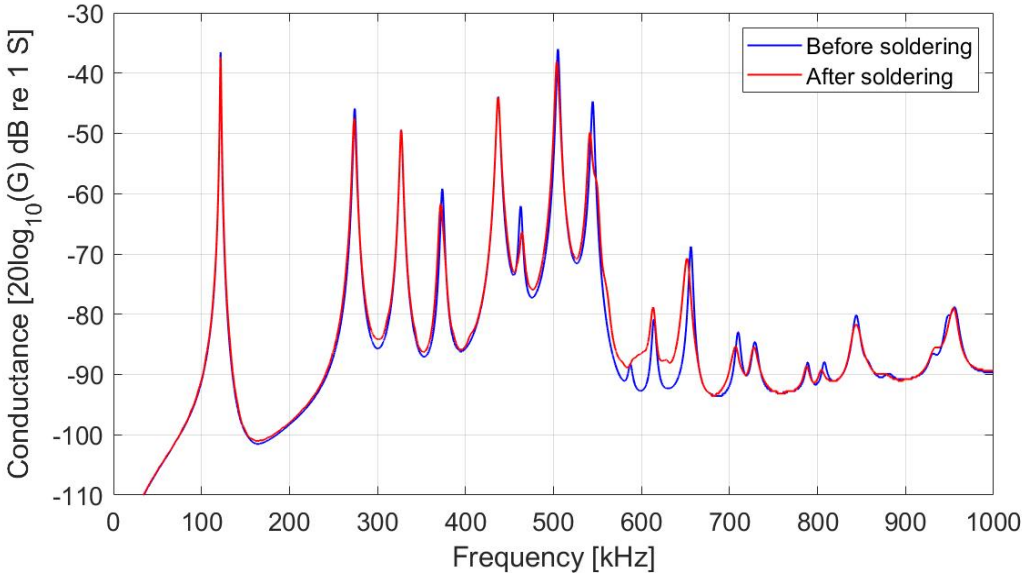

(a)

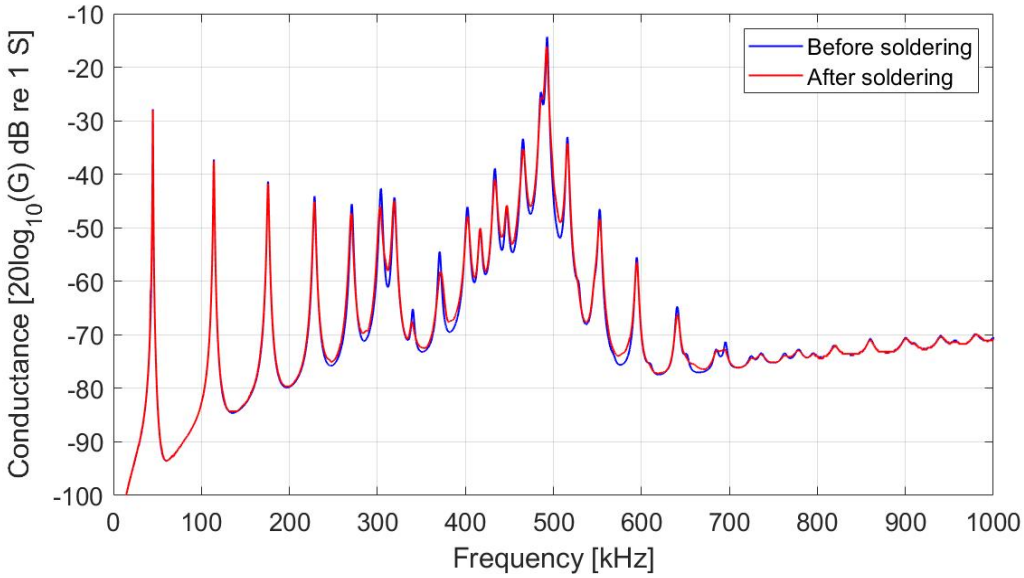

(b)

Figure 6.1: The best soldered disk with (D_p x T_p) of 16 x 4 mm and 44 x 4 mm. The measured conductance in air from 1-1000 kHz, before and after (a) disk 16-3 and (b) disk 44-7 are soldered.

Disk 44-7 in Fig. 6.1b is used in one of the constructed transducers. Disk 44-7 was soldered at 250 °C without preheating. Disk 16-3 shown in Fig. 6.1a is not used in one of the transducers since the result after attaching the front layer was not satisfying. Disk 16-3 was preheated with warm air and soldered right below 250 °C.

The result after a wire is soldered on disk 44-2 and 44-5 is shown in Fig. 6.2, where the log of the conductance is plotted against the frequency.

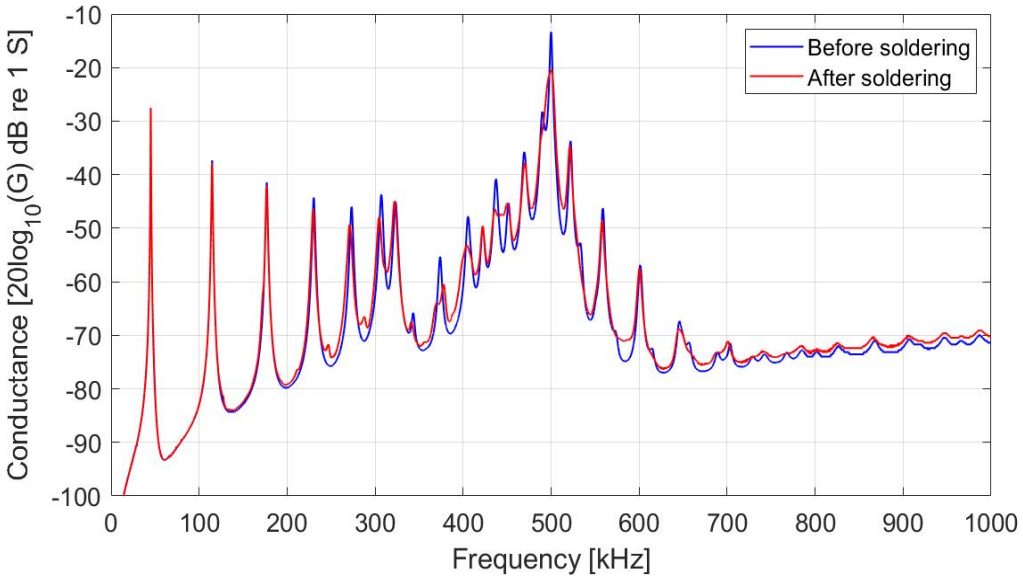

(a)

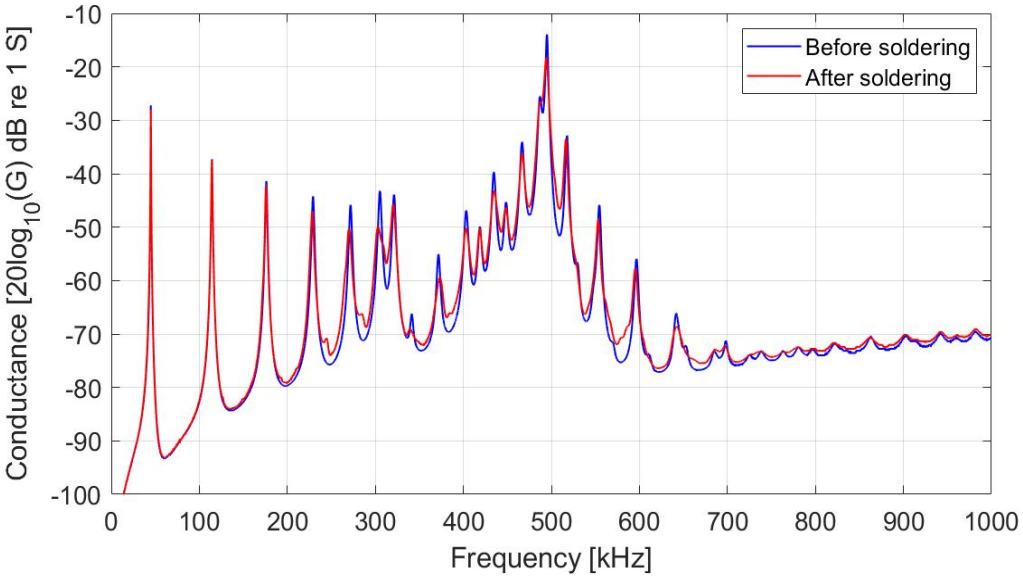

(b)

Figure 6.2: The measured conductance in air from 1-1000 kHz before and after (a) disk 44-2 and (b) disk 44-5 is soldered.

Disk 44-2 and 44-5 in Figs. 6.2a and 6.2b is soldered with the method described in Sec. 3.2, where the elements first were preheated with warm air and then soldered right below 250 °C. Both these disks are used in constructed transducers.

The result after a wire is soldered on disk 16-5 and 16-10 is shown in Fig. 6.3, where the log of the conductance is plotted against the frequency.

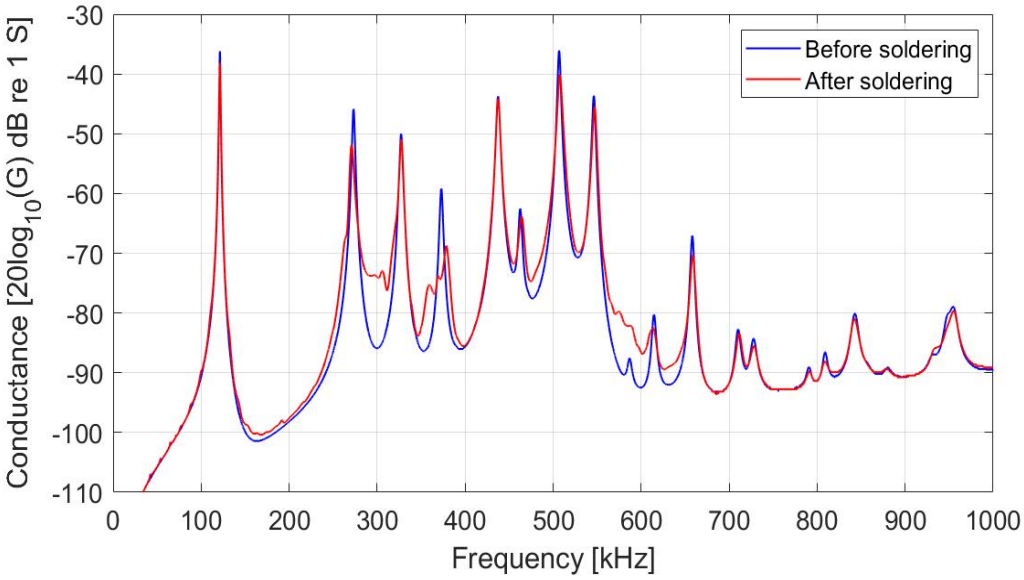

(a)

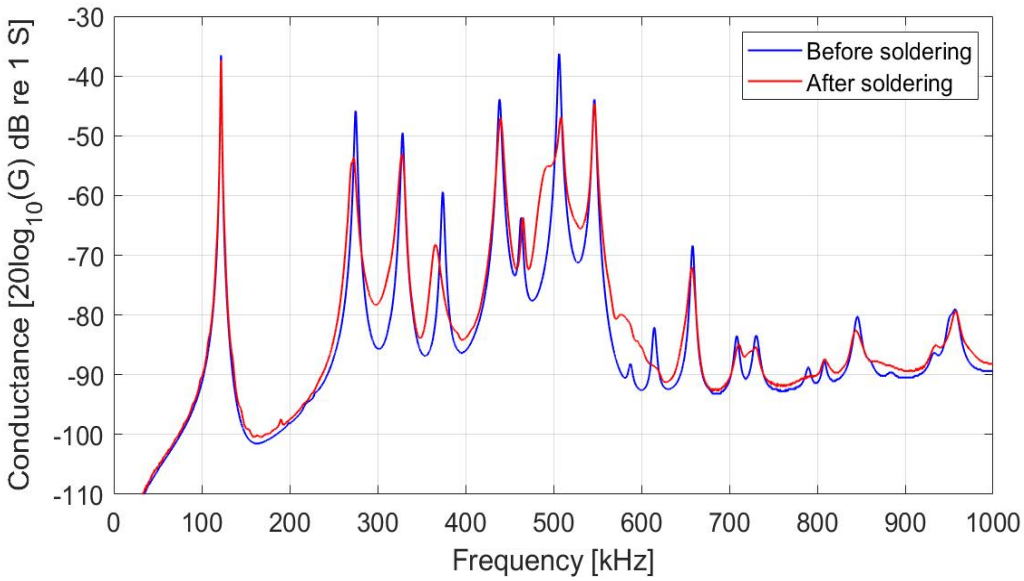

(b)

Figure 6.3: The measured conductance in air from 1-1000 kHz before and after (a) disk 16-5 and (b) disk 16-10 is soldered.

Disk 16-5 in Fig. 6.3a was soldered at 250 °C without any preheating. Disk 16-10 was soldered the same way as disk 44-5 in Fig. 6.2b. Both disk 16-5 and 16-10 is used in the constructed transducers.

In Figs. 6.4 and 6.5 some of the results after the more controlled soldering process described in Sec. 3.3 is shown, where the results were more similar to each other than after the other methods.

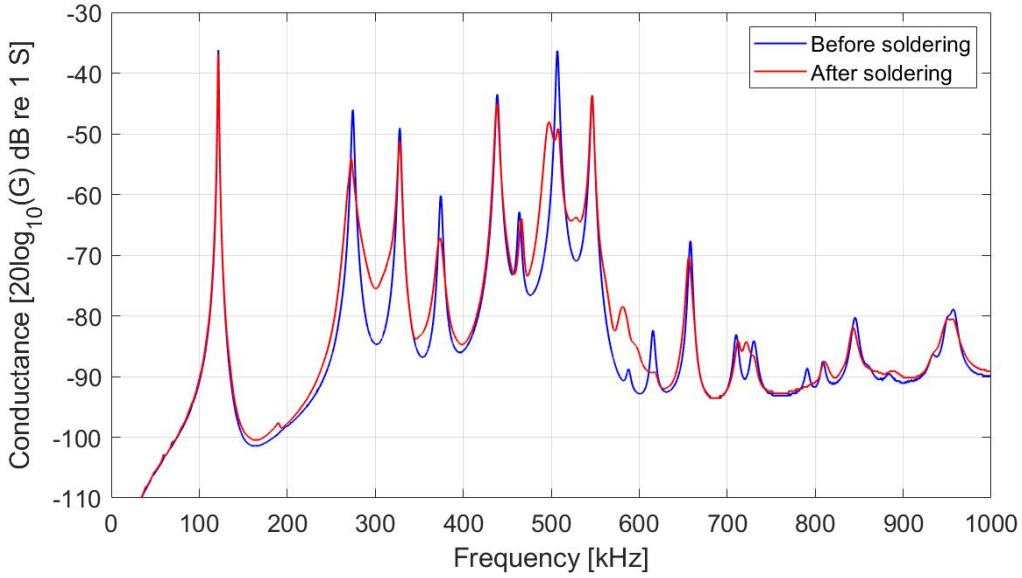

(a)

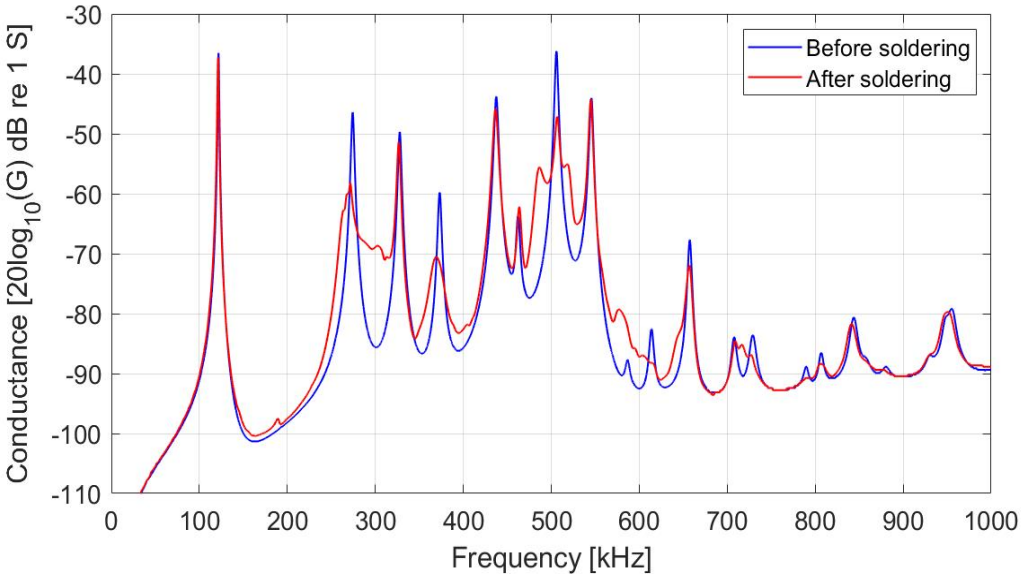

(b)

Figure 6.4: The measured conductance in air from 1-1000 kHz before and after (a) disk 16-6 and (b) disk 16-9 is soldered.

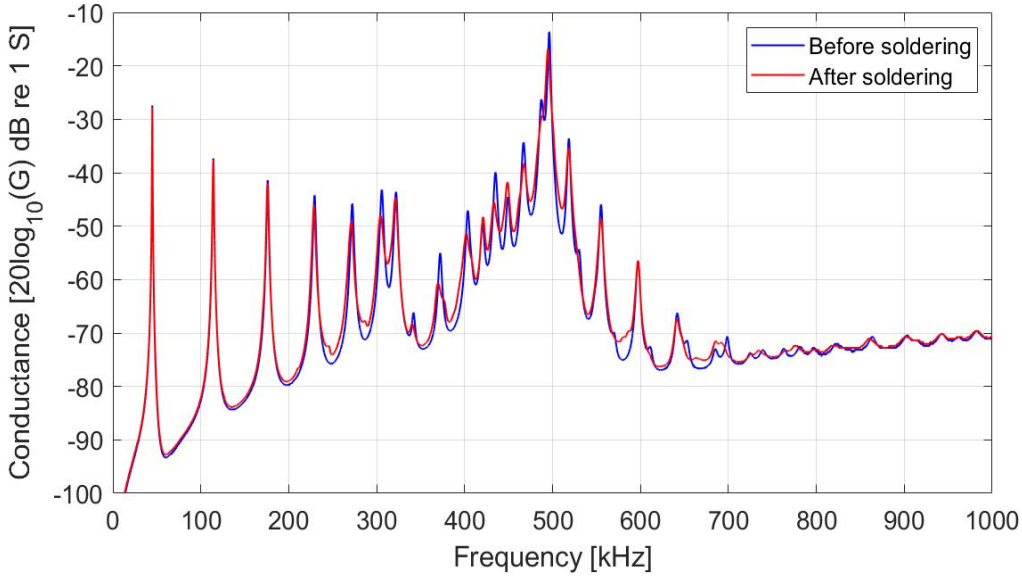

(a)

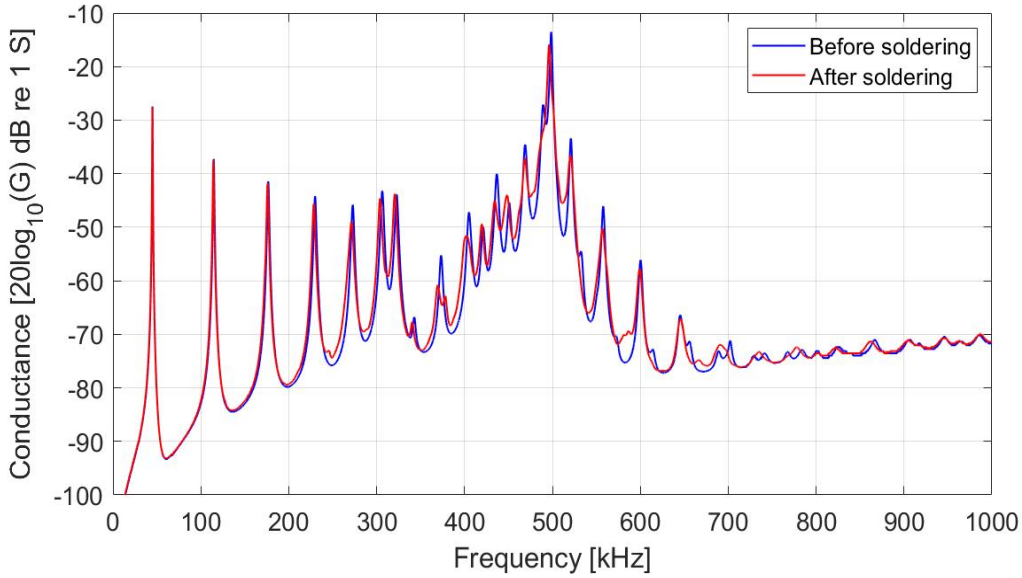

(b)

Figure 6.5: The measured conductance in air from 1-1000 kHz before and after (a) disk 44-4 (a) and (b) disk 44-6 is soldered.

As seen in Figs. 6.4 and 6.5 the deviations between the conductance measurements conducted before and after the disk are soldered are more similar to each other than for the other methods used for soldering. Disk 16-6 in Fig. 6.4a is used further in a constructed transducer.

The results presented of the measured conductance before and after the Pz27 disks are soldered shows a difference in the conductance after the disks are soldered compared to the measured conductance before the disks are soldered. The change in the measured conductance after the disks are soldered makes the measured conductance agree less with the simulations of the piezoelectric disks. The change can also affect the agreement between the measurements and simulations further in the construction process. It is seen that it is a bigger difference for the measured conductance before and after disks with (D_p x T_p) of 16 x 4 mm is soldered than for disks with (D_p x T_p) of 44 x 4 mm.

6.2.2 How the heat from the oven and soldering iron affects the disk

How the heating process affected the Pz27-disk were investigated. First, a disk (44-18) without any solder or front layer was heated up in the oven, the same as done in the last controlled soldering process described in Sec. 3.3. Then admittance measurements were conducted after the disk cooled down. Next, the disk was heated again in the oven before the soldering iron was put on the disk for five seconds at 270 °C to see if this affected the measurements further. The results of the measured conductance in log scale before and after heat is applied to the disk are shown in Fig. 6.6.

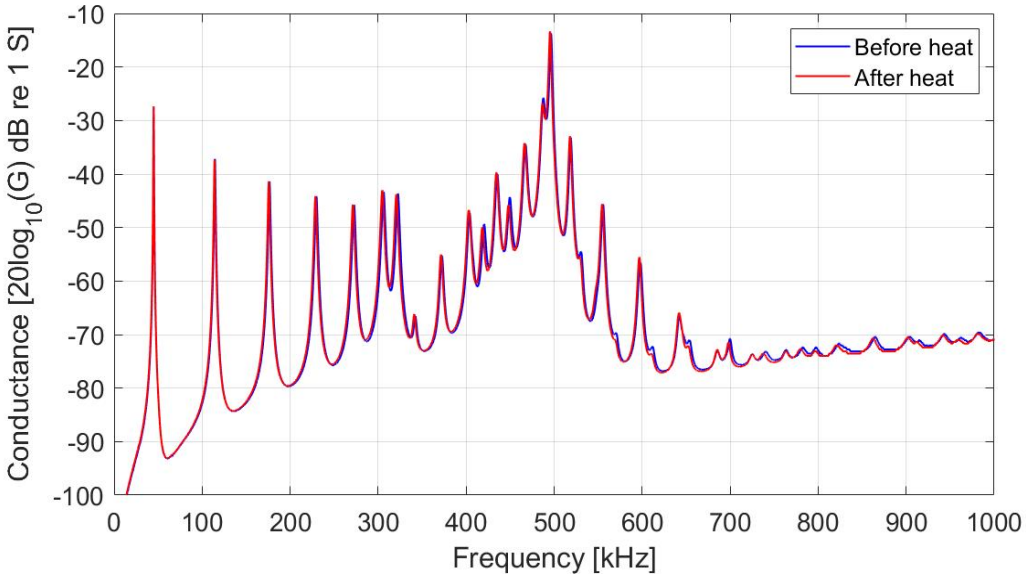

(a)

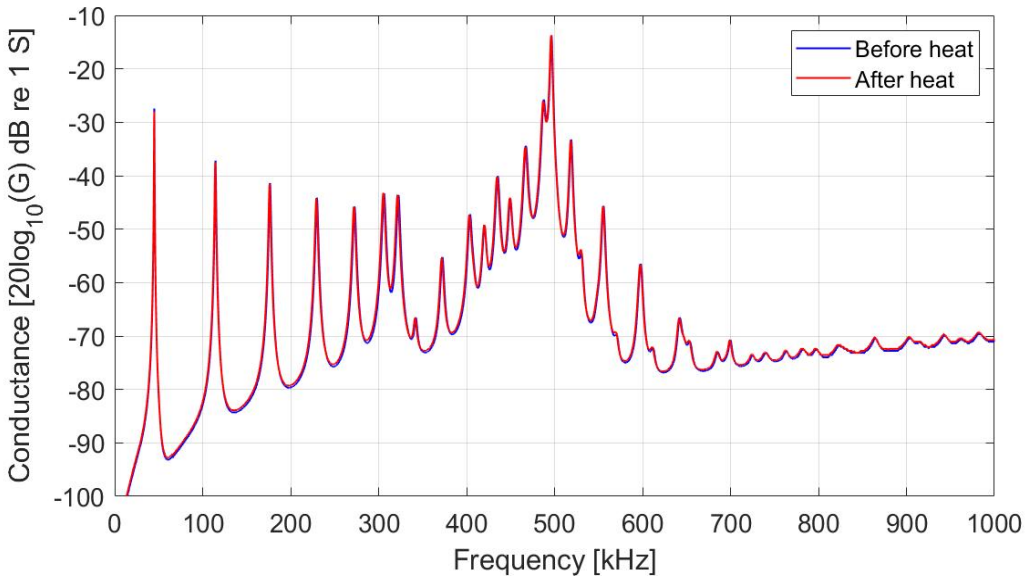

(b)

Figure 6.6: The results of the conductance measurements in air from 1-1000 kHz, before and after disk 44-18 are heated. (a) Before and after disk 44-18 are heated in the oven. (b) Before and after disk 44-18 are heated in the oven and with the soldering iron without any solder.

The soldering iron was put on early and caused electrical shocks. It was then taken off again, waited 15 seconds, then held on for 5 seconds. As shown in Figs. 6.6a and 6.6b the heating process didn't affect the disk much. Interestingly, the measurements show more deviation after only using the oven than when using the oven and soldering iron. However, this could only be due to deviations in the Impedance analyzer.

6.2.3 The results after attaching front layers to the piezoelectric disks

In this section, the admittance measurements and simulation results after attaching the Pz27 disks to the front layers are presented. All the disks attached to a front layer presented are not used further. Only six disks with front layers are used further, three disks with (D_p x T_p) of 44 x 4 mm and three disks with (D_p x T_p) of 16 x 4 mm, but the results are shown to show all the methods and problems along the way. This section is divided into two parts, where the first part shows the disks with (D_p x T_p) of 44 x 4 mm attached to front layers, and the second part shows disks with (D_p x T_p) of 16 x 4 mm attached to front layers. The material constants used for the front layer and the conductive adhesive layer in the simulations are presented in Tabs. 5.3 and 5.4.

Disks with (D_p x T_p) of 44 x 4 mm attached to front layers

Adhesive, 8331S, from GM chemicals [24] was used for attaching disk 44-1 to a front layer. The front layer was measured to (D_{fl} x T_{fl}) of 48.00 x 1.054 mm, and the conductive adhesive layer was measured to 0.285 mm. Fig. 6.7a shows measured conductance in log-scale after the soldered disk is attached to a front layer (blue) with conductive adhesive and the simulation (red). Fig. 6.7a shows that the measured conductance is higher than the simulation, which could be due to some conductive adhesive spots on the side and top of the disk, which can give a higher resistance.

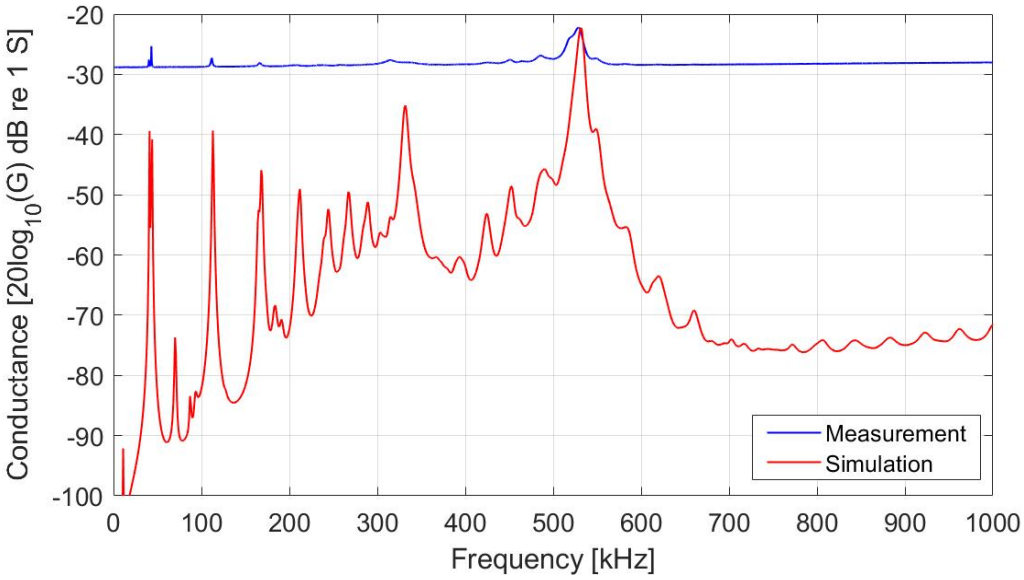

(a)

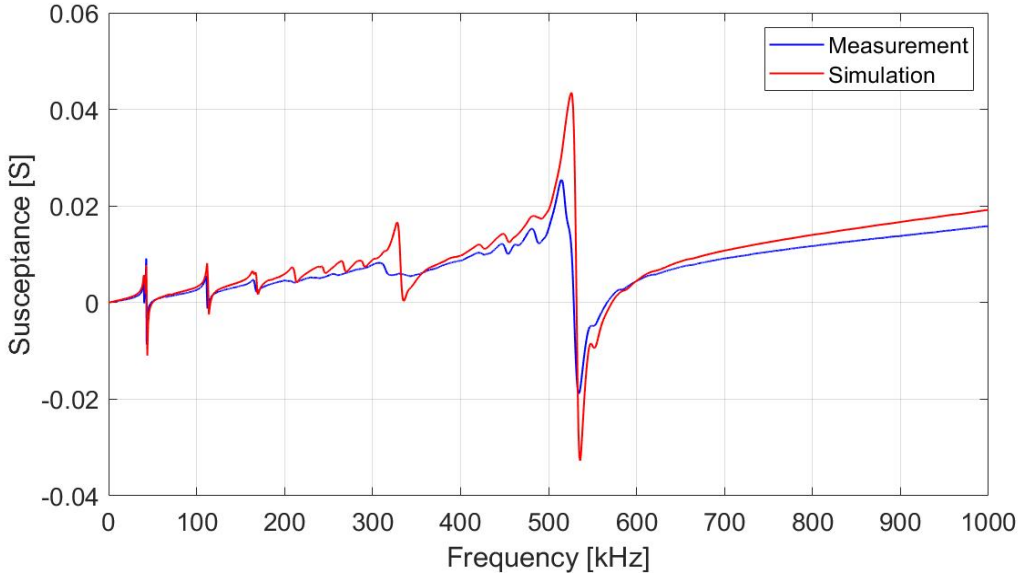

(b)

Figure 6.7: The admittance results after disk 44-1 are attached to a front layer with conductive adhesive with a thickness of 0.285 mm. The measured admittance in air (blue) compared to the simulation (red) from 1-1000 kHz. (a) The conductance. (b) The susceptance.

The top of the thickness mode on the measurement in Fig. 6.7a matches the thickness mode on the simulated construction and the first resonance modes. Fig. 6.7b shows measured susceptance (blue) and simulated susceptance (red). The measured susceptance matches the simulated susceptance better than the measured conductance.

Simulations of disk 44-1 with the front layer and with different thicknesses of the conductive adhesive layer were made to see how the thickness layer changes the admittance. The results of the conductance and the susceptance is given in Figs. 6.8a and 6.8b, where the log of the conductance and the susceptance is plotted against the frequency, respectively.

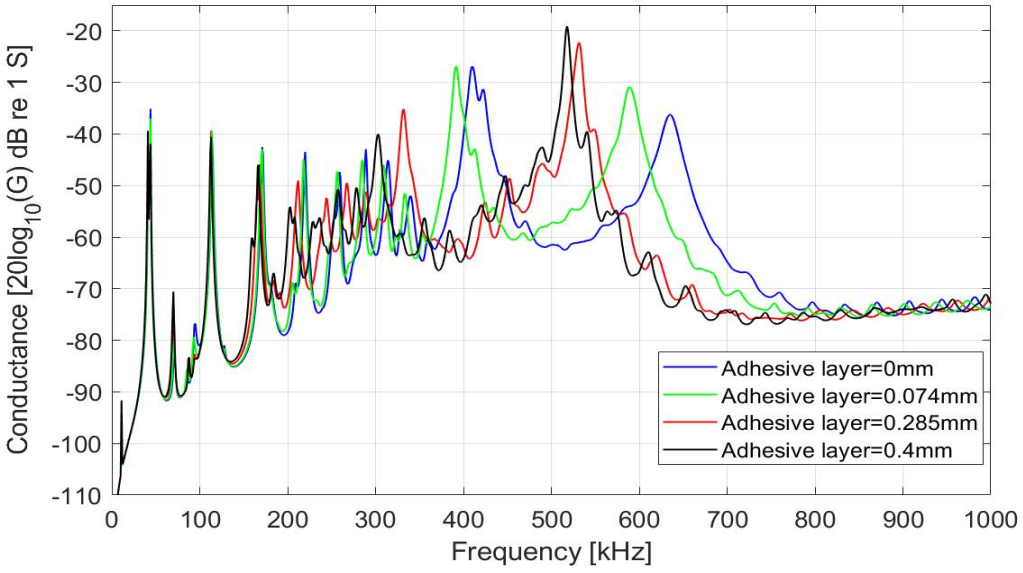

(a)

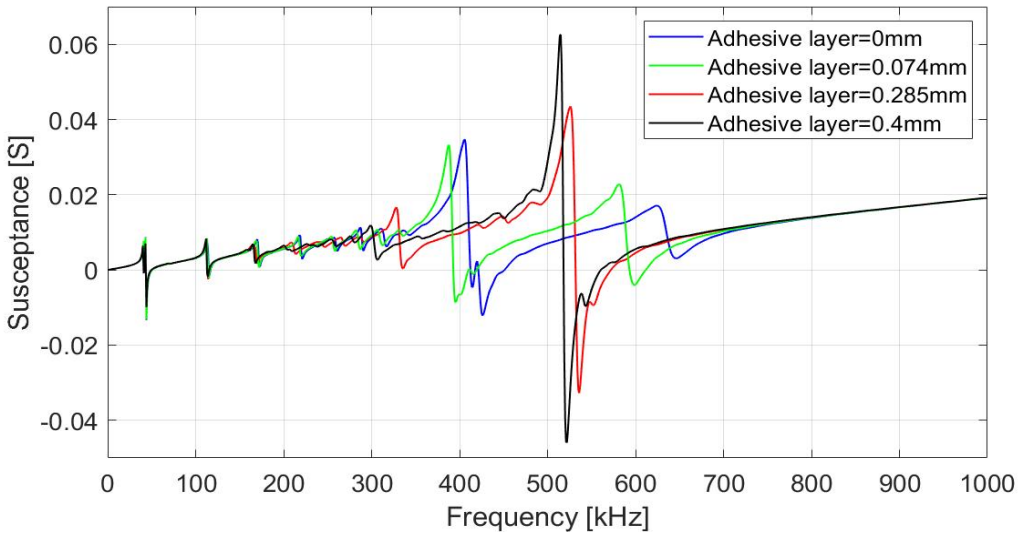

(b)

Figure 6.8: The results of the admittance simulations in vacuum of disk 44-1 with front layer and with different thicknesses of the conductive adhesive layer from 1-1000 kHz, (blue = 0 mm thickness, red = 0.285 mm thickness, green = 0.074 mm thickness and black = 0.4 mm thickness). (a) The conductance. (b) The susceptance.

Fig. 6.8a shows simulations of the conductance of disk 44-1 with front layer along with different thicknesses of the conductive adhesive. Only disk and front layer (blue), the thickness Aanes [1] used (green), the thickness of the conductive adhesive layer measured on disk 44-1 with front layer (red) and a thicker conductive adhesive layer off 0.4 mm (black). Fig. 6.8b shows the same simulations only with susceptance instead. This simulation shows that the thicker the conductive adhesive layer is, the less splitting of the thickness mode happens in the conductance, giving a higher resonance around the thickness mode. Which states that getting a thin layer of the conductive adhesive is essential since a split is wanted for the transducer to achieve a better response over a broader frequency range [16].

A front layer with dimensions (D_{fl} x T_{fl}) of 51.87 x 1.005 mm was attached to disk 44-2 with the conductive adhesive, 8331S, from GM chemicals [24]. The thickness of the conductive adhesive on disk 44-2 with the front layer was measured to be 0.120 mm. The admittance results are presented in Figs. 6.9a and 6.9b, where the log of the conductance and the susceptance is plotted against the frequency, respectively.

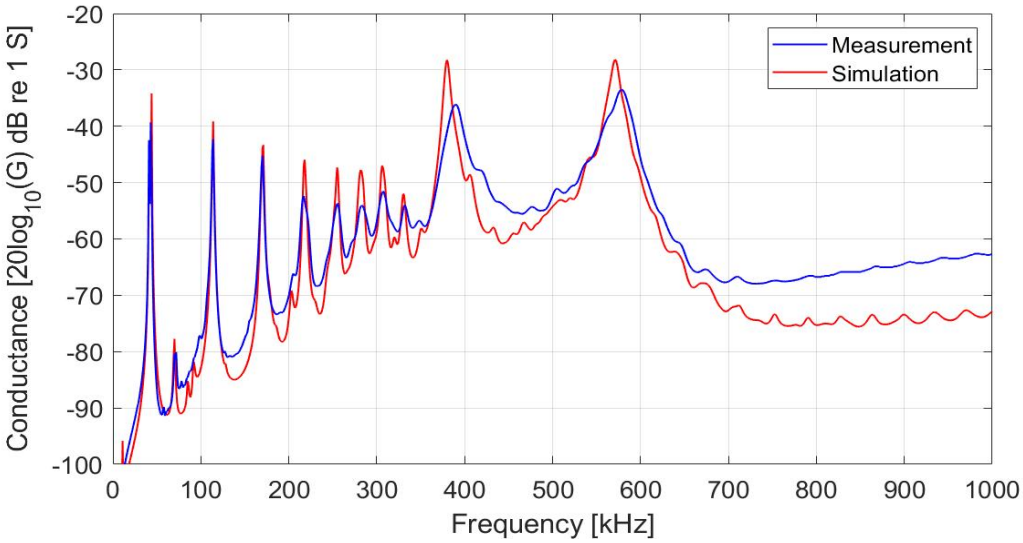

(a)

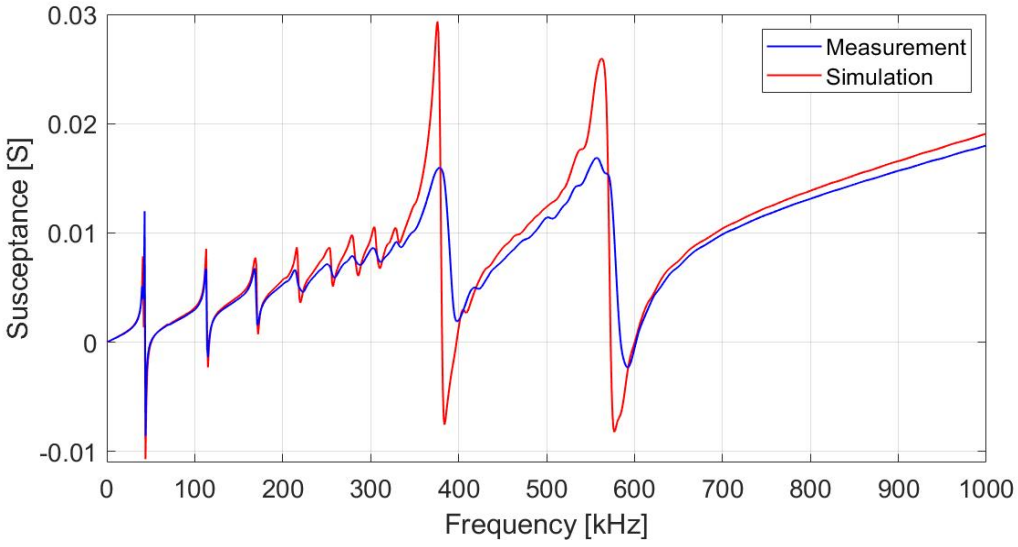

(b)

Figure 6.9: The admittance results after disk 44-2 are attached to a front layer with a conductive adhesive layer with thickness of 0.120 mm. The measured admittance in air (blue) compared to the simulation (red) from 1-1000 kHz. (a) The conductance. (b) The susceptance.

As seen in Fig. 6.9a, the conductance measurements (blue) of disk 44-2 with the front layer are in closer agreement with the simulation than the conductance measurement for disk 44-1 with the front layer in Fig. 6.7a was. The closer agreement between the measured conductance and the simulation of disk 44-2 with the front layer shows that it is important to avoid getting any conductive adhesive on the side of the disk. As seen in Fig. 6.2a disk 44-2 was not the best soldered disk. The measured conductance deviated after 200 kHz compared to the measured conductance before soldering. The measured change in the conductance after disk 44-2 was soldered affects the agreement between the admittance measurement for disk 44-2 with the front layer as well, and is one reason why the measurements do not agree well with the simulation around the thickness mode. As seen in Fig. 6.9a, it is a small frequency displacement in the thickness mode between the measurement and the simulation. After 700 kHz, the measured conductance is higher than the simulation. The measured susceptance in Fig. 6.9b are closer to the simulation after 700 kHz than the measured conductance, but around the thickness mode, the measured susceptance is not in close agreement with the simulation.

Several measurements are made to see if the measured conductance can be closer to the simulation above 700 kHz to agree better to the simulation by adjusting the measurement setup by changing the place and attachment on the wire on the front layer to get better contact with the front electrode of the disk. Also, adjustments in the simulations are made to see if it is possible to make the simulations closer to the measurements. The adjusted simulations seen in Fig. 6.10a and 6.10b is made with a small clump of solder in the middle of the back of disk 44-2, and the thickness of the conductive adhesive is changed to 0.088 mm.

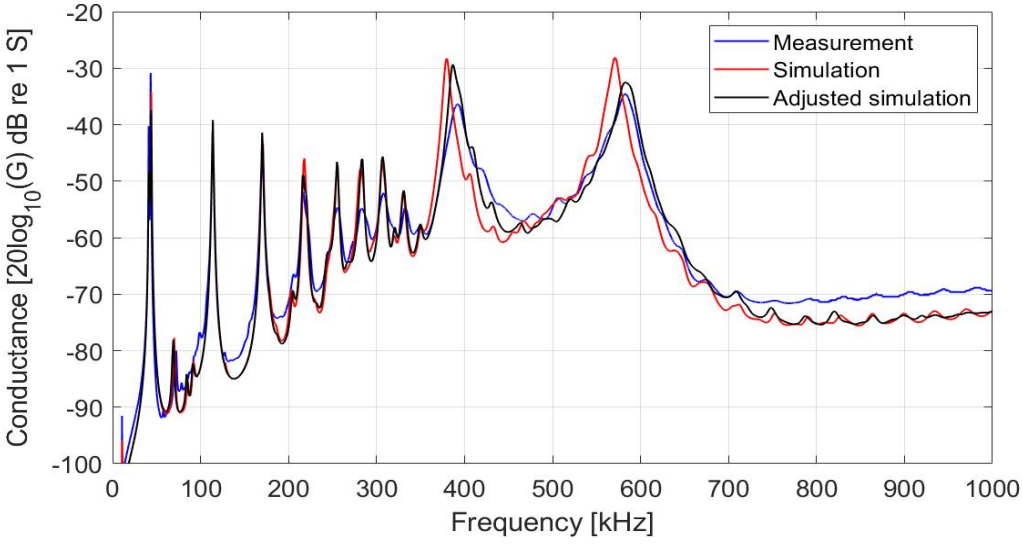

(a)

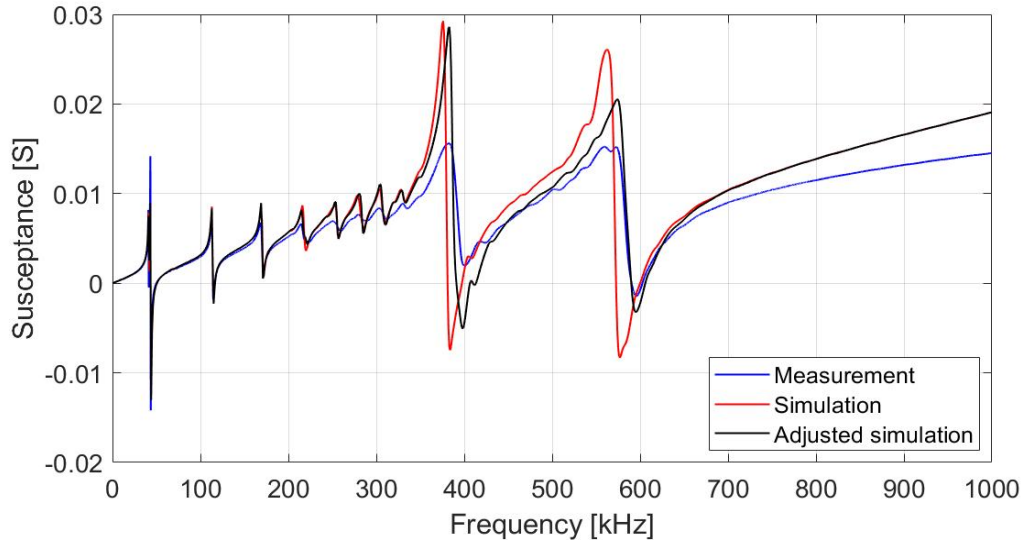

(b)

Figure 6.10: The admittance results after disk 44-2 are attached to a front layer with conductive adhesive. The measurement (blue) compared to the simulation of disk 44-2 with a conductive adhesive layer with thickness of 0.120 mm, and front layer (red), and the simulation of disk 44-2 with solder with a radius of 3 mm and a thickness of 0.3 mm, front layer and a conductive adhesive layer with thickness of 0.088 mm. (a) The conductance. (b) The susceptance.

As seen in Fig. 6.10a, by adjusting the measurement setup, the conductance measurements are closer to the simulation in the frequency region 700 - 1000 kHz than the measurement shown in Fig. 6.9a. However the measured susceptance in Fig. 6.9b are closer than the measured susceptance in Fig. 6.10b. The reason the measured conductance is closer to the simulation and not the measured susceptance could be because of the zero adjustments of the Impedance Analyzer done before conducting the measurements. It is seen that it is harder to zero-adjust the susceptance than the conductance. The adjusted simulations are in closer agreement with the measurement around the thickness mode than the simulation without solder, as seen in Figs. 6.10a and 6.10b.

The same simulation setup is used further to simulate a finished transducer in water to see the difference between the simulation of disk 44-2 with the front layer and the measured thickness of the conductive adhesive layer, and the adjusted simulation with another thickness of the conductive adhesive layer and with solder. The results are shown in Figs 6.11, where the log of the conductance and the source sensitivity is plotted against the frequency, respectively.

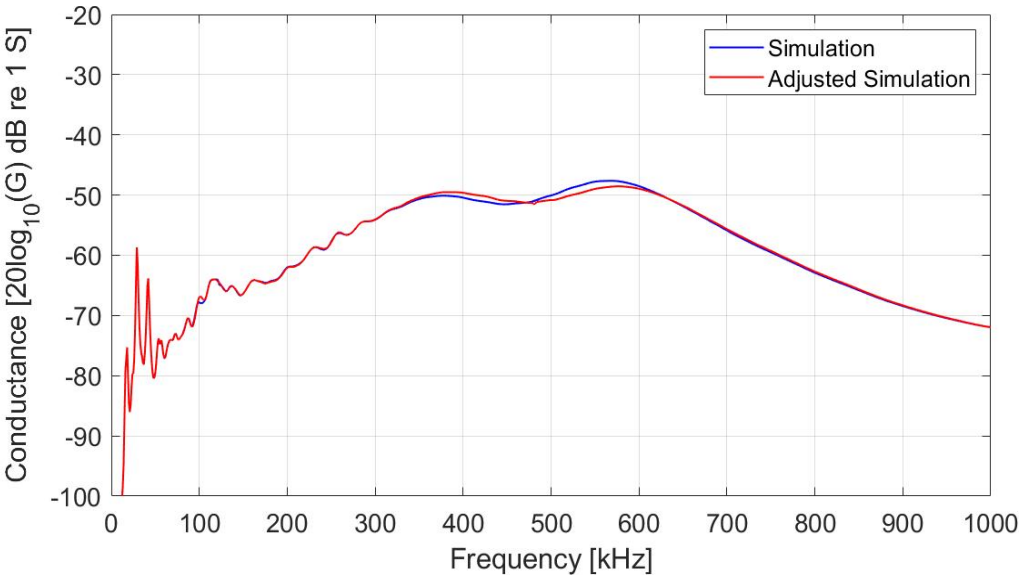

(a)

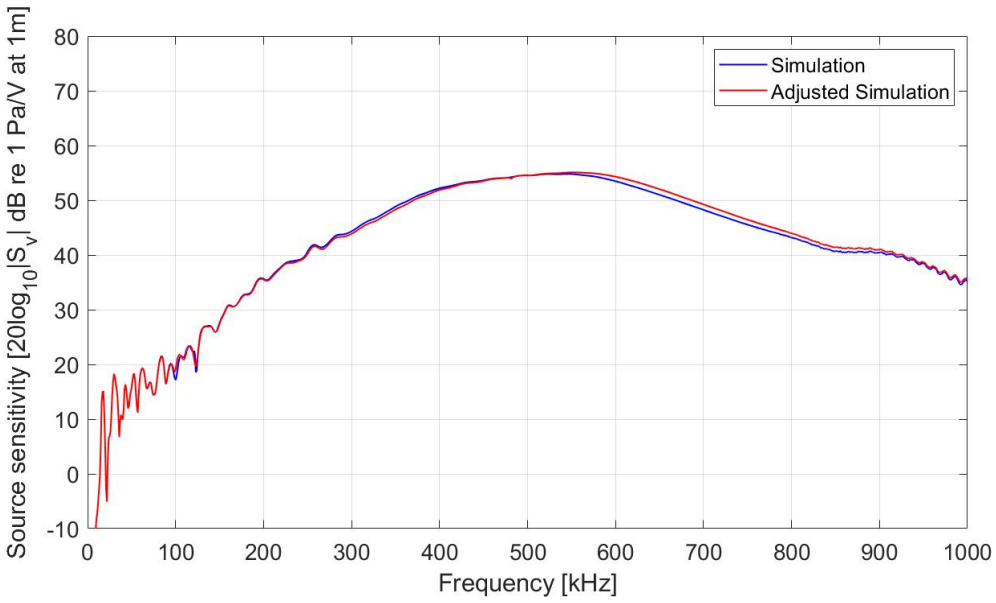

(b)

Figure 6.11: The simulated conductance (a) and the source sensitivity (b) in water of a transducer with disk 44-2 attached to a front layer with a conductive adhesive layer thickness of 0.120 mm, tungsten epoxy with Z=16.8 MRayl backing layer with a steel casing (blue), and with disk 44-2 with solder attached to a front layer with a conductive adhesive layer with a thickness of 0.088 mm, tungsten epoxy with Z=16.8 MRayl backing layer with a steel casing (red).

The simulation of the transducer is made with a tungsten epoxy backing layer with the material constants in Tab. 5.8. The results in Fig. 6.11 shows that it is a small difference between the two simulation setup, and the effect of the solder will not change the source sensitivity response much. Therefore disk 44-2 is used further to construct a transducer where a clump of solder and a conductive adhesive thickness layer of 0.088 mm is used in the simulations further in the construction process.

A front layer with dimensions (D_{fl} x T_{fl}) of 51.16 x 1.213 mm was attached to disk 44-4, where the conductive adhesive (8330D from MG Chemicals [22]) was used. The thickness of the conductive adhesive layer was measured to be 0.062 mm. The results are shown in Figs. 6.12a and 6.12b, where the log of the conductance and the susceptance is plotted against the frequency, respectively.

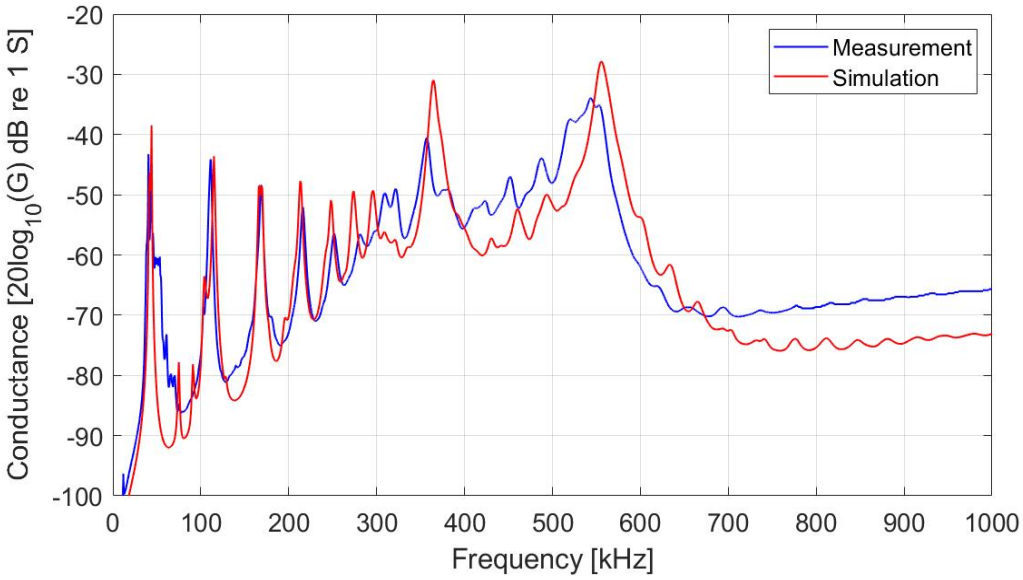

(a)

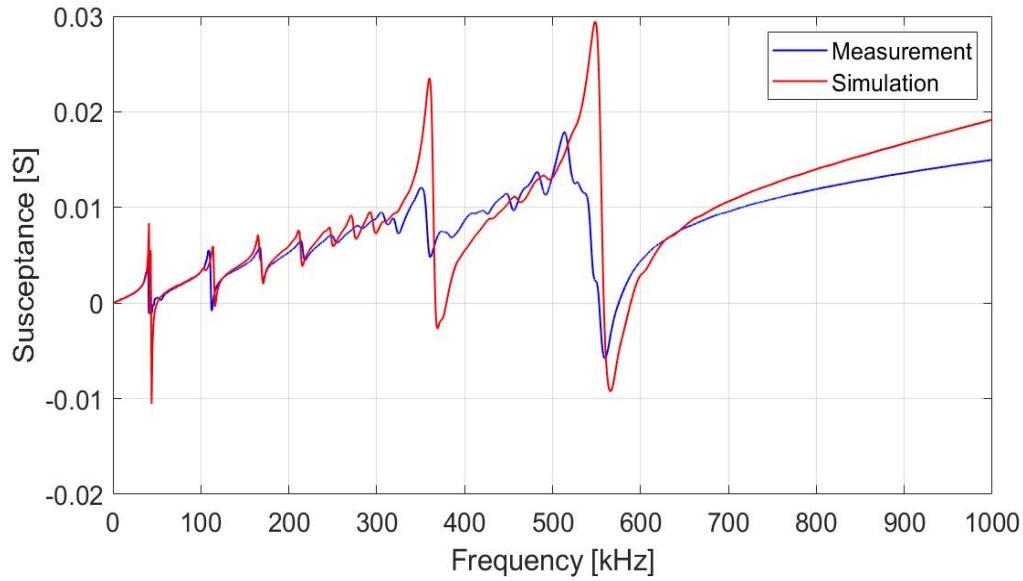

(b)

Figure 6.12: The admittance results after disk 44-4 are attached to a front layer with a conductive adhesive layer with thickness of 0.062 mm. The measured admittance in air (blue) compared to the simulation (red) from 1-1000 kHz. (a) The conductance. (b) The susceptance.

As seen in Fig. 6.12a and 6.12b, the admittance measurement of disk 44-4 with the front layer is not in close agreement with the simulation, especially between 300-1000 kHz. The difference between the measured and simulated admittance is probably because the disk and front layer were taken apart after the conductive adhesive was applied, which could cause some air in the conductive adhesive.

A front layer with dimensions (D_{fl} x T_{fl}) of 51.15 x 1.194 mm was attached to disk 44-5. The conductive adhesive layer was measured to be 0.132 mm. The results are shown in Figs. 6.13a and 6.13b, where the log of the conductance and susceptance is plotted against the frequency, respectively.

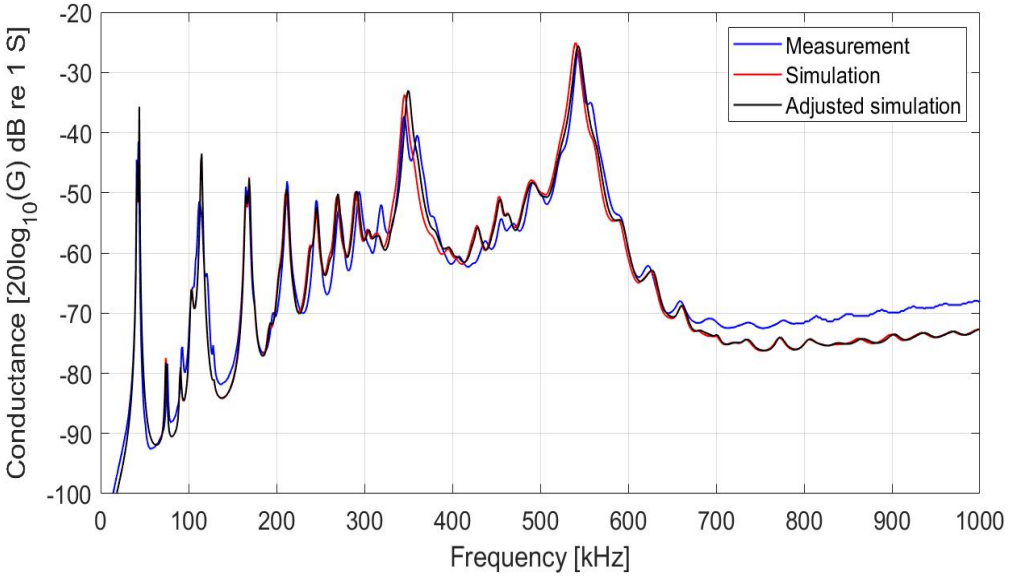

(a)

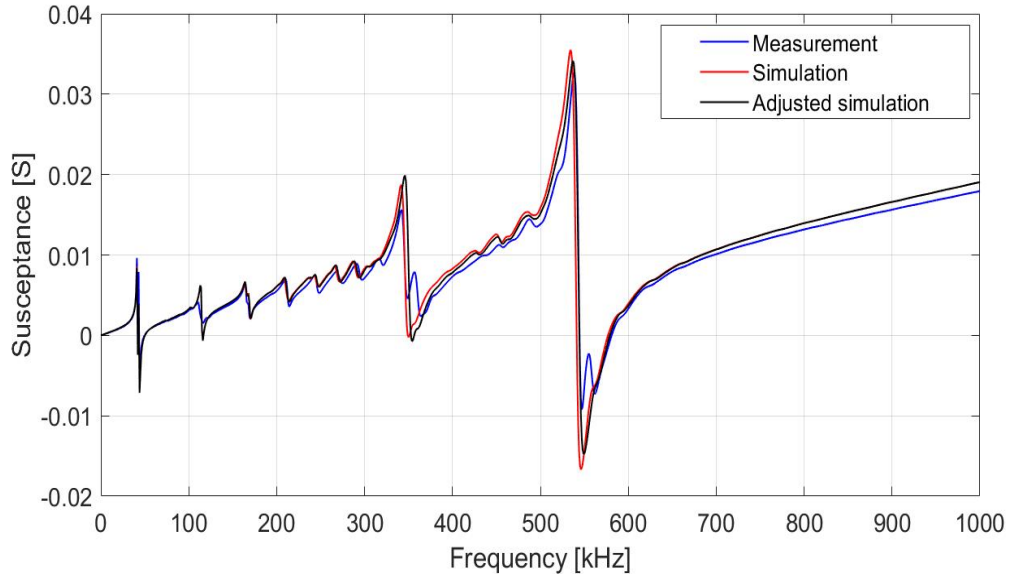

(b)

Figure 6.13: The admittance results after disk 44-5 are attached to a front layer with conductive adhesive. The measured admittance in air (blue) compared to the simulation of disk 44-5 with a conductive adhesive layer thickness of 0.132 mm and front layer (red), and the simulation of disk 44-5 with front layer and a conductive adhesive layer with thickness of 0.118 mm (black). (a) The conductance. (b) The susceptance.

A minor adjustment in the conductive adhesive layer gave a small displacement in frequency for the resonances, so the simulation with a change in the conductive adhesive layer was in closer agreement with the measurement than the simulation with the measured thickness of the conductive adhesive layer, as seen in Fig. 6.13a and 6.13b. It is still a difference between the measurement and simulation in the frequency range of 700-1000 kHz, but the measurements and simulations are in close agreement for the resonances and thickness mode. Disk 44-5 with the front layer is used further in the construction process, where a thickness of the conductive adhesive layer of 0.118 mm is used in the simulations further.

For attaching disk 44-7 to a front layer with dimensions (D_{fl} x T_{fl}) of 51.16 x 1.172 mm, the exact same method as for disk 44-5 was used since this method gave a close agreement between the measurement and simulation as seen in Fig. 6.13. The result is given in Fig. 6.14a and 6.14b, where the log of the conductance and the susceptance is plotted against the frequency, respectively.

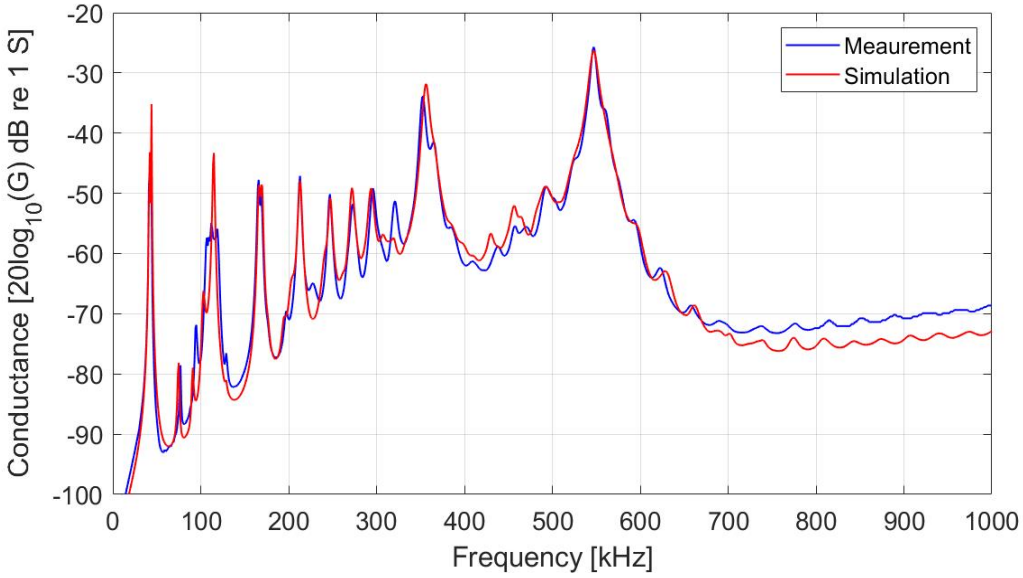

(a)

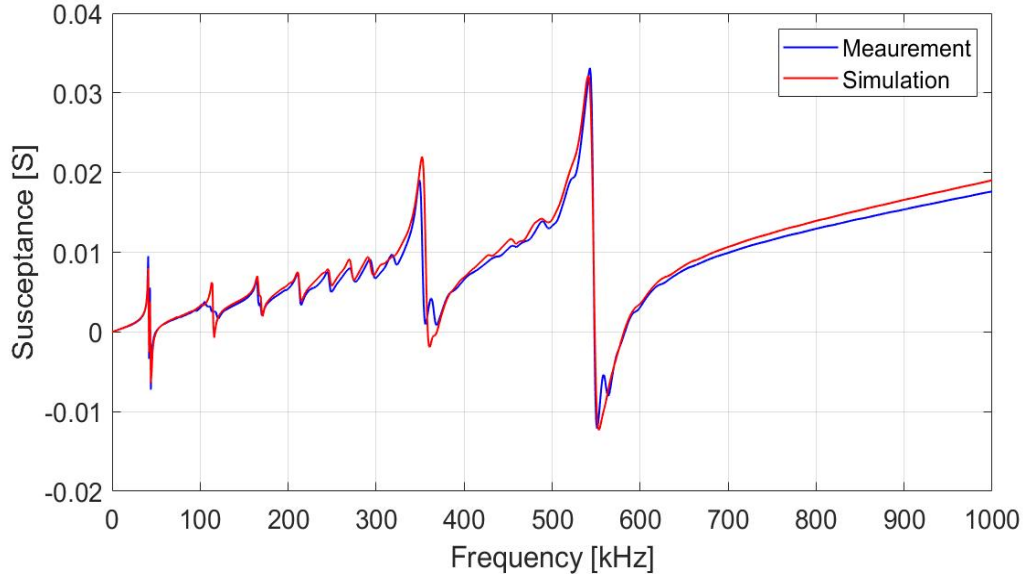

(b)

Figure 6.14: The admittance results after disk 44-7 are attached to a front layer with conductive adhesive. The measured admittance in air (blue) compared to the simulation of disk 44-7 with front layer and a conductive adhesive layer with thickness of 0.106 mm (red). (a) The conductance. (b) The susceptance.

As shown in Figs. 6.14a and 6.14b, the admittance measurements are in close agreement to the simulation. The conductive adhesive layer is measured to be 0.106 mm, and no adjustments in the thickness layer in the simulations are made. This disk is used further in the construction process. Disk 44-7 had the least deviations between the conductance measurement before and after the disk was soldered, seen in Fig. 6.1b. The result in Fig. 6.1b can explain why disk 44-7 attached to a front layer are in closer agreement with the simulations than what measurements of disk 44-2 and 44-5 with front layers in Figs. 6.10 and 6.13 was before the conductive adhesive layer was adjusted in the simulations.

Disks with (D_p x T_p) of 16 x 4 mm attached to front layers

The conductive adhesive, 8330D [22], from MG Chemicals was used to attach disk 16-7 to a front layer with dimensions (D_{fl} x T_{fl}) of 23.986 x 1.007 mm. The conductive adhesive layer was measured to be 0.002 mm. However, the soldered wire attached to disk 16-7 fell off when the disk was attached to the front layer. Therefore,

the disk was soldered again, using old and new solder, in case the electrode got broken when taking the old solder off. The results of the conductance and susceptance for disk 16-7 with the front layer is shown in Figs. 6.15a and 6.15b, where the log of the conductance and the susceptance is plotted against the frequency, respectively.

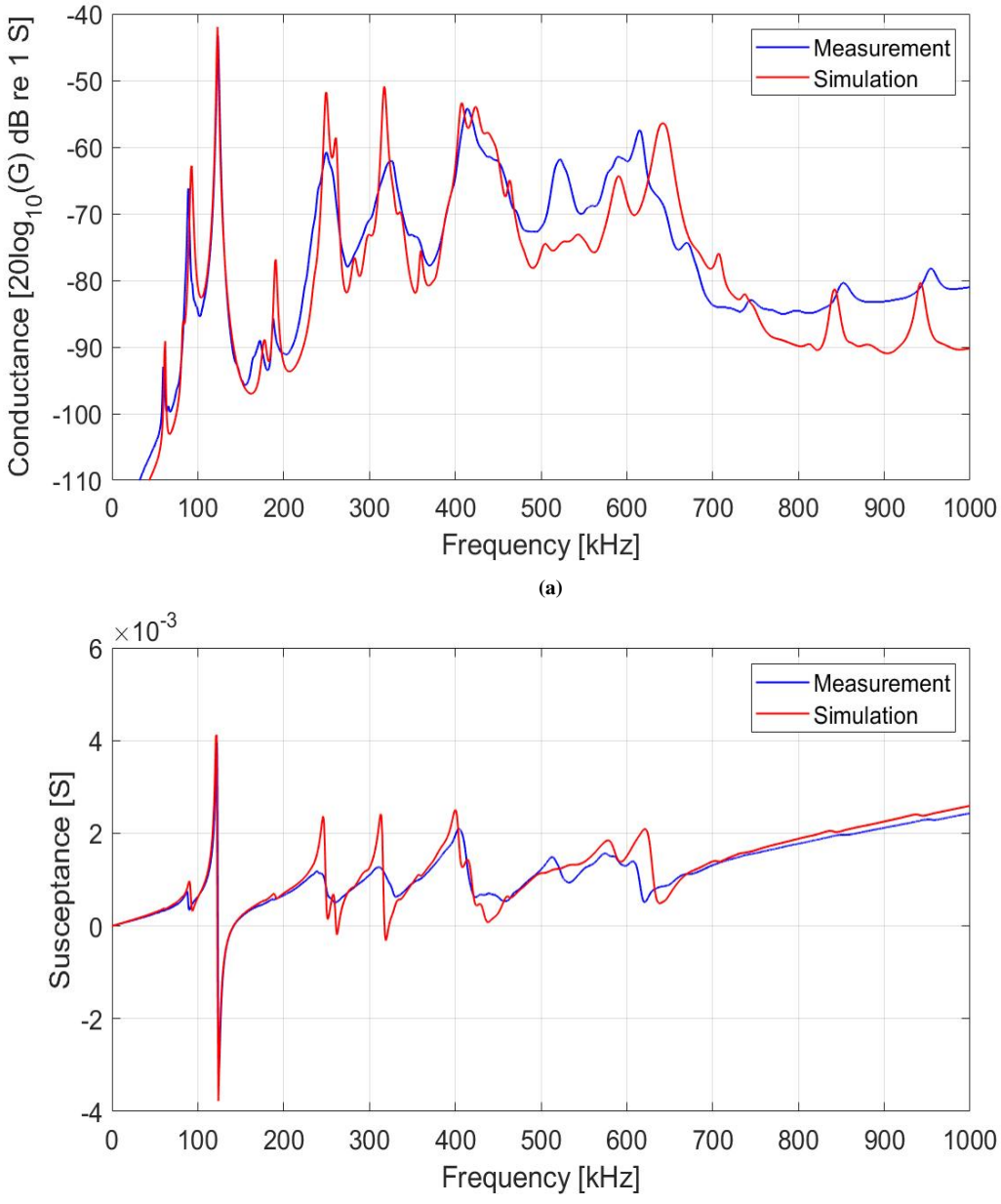

Figure 6.15: The admittance results after disk 16-7 are attached to a front layer with a conductive adhesive layer with thickness of 0.002 mm. The measured admittance in air (blue) compared to the simulation (red) from 1-1000 kHz. (a) The conductance. (b) The susceptance.

Some of the deviations seen in Fig. 6.15a could be due to the new soldering. The measured conductance agrees with the simulation between 50 - 450 kHz, but the measured resonances are lower than the simulations. Between 500-100 kHz, the measurement is not in close agreement with the simulation. The measured susceptance is in agreement with the simulations between 100 - 200 kHz and 650 - 1000 kHz. In the resonance frequencies, the measurements are lower than the simulations, and deviation between the simulation and measurements is seen in the thickness mode.

Some adjustments in the simulation setup were made, where a clump of solder and a vacuum gap in the conductive adhesive layer was simulated. Fig. 6.16 shows the measurement of disk 16-7 (blue), the simulation shown in Fig.

6.15 (red), simulation with the same setup as in Fig. 6.15 but with a conductive adhesive thickness of 0.040 mm and with a solder clump added (green) and simulation with a vacuum gap and solder (black). The simulations of the solder are with the solder size that gives the best agreement compared to the measurement, the same with the vacuum gap.

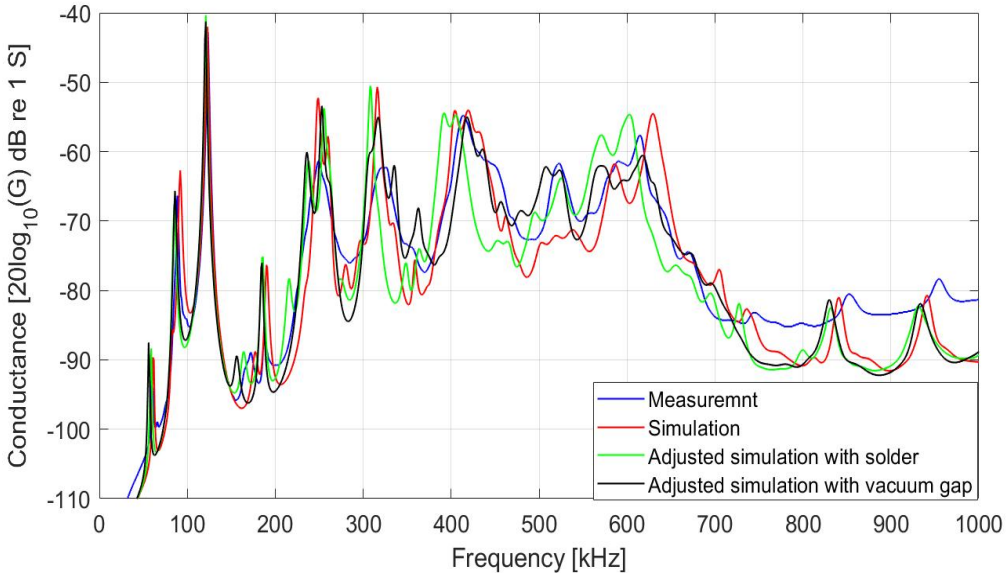

Figure 6.16: The measured conductance in air of disk 16-7 with front layer and conductive adhesive layer from 1-1000 kHz (blue) compared to the simulation of disk 16-7 with front layer and a conductive adhesive layer with thickness of 0.002 mm (red), simulation of disk 16-7 with solder with a thickness of 0.03 mm and a radius of 3 mm, front layer and a conductive adhesive layer with thickness of 0.040 mm (green) and simulation of disk 16-7 with solder with a thickness of 0.03 mm and a radius of 3 mm, front layer and an vacuum gap with a radius of 0.85 mm in the conductive adhesive as shown in Fig. 5.13 (black).

When comparing the different simulation setups with the conductance measurement in Fig. 6.16, it is seen that the adjusted simulations with another thickness of the conductive adhesive, solder and vacuum gap agree better with the measurement around the thickness mode, especially around 500 kHz than the simulation with the measured thickness of the conductive adhesive and without solder and vacuum. When looking at the frequency range 400 - 600 kHz in the thickness mode in Fig. 6.16, the simulation with solder and a vacuum gap in the conductive adhesive is in closer agreement with the measurements than the other simulations. Since the simulation with solder and vacuum gap in the conductive adhesive layer is in closest agreement to the measurement, it seems that some air is trapped in the conductive adhesive layer between disk 16-7 and the front layer, and that the extra load of the solder affects the admittance measurements.

In Fig. 6.17 different dimensions of the solder clump are simulated and compared to the conductance measurement of disk 16-7 to show how the conductance varies depending on the dimension of the solder.

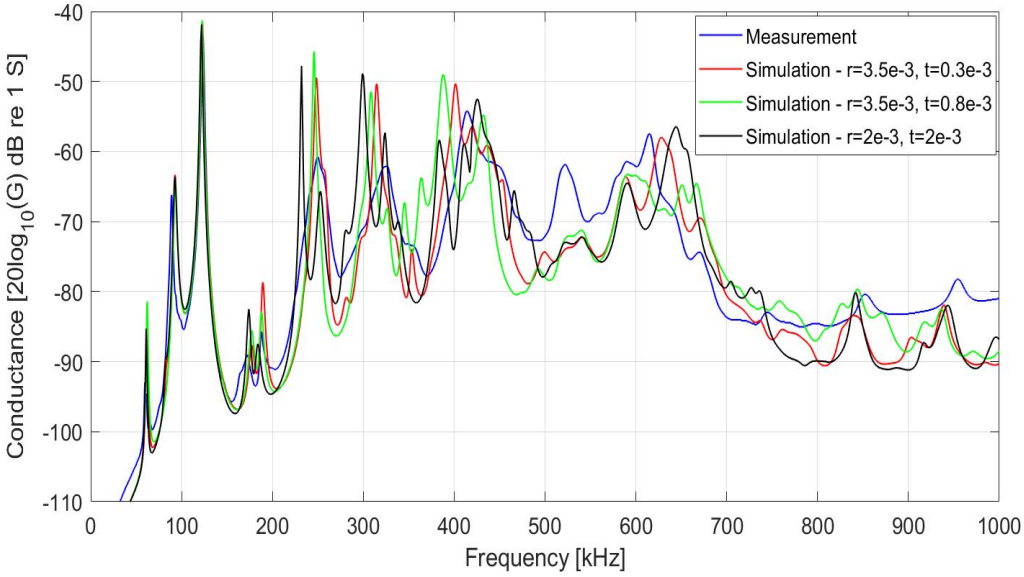

Figure 6.17: The measured conductance in air of disk 16-7 with front layer and conductive adhesive layer (blue) compared to the simulation of disk 16-7 with front layer and a conductive adhesive layer with thickness of 0.040 mm and solder with a radius of 3.5 mm and thickness of 0.3 mm (red), simulation with solder with a radius of 3.5 mm and a thickness of 0.5 mm (green) and with solder with a radius of 2 mm and a thickness of 2 mm (black).

In Fig. 6.17 it is seen that it is a variation of where the resonance frequencies are with the different sizes of the solder. The variations in the conductance between different dimensions of the solder show that the extra load the solder contributes affects the conductance.

A front layer with dimensions (D_{fl} x T_{fl}) of 23.020 x 1.060 mm was attached to disk 16-2. The conductive adhesive layer was measured to 0.031 mm. No further attempts on adjusting the simulations to the measurement were made. The results are shown in Figs. 6.18a and 6.18b, where the log of the conductance and the susceptance is plotted against the frequency, respectively.

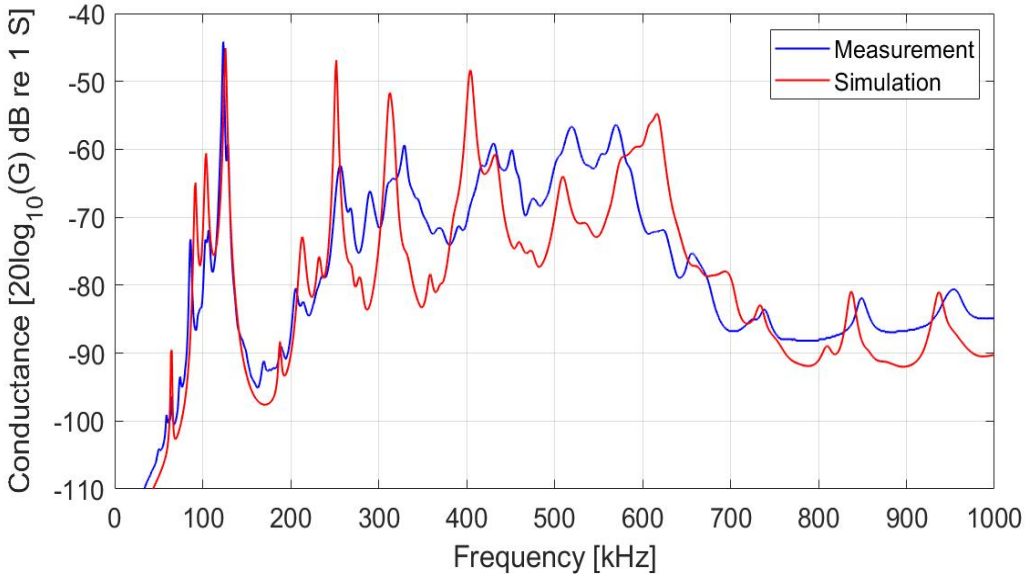

(a)

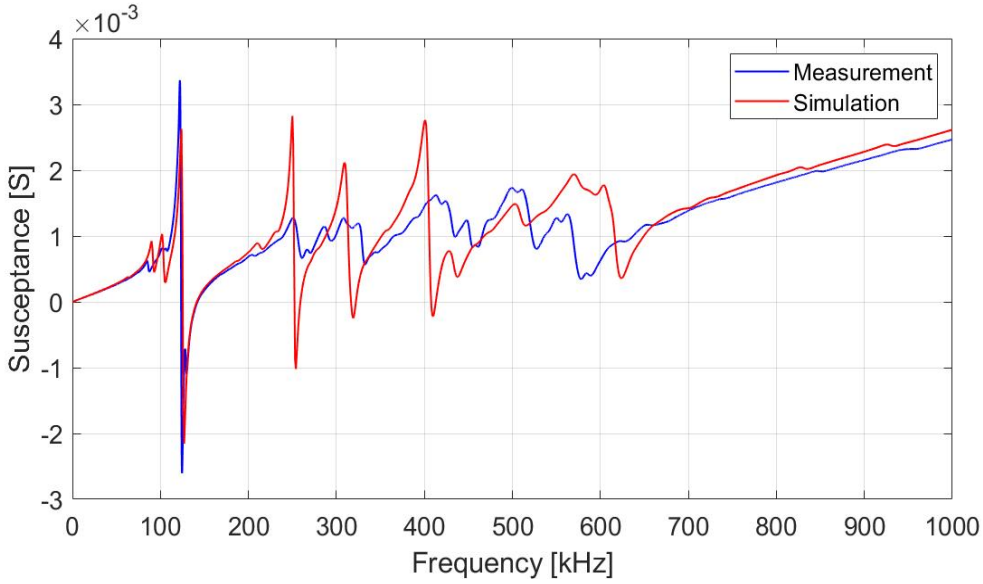

(b)

Figure 6.18: The admittance results after disk 16-2 are attached to a front layer with a conductive adhesive layer with thickness of 0.031 mm. The measured admittance in air (blue) compared to the simulation (red) from 1-1000 kHz. (a) The conductance. (b) The susceptance.

The measured admittance shown in Fig. 6.18a and 6.18b are not in close agreement with the simulations. Seen from the deviations in Fig. 6.18 compared to simulations of air and vacuum gap in Fig. 6.16, it seems that some air could be trapped in the conductive adhesive layer between disk 16-2 and the front layer. The deviation could be because the disk and the front layer were taken apart after the conductive adhesive was applied in between, which is also seen from disk 44-4 in Fig. 6.12 that this could cause a difference between the measurement and simulation.

Disk 16-4 was attached to a front layer with dimensions (D_{fl} x T_{fl}) of 23.037 x 1.132 mm. When taking off the holder, the tape loosened, so some adhesive got attached to the side of the disk. The conductive adhesive on the side of the disk might explain some of the deviations seen in Figs. 6.19a and 6.19b. The thickness of the conductive adhesive was measured to be 0.123 mm.

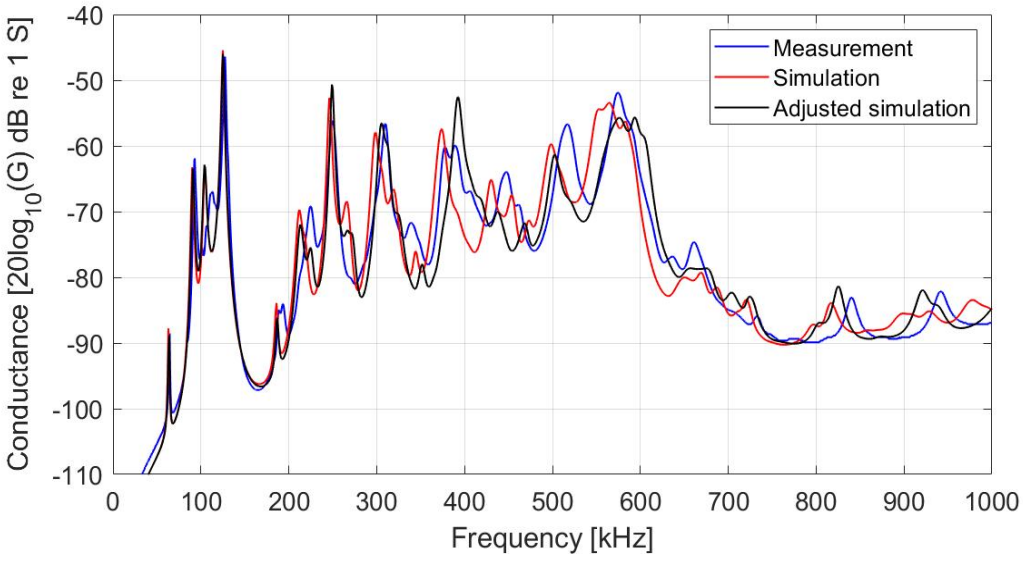

(a)

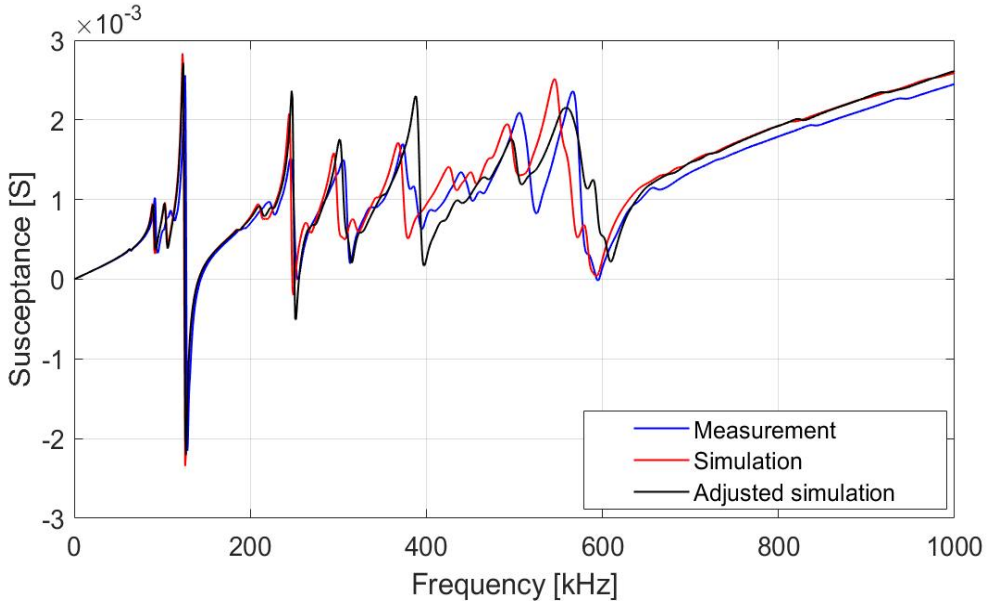

(b)

Figure 6.19: The admittance results after disk 16-4 are attached to a front layer with conductive adhesive. The measured admittance in air (blue) compared to the simulation of disk 16-4 with front layer and a conductive adhesive layer with thickness of 0.123 mm (red), and the simulation of disk 16-4 with solder with a radius of 3.5 mm and a thickness of 0.03 mm, front layer and a conductive adhesive layer with thickness of 0.053 mm. (a) The conductance. (b) The susceptance.

As seen in Fig. 6.19a and 6.19b, the measurement (blue) are compared to the simulation with a conductive adhesive layer of 0.123 mm (red) and a simulation with a thickness of the conductive adhesive of 0.053 mm with solder with a radius of 3.5 mm and a thickness of 0.03 mm (black). The simulation with a conductive adhesive thickness of 0.053 mm and solder is in closer agreement with the measurement than the simulation with a conductive adhesive thickness of 0.123 mm.

Disk 16-5 was applied to a front layer with dimensions (D_{fl} x T_{fl}) of 23.031 x 1.123 mm. The conductive adhesive layer was measured to be 0.056 mm. The results are shown in Figs. 6.20a and 6.20b, where the log of the conductance and the susceptance is plotted against the frequency, respectively.

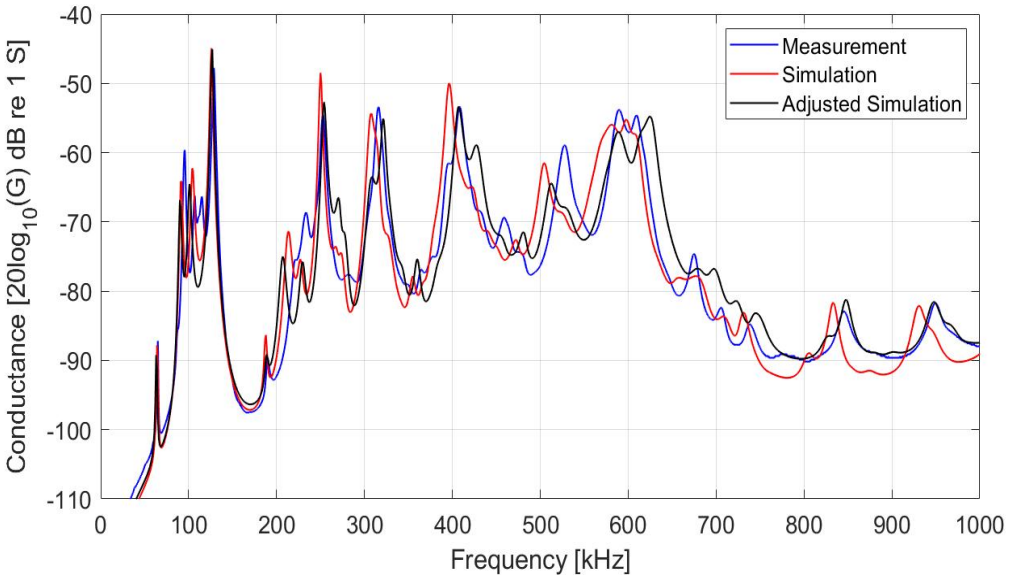

(a)

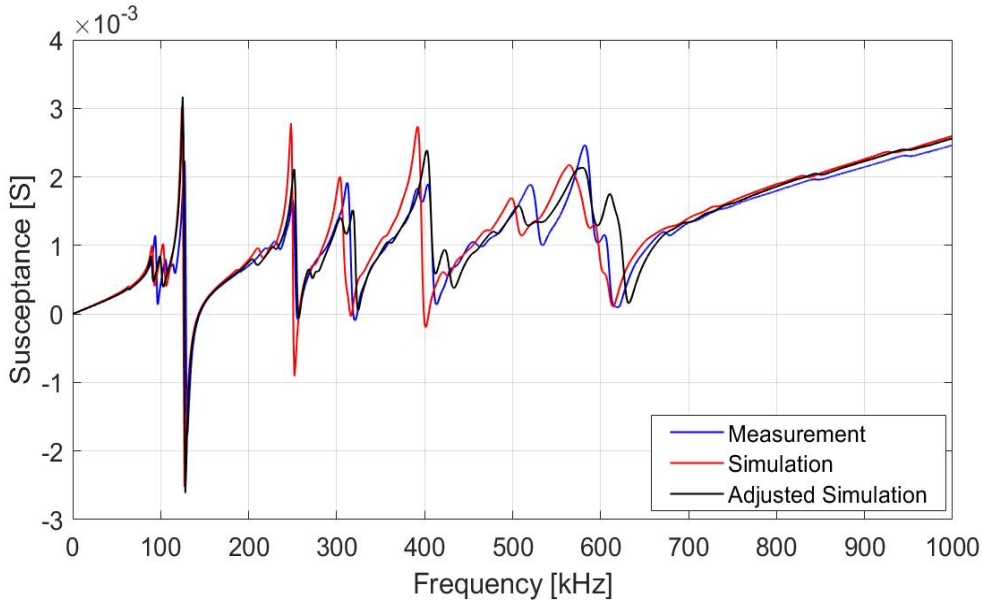

(b)

Figure 6.20: The admittance results after disk 16-5 are attached to a front layer with conductive adhesive. The measured admittance in air from 1-1000 kHz (blue) compared to the simulation of disk 16-5 with front layer and a conductive adhesive layer with a thickness of 0.056 mm (red), and the simulation of disk 16-5 with front layer and a conductive adhesive layer with a thickness of 0.036 mm. (a) The conductance. (b) The susceptance.

As seen in Fig. 6.20a the adjusted simulations, where the conductive adhesive thickness layer is adjusted, agrees at the first resonance frequencies, and also at $850-950$ kHz, it agrees better to the measurement than the simulation with a conductive adhesive thickness of 0.056 mm. The adjusted simulations of the susceptance also agree better with the measurement, as seen in Fig. 6.20b, than the simulation with a conductive adhesive layer with a thickness of 0.056 mm. Disk 16-5 is used further in the construction process, with the adjusted conductive thickness layer in the simulations.

A front layer with dimensions (D_{fl} x T_{fl}) of 23.040 x 1.115 mm was attached to disk 16-10. The results are shown in Figs. 6.21a and 6.21b, where the log of the conductance and the susceptance is plotted against the frequency, respectively.

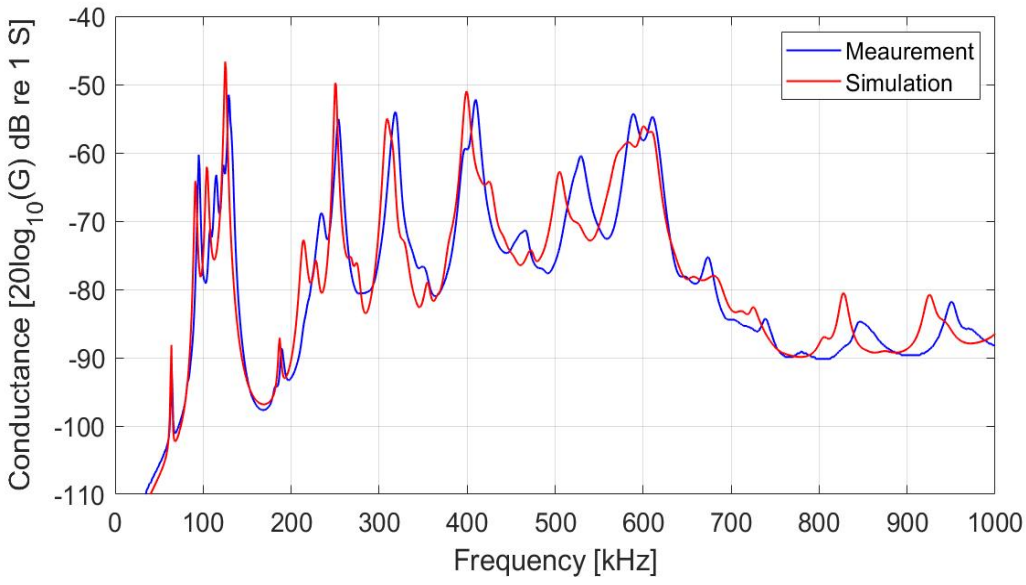

(a)

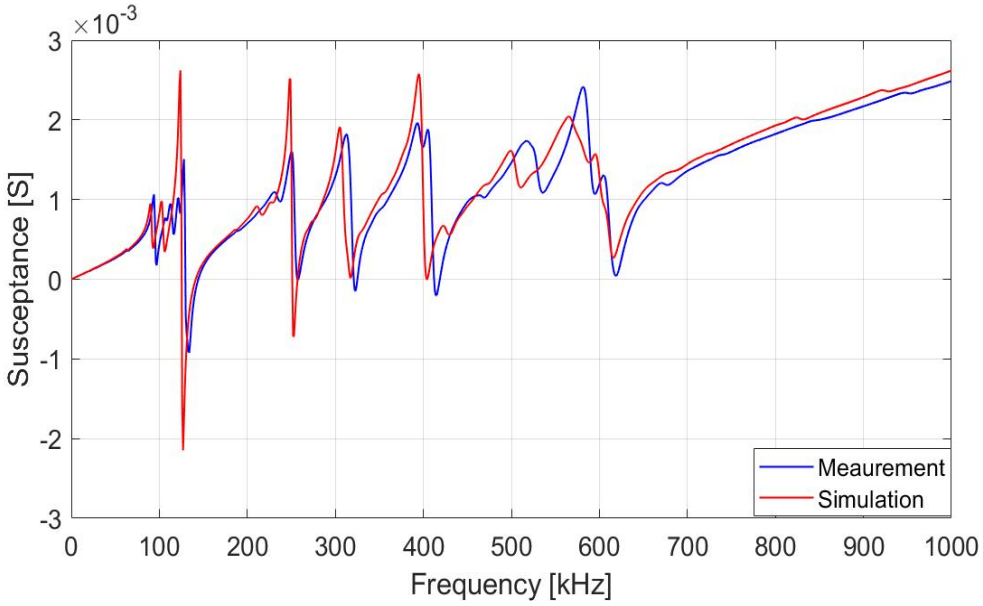

(b)

Figure 6.21: The admittance results after disk 16-10 are attached to a front layer with conductive adhesive. The measured admittance in air from 1-1000 kHz (blue) compared to the simulation of disk 16-10 with front layer and a conductive adhesive layer with a thickness of 0.030 mm (red). (a) The conductance. (b) The susceptance.

The conductive adhesive layer is measured to be 0.033 mm. Still, with a small adjustment in the conductive adhesive layer, 0.030 mm, the simulations agree better with the measurement which is used in the simulations seen in Fig. 6.21a and 6.21b. Disk 16-10 is used further in the construction process with the same simulation setup.

Disk 16-6 was attached to a front layer with dimensions (D_{fl} x T_{fl}) of 23.928 x 1.022 mm. However, after this disk got soldered, the result (see Fig. 6.4a) was not satisfying but was the best of them that was left, and no more time was wanted to be used on the soldering process. The conductive adhesive layer was measured to be 0.045 mm. The results are shown in Figs. 6.22a and 6.22b, where the log of the conductance and the susceptance is plotted against the frequency, respectively.

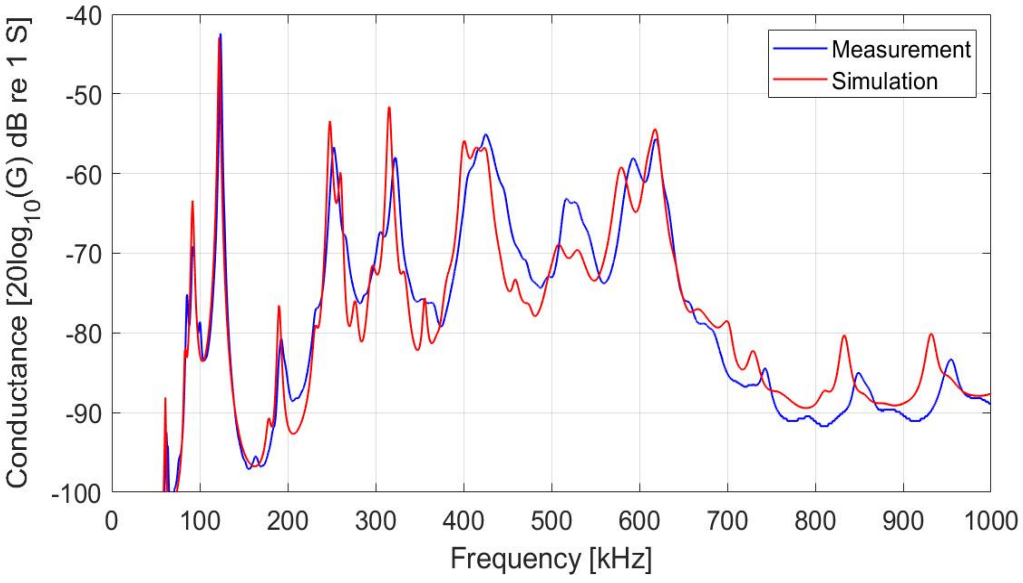

(a)

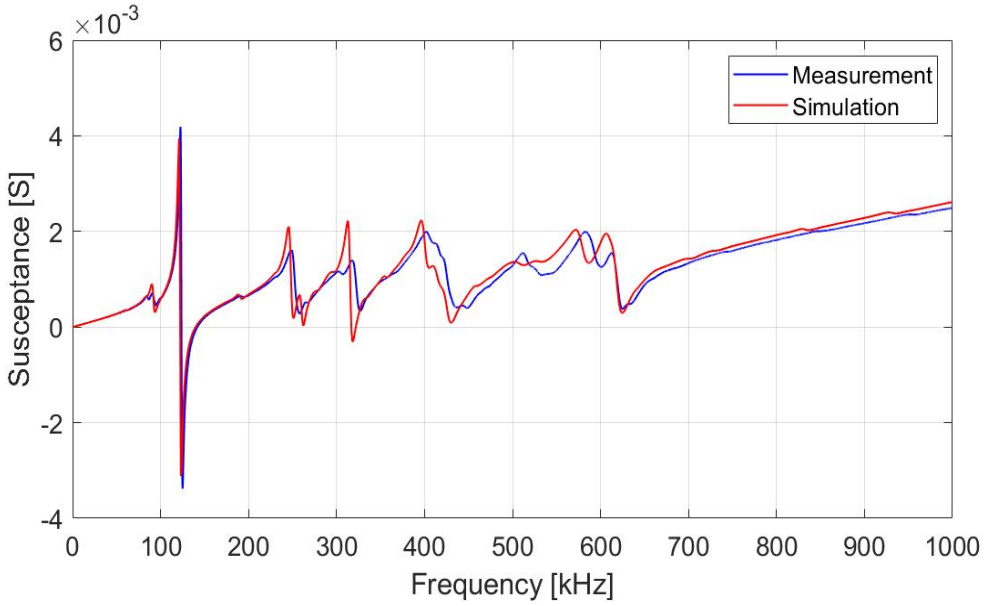

(b)

Figure 6.22: The admittance results after disk 16-6 are attached to a front layer with conductive adhesive. The measured admittance in air from 1-1000 kHz (blue) compared to the simulation of disk 16-6 with front layer and a conductive adhesive layer with a thickness of 0.045 mm (red). (a) The conductance. (b) The susceptance.

The result shown in Fig. 6.22 shows many of the same deviations as the other disks with dimensions (D_p x T_p) of 16 x 4 mm attached to a front layer, see Figs. 6.20 and 6.21, disk 16-6 is therefore used further in one of the constructed transducers.

Based on the results shown in this section, disk 44-2 in Fig. 6.10 , 44-5 in Fig. 6.13 , 44-7 in Fig. 6.14, 16-5 in Fig. 6.20 , 16-10 in Fig. 6.21 and 16-6 in Fig. 6.22 is used further in the construction process. For attaching the disks with (D_p x T_p) of 44 x 4 mm and the disks with (D_p x T_p) of 16 x 4 mm, it is shown that it is important to avoid taking the disk and the front layer apart when the conductive adhesive has been applied for avoiding air bubbles. It is also seen that it is important to make sure that the conductive adhesive has reached room temperature before using it to make it easier to mix and apply more evenly. It is also shown that the load of the solder can affect the measurements. For the disk with dimensions (D_p x T_p) of 16 x 4 mm attached to front layers, it has been shown with disk 16-5, 16-6 and 16-10 that the agreement between the measurement and simulation are closer when a clump of the conductive adhesive has been applied in the middle of the disk as explained in Sec. 3.4, instead of in the middle of the front layer before pressing the disk and the front layer together. A closer agreement between the measurements and the simulations for disks with dimensions (D_p x T_p) of 44 x 4 mm than for the disks with (D_p x T_p) of 16 x 4 mm is seen. The difference in the agreement between the dimensions could be because of the results from the soldering. More deviations between the measurements before and after the disks with (D_p x T_p) of 16 x 4 mm were soldered where seen than for the disks with (D_p x T_p) of 44 x 4 mm was soldered. As well, since the disks with (D_p x T_p) of 16 x 4 mm are smaller than the disks with (D_p x T_p) of 44 x 4 mm, the load of the wire can affect the electrical measurement more.

6.2.4 The results after casings are attached to the front layers

This section presents the measurement and simulation results after the casing is attached to the front layers. The material constants for steel in Tab. 5.6 are used in all the simulations. The method used for attaching the casing to the front layer is explained in Sec. 3.5. For the first casing attached the front layer with disk 44-2, measurements were conducted after the normal adhesive was set for 24 hours. The measurement showed a high response above 650 kHz, as seen in the blue curve in Fig. 6.23. Therefore a thin layer of conductive adhesive was applied on the inner side of the casing in the connection to the front layer, and the conductance was measured again (red curve). Some spots without any conductive adhesive in the connection between the inner side of the casing and the front layer were seen. Therefore, it was tried to cover the parts between the front layer and the casing that had some unglued spots, and the conductance was measured again (black curve).

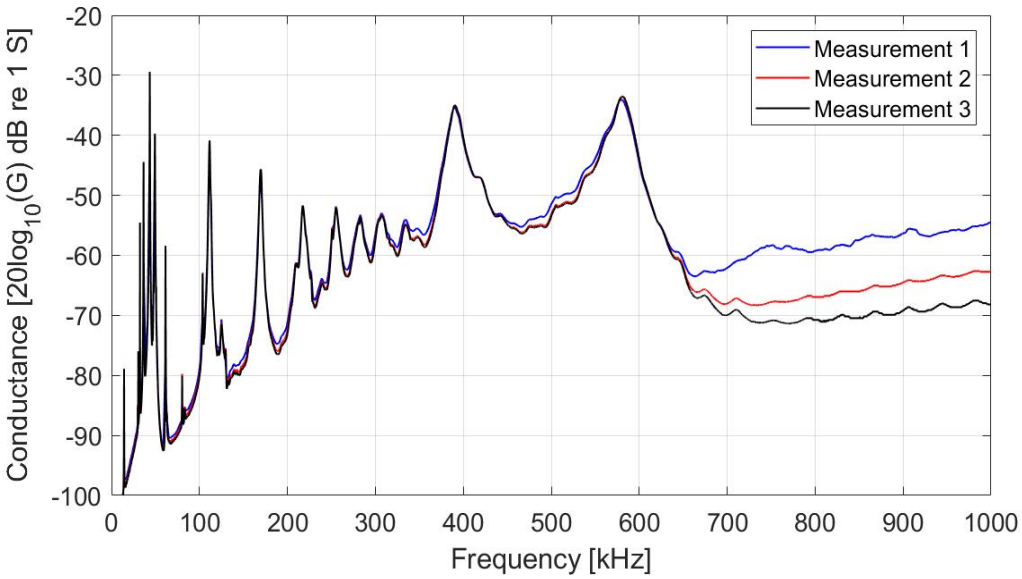

Figure 6.23: The measured conductance in air from 1-1000 kHz of disk 44-2 with front layer and casing. The measurement conducted after the normal adhesive was set for 24 hours (blue), the measurement conducted after a thin layer of conductive adhesive was applied (red), and the measurement conducted after a thicker layer of conductive adhesive was applied (black).

Fig. 6.23 shows measurements before and after more conductive adhesive were applied in the connection between the steel casing and the front layer. The red curve shows the measurements after some conductive adhesive is applied, but not around the hole connection. The black curve is measured after a thin layer is applied around the whole inner side of the casing in the connection to the front layer. As seen in Fig. 6.23, the conductance measured above 700 kHz is lower with some conductive adhesive but even lower when the hole connection is covered with conductive adhesive (black). The dimensions of the materials used in the simulation are presented in Tab. 6.1. Disk 44-2 have dimensions (D_p x T_p) of 43.93 x 3.978 mm. The front layer used has dimensions (D_{fl} x T_{fl}) of 51.87 x 1.005 mm. The thickness of the conductive adhesive T_{ca} is 0.121 mm, the casing thickness T_{c1} is 2.553 mm and the casing length L_{c1} is 45.43 mm. The solder used in the simulation has a radius R_s of 3 mm and a thickness T_s of 0.03 mm.

Table 6.1: Dimensions of the materials used for simulating disk 44-2 with front layer, conductive adhesive layer, solder and steel casing.

D_p [mm]	43.93	T_p [mm]	3.978
D_{fl} [mm]	51.87	T_{fl} [mm]	1.005
T_{ca} [mm]	0.121	T_{c1} [mm]	2.553
L_{c1} [mm]	45.43	R_s [mm]	3.00
T_s [mm]	0.03		

The simulation is compared to the measurement (black curve) from Fig. 6.23. The results are shown in Figs. 6.24a and 6.24b, where the log of the conductance and the susceptance is plotted against the frequency, respectively.

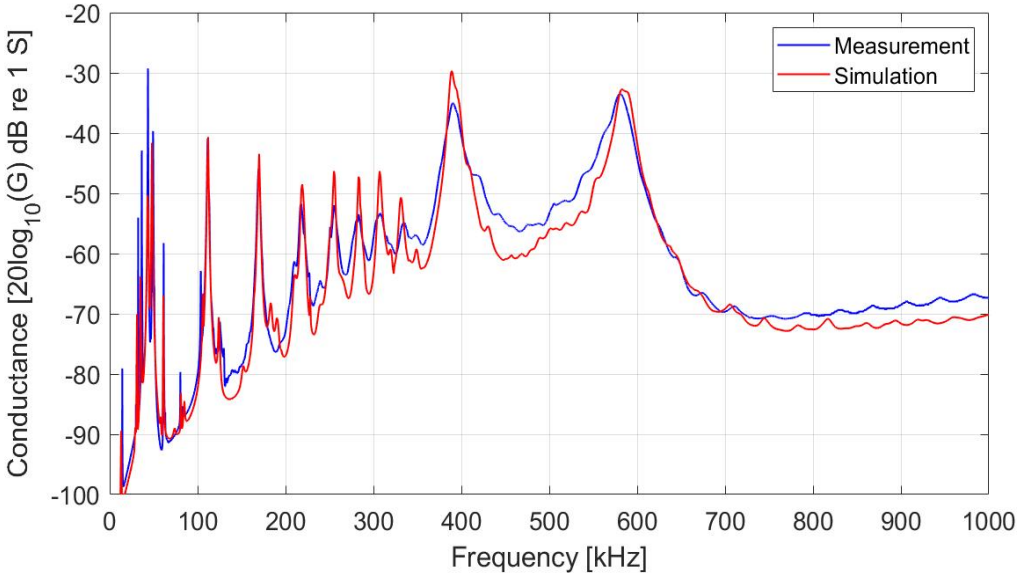

(a)

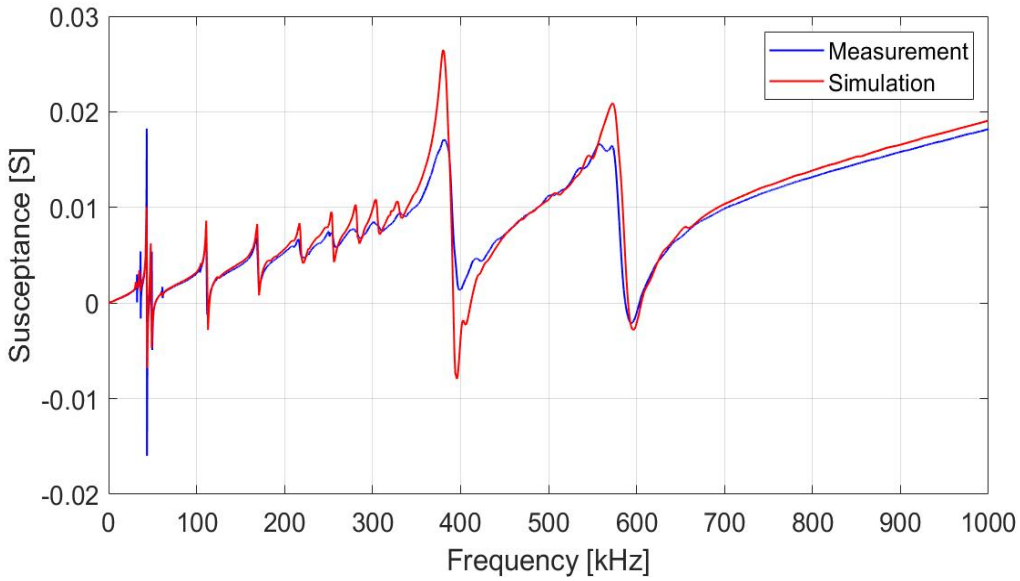

(b)

Figure 6.24: The admittance results after disk 44-2 with front layer and conductive adhesive are attached to a steel casing. The measured admittance in air from 1-1000 kHz (blue) compared to the simulation (red). (a) The conductance. (b) The susceptance.

As seen in Fig. 6.24a and 6.24b, the conductance measurement taken after a layer of conductive adhesive are applied in the connection between the inner side of the casing and the front layer agrees better to the simulation in the frequency range 700-1000 kHz. Therefore conductive adhesive is applied after the other casings are attached to the front layers.

The results after attaching a steel casing to the front layer with disk 44-5 are shown in Figs. 6.25a and 6.25b, where the log of the conductance and the susceptance is plotted against the frequency, respectively.

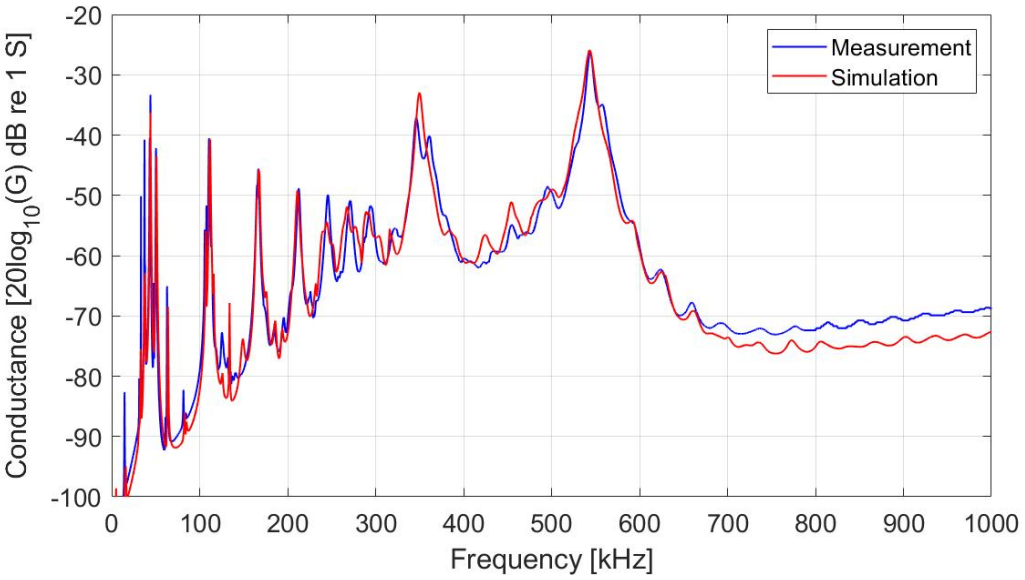

(a)

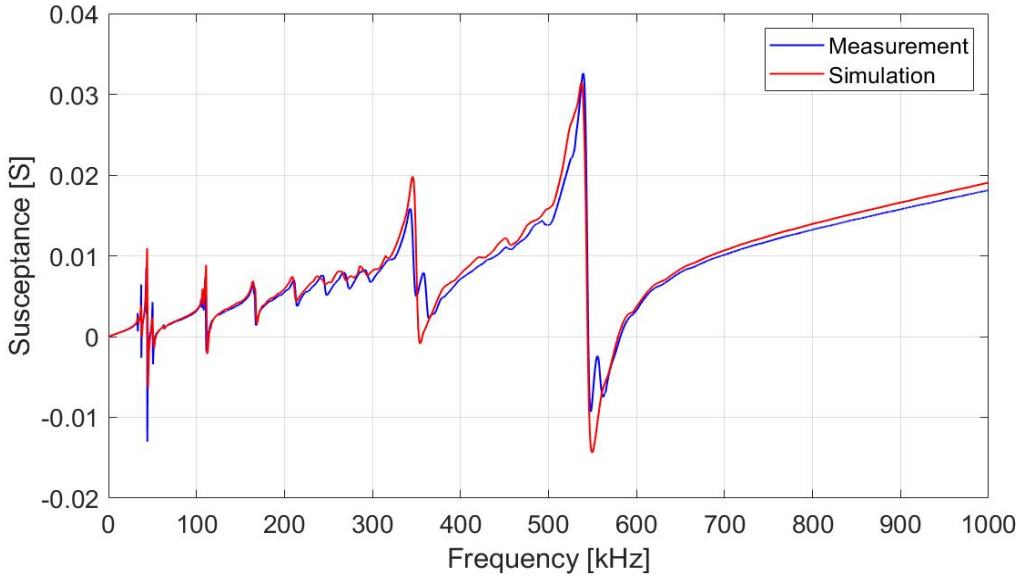

(b)

Figure 6.25: The admittance results after disk 44-5 with front layer and conductive adhesive are attached to a steel casing. The measured admittance in air from 1-1000 kHz (blue) compared to the simulation (red). (a) The conductance. (b) The susceptance.

After attaching the casing to the front layer with disk 44-5, simulations are in close agreement with the measurements for the first resonance frequencies and around the thickness mode as seen in Fig. 6.25. The same deviations above 700 kHz seen in Fig. 6.13 are still present as seen in Fig. 6.25a and 6.25b.

The dimensions of the materials used in the simulation in Fig. 6.25 are presented in Tab. 6.2. Disk 44-5 have dimensions (D_p x T_p) of 44.02 x 4.004 mm. The front layer used has dimensions (D_{fl} x T_{fl}) of 51.15 x 1.194 mm. The thickness of the conductive adhesive T_{ca} is 0.118 mm, the casing thickness T_{c1} is 2.510 mm and the casing length L_{c1} is 45.14 mm.

Table 6.2: Dimensions of the materials used for simulating disk 44-5 with front layer, conductive adhesive layer and steel casing.

D_p [mm]	44.02	T_p [mm]	4.004
D_{fl} [mm]	51.15	T_{fl} [mm]	1.194
T_{c1} [mm]	2.510	L_{c1} [mm]	45.14
T_{ca} [mm]	0.118		

The results after the front layer with disk 44-7 are attached to a steel casing are shown in Figs. 6.26a and 6.26b, where the log of the conductance and the susceptance is plotted against the frequency, respectively.

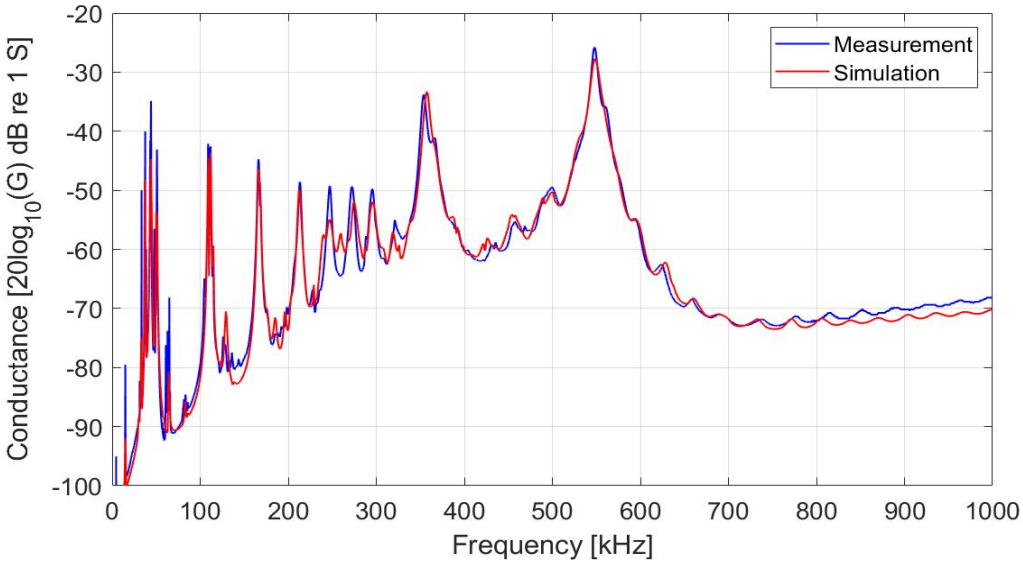

(a)

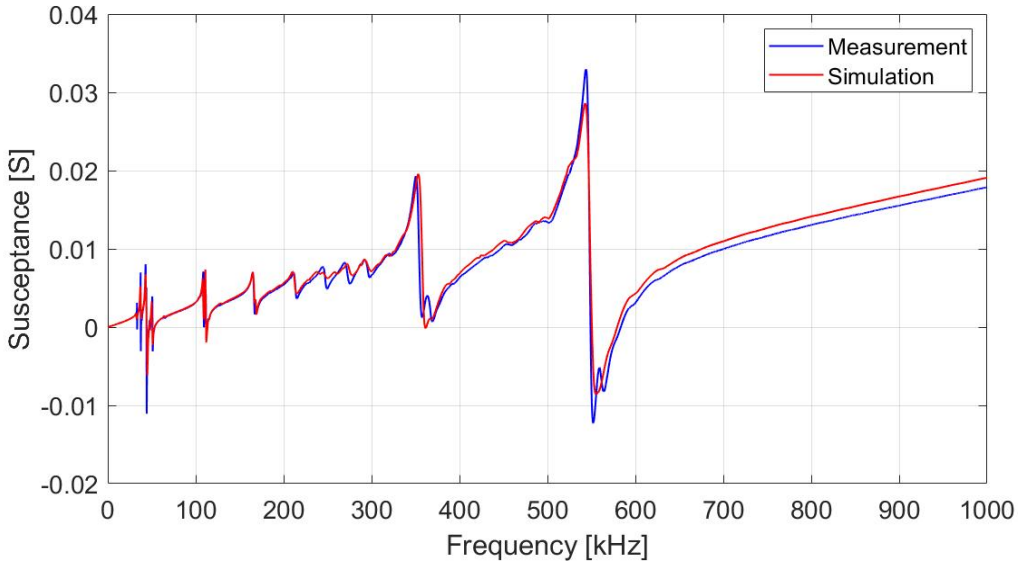

(b)

Figure 6.26: The admittance results after disk 44-7 with front layer and conductive adhesive are attached to a steel casing. The measured admittance in air from 1-1000 kHz (blue) compared to the simulation (red). (a) The conductance. (b) The susceptance.

After attaching a casing to the front layer with disk 44-7, the simulations are in closer agreement with the

measurements as seen in Fig. 6.26a and 6.26b compared to the result seen in Fig. 6.25. Some deviations between the measurement and simulation are seen around $250 - 300$ kHz in Figs. 6.26a and 6.26b.

The dimensions of the materials used in the simulation in Fig. 6.26 are presented in Tab. 6.3. Disk 44-7 have dimensions (D_p x T_p) of 44.03 x 4.017 mm. The front layer used has dimensions (D_{fl} x T_{fl}) of 51.16 x 1.172 mm. The thickness of the conductive adhesive T_{ca} is 0.106 mm, the casing thickness T_{c1} is 2.610 mm and the casing length L_{c1} is 45.06 mm.

Table 6.3: Dimensions of the materials used for simulating disk 44-7 with front layer, conductive adhesive layer and steel casing.

D_p [mm]	44.03	T_p [mm]	4.017
D_{fl} [mm]	51.16	T_{fl} [mm]	1.172
T_{c1} [mm]	2.610	L_{c1} [mm]	45.06
T_{ca} [mm]	0.106		

The admittance results after attaching a steel casing to the front layer with disk 16-5 are shown in Figs. 6.27a and 6.27b, where the log of the conductance and the susceptance is plotted against the frequency, respectively.

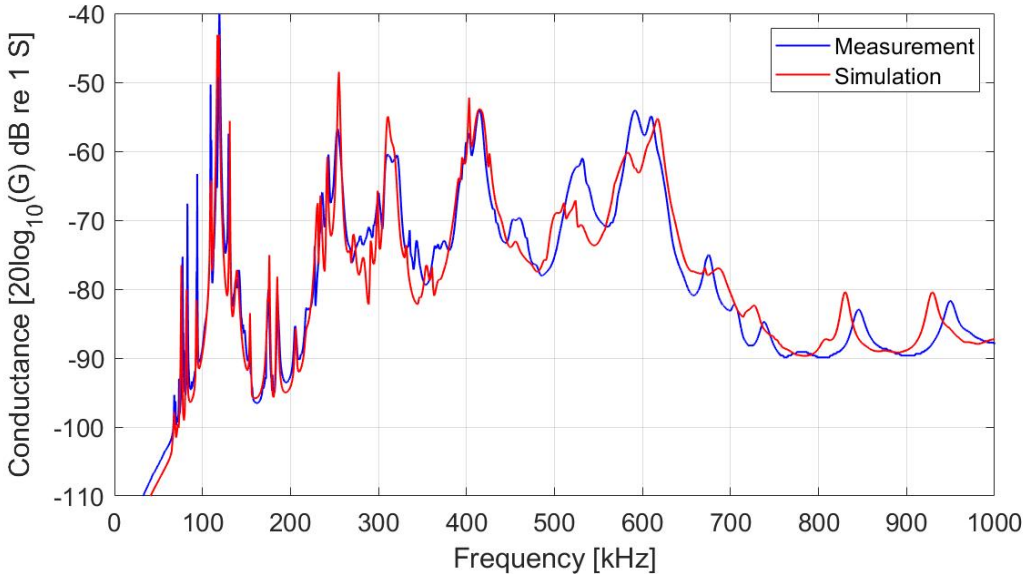

(a)

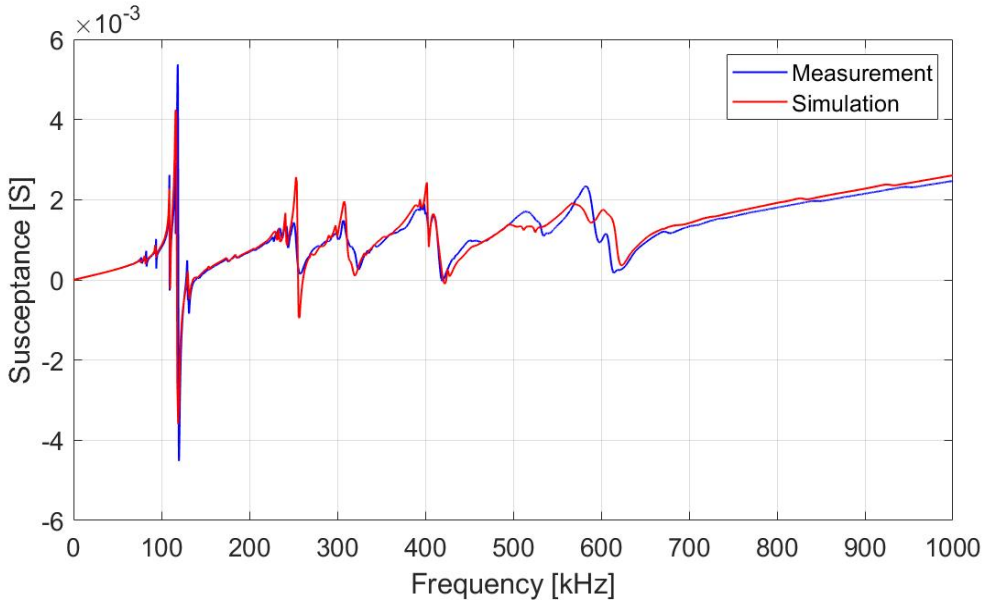

(b)

Figure 6.27: The admittance results after disk 16-5 with front layer and conductive adhesive are attached to a steel casing. The measured admittance in air from 1-1000 kHz (blue) compared to the simulation (red). (a) The conductance. (b) The susceptance.

A reasonable agreement between the measurement and simulation is seen in Fig. 6.27, in the frequencies 800-1000 kHz, it was a closer agreement between the measurement and simulation before the casing was attached in Fig. 6.20a than seen in Fig. 6.27a.

The dimensions of the materials used in the simulation in Fig. 6.27 are presented in Tab. 6.4. Disk 16-5 have dimensions (D_p x T_p) of 16.171 x 3.973 mm. The front layer used has dimensions (D_{fl} x T_{fl}) of 23.031 x 1.123 mm. The thickness of the conductive adhesive T_{ca} is 0.036 mm, the casing thickness T_{c1} is 2.050 mm and the casing length L_{c1} is 45.01 mm.

Table 6.4: Dimensions of the materials used for simulating disk 16-5 with front layer, conductive adhesive layer and steel casing.

D_p [mm]	16.171	T_p [mm]	3.973
D_{fl} [mm]	23.031	T_{fl} [mm]	1.123
T_{c1} [mm]	2.050	L_{c1} [mm]	45.01
T_{ca} [mm]	0.036		

The results after attaching the front layer with disk 16-10 to a steel casing are shown in Figs. 6.28a and 6.28b, where the log of the conductance and the susceptance is plotted against the frequency, respectively. The dimensions of the materials used in the simulation are presented in Tab. 6.5. Disk 16-10 have dimensions (D_p x T_p) of 16.196 x 3.974 mm. The front layer used has dimensions (D_{fl} x T_{fl}) of 23.040 x 1.115 mm. The thickness of the conductive adhesive T_{ca} is 0.030 mm, the casing thickness T_{c1} is 2.040 mm and the casing length L_{c1} is 45.02 mm.

Table 6.5: Dimensions of the materials used for simulating disk 16-10 with front layer, conductive adhesive layer and steel casing.

D_p [mm]	16.196	T_p [mm]	3.974
D_{fl} [mm]	23.040	T_{fl} [mm]	1.115
T_{c1} [mm]	2.040	L_{c1} [mm]	45.02
T_{ca} [mm]	0.030		

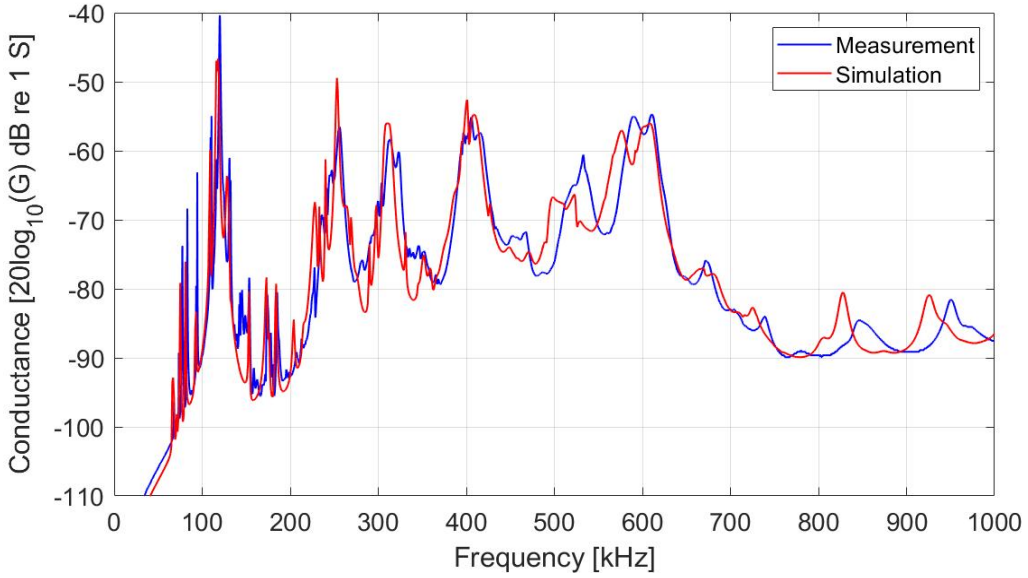

(a)

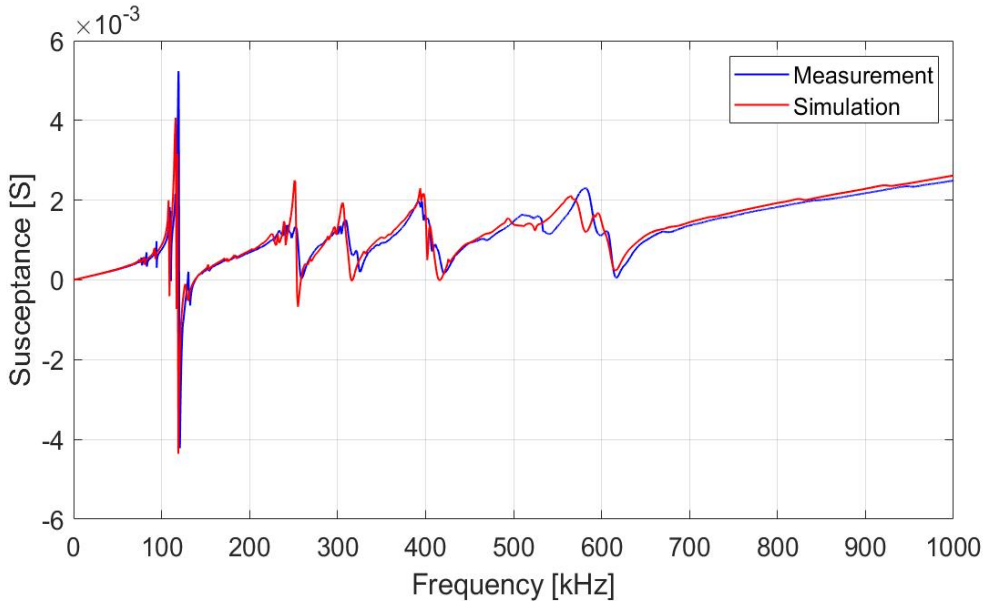

(b)

Figure 6.28: The admittance results after disk 16-10 with front layer and conductive adhesive are attached to a steel casing. The measured admittance in air from 1-1000 kHz (blue) compared to the simulation (red). (a) The conductance. (b) The susceptance.

A closer agreement between the measurement and the simulation for the first resonances at 50-450 kHz is seen in Figs. 6.28a and 6.28b than seen in Figs. 6.21a and 6.21b. As well, a closer agreement between the measured susceptance and simulation in Fig. 6.28b in the frequency range 600-1000 kHz compared to Fig. 6.21b.

The results after attaching the front layer with disk 16-6 to a steel casing are shown in Figs. 6.29a and 6.29b, where the log of the conductance and the susceptance is plotted against the frequency, respectively. The dimensions of the materials used in the simulation are presented in Tab. 6.6. Disk 16-6 have dimensions (D_p x T_p) of 16.206 x 3.974 mm. The front layer used has dimensions (D_{fl} x T_{fl}) of 23.928 x 1.022 mm. The thickness of the conductive adhesive T_{ca} is 0.045 mm, the casing thickness T_{c1} is 2.597 mm and the casing length L_{c1} is 44.33 mm.

Table 6.6: Dimensions of the materials used for simulating disk 16-6 with front layer, conductive adhesive layer and steel casing.

D_p [mm]	16.206	T_p [mm]	3.974
D_{fl} [mm]	23.928	T_{fl} [mm]	1.022
T_{ca} [mm]	0.045	T_{c1} [mm]	2.597
L_{c1} [mm]	44.33		

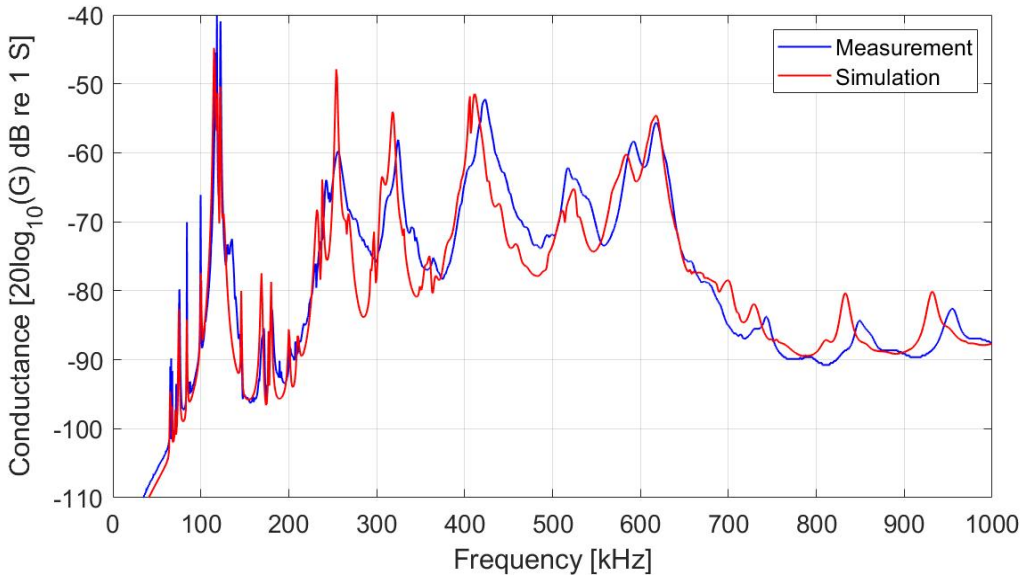

(a)

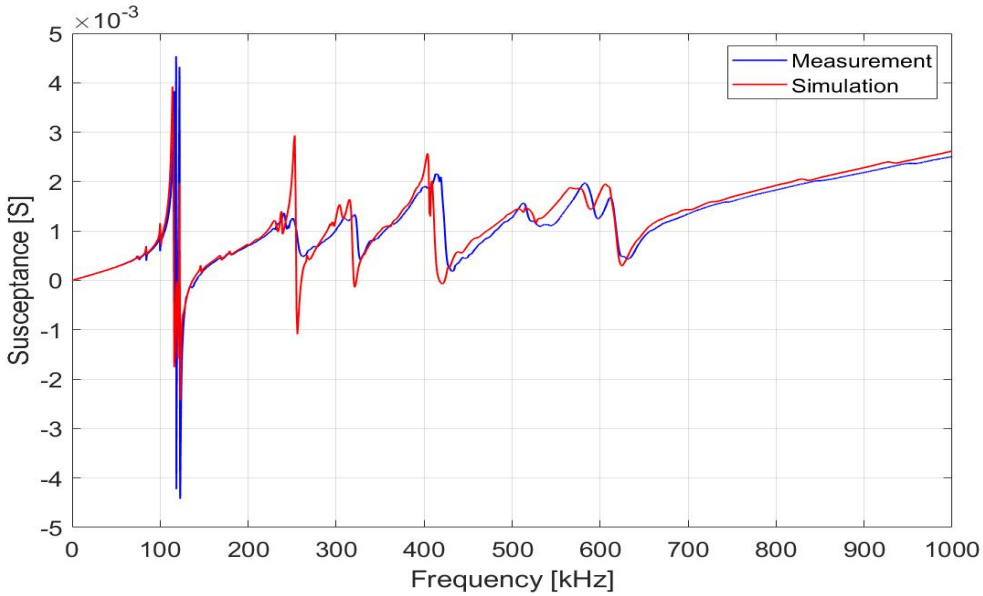

(b)

Figure 6.29: The admittance results after disk 16-6 with front layer and conductive adhesive are attached to a steel casing. The measured admittance in air from 1-1000 kHz (blue) compared to the simulation (red). (a) The conductance. (b) The susceptance.

In Figs. 6.29a and 6.29b it is still deviations between the measurement and simulations for the resonances at 300-450 kHz, as seen in Figs. 6.22a and 6.22b.

The resistance between the conductive adhesive on all the front layers and the casings was measured down to $4-5\Omega$. The low resistance states that a good electrical connection is obtained between the front electrode on the disks and the steel casings. It is also shown that it is important to apply conductive adhesive where the front layer meets the casing inside the casing to achieve better contact, see Fig. 6.23.

6.2.5 The results after pouring the backing layer in the construction

This section presents the results after backing layers are made in all the casings. The results after the backing layer are made in the casing attached to disk 44-2 with the front layer is shown in Figs. 6.30a and 6.30b, where the log of the conductance and the susceptance is plotted against the frequency, respectively.

The dimensions of the materials used in the simulation are presented in Tab. 6.7. Disk 44-2 have dimensions (D_p x T_p) of 43.93 x 3.978 mm. The front layer used has dimensions (D_{fl} x T_{fl}) of 51.87 x 1.005 mm. The thickness of the conductive adhesive T_{ca} is 0.121 mm, the casing thickness T_{c1} is 2.553 mm and the casing length L_{c1} is 45.43 mm. The radius of the cone in the backing layer R_{air} is 5 mm and the thickness T_{air} is 10 mm. The solder used in the simulation has a radius R_s of 3 mm and a thickness T_s of 0.03 mm. The material constants presented in Tab. 5.7 is used for simulating the backing layer.

Table 6.7: Dimensions of the materials used for simulating disk 44-2 with front layer, conductive adhesive layer, steel casing and backing layer.

D_p [mm]	43.93	T_p [mm]	3.978
D_{fl} [mm]	51.87	T_{fl} [mm]	1.005
T_{ca} [mm]	0.121	T_{c1} [mm]	2.553
L_{c1} [mm]	45.43	R_s [mm]	3
T_s [mm]	0.03	R_{air} [mm]	5
T_{air} [mm]	10		

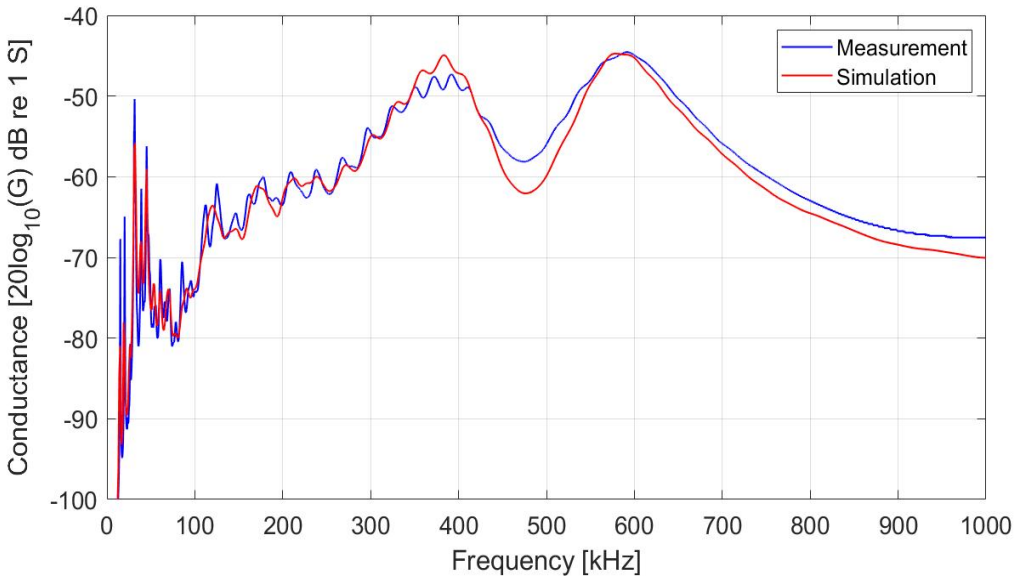

(a)

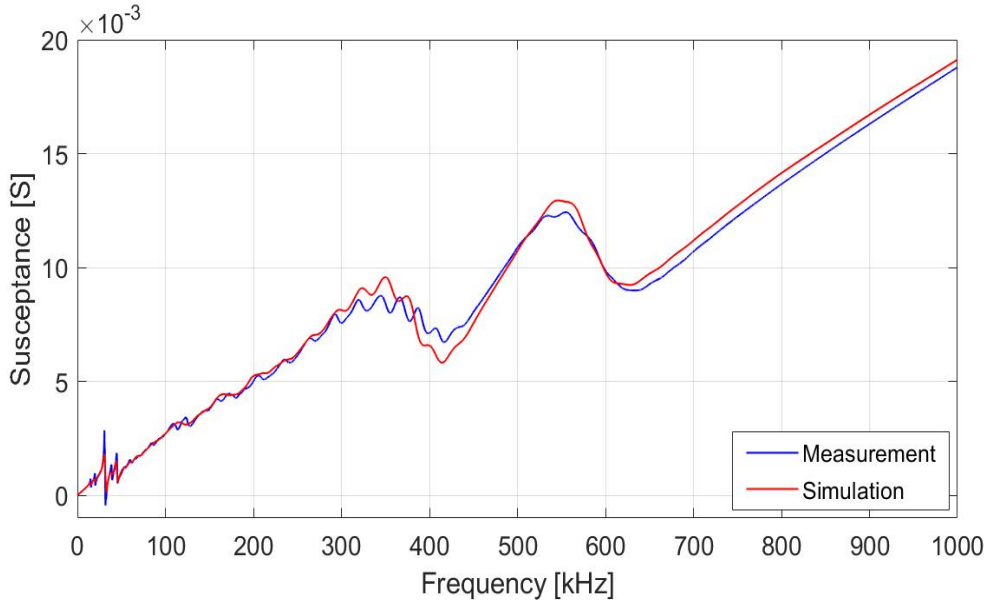

(b)

Figure 6.30: The admittance results after the backing layer are poured inside the casing attached to disk 44-2 with front layer and a conductive adhesive layer. The measured admittance in air from 1-1000 kHz (blue) compared to the simulation (red). (a) The conductance. (b) The susceptance.

Some deviations between the measurement and simulations in Figs. 6.30a and 6.30b is seen especially around the thickness mode. The backing layer was simulated with different Q-factors to see if it was a problem with the damping in the backing layer. The results are compared to the measurements and are given in Fig. 6.31.

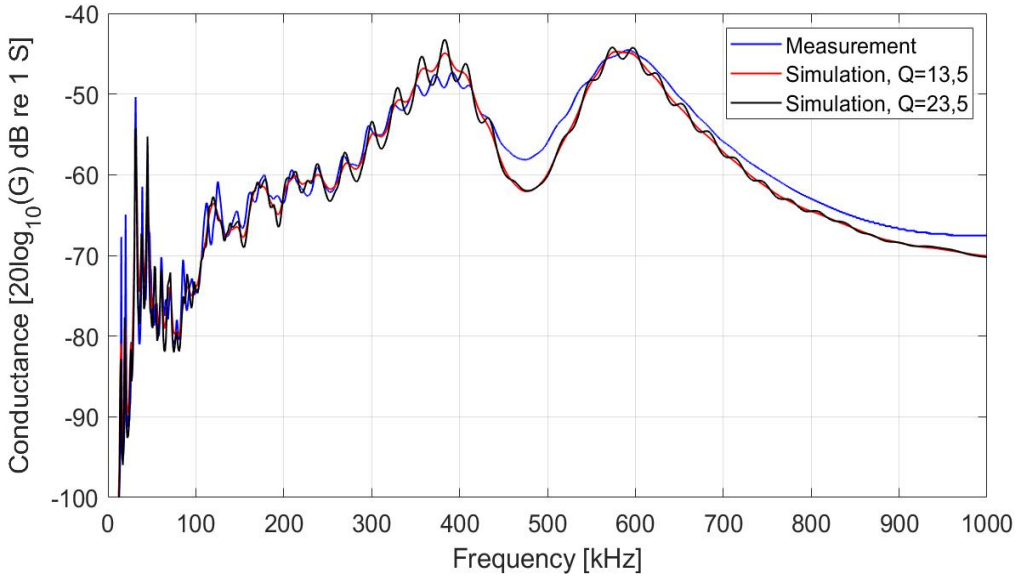

Figure 6.31: The measured conductance in air (blue) after the backing layer are poured inside the casing attached to disk 44-2 with front layer and conductive adhesive. The measured conductance from 1-1000 kHz (blue) compared to the simulation with a Q-factor of 13.5 in the backing layer (red) and the simulation with a Q-factor of 23.5 in the backing layer.

In Fig. 6.30a and 6.30b, the backing layer is simulated with $Z = 11.9$ MRayl, with $Q = 13.5$, and with $Q = 23.5$ to see if there is a problem with the damping in the backing layer. Based on the result in Fig. 6.31, the backing layer should be longer to give higher damping. Since the backing layer is poured right into the casing, and the backing layer is not uniformly, the material constants used in the simulations are not measured, making the simulation not agree well with the measurements.

The results after the backing layer are made inside the casing attached to disk 44-5 with the front layer is shown in Figs. 6.32a and 6.32b, where the log of the conductance and the susceptance is plotted against the frequency, respectively.

The dimensions of the materials used in the simulation are presented in Tab. 6.8. Disk 44-5 have dimensions (D_p x T_p) of 44.02 x 4.004 mm. The front layer used has dimensions (D_{fl} x T_{fl}) of 51.15 x 1.194 mm. The thickness of the conductive adhesive T_{ca} is 0.118 mm, the casing thickness T_{c1} is 2.510 mm and the casing length L_{c1} is 45.14 mm. The radius of the cone in the backing layer R_{air} is 5 mm and the thickness T_{air} is 10 mm. The material constants presented in Tab. 5.7 is used for simulating the backing layer.

Table 6.8: Dimensions of the materials used for simulating disk 44-5 with front layer, conductive adhesive layer, steel casing and backing layer.

D_p [mm]	44.02	T_p [mm]	4.004
D_{fl} [mm]	51.15	T_{fl} [mm]	1.194
T_{c1} [mm]	2.510	L_{c1} [mm]	45.14
R_{air} [mm]	5	T_{air} [mm]	10
T_{ca} [mm]	0.118		

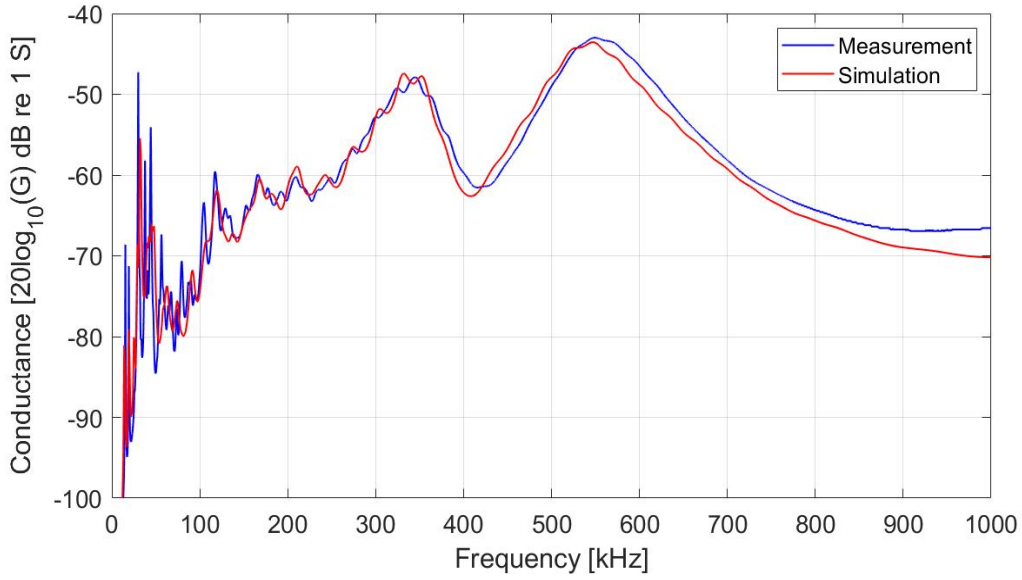

(a)

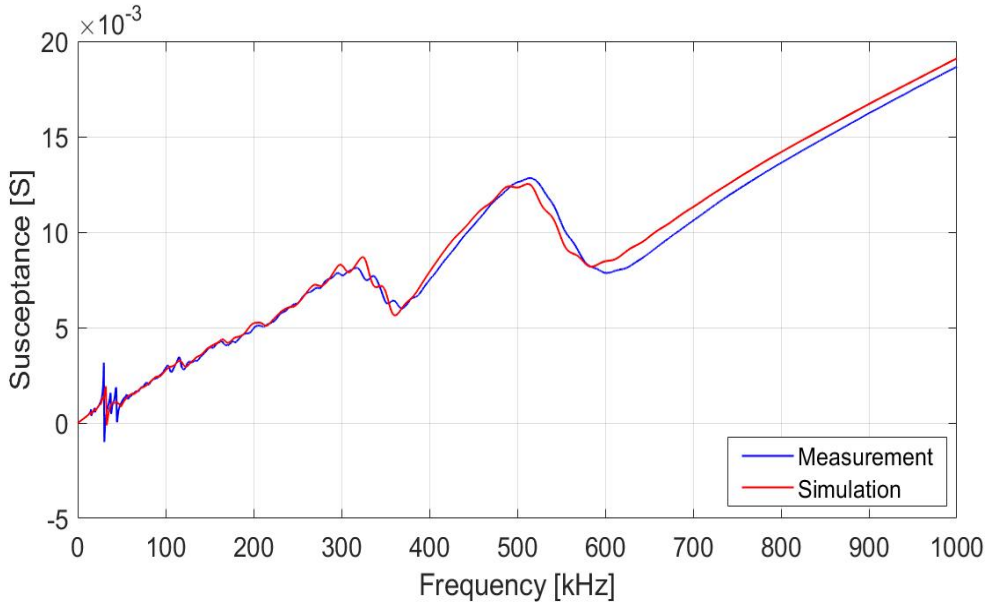

(b)

Figure 6.32: The admittance results after the backing layer are poured inside the casing attached to disk 44-5 with front layer and conductive adhesive. The measured admittance in air from 1-1000 kHz (blue) compared to the simulation (red). (a) The conductance. (b) The susceptance.

The deviations seen in Fig. 6.32a and 6.32b after pouring the backing layer in the casing with disk 44-5 is smaller than for the results after the backing layer is made inside the casing with disk 44-2 shown in Fig. 6.30. The same material constants for the backing layer is used here. The cone in the back was not that straight in this backing layer, as shown in Sec. 3.6, which could make fewer reflections inside the backing layer and therefore give better results. As well, the measurements in Fig. 6.13 was in closer agreement with the simulation than the measurement in Fig. 6.10.

The results after the backing layer are made inside the casing attached to disk 44-7 with the front layer is presented in Figs. 6.33a and 6.33b, where the log of the conductance and the susceptance is plotted against the frequency, respectively. The dimensions of the materials used in the simulation are presented in Tab. 6.9. Disk 44-7 have dimensions (D_p x T_p) of 44.03 x 4.017 mm. The front layer used has dimensions (D_{fl} x T_{fl}) of 51.16 x 1.172 mm. The thickness of the conductive adhesive T_{ca} is 0.106 mm, the casing thickness T_{c1} is 2.610 mm and the casing length L_{c1} is 45.06 mm. The radius of the cone in the backing layer R_{air} is 7 mm and the thickness T_{air} is 10 mm. The material constants presented in Tab. 5.7 is used for simulating the backing layer.

Table 6.9: Dimensions of the materials used for simulating disk 44-7 with front layer, conductive adhesive layer, steel casing and backing layer.

D_p [mm]	44.03	T_p [mm]	4.017
D_{fl} [mm]	51.16	T_{fl} [mm]	1.172
T_{c1} [mm]	2.610	L_{c1} [mm]	45.06
R_{air} [mm]	7	T_{air} [mm]	10
T_{ca} [mm]	0.106		

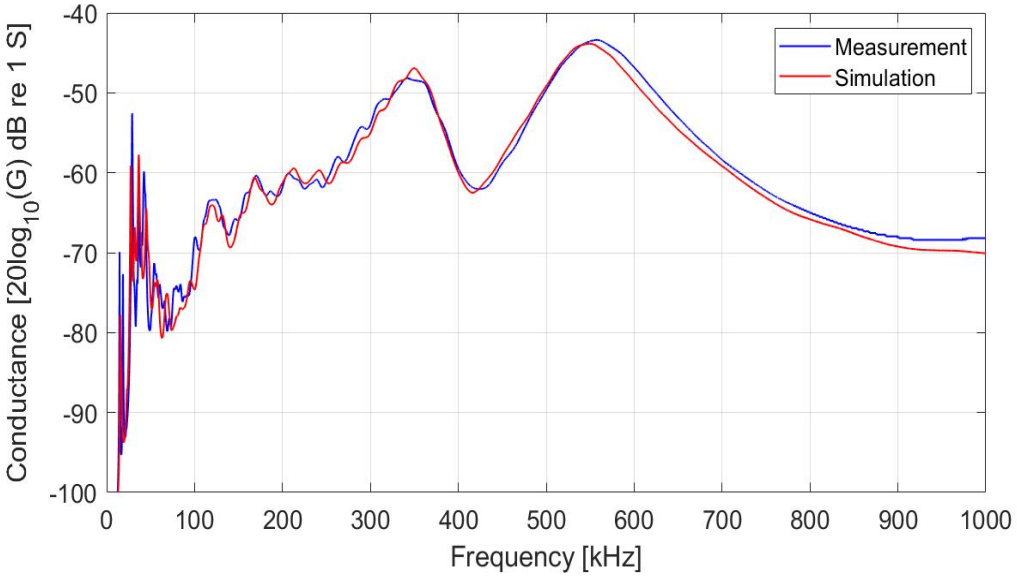

(a)

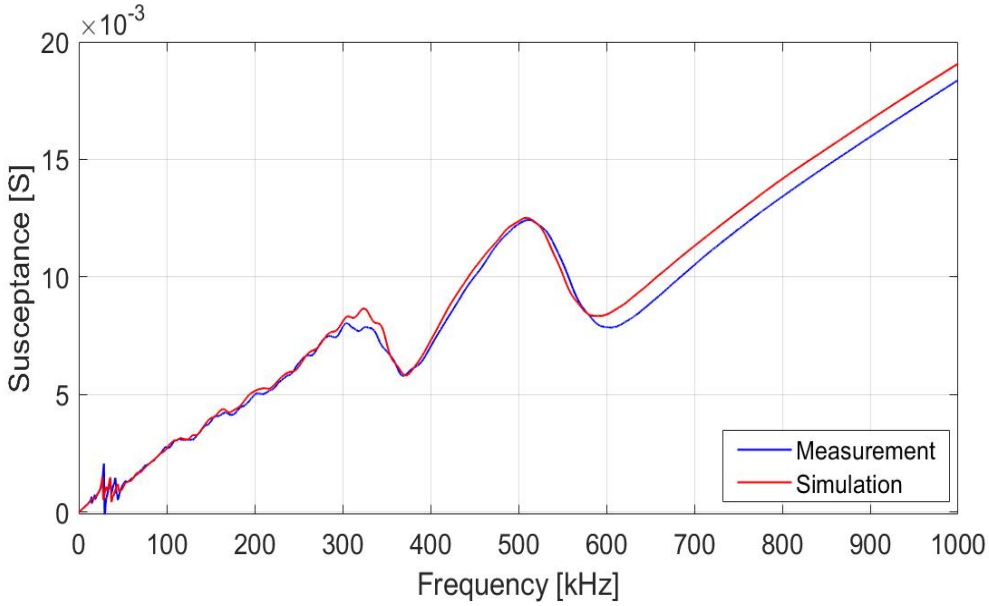

(b)

Figure 6.33: The admittance results after the backing layer are poured inside the casing attached to disk 44-7 with front layer and conductive adhesive. The measured admittance in air from 1-1000 kHz (blue) compared to the simulation (red). (a) The conductance. (b) The susceptance.

The deviations seen in Fig. 6.33a and 6.33b after pouring the backing layer inside the casing attached with disk 44-7 is even smaller than for disk 44-5 in Fig. 6.32. The same material constants for the backing layer is used here. The cone in the back was more uneven, as shown in Sec. 3.6, which could make even fewer reflections going back, giving better results. The measurements in Fig. 6.14 was in closer agreement with the simulation than the measurement in Fig. 6.13.

The results after the backing layer are made inside the casing attached to disk 16-5 with the front layer is presented in Figs. 6.34a and 6.34b, where the log of the conductance and the susceptance is plotted against the frequency, respectively. The dimensions of the materials used in the simulation are presented in Tab. 6.10. Disk 16-5 have dimensions (D_p x T_p) of 16.171 x 3.973 mm. The front layer used has dimensions (D_{fl} x T_{fl}) of 23.031 x 1.123 mm. The thickness of the conductive adhesive T_{ca} is 0.036 mm, the casing thickness T_{c1} is 2.050 mm and the casing length L_{c1} is 45.01 mm. The radius of the cone in the backing layer R_{air} is 5 mm and the thickness T_{air} is 10 mm. The material constants presented in Tab. 5.7 is used for simulating the backing layer.

Table 6.10: Dimensions of the materials used for simulating disk 16-5 with front layer, conductive adhesive layer, steel casing and backing layer.

D_p [mm]	16.171	T_p [mm]	3.973
D_{fl} [mm]	23.031	T_{fl} [mm]	1.123
T_{c1} [mm]	2.050	L_{c1} [mm]	45.01
R_{air} [mm]	5	T_{air} [mm]	10
T_{ca} [mm]	0.036		

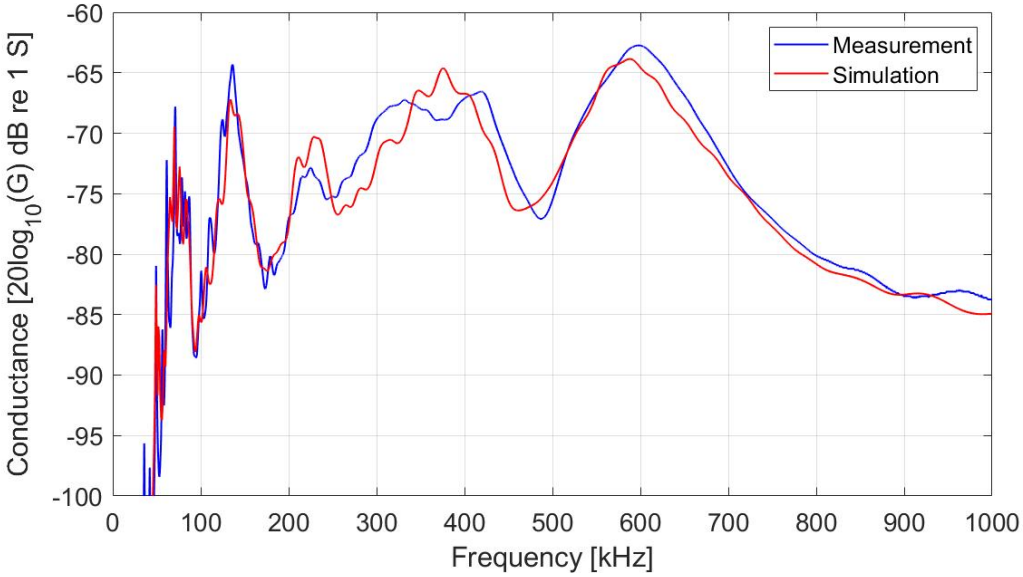

(a)

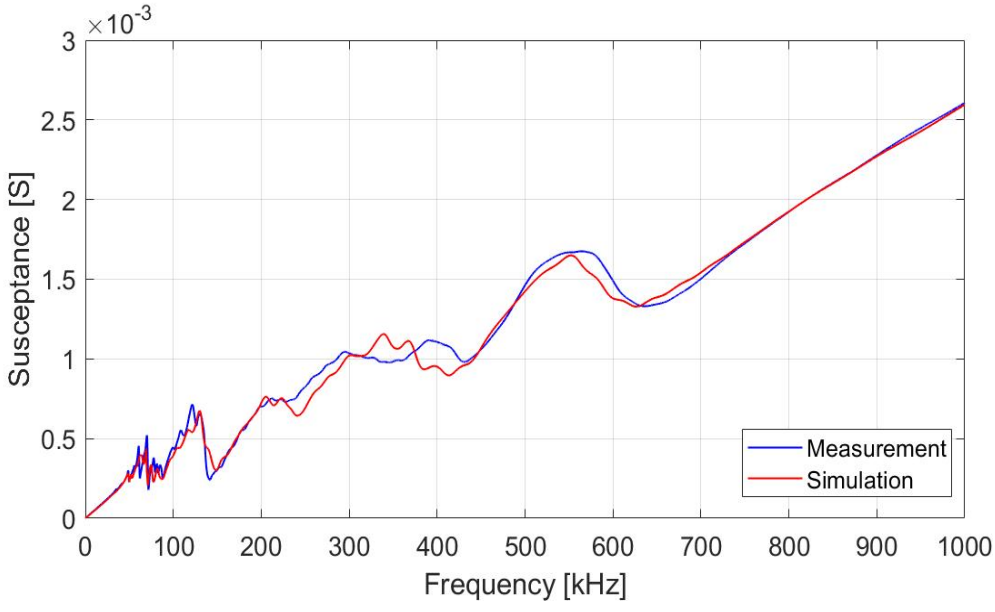

(b)

Figure 6.34: The admittance results after the backing layer are poured inside the casing attached to disk 16-5 with front layer and conductive adhesive. The measured admittance in air from 1-1000 kHz (blue) compared to the simulation (red). (a) The conductance. (b) The susceptance.

Some more deviations is seen in Fig. 6.34a and 6.34b compared to the results in Fig. 6.33, especially around $200-500$ kHz. More deviations is also seen in the results in Fig. 6.20 compared to the results in Fig. 6.14, therefore the deviations between the measurement and simulations in Fig. 6.34 is probably from the deviations

between the measurement and simulation in Fig. 6.20, after disk 16-5 was attached to a front layer, and not because of how the backing layer is made compared to how it is made in Fig. 6.33.

The results after the backing layer are made inside the casing attached to disk 16-10 with the front layer is presented in Figs. 6.35a and 6.35b, where the log of the conductance and the susceptance is plotted against the frequency, respectively. The dimensions of the materials used in the simulation are presented in Tab. 6.11. Disk 16-10 have dimensions (D_p x T_p) of 16.196 x 3.974 mm. The front layer used has dimensions (D_{fl} x T_{fl}) of 23.040 x 1.115 mm. The thickness of the conductive adhesive T_{ca} is 0.030 mm, the casing thickness T_{c1} is 2.040 mm and the casing length L_{c1} is 45.02 mm. The radius of the cone in the backing layer R_{air} is 5 mm and the thickness T_{air} is 10 mm.

Table 6.11: Dimensions of the materials used for simulating disk 16-10 with front layer, conductive adhesive layer, steel casing and backing layer.

D_p [mm]	16.196	T_p [mm]	3.974
D_{fl} [mm]	23.040	T_{fl} [mm]	1.115
T_{c1} [mm]	2.040	L_{c1} [mm]	45.02
R_{air} [mm]	5	T_{air} [mm]	10
T_{ca} [mm]	0.030		

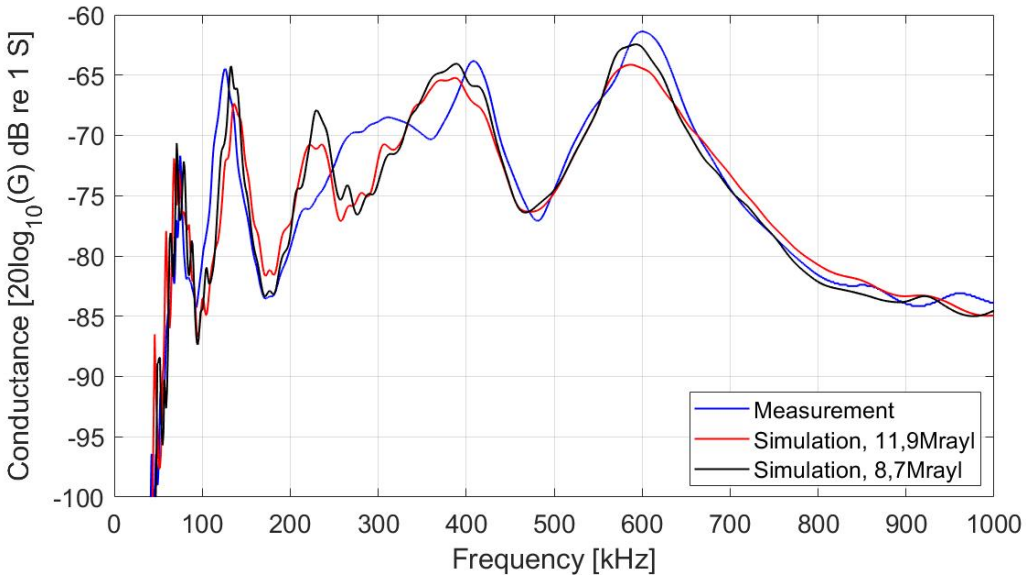

(a)

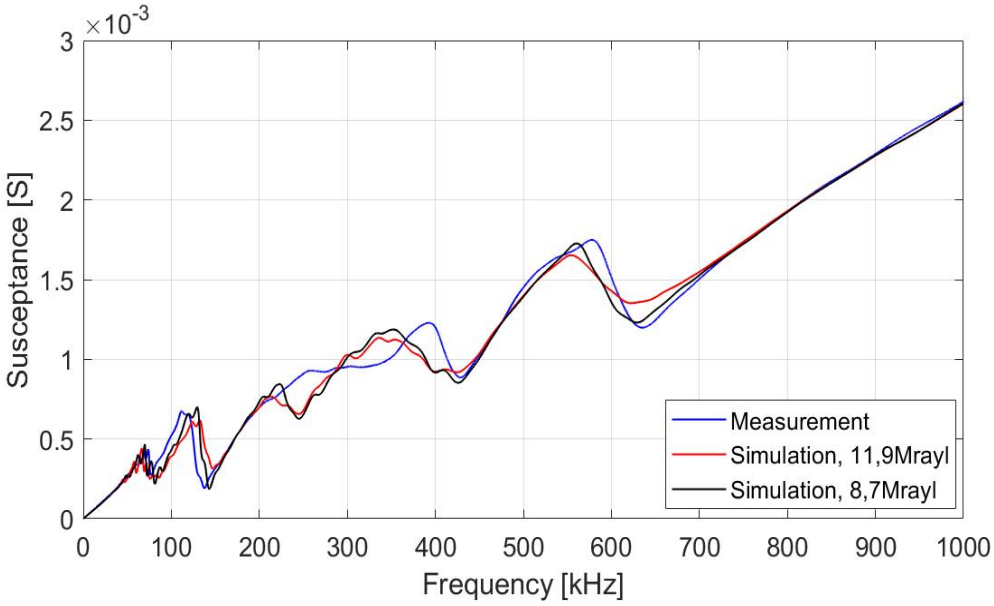

(b)

Figure 6.35: The admittance results after the backing layer are poured inside the casing attached to disk 16-10 with front layer and conductive adhesive. The measured admittance in air from 1-1000 kHz (blue) compared to the simulation (red). (a) The conductance. (b) The susceptance.

The results after pouring the backing layer inside the casing with disk 16-10 deviate more from the simulations as seen in Fig. 6.35a and 6.35b compared to the results in Fig. 6.34. Compared to the measurement result in Fig. 6.34, the resonance at around 120 kHz has shifted in frequency. The backing layer has been simulated with two different acoustic impedance's, $Z_p = 11.9$ MRayl (red curve) and $Z_p = 8.7$ MRayl (black curve). The material constants presented in Tab. 5.7 is used for simulating the backing layer with $Z_p = 11.9$ MRayl, and the material constants in Tab. 5.9 are used for simulating the backing layer with $Z_p = 8.7$ MRayl. The black curve is in closer agreement with the measurement even though the backing layer is made the same way as for disk 16-5. This difference could be due to some air being trapped in the backing layer for this structure.

The results after the backing layer are made inside the casing attached to disk 16-6 with the front layer is shown in Figs. 6.36a and 6.36b, where the log of the conductance and the susceptance is plotted against the frequency, respectively. The dimensions of the materials used in the simulation are presented in Tab. 6.12. Disk 16-6 have dimensions (D_p x T_p) of 16.206 x 3.974 mm. The front layer used has dimensions (D_{fl} x T_{fl}) of 23.928 x 1.022 mm. The thickness of the conductive adhesive T_{ca} is 0.045 mm, the casing thickness T_{c1} is 2.597 mm and the casing length L_{c1} is 44.33 mm. The radius of the cone in the backing layer R_{air} is 5 mm and the thickness T_{air} is 10 mm.

Table 6.12: Dimensions of the materials used for simulating disk 16-6 with front layer, conductive adhesive layer, steel casing and backing layer.

D_p [mm]	16.206	T_p [mm]	3.974
D_{fl} [mm]	23.928	T_{fl} [mm]	1.022
T_{ca} [mm]	0.045	T_{c1} [mm]	2.597
L_{c1} [mm]	44.33	R_{air} [mm]	5
T_{air} [mm]	10		

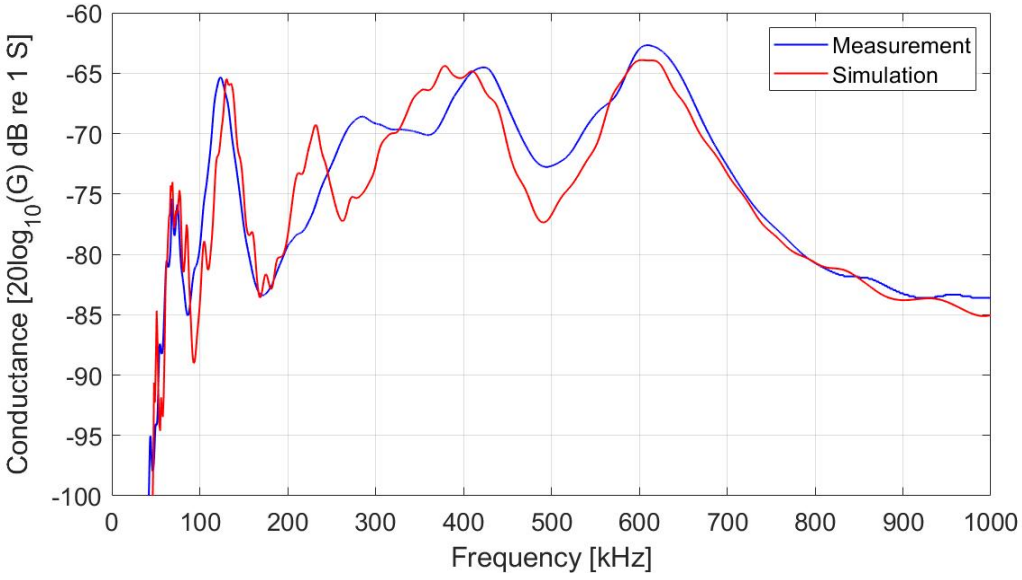

(a)

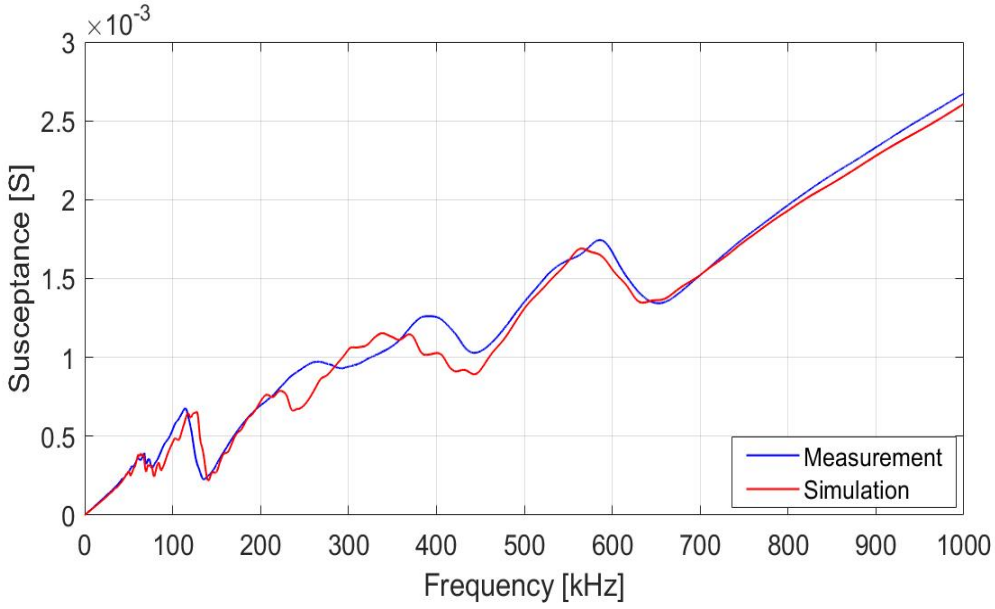

(b)

Figure 6.36: The admittance results after the backing layer are poured inside the casing attached to disk 16-6 with front layer and conductive adhesive. The measured admittance in air from 1-1000 kHz (blue) compared to the simulation (red). (a) The conductance. (b) The susceptance.

The measurement results after pouring the backing layer inside the casing with disk 16-6 in Fig. 6.36 deviate more from the simulation than the result after the backing layer is poured inside the casing with disk 16-5 in Fig. 6.34, but less than disk 16-10 in Fig. 6.35. Compared to the measurement result from disk 16-5 in Fig. 6.34, the resonance at around 120 kHz has shifted in frequency, as also seen for disk 16-10 in Fig. 6.35. The backing layer has been simulated with an acoustic impedance of $Z_p = 10.1$ MRayl, which are in closer agreement with the measurement than a simulation with a backing layer with $Z_p = 11.9$ MRayl. The material constants presented in Tab. 5.7 is used for simulating the backing layer with $Z_p = 11.9$ MRayl, and the material constants in Tab. 5.10 are used for simulating the backing layer with $Z_p = 10.1$ MRayl.

In this section, the results after several Pz27 disks are attached to front layers compared to simulations are presented with varying results. Then, six disks with a satisfying agreement between the admittance measurements and simulations are taken further where a casing has been attached around the front layers with the Pz27 disks attached. Additionally, a backing layer is made inside the casings with varying results regarding the backing

layer's impedance. For the tungsten epoxy backing layers, it is shown when comparing the measurements to the simulations that the impedance of the backing layer are different even though the same mass ratio of the components is used for all the backing layers. Several ripples in the measurements are seen, which could be because of the change in the gradient in the backing layer. From a test of the backing layer shown in Sec. 3.6, it is seen that the gradient is changing. More tungsten grains are at the bottom than at the top. Since this change is not measured, this is not taken into account in the simulations. However, the measurements are in reasonable agreement with the simulations, but the backing layer should have been longer to avoid the ripples seen in the measurements for being in even closer agreement.

6.3 Final construction results

This section presents the final results from the constructed transducers in air and water after the back casing and connector are attached. The dimensions for all the materials for each transducer are presented in tables before the results of each transducer. The approximated dimensions of the vacuum cones used in the simulations are also given in tables with the different dimensions. The vacuum cone is not uniformly in the centre of any transducers, so only an approximation is provided by measuring the diameter and depth in different places. Due to time constraints, the acoustic measurements are only conducted for transducer no. 3 and 4. The length of the backing layer is not measured since the backing layer is dried inside the casing. However, for simulation purposes, it is found by subtracting the Pz27 disk, the front layer, the conductive adhesive layer, and the back casing thickness from the total length.

6.3.1 Transducer 1

This section presents the results for the transducer constructed with disk 44-2 (D_p x T_p) of 43.93 x 3.978 mm. The dimensions of the materials are presented in Tab. 6.13. The front layer used has dimensions (D_{fl} x T_{fl}) of 51.87 x 1.005 mm. The thickness of the conductive adhesive T_{ca} is 0.121 mm. The casing thickness T_{c1} is 2.553 mm, the thickness of the back casing T_{c2} is 3.921 mm and the length of the casing L_{c1} is 45.43 mm. The solder used in the simulation has a radius R_s of 3 mm and a thickness T_s of 0.03 mm. The radius of the cone in the backing layer R_{air} is 5 mm and the thickness T_{air} is 10 mm. The tungsten epoxy backing layer is simulated with the values given in Tab. 5.7.

Table 6.13: Dimensions of the materials used in prototype transducer no. 1.

D_p [mm]	43.93	T_p [mm]	3.978
D_{fl} [mm]	51.87	T_{fl} [mm]	1.005
T_{ca} [mm]	0.121	T_{c1} [mm]	2.553
L_{c1} [mm]	45.43	T_{c2} [mm]	3.921
R_s [mm]	3	T_s [mm]	0.03
R_{air} [mm]	5	T_{air} [mm]	10

The admittance measurements and simulations conducted in air is presented in Figs. 6.37a and 6.37b, where the log of the conductance and the susceptance is plotted against the frequency, respectively.

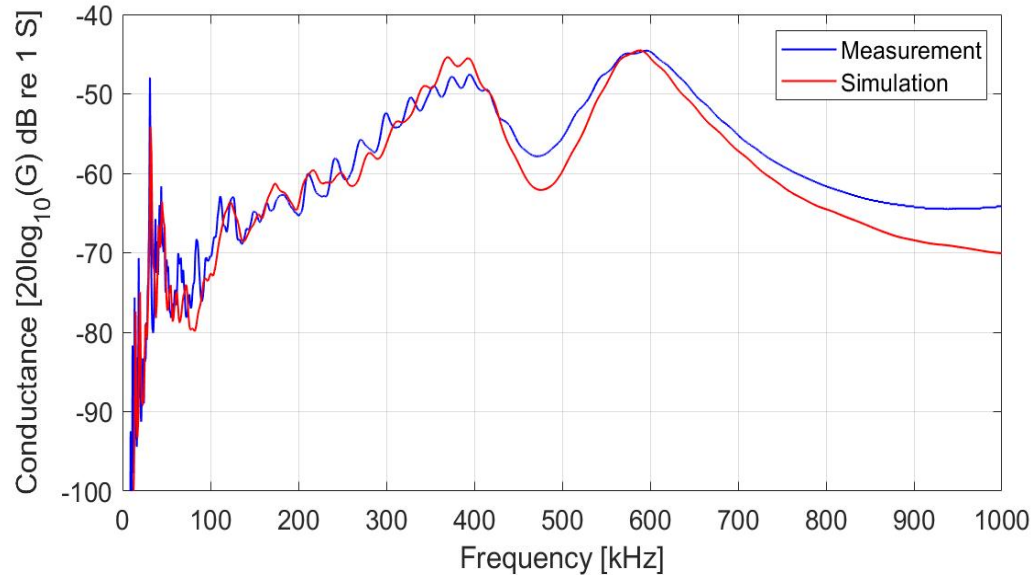

(a)

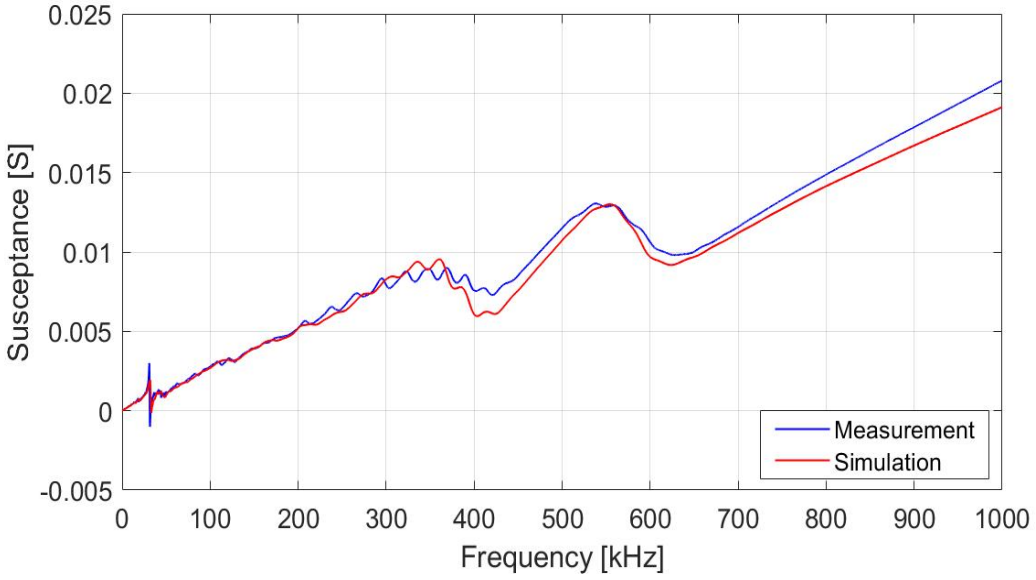

(b)

Figure 6.37: The admittance results of prototype no. 1 (with disk 44-2) in air. The measured admittance in air from 1-1000 kHz (blue) compared to the simulation (red). (a) The conductance. (b) The susceptance.

The measurements in Fig. 6.37 for a finished transducer with disk 44-2 deviate more with the simulations in the frequency range 250-350kHz and 800-1000 kHz than the measurements in Fig. 6.30, but the same deviations around the thickness mode at 400-600 kHz in Fig. 6.30 is also seen in Fig. 6.37.

The admittance measurements and simulations of the finished prototype no. 1 in water are shown in Figs. 6.38a and 6.38b, where the log of the conductance and the susceptance is plotted against the frequency, respectively.

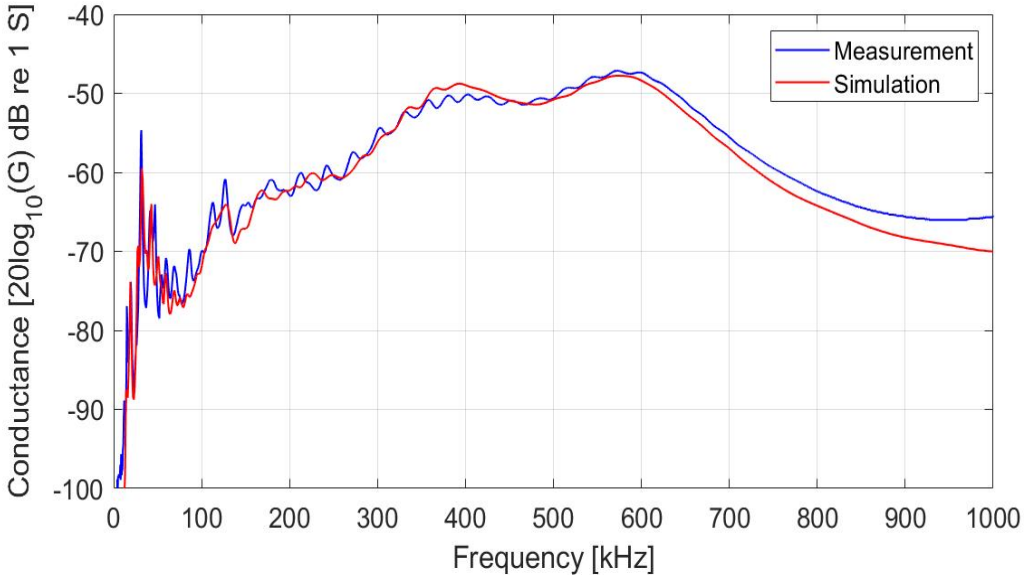

(a)

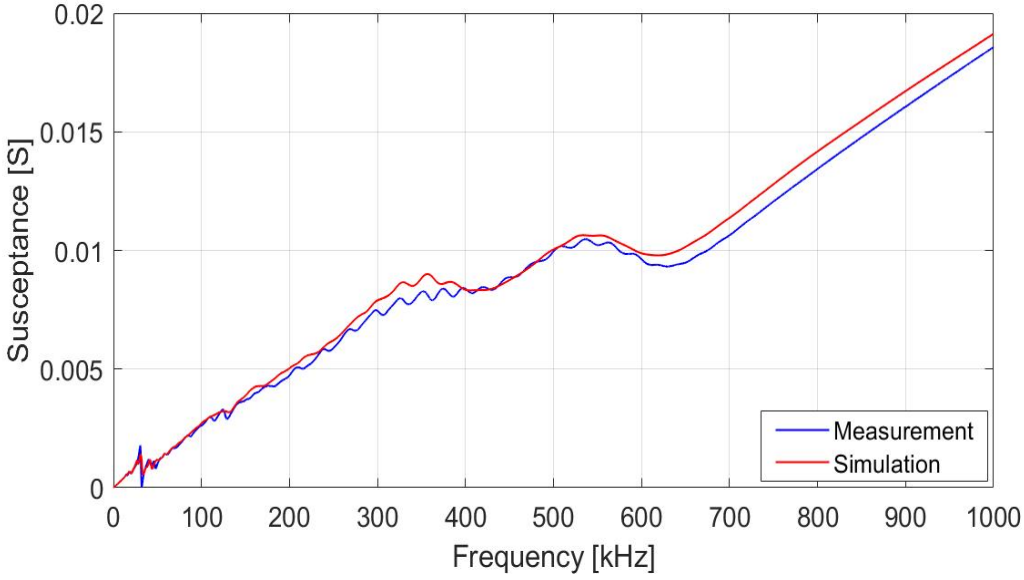

(b)

Figure 6.38: The admittance results of prototype no. 1 (with disk 44-2) in water. The measured admittance in water from 4-1000 kHz (blue) compared to the simulation (red). (a) The conductance. (b) The susceptance.

As seen in Figs. 6.38a and 6.38b the measurements conducted in water are in closer agreement to the simulation around the thickness mode at 400-600 kHz than the measurements conducted in air in Fig. 6.37. The measurements still have more ripples than the simulations, which could be because the backing layer is not uniformly and therefore are not damping as much as the simulated backing layer.

6.3.2 Transducer 2

This section presents the result for the transducer constructed of disk 44-5 (D_p x T_p) of 44.02 x 4.004 mm. The dimensions of the materials used are presented in Tab. 6.14. The front layer used has dimensions (D_{fl} x T_{fl}) of 51.15 x 1.194 mm. The thickness of the conductive adhesive T_{ca} is 0.118 mm, the casing thickness T_{c1} is 2.510 mm, and the thickness of the back casing T_{c2} is 3.911 mm. The length of the casing L_{c1} is 45.14 mm. The radius of the cone in the backing layer R_{air} is 5 mm and the thickness T_{air} is 10 mm. The tungsten epoxy backing layer is simulated with the values given in Tab. 5.7 with an impedance of 11.9 MRayl since this gives the best agreement

with the measurements.

Table 6.14: Dimensions of the materials used in transducer no. 2.

D_p [mm]	44.02	T_p [mm]	4.004
D_{fl} [mm]	51.15	T_{fl} [mm]	1.194
T_{c1} [mm]	2.510	L_{c1} [mm]	45.14
T_{ca} [mm]	0.118	T_{c2} [mm]	3.911
R_{air} [mm]	5	T_{air} [mm]	10

The admittance measurements and simulations conducted in air is presented in Figs. 6.39a and 6.39b, where the log of the conductance and the susceptance is plotted against the frequency, respectively.

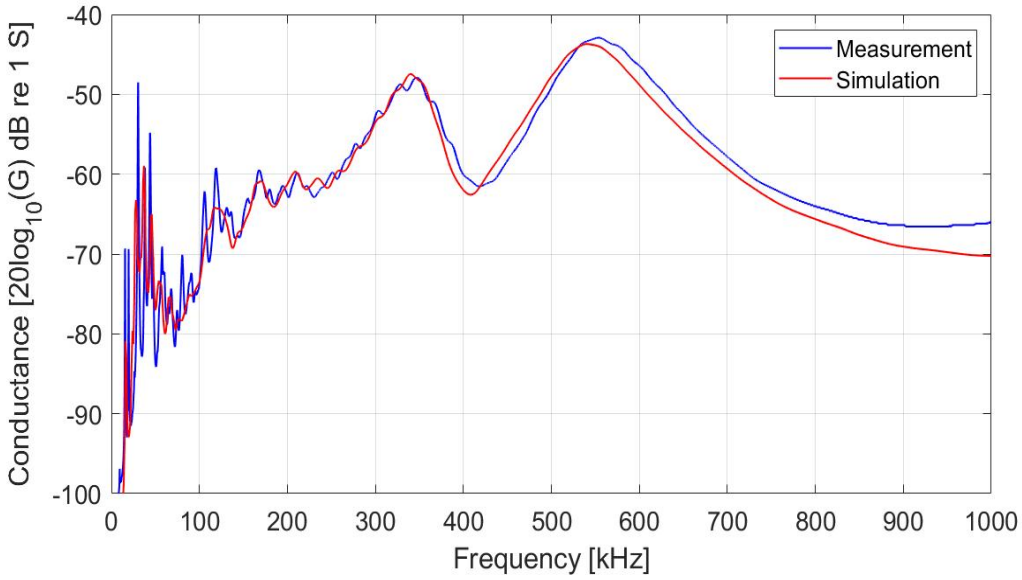

(a)

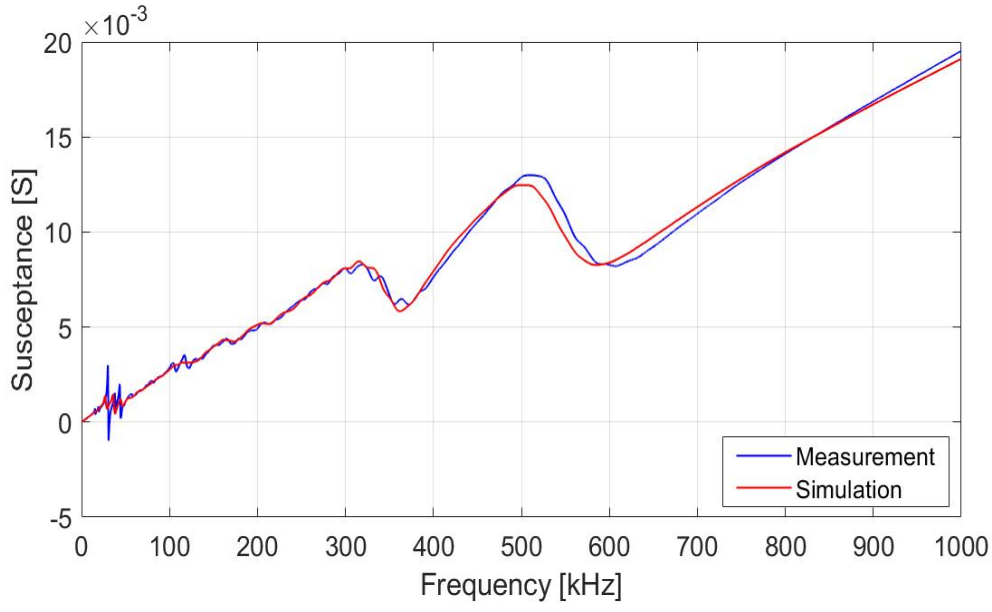

(b)

Figure 6.39: The admittance results of prototype no. 2 (with disk 44-5) in air. The measured admittance in air from 1-1000 kHz (blue) compared to the simulation (red). (a) The conductance. (b) The susceptance.

The measured conductance in Fig. 6.39a are in the same close agreement to the simulation as for the measured conductance in Fig. 6.32a, only the simulation in Fig. 6.39a have less ripples at 250-350 kHz than the simulation in Fig. 6.32a. The measured susceptance in Fig. 6.39b are in closer agreement with the simulation at 750-850 kHz than the measurement in Fig. 6.32b and also at 250-350 kHz, where fewer ripples in the simulation are seen compared to the simulation in Fig. 6.32b.

The admittance measurements and simulations of the finished prototype no. 2 in water are shown in Figs. 6.40a and 6.40b, where the log of the conductance and the susceptance is plotted against the frequency, respectively.

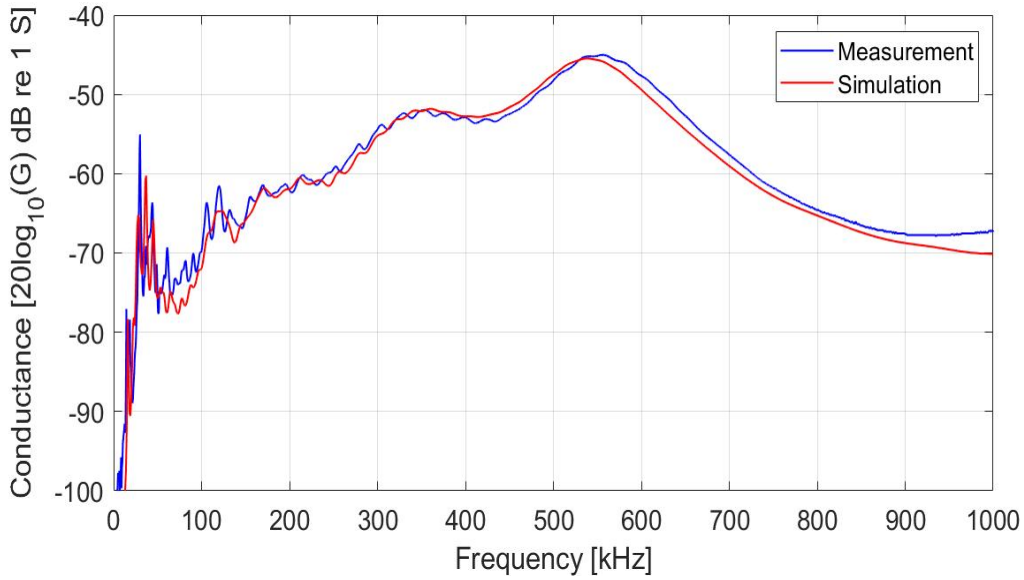

(a)

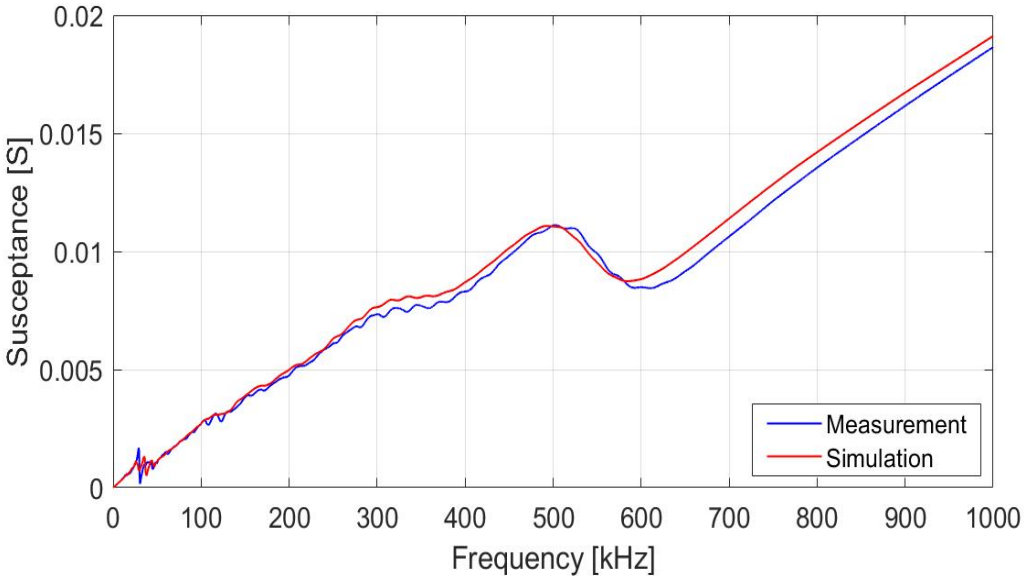

(b)

Figure 6.40: The admittance results of prototype no. 2 (with disk 44-5) in water. The measured admittance in water from 4-1000 kHz (blue) compared to the simulation (red). (a) The conductance. (b) The susceptance.

The difference between the measurement and simulation seen in Fig. 6.40 is similar to the admittance results in air seen in Fig. 6.39. The susceptance measurement in water deviates more from the simulation at 300-350 kHz and 700-1000 kHz in Fig. 6.40 than in the susceptance results in Fig. 6.39b.

6.3.3 Transducer 3

This section presents the result for the transducer constructed of disk 44-7 (D_p x T_p) of 44.03 x 4.017 mm. The dimensions of the different materials used are presented in Tab. 6.15. The front layer used has dimensions (D_{fl} x T_{fl}) of 51.16 x 1.172 mm. The thickness of the conductive adhesive T_{ca} is 0.106 mm. The casing thickness T_{c1} is 2.610 mm, and the thickness of the back casing T_{c2} is 3.890 mm. The length of the casing L_{c1} is 45.06 mm. The radius of the cone in the backing layer R_{air} is 7 mm and the thickness T_{air} is 10 mm. The tungsten epoxy backing layer is simulated with the values given in Tab. 5.7 with an impedance of 11.9 MRayl since this gives the best agreement with the measurements.

Table 6.15: Dimensions of the materials used in prototype transducer no. 3.

D_p [mm]	44.03	T_p [mm]	4.017
D_{fl} [mm]	51.16	T_{fl} [mm]	1.172
T_{c1} [mm]	2.610	L_{c1} [mm]	45.06
T_{ca} [mm]	0.106	T_{c2} [mm]	3.890
R_{air} [mm]	7	T_{air} [mm]	10

The admittance measurements and simulations conducted in air are presented in Figs. 6.41a and 6.41b, where the log of the conductance and the susceptance is plotted against the frequency, respectively.

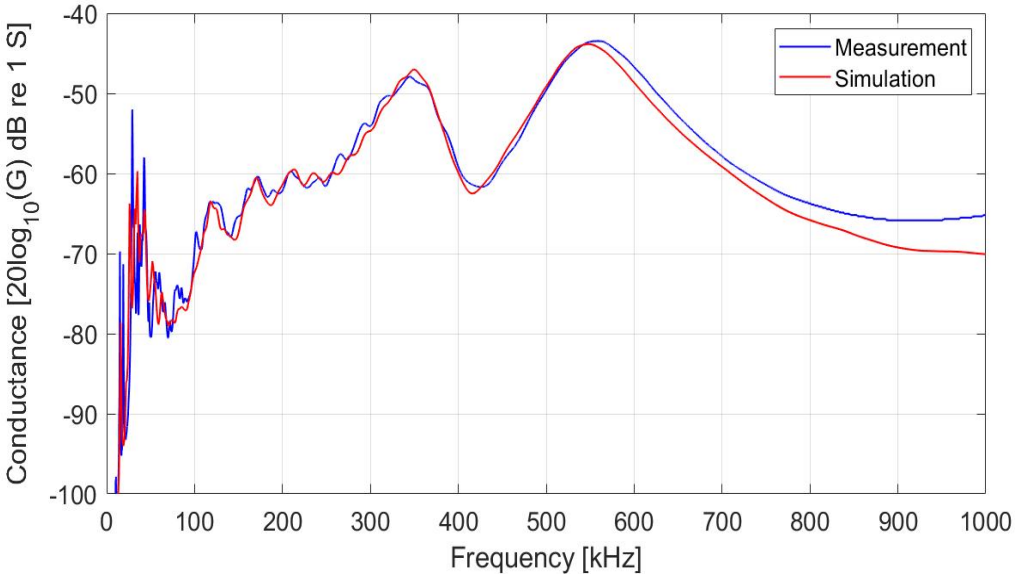

(a)

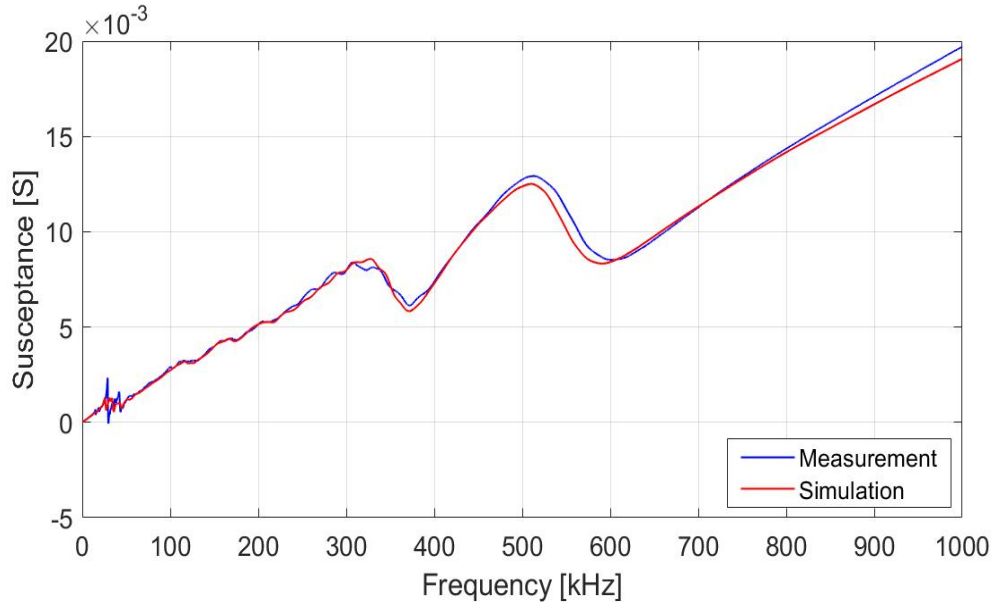

(b)

Figure 6.41: The admittance results of prototype no. 3 (with disk 44-7) in air. The measured admittance in air from 1-1000 kHz (blue) compared to the simulation (red). (a) The conductance. (b) The susceptance.

The measured admittance is in close agreement with the simulation, as seen in Fig. 6.41. The measured conductance in Fig. 6.41a deviates more from the simulation at 700-1000 kHz than the measurement in Fig. 6.33a, but the measured susceptance in Fig. 6.41b are in closer agreement with the simulation at 600-1000 kHz than the measurement in Fig. 6.33b.

The admittance measurements and simulations of the finished prototype no. 3 in water is shown in Figs. 6.42a and 6.42b, where the log of the conductance and the susceptance is plotted against the frequency, respectively.

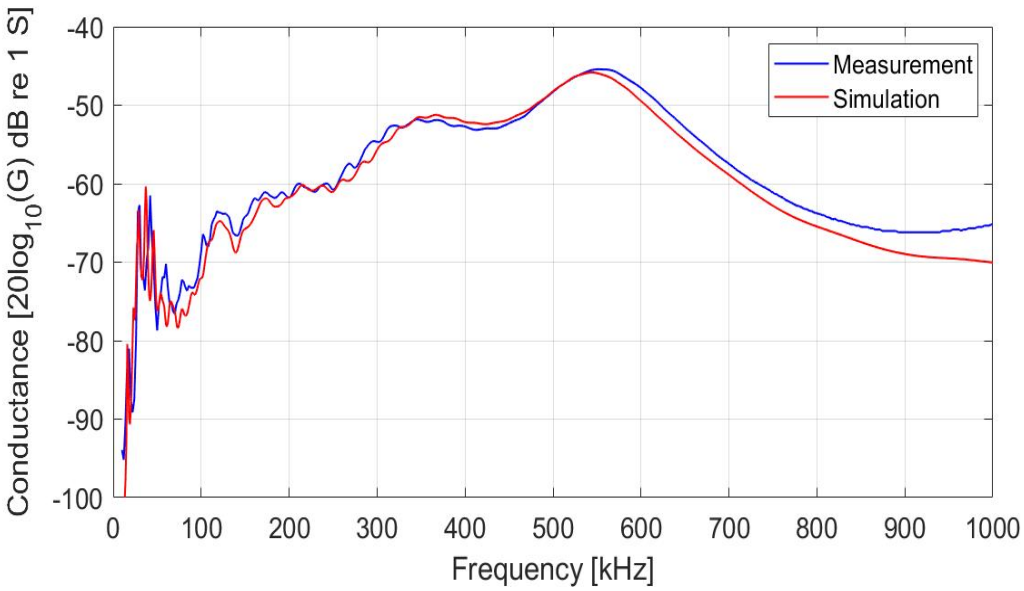

(a)

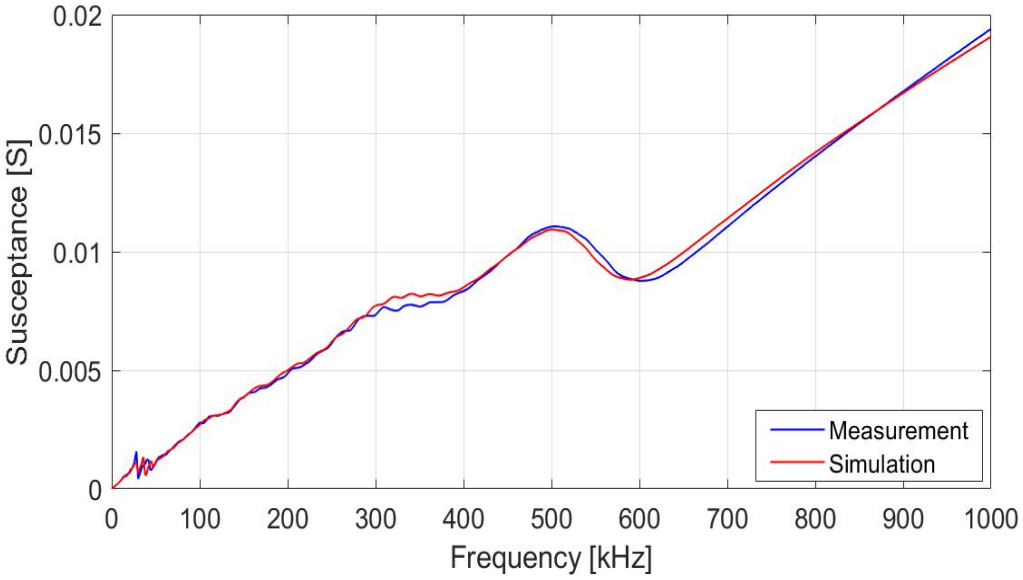

(b)

Figure 6.42: The admittance results of prototype no. 3 (with disk 44-7) in water. The measured admittance in water from 4-1000 kHz (blue) compared to the simulation (red). (a) The conductance. (b) The susceptance.

A deviation between the measured conductance compared to the simulation at 600-1000 kHz is still seen in Fig. 6.42a as also seen for the measurement in air in Fig. 6.41a. A close agreement between the measured susceptance and the simulation is seen in Fig. 6.42b, as also shown for the measurement in air in Fig. 6.41b.

The measured source sensitivity is compared to the simulation in Fig. 6.43, where the source sensitivity is plotted against the frequency, in the frequency range $200 - 1000$ kHz.

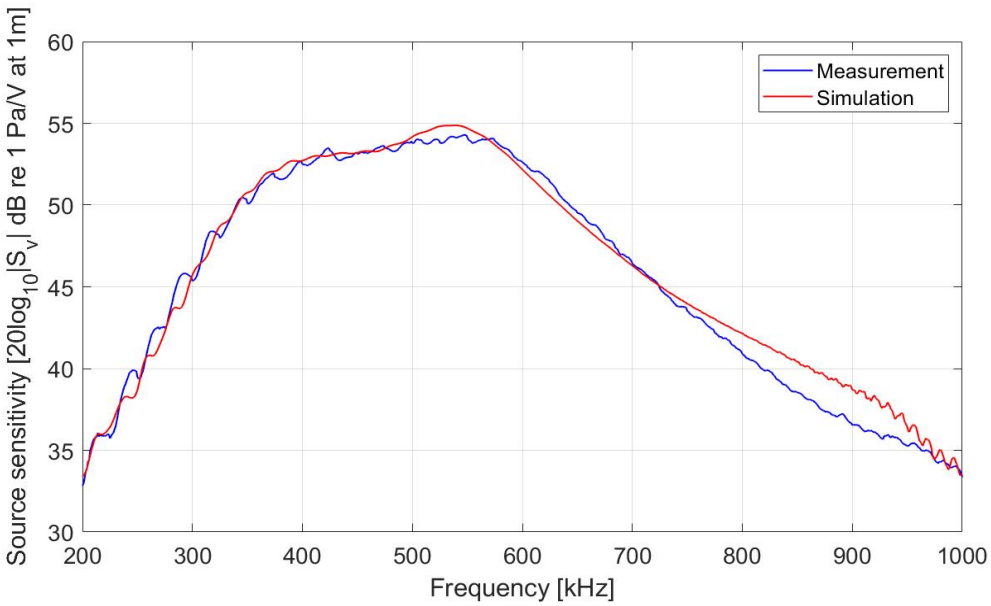

Figure 6.43: The result of the source sensitivity measurement in water for prototype no. 3 (with disk 44-7). The measured source sensitivity (blue) compared to the simulation (red).

The measured source sensitivity in Fig. 6.43 has the same ripples as seen in the admittance measurements, unlike the simulation. However, the simulation agrees well with the measurements, only around $800 - 950$ kHz, the simulation has a higher value than the measurement. This difference could be because the Rayleigh distance after 800 kHz is not fulfilled, but it is in close agreement with the simulation after 950 kHz. The bandwidth of the

measurement curve (blue) in Fig. 6.43 is 266 kHz.

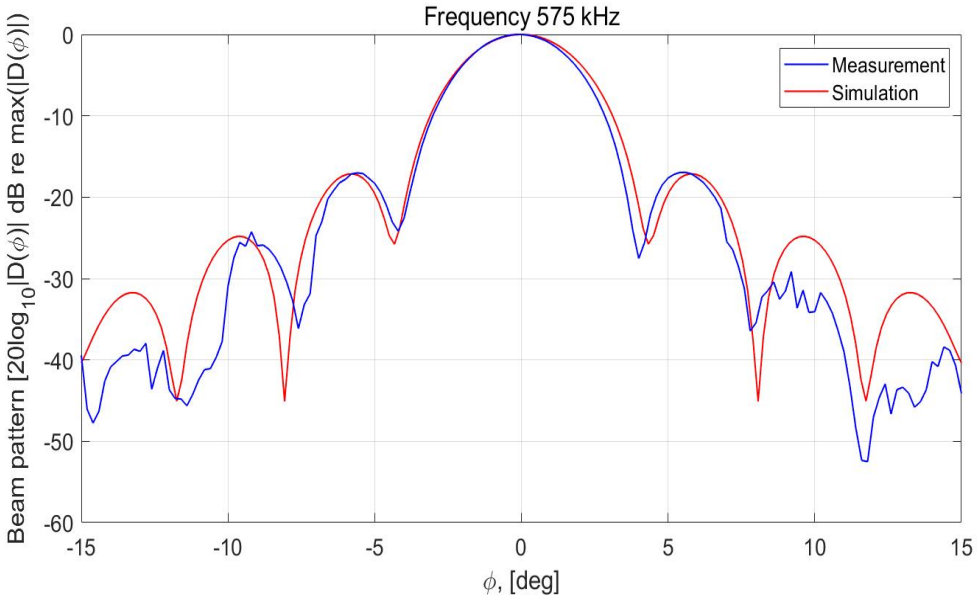

Figure 6.44: The results of the directivity measurements in water for prototype no. 3 (with disk 44-7). The measured beam pattern at 575 kHz (blue) compared to the simulation (red).

For the main lobe for transducer no. 3 at 575 kHz in Fig. 6.44, a reasonable agreement between the measurement and simulation is seen between -7.5 and 7.5 degrees. After 7.5 degrees, the measurements are not close to the simulation. A steady-state region further away from the main lobe was not obtained in the directivity measurements as explained in Sec. 4.4, which is why the measurement is not close to the simulation after 7.5 degrees. The beam radius of transducer no. 3 measured at the main lobe from the center down 3 dB is 1.8 degrees.

6.3.4 Transducer 4

This section presents the result for the transducer constructed of disk 16-5 (D_p x T_p) of 16.171 x 3.973 mm. The dimensions of the materials used are presented in Tab. 6.16. The front layer used has dimensions (D_{fl} x T_{fl}) of 23.031 x 1.123 mm. The thickness of the conductive adhesive T_{ca} is 0.036 mm. The casing thickness T_{c1} is 2.050 mm, and the thickness of the back casing T_{c2} is 3.960 mm. The length of the casing L_{c1} is 45.01 mm. The radius of the cone in the backing layer R_{air} is 5 mm and the thickness T_{air} is 10 mm. The tungsten epoxy backing layer is simulated with the values given in Tab. 5.7 with an impedance of 11.9 MRayl since this gives the best agreement with the measurements.

Table 6.16: Dimensions of the materials used in prototype transducer no. 4.

D_p [mm]	16.171	T_p [mm]	3.973
D_{fl} [mm]	23.031	T_{fl} [mm]	1.123
T_{c1} [mm]	2.050	L_{c1} [mm]	45.01
T_{ca} [mm]	0.036	T_{c2} [mm]	3.960
R_{air} [mm]	5	T_{air} [mm]	10

The admittance measurements and simulations conducted in air is presented in Figs. 6.45a and 6.45b, where the log of the conductance and the susceptance is plotted against the frequency, respectively.

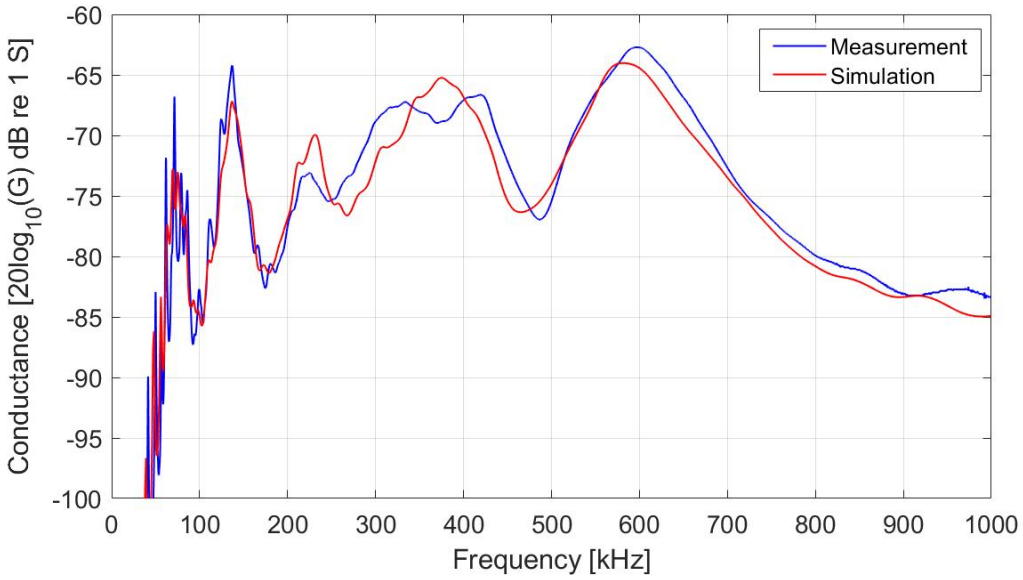

(a)

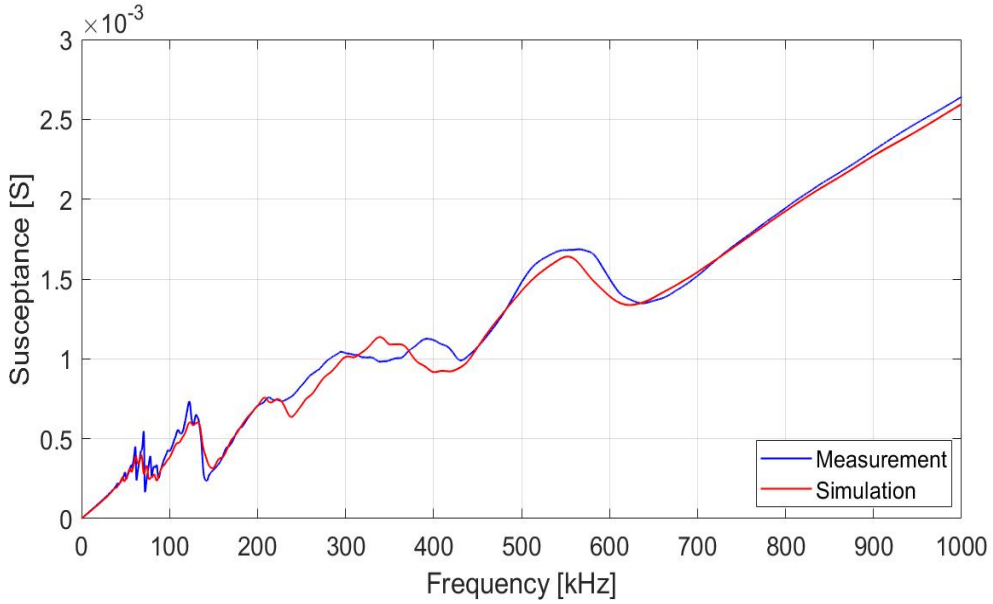

(b)

Figure 6.45: The admittance results of prototype no. 4 (with disk 16-5) in air. The measured admittance in air from 1-1000 kHz (blue) compared to the simulation (red). (a) The conductance. (b) The susceptance.

The measured and simulated admittance in Fig. 6.45 is in reasonable agreement with each other, the same as the results in Fig. 6.34 shows.

The admittance measurements and simulations of the finished prototype no. 4 in water are shown in Figs. 6.46a and 6.46b, where the log of the conductance and the susceptance is plotted against the frequency, respectively.

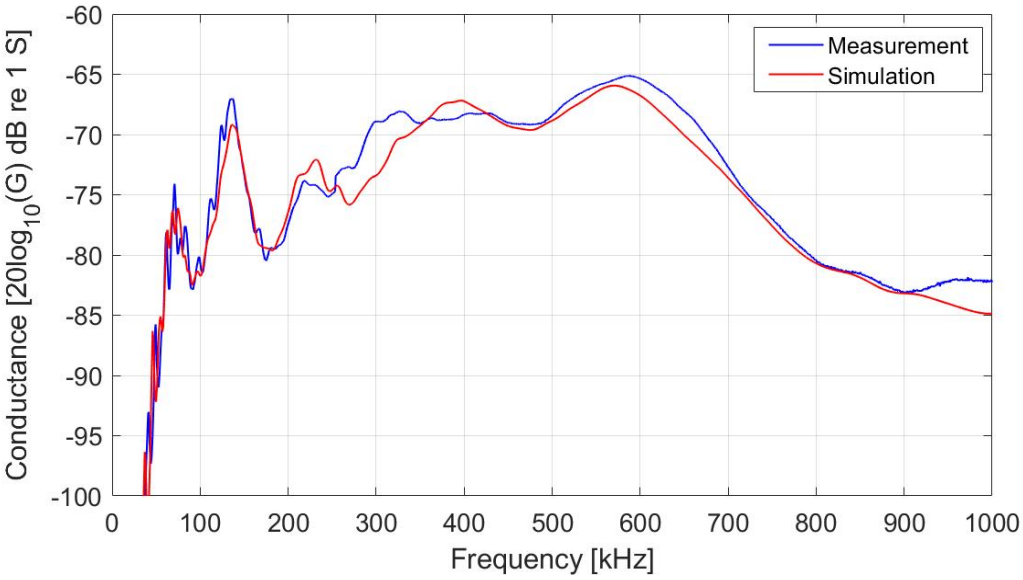

(a)

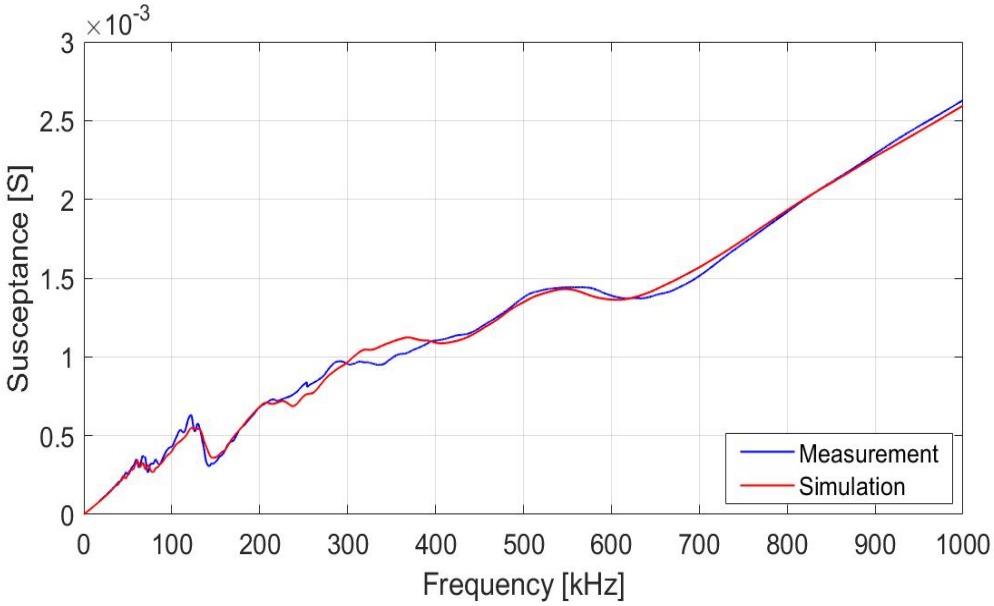

(b)

Figure 6.46: The admittance results of prototype transducer no. 4 (with disk 16-5) in water. The measured admittance in water from 4-1000 kHz (blue) compared to the simulation (red). (a) The conductance. (b) The susceptance.

As seen in Figs. 6.46a the conductance measurements conducted in water shows the same deviations between the measurement and simulations at 200-600 KHz as for the results in Fig. 6.45a from air. The measured susceptance in water shown in Fig. 6.46b has a closer agreement with the simulation at 200-600 kHz than the measurement in air in Fig. 6.45b.

In Fig. 6.47 the source sensitivity measurement is compared to the simulation, where the source sensitivity is plotted against the frequency, in the frequency range $200 - 1000$ kHz.

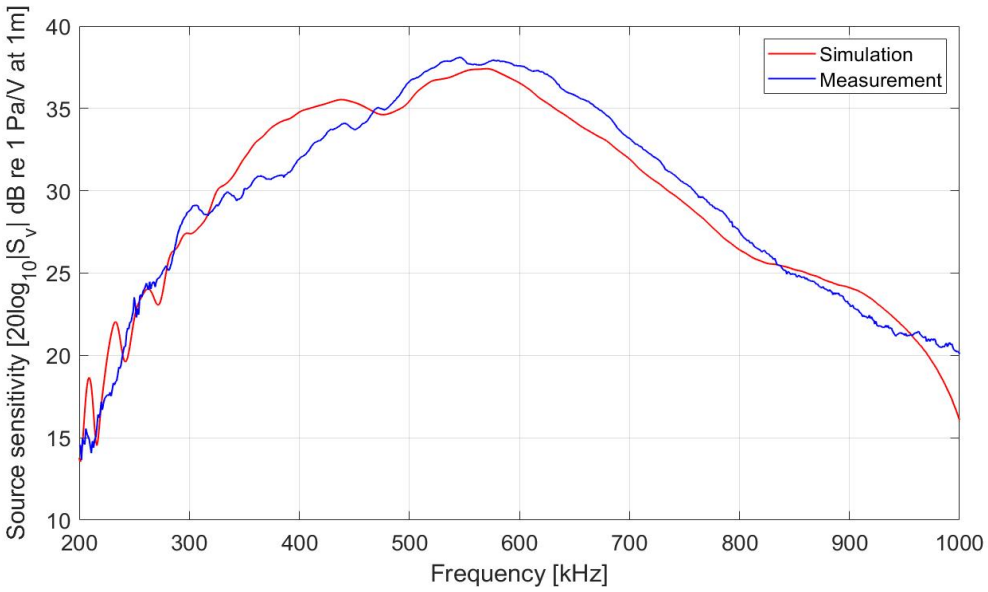

Figure 6.47: The results of the source sensitivity measurement in water for prototype no. 4 (with disk 16-5). The measured source sensitivity (blue) compared to the simulation (red).

Some deviations between the measurement and simulation of the source sensitivity are seen in Fig. 6.47. Some disturbance is seen in the frequency range $200 - 250$ kHz, the same as seen in the measurements conducted with Aanes prototype transducer no. 3 in Fig. 4.12. For transducer no. 4 the connector are sticking out in the back as shown in Fig. 3.11b, which could cause reflections in the source sensitivity measurements. The bandwidth of the measurement curve (blue) in Fig. 6.47 is 266 kHz. Higher than the bandwidth measured of the prototype transducer no. 3 in [1], but lower than the measured bandwidth of transducer no. 3 in Fig. 6.43. In the simulations in Fig. 5.8b, it is seen that a tungsten epoxy backing layer gives a broader bandwidth than an HCP70 backing layer. Therefore, transducer no. 4 will have a wider bandwidth than measured for transducer no. 3 from [1] with an HCP70 backing layer. It is also seen that a higher pressure amplitude is measured for transducer no. 3 in Fig. 6.43 than for transducer no. 4 in Fig. 6.47 because the transducer no. 3 has a wider source and therefore radiates a higher pressure amplitude.

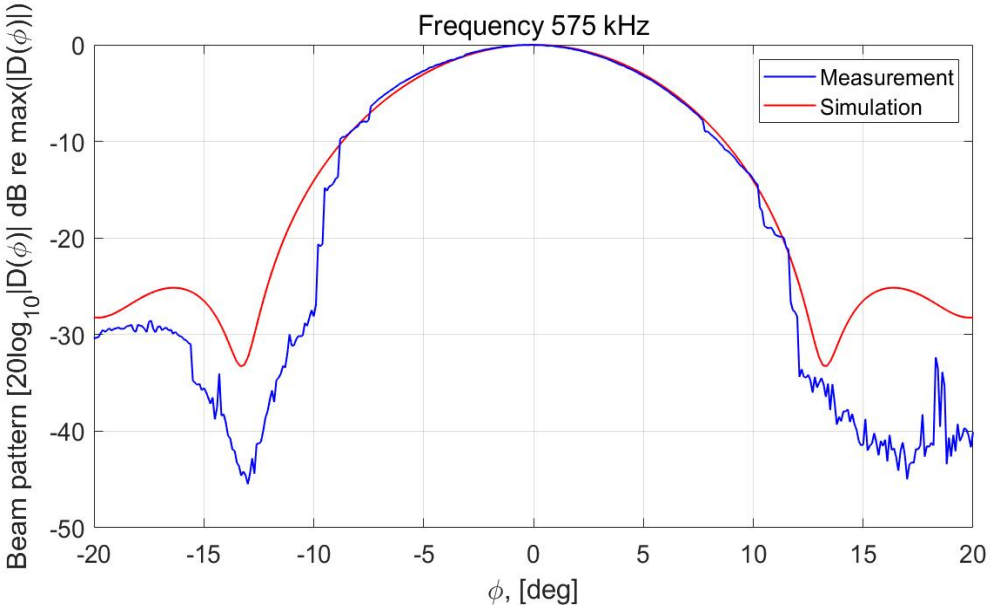

Figure 6.48: The results of the directivity measurements in water for prototype no. 4 (with disk 16-5). The measured directivity pattern at 575 kHz (blue) compared to the simulation (red).

For transducer no. 4, the directivity pattern measured at 575 kHz in Fig. 6.48 also shows a close agreement between the measurement and simulation between -7.5 and 7.5 degrees, the same as for transducer no. 3, but since the main lobe for transducer no. 4 is wider than for transducer no. 3, the measured main lobe for transducer no. 4 is not in close agreement with the simulation because of the problems with the steady-state explained in Sec. 4.4. As seen in the simulations, the main lobe for transducer no. 4 at 575 kHz goes 13 degrees out, but for transducer no. 3 the main lobe only goes 4 degrees out. The beam radius of transducer no. 4 measured at the main lobe down 3 dB is 5 degrees. The difference in the main lobe is expected since a transducer with a smaller source has a smaller effective radius which gives a broader main lobe [15].

6.3.5 Transducer 5

This section presents the result for the transducer constructed with disk 16-10 (D_p x T_p) of 16.196 x 3.974 mm. The dimensions of the materials used are presented in Tab. 6.17. The front layer used has dimensions (D_{fl} x T_{fl}) of 23.040 x 1.115 mm. The thickness of the conductive adhesive T_{ca} is 0.030 mm. The casing thickness T_{c1} is 2.040 mm, and the thickness of the back casing T_{c2} is 3.899 mm. The length of the casing L_{c1} is 45.02 mm. The radius of the cone in the backing layer R_{air} is 5 mm and the thickness T_{air} is 10 mm. The tungsten epoxy backing layer is simulated with the values given in Tab. 5.9 with an impedance of 8.7 MRayl since this gives the best agreement with the measurements.

Table 6.17: Dimensions of the materials used in prototype transducer no. 5.

D_p [mm]	16.196	T_p [mm]	3.974
D_{fl} [mm]	23.040	T_{fl} [mm]	1.115
T_{c1} [mm]	2.040	L_{c1} [mm]	45.02
T_{ca} [mm]	0.030	T_{c2} [mm]	3.899
R_{air} [mm]	5	T_{air} [mm]	10

The admittance measurements and simulations conducted in air is presented in Figs. 6.49a and 6.49b, where the log of the conductance and the susceptance is plotted against the frequency, respectively.

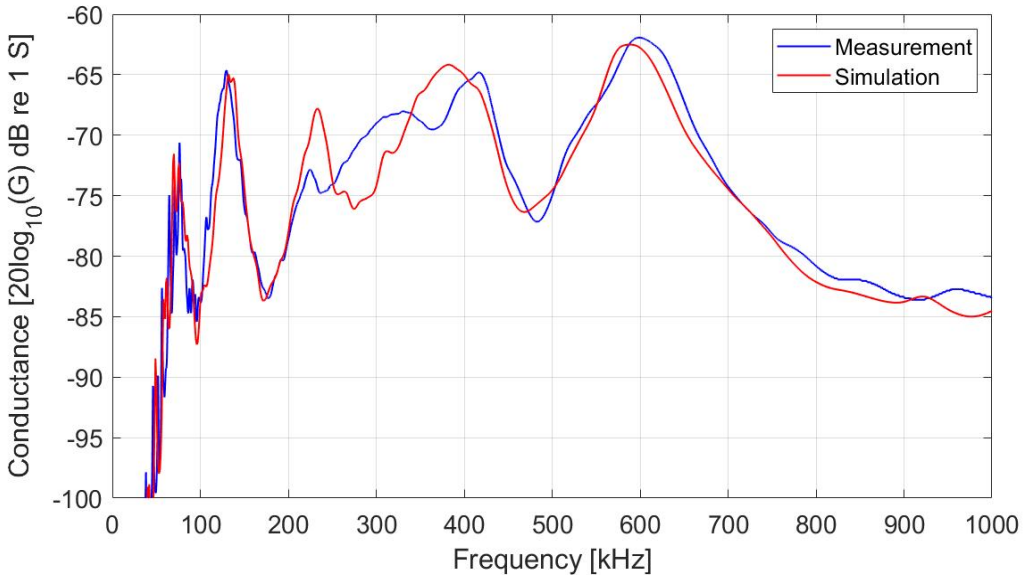

(a)

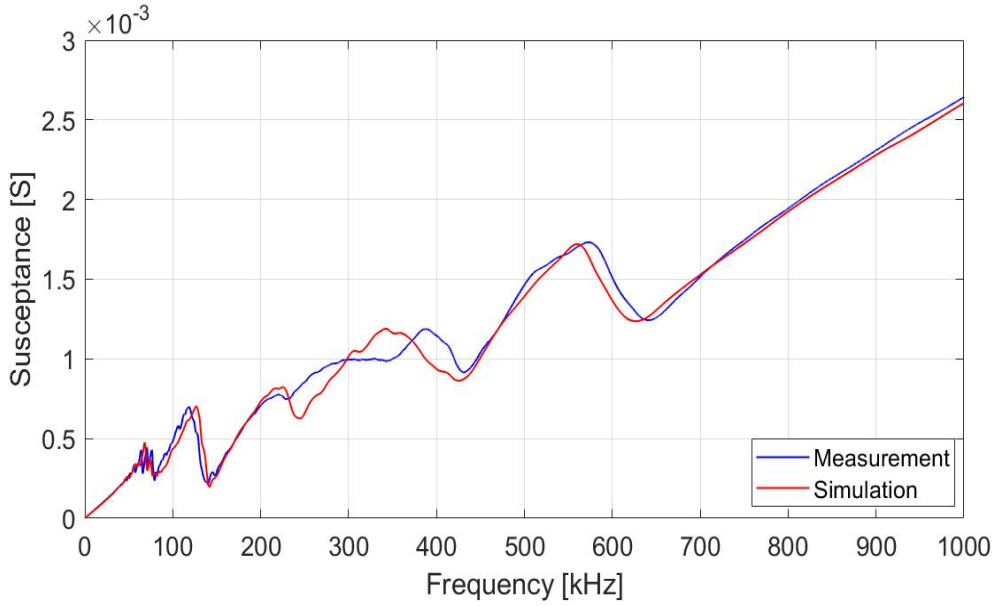

(b)

Figure 6.49: The admittance results of prototype no. 5 (with disk 16-10) in air. The measured admittance in air from 1-1000 kHz (blue) compared to the simulation (red). (a) The conductance. (b) The susceptance.

A closer agreement between the measured conductance and simulation in Fig. 6.49a is seen at the resonance at 120 kHz and 600 kHz than in Fig. 6.35a. The measured susceptance in Fig. 6.49b shows the same deviations between the simulation as seen in Fig. 6.35b.

The admittance measurements and simulations of the finished prototype no. 5 in water are shown in Figs. 6.46a and 6.46b, where the log of the conductance and the susceptance is plotted against the frequency, respectively.

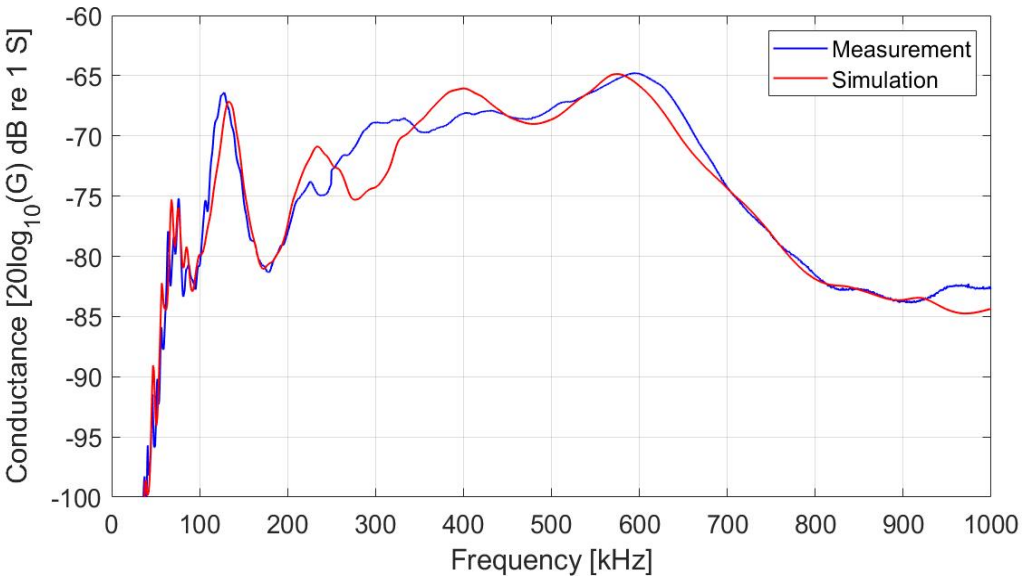

(a)

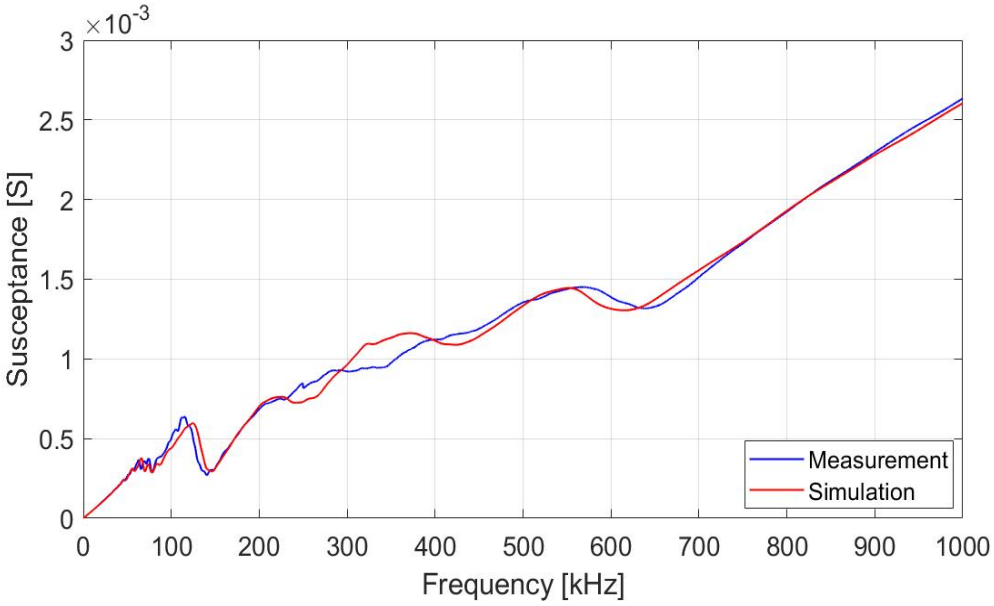

(b)

Figure 6.50: The admittance results of prototype no. 5 (with disk 16-10) in water. The measured admittance in water from 4-1000 kHz (blue) compared to the simulation (red). (a) The conductance. (b) The susceptance.

As seen in Figs. 6.50a and 6.50b, the admittance measurements conducted in water are in closer agreement with the simulations than for the results conducted in air shown in Fig. 6.49. The closer agreement between the measurement in water and simulation could be because the resonances in the thickness mode are damped more in water and therefore agrees better with the simulation.

6.3.6 Transducer 6

This section presents the result for the transducer constructed of disk 16-6 (D_p x T_p) of 16.206 x 3.974 mm. The dimensions of the materials used are presented in Tab. 6.18. The front layer used has dimensions (D_{fl} x T_{fl}) of 23.928 x 1.022 mm. The thickness of the conductive adhesive T_{ca} is 0.045 mm. The casing thickness T_{c1} is 2.597 mm, and the thickness of the back casing T_{c2} is 3.866 mm. The length of the casing L_{c1} is 44.33 mm. The radius of the cone in the backing layer R_{air} is 5 mm and the thickness T_{air} is 10 mm. The tungsten epoxy backing layer is simulated with the values given in Tab. 5.10 with an impedance of 10.1 MRayl since this gives the best agreement with the measurements.

Table 6.18: Dimensions of the materials used in prototype transducer no. 6.

D_p [mm]	16.206	T_p [mm]	3.974
D_{fl} [mm]	23.928	T_{fl} [mm]	1.022
T_{ca} [mm]	0.045	T_{c1} [mm]	2.597
L_{c1} [mm]	44.33	T_{c1} [mm]	3.866
R_{air} [mm]	5	T_{air} [mm]	10

The admittance measurements and simulations conducted in air is presented in Figs. 6.51a and 6.51b, where the log of the conductance and the susceptance is plotted against the frequency, respectively.

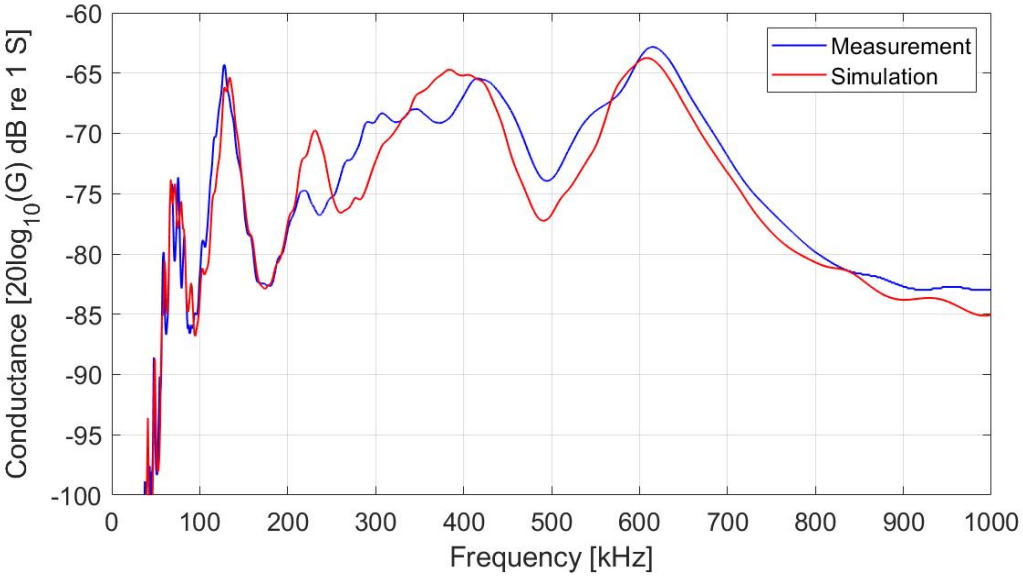

(a)

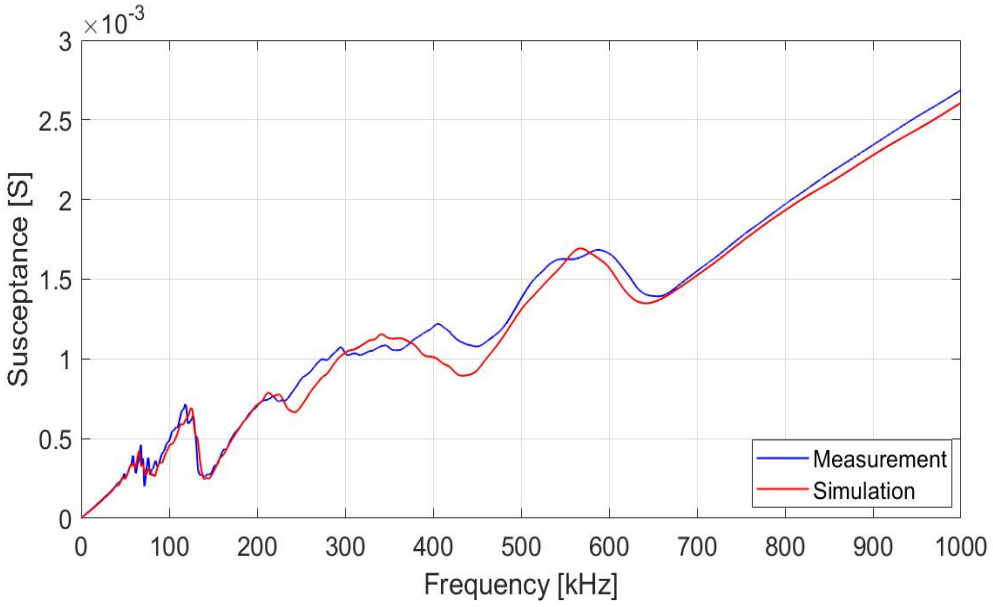

(b)

Figure 6.51: The admittance results of prototype no. 6 (with disk 16-6) in air. The measured admittance in air from 1-1000 kHz (blue) compared to the simulation (red). (a) The conductance. (b) The susceptance.

The result in Fig. 6.51 still shows the same deviations between the measurement and simulations as shown in Fig. 6.36, the measurement at 120 kHz in Fig. 6.51a are closer to the simulation than the measurement in Fig. 6.36a.

The admittance measurements and simulations of the finished prototype no. 6 in water are shown in Figs. 6.52a and 6.52b, where the log of the conductance and the susceptance is plotted against the frequency, respectively.

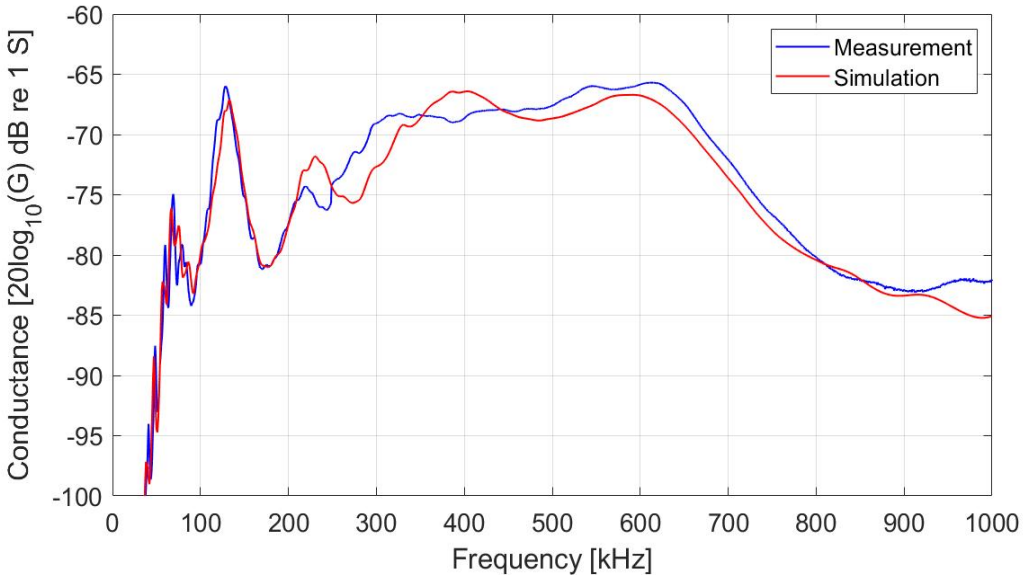

(a)

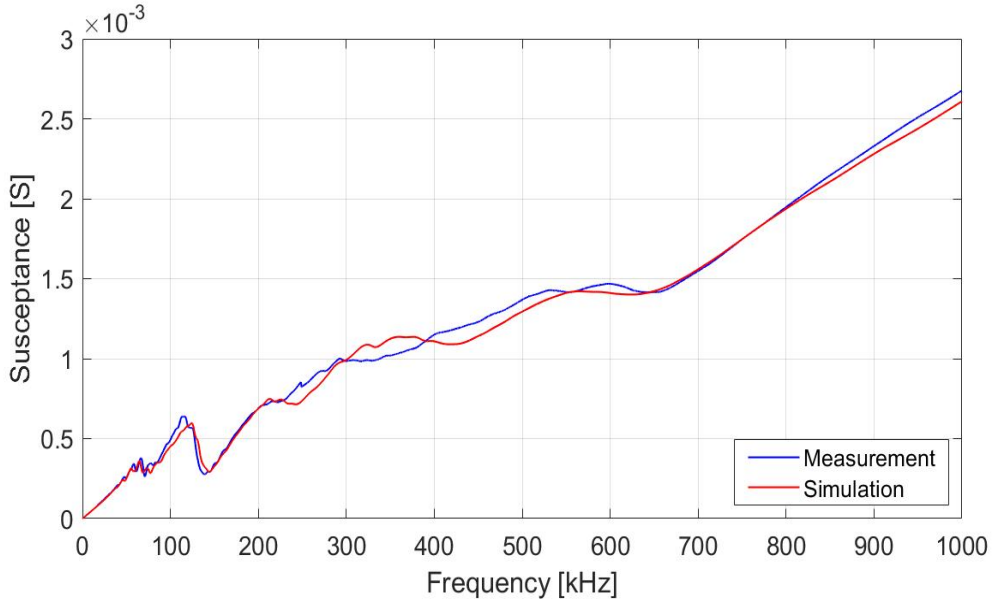

(b)

Figure 6.52: The admittance results of prototype no. 6 (with disk 16-6) in water. The measured admittance in water from 4-1000 kHz (blue) compared to the simulation (red). (a) The conductance. (b) The susceptance.

As seen in Figs. 6.52a and 6.52b the admittance measurements conducted in water are in closer agreement with the simulations at 200-600 kHz than for the results conducted in air in Fig. 6.51. The closer agreement between the measurement in water and simulation could be because the resonances in the thickness mode get more damped down in water than in air, making the measurement and simulations in closer agreement.

This section shows the electrical measurements of the finished prototypes in air and water compared to simulations. For transducers no. 1, 2 and 3, it has been shown that the measurements in air and water shows more ripples at 1-600 kHz than the simulations. Transducer no. 3 has the best agreement between the electrical measurements and the simulations, see Figs. 6.41a and 6.42a. Therefore transducer no. 3 also have been used to measure the source sensitivity and beam pattern. The sensitivity measurements also show more ripples than the simulation but still has a good agreement between the measurement and the simulation except at 750-950 kHz in Fig. 6.43. The difference above 750 kHz could be because the transducer is not in the far-field above 800 kHz.

For transducers no. 4, 5 and 6, the measurement and simulations are in close agreement from 1-200 kHz and

600-1000 kHz. However, a difference between the measurements and simulations is seen in the resonances and the thickness mode at 250-550 kHz. The same difference in the source sensitivity measurement for transducer no. 4 in Fig. 6.47 is seen. For the beam pattern measurements for transducer no. 3 and 4 in Figs. 6.44 and 6.48, problems with signals have been met, where a steady-state region has not been obtained. However, results that show the main lobe at 575 kHz has been achieved for transducer no. 4 in Fig. 6.44.

Chapter 7

Conclusion and outlook

In this chapter, a short conclusion of the overall findings is presented in Sec. 7.1. In Sec. 7.2, a few suggestions for improving the agreement between the measurements and the finite element simulations are given.

7.1 Conclusion and overall findings

In this work, ultrasonic piezoelectric transducers have been developed with a thickness mode at 500 kHz. The transducers are made with Pz27 disks, a front layer, a tungsten epoxy backing layer, a steel casing and a UHF connector. A detailed description of the construction process is shown with admittance measurements compared to simulations of every step. All the different methods used for attaching the disks to the front layers are explained, and the admittance results are shown. Finally, six transducers, three with a ka number of 17 and three with a ka number of 46, have been constructed. A reasonable agreement between the measurements and simulations has been achieved.

It is seen that the heat from the soldering process only gives a minor change in the measured conductance of the disk, see Fig. 6.6. However, to solder the disk without changing the electrical response has been a big challenge. It is seen that the conductance measurements after the disk are soldered compared to before the disk was soldered deviated more for disks with (D_p x T_p) of 16 x 4 mm than for the disks with (D_p x T_p) of 44 x 4 mm, see Sec. 6.2.1. The change in the conductance measurement after soldering could be due to the load a wire and the solder contributes. A disk with (D_p x T_p) of 16 x 4 mm will probably be more affected by the load than a disk with (D_p x T_p) of 44 x 4 mm . When the electrical measurements were conducted, the wire was longer than needed, which could have affected the results. However, it is still a significant change in the admittance measurements before and after the disk with (D_p x T_p) of 16 x 4 mm are soldered, giving a more significant error for the measurements conducted in the construction process, seen in Sec. 6.3.

For the disk attached to a front layer where the measurements haven't been in close agreement with the simulations, adjusted simulations have been made. The thickness of the conductive adhesive has been adjusted, which have made the simulations in closer agreement with the measurements. A clump of solder has been simulated for three disks with a front layer, disks 44-2, 16-7 and 16-4. A vacuum gap has also been simulated in the conductive adhesive for disk 16-7. A vacuum gap was simulated to see if the deviation between the measurement and simulation could be due to some air in the conductive adhesive, which the simulation confirmed in Fig. 6.16. A method for attaching the disk to the front layers has been found after multiple tries and verified with disk 44-5, 44-7,16-5, 16-10 and 16-6 in Figs. 6.13, 6.14, 6.20, 6.21 and 6.22.

It is seen that how close the electrical measurements of the piezoelectric disks before and after soldering are critical. Disks that have been soldered where the measured admittance is in close agreement with the admittance measurements conducted before the disk are soldered, are in closer agreement with the simulations in the further construction process, e.g. disk 44-7.

The tungsten epoxy mix has been dried inside the casing of the transducer, giving little control over the material parameters. It was seen from tests that the gradient changes in the layer. Even though the mixture is made with the same relation between tungsten grains and epoxy for all the transducers, it is seen that the material parameters are different based on the comparison between measurements and simulations. The difference could be due to some air being trapped inside these backing layers. The gradient in the backing layer changes outwards in the

backing layer, where it is highest near the piezoelectric disk and lowest at the back. This gradient change is not taken into account in the simulations. Since the epoxy was dried inside the casing, the impedance change was seen based on comparing simulations with different impedances in the backing layers. Since the material parameters of the backing layers are different, it is not made a sample for measuring, since the impedance will not be the same in the sample and in the transducer. It is also seen that the backing layer should be even longer to avoid the ripples seen in the measurements, based on the simulations shown in Sec. 5.5. The vacuum cones made in the backing layers are not made in the middle of the backing material and is not uniformly. For this reason, the vacuum cones in the simulations are only approximated, which can make the agreement between the measurements and the simulation less. However, some of the transducers with a very uneven vacuum cone has achieved good agreements between the measurement and simulations despite the uncertainties in the backing layer, e.g. transducer no. 3 in Sec. 6.3.3.

When zero calibrating the Impedance Analyzer with the cables used for measuring electrically on the finished prototype transducers in air and water, the values changed from time to time, affecting the measurements. When measuring in air, the amplitude of the susceptance varied depending on how well the calibration had been executed, as shown in Figs 6.9b and 6.10b. However, when calibrating the Impedance analyzer on a value that worked for the impedance measurements in air, the impedance measurements in water was too low to measure. Therefore, it was seen that the calibration had to be less good for measuring in water. When calibrating the Impedance analyzer with the two cables connected together used for measuring in water, the values got too low. Therefore only one cable had to be used when calibrating the Impedance Analyzer.

The electrical measurements in water were hard to conduct. The measurements stopped many times at different frequencies because the values were too high, even though the measurement range changed automatically. In addition, the variation made it hard to measure at a small step frequency. Therefore, the measurements conducted for water are only made with a step frequency of 500 Hz, not 100 Hz, which is used for the other measurements conducted in the construction process.

This author did not verify the acoustic measurements for prototype no. 3 transducer in [1], some discrepancies between the measurements conducted by this author and the measurements conducted in [1] were seen for the source sensitivity measurement in Fig. 4.12. However, acoustic measurements on the transducer no. 3 constructed in this thesis were in close agreement with the simulations, see Fig. 6.43. Unfortunately, for transducer no. 4, electrical measurements have not been in close agreement with the simulations on all the frequencies. Still, the discrepancies between the acoustic measurements and the simulations for transducer no. 4 in Fig. 6.47 are on the same frequencies as for the conductance in Fig. 6.46a.

It could be some ageing effects on the transducers made by Aanes [1] since there is some difference between both the electrical measurements and the acoustic measurements conducted by this author compared to the measurements in [1], see Figs. 4.10 and 4.12. Still, the measurements conducted on the transducers in this work are in agreement with the finite element simulations. In addition, it could be because of the hydrophone, but since the measurements for 44-7 in Fig. 6.43 are in close agreement with the simulations, the effect is likely small. A steady-state region was not obtained for the beam pattern measurements conducted in this work for all the measured angles, see Figs. 4.13, 6.44 and 6.48, because of a lack of time to figure out the faults with the signals.

7.2 Further work

Several suggestions for improving the measurements and similarities between the measurements and finite element simulations are found based on the experience gained from this work. For improving the similarities between the measurements and simulations, adjustments to the material constants should be made for the different dimensions of the piezoelectric disks. It is also beneficial to work more on how the disks should be soldered to avoid deviations between the electrical measurements conducted before and after the disks are soldered. Another method that gives better electrical contact with the front electrode can probably make the measurements and the simulations more alike in the frequencies above 700 kHz, since it is seen that the difference between the measurements and simulations varies at 700 to 1000 kHz between the transducers. The backing layer should be made outside the casing, so it is possible to measure the material parameters on each backing layer, making the simulations in closer agreement with the measurements. The hydrophone used for the acoustic measurements should be calibrated for further use to avoid too many measurement uncertainties. A way to measure electrically on the transducers from 1 kHz in water using the Impedance Analyzer should also be found, and a better way to zero-calibrate the Impedance analyzer with longer cables.

References

[1] M. Aanes, *Interaction of piezoelectric transducer excited ultrasonic pulsed beams with a fluid-embedded viscoelastic plate, Dissertation for the degree philosophiae doctor at the University of Bergen, Department of Physics and Technology, 2013*.

[2] I. Ravndal, *Normal Incidence Ultrasonic Beam Transmission Through Steel Plates. Measuring and Modelling The Transmission Coefficient. Master thesis, University of Bergen, Department of Physics and Technology, 2020*.

[3] S. Midtbø, *Beam diffraction effects in guided-wave transmission of fluid embedded elastic plate. Influence of receiver distance and finite aperture. Masters thesis, University of Bergen, Department of Physics and Technology, 2018*.

[4] J. Kocbach, *Finite element modeling of ultrasonic piezoelectric transducers. Dissertation for the degree philosophiae doctor at University of Bergen, Department of Physics and Technology, 2000*.

[5] M. Aanes, K. D. Lohne, P. Lunde, and M. Vestrheim., *Transducer beam diffraction effects in sound transmission near leaky Lamb modes in elastic plates at normal incidence, 2015*.

[6] ——, "Beam diffraction effects in sound transmission of a fluid-embedded viscoelastic plate at normal incidence", *The Journal of the Acoustical Society of America*, 2016.

[7] ——, "Finite aperture influence on energy concentration, frequency shift, and signal enhancement, for acoustic transmission in the negative group velocity region of the S1 leaky Lamb mode", 2016.

[8] *Type Pz27 datasheet, Meggit AS, Porthusvej 4, DK3490, Kvistgaard, Denmark, 2020*.

[9] A. Gachagan, P. Reynolds, G. Hayward, and A. McNab, "Construction and evaluation of a new generation of flexible ultrasonic transducers", 1996.

[10] M. Castaings, R. S. Monkhouse, M. J. Lowe, and P. Cawley, "The performance of flexible interdigital PVDF lamb wave transducers", *Acustica*, 1999.

[11] D. Hidayat, N. S. Syafei, B. M. Wibawa, M. Taufik, A. Bahtiar, and Risdiana, "Metal-polymer composite as an acoustic attenuating material for ultrasonic transducers", 2020.

[12] P. K. Bolstad, A. Le, L. Hoff, and T. Manh, *Intermetallic bonding as an alternative to polymer adhesives in ultrasound transducers, 2019*.

[13] A. A. Abas, D. M. P. Ismail, S. Sani, and M. N. I. Ahmed, *Effect of backing layer composition on ultrasonic probe bandwidth, NDT Group Industrial Technology Division, 2016*.

[14] K. Sugawara, M. Nishihira, and K. Imano, "Experimental Study of Acoustic Properties of (0-3) Composite Materials for Intermediate Layer or Backing of Ultrasonic Transducers", *Japanese Journal of Applied Physics*, 2005.

[15] L.E.Kinsler, A.R.Frey, A.B.Coppens, and J.V.Sanders, *Fundamentals of Acoustics, Fourth Edition, 2000*.

[16] M. Vestrheim, *Phys373 - akustiske målesystemer - forelesningsnotater, [in Norwegian]. Course at Department of Physics and Technology, University of Bergen, 2008*.

[17] ——, *Phys 272 - akustiske transdusere - forelesningsnotater, [in Norwegian]. Course at Department of Physics and Technology, University of Bergen, 2017*.

[18] M. M. Sæther, *Elastic wave velocities and attenuation under methane hydrate growth in Bendtheim sandstone - measurements and modelling. Dissertation for the degree philosophiae doctor at the University of Bergen, Department of Physics and Technology, 2018*.

[19] *Sn63Pb37, ELSOLD GmbH Co. KG, D-38611 Goslar, 2021*.

[20] *Techno HA-02 forced air convection reflow oven User Manual, Technoprint, Veldzichtweg 10B, 3851 SH Ermelo, Netherlands, 2000*.

[21] *Eccosorb MF114, Laird Technologies - Emerson Cuming Microwave Products, 28 York Avenue, Randolph, MA 02369, USA, 2022*.

[22] *8330D-Silver Conductive Epoxy Adhesive, MG Chemicals, 9347- 193rd Street, Surrey, BC, V4N 4E7,Canada, 2021*.

[23] *8331 - Silver Conductive Epoxy Adhesive, MG Chemicals, 9347- 193rd Street, Surrey, BC, V4N 4E7,Canada, 2021.*
[24] *8331S - Silver Conductive Epoxy Adhesive, MG Chemicals, 9347- 193rd Street, Surrey, BC, V4N 4E7,Canada, 2021.*
[25] *Loctite Power Epoxy, Extra time, Henkel Norway AS, Bryggegata 6, 0250 Oslo, Norway, 2021.*
[26] *Avoid Air Bubbles In Mixed Epoxy Systems, 2021, Accessed on: Oct. 28, 2021.* [Online]. Available: `https://www.masterbond.com/techtips/avoid-air-bubbles-mixed-epoxy-systems`.
[27] *Cold Mounting systems for all materialografhic applications, Struers ApS, Pederstrupvej 84, DK-2750 Ballerup, Denmark, 2000.*
[28] *83-1R (SO-239) coaxial connector, Amphenol RF, Danbury, CT, USA, 2021.*
[29] *High-Accuracy Digimatic Micrometer MDH-25MB, Mitutoyo Europe GmbH, 41469 Neuss, Germany, 2022.*
[30] *Caliper S_{Cal} pro IP67, Sylvac SA, Avenue des Sciences 19, 1400 Yverdon-les-Bains-CH, Switzerland, 2021.*
[31] *Operation and Service Manual Model 4192A LF Impedance Analyzer, Yokogawa-Hewlett-Packard Ltd, Tokyo, Japan, 1983.*
[32] *Agilent 33120A User's guide Edition 6, March 2002, Publication number 33120-90006, Agilent Technologies, Inc. 1994-2002.*
[33] *Precision Acoustics Ltd, Hampton Farm Business Park, Higher Bockhampton, Dorchester, Dorset, U.K.*
[34] *Datasheet for Femto HVA-10M-60-F 10 MHz High Input Impedance Voltage Amplifier, FEMTO Messtechnik GmbH Berlin Germany, 2022.*
[35] *Operating and maintenance manual for Model 3202 solid state variable filter, Krohn-Hite Massachusetts USA, 2022.*
[36] *Digital Phosphor Oscilloscopes User Manual DPO3000 series, Tektronix Inc, Beaverton, OR. USA, 2022.*
[37] *PRS-110 Precision Rotation Stage User Manual, PiMicos GmbH Eschbach Germany, 2022.*
[38] *Linear Motor Stage LMS-100 , PiMicos Gmbh Eschbach Germany, 2022.*
[39] *404XE T07 Linear Positioning Tables Catalog 8087, Parker Automation USA, 2022.*
[40] *404XE T09 Linear Positioning Tables Catalog 8087, Parker Automation USA, 2022.*
[41] V. Knappskog, *Radiellmode svingninger i piezoelektriske ultralydtransdusere for luft, målinger og endelig element analyser [in norwegian], Master thesis, University of Bergen, Department of Physics and Technology, 2007.*
[42] *CurveSnap.exe, 2021, Accessed on: May 20, 2021.* [Online]. Available: `https://curvesnap.en.softonic.com/`.
[43] *Private communication with Mathias Sæther at the Department of Physics and Technology, University of Bergen, 2021.*
[44] A. R. Selfridge, "Approximate Material Properties in Isotropic Materials", *IEEE Transactions on Sonics and Ultrasonics*, 1985.

Appendix A

Appendices

A.1 FEMP files used for the simulation setup

The different MATLAB cripts and files used for the simulations is presented here.

A.1.1 Read in project file with fluid

```
function [read]=read_inn_project(read,commands);
%%%%%%%%%%%%%%%%%%%%%%%%%%%%%%%%%%%%%%%%%%%%%%%%%%%%%%%%%%%%%%%%%%%%%%%%%%%%%%
% Read .inn-file. Note that this function calls a project specific
% read_inn_project.m which should be in the working directory
%
% Part of FEMP (Finite Element Modeling of Piezoelectric structures)
% Programmed by Jan Kocbach (jan@kocbach.net)
% (C) 2000 Jan Kocbach. This file is free software; you can redistribute
% it and/or modify it only under the the terms of the GNU GENERAL PUBLIC
% LICENSE which should be included along with this file.
% (C) 2000-2010 Christian Michelsen Research AS
%%%%%%%%%%%%%%%%%%%%%%%%%%%%%%%%%%%%%%%%%%%%%%%%%%%%%%%%%%%%%%%%%%%%%%%%%%%%%%

% Put a file read_inn_project.m in your project directory to define local
% FEMP input commands. Also include init_const_project.m in this directory
% and define the commands there.
global glob;
read=read;

if ~isempty(read.piezodiskfrontlim)
    read.points=[]; read.areas=[]; read.materials=[]; read.dof=[];
    read.restraints=[];
   % Make read.points, read.areas,read.dof,read.restraints etc. etc.
    r=read.piezodiskfrontlim(1,1,:);
    t=read.piezodiskfrontlim(1,2,:);
    rfront=read.piezodiskfrontlim(1,3,:);
    tfront=read.piezodiskfrontlim(1,4,:);
    elr=read.piezodiskfrontlim(1,5,:);
    matnum=read.piezodiskfrontlim(1,6,:);
    matnumfront=read.piezodiskfrontlim(1,7,:);
    tlim=read.piezodiskfrontlim(1,8,:);
    matnumlim=read.piezodiskfrontlim(1,9,:);
    tbak=read.piezodiskfrontlim(1,10,:);
    matnumbak=read.piezodiskfrontlim(1,11,:);
    matnumtin=read.piezodiskfrontlim(1,12,:);
```

```
tinr=read.piezodiskfrontlim(1,13,:);%Radius of the solder
tin=read.piezodiskfrontlim(1,14,:);%Thickness of the solder

tc=2.99735e-3;%thickness of the back casing
tc2=1.099e-3;%thickness of the steel casing
tair=10e-3;%depth of the vacuum cone
rluft=7.5e-3;%Radius of the vacuum cone
w=2.046e-3-1.099e-3;%Thickness of hatch in the steel casing
tbak=45.01e-3-t-tfront-tair-tlim-gap-tc; %Thickness of the
%backing layer
ttot =(t+tfront+tbak+tair+tlim+tc+gap)/2;

matnumstaal=80;
matnumf=100;
Rinf=80e-3;
Rinf2=Rinf*2;

t1=(rluft)/3;%The radius of the vacuum cone is divided into three
t2=t1*2;
t3=tair/3;%The thickness of the vacuum cone is divided into three
t4=t3*2;

theta_coord=[
     tinr -ttot+tc+tair+tbak+t+tlim+tfront;
     tinr+luft -ttot+tc+tair+tbak+t+tlim+tfront;
     rluft -ttot+tc+tair+tbak+t+tlim+tfront;
     r -ttot+tc+tair+tbak+t+tlim+tfront;
     rfront -ttot+tc+tair+tbak+t+tlim+tfront;
     rfront+tc2 -ttot+tc+tair+tbak+t+tlim+tfront;
     rfront+tc2 -ttot+tc+tair+tbak+t+tlim;
     rfront+tc2 -ttot+tc+tair+tbak+t;
     rfront+tc2 -ttot+tc+tair+tbak;
     rfront+tc2 -ttot+tc+tair+tbak-tin;
     rfront+tc2 -ttot+tc+tair;
     rfront+tc2 -ttot+tc;
     rfront+tc2 -ttot;
     rfront -ttot;
     r -ttot;
     rluft -ttot;
     tinr+luft -ttot;
     tinr -ttot;
     t1 -ttot+tc+tair+tbak+t+tlim+tfront;
     t2 -ttot+tc+tair+tbak+t+tlim+tfront;
     rfront+tc2 -ttot+tc+tair-t3;
     rfront+tc2 -ttot+tc+tair-t4;
     t2 -ttot;
     t1 -ttot];

theta = atan(theta_coord(:,1)./theta_coord(:,2));
sdof1=size(read.dof,1);sdof2=size(read.dof,2);
for s=1:size(r,3)
read.points(:,:,s)=[1 0 -ttot(s)+tc(s)+tair(s)+tbak(s)-tin(s);
2 tinr(s) -ttot(s)+tc(s)+tair(s)+tbak(s)-tin(s);
3 tinr(s)+luft(s) -ttot(s)+tc(s)+tair(s)+tbak(s)-tin(s);
4 r(s) -ttot(s)+tc(s)+tair(s)+tbak(s)-tin(s);
5 rfront(s) -ttot(s)+tc(s)+tair(s)+tbak(s)-tin(s);
6 0 -ttot(s)+tc(s)+tair(s)+tbak(s);
7 tinr(s) -ttot(s)+tc(s)+tair(s)+tbak(s);
```

```
8 tinr(s)+luft(s) -ttot(s)+tc(s)+tair(s)+tbak(s);
9 r(s) -ttot(s)+tc(s)+tair(s)+tbak(s);
10 rfront(s) -ttot(s)+tc(s)+tair(s)+tbak(s);
11 0 -ttot(s)+tc(s)+tair(s)+tbak(s)+t(s);
12 tinr(s) -ttot(s)+tc(s)+tair(s)+tbak(s)+t(s);
13 tinr(s)+luft(s) -ttot(s)+tc(s)+tair(s)+tbak(s)+t(s);
14 rluft(s) -ttot(s)+tc(s)+tair(s)+tbak(s);
15 rluft(s) -ttot(s)+tc(s)+tair(s)+tbak(s)+t(s);
16 r(s) -ttot(s)+tc(s)+tair(s)+tbak(s)+t(s);
17 rfront(s) -ttot(s)+tc(s)+tair(s)+tbak(s)+t(s);
18 0 -ttot(s)+tc(s)+tair(s)+tbak(s)+t(s)+tlim(s);
19 tinr(s) -ttot(s)+tc(s)+tair(s)+tbak(s)+t(s)+tlim(s);
20 tinr(s)+luft(s) -ttot(s)+tc(s)+tair(s)+tbak(s)+t(s)+tlim(s);
21 rluft(s) -ttot(s)+tc(s)+tair(s)+tbak(s)+t(s)+tlim(s);
22 r(s) -ttot(s)+tc(s)+tair(s)+tbak(s)+t(s)+tlim(s);
23 rfront(s) -ttot(s)+tc(s)+tair(s)+tbak(s)+t(s)+tlim(s);
24 0 -ttot(s)+tc(s)+tair(s)+tbak(s)+t(s)+tlim(s)+tfront(s);
25 tinr(s) -ttot(s)+tc(s)+tair(s)+tbak(s)+t(s)+tlim(s)+tfront(s);
26 tinr(s)+luft(s) -ttot(s)+tc(s)+tair(s)+tbak(s)+t(s)+tlim(s)
+tfront(s);
27 rluft(s) -ttot(s)+tc(s)+tair(s)+tbak(s)+t(s)+tlim(s)+tfront(s);
28 r(s) -ttot(s)+tc(s)+tair(s)+tbak(s)+t(s)+tlim(s)+tfront(s);
29 rfront(s) -ttot(s)+tc(s)+tair(s)+tbak(s)+t(s)+tlim(s)+tfront(s);
30 0 -ttot(s)+tc(s)+tair(s);
31 tinr(s) -ttot(s)+tc(s)+tair(s);
32 tinr(s)+luft(s) -ttot(s)+tc(s)+tair(s);
33 rluft(s) -ttot(s)+tair(s)+tc(s);
34 r(s) -ttot(s)+tair(s)+tc(s);
35 rfront(s) -ttot(s)+tair(s)+tc(s);
36 rluft(s) -ttot(s)+tc(s);
37 r(s) -ttot(s)+tc(s);
38 rfront(s) -ttot(s)+tc(s);
39 rluft(s) -ttot(s)+tair(s)+tc(s)+tbak(s)-tin(s);
40 rfront(s)+tc2(s) -ttot(s)+tc(s)+tair(s)+tbak(s)+t(s)+tlim(s)
+tfront(s);
41 rfront(s)+tc2(s) -ttot(s)+tc(s)+tair(s)+tbak(s)+t(s)+tlim(s);
42 rfront(s)+tc2(s) -ttot(s)+tc(s)+tair(s)+tbak(s)+t(s);
43 rfront(s)+tc2(s) -ttot(s)+tc(s)+tair(s)+tbak(s);
44 rfront(s)+tc2(s) -ttot(s)+tc(s)+tair(s)+tbak(s)-tin(s);
45 rfront(s)+tc2(s) -ttot(s)+tair(s)+tc(s);
46 rfront(s)+tc2(s) -ttot(s)+tc(s);
47 rfront(s)+tc2(s) -ttot(s);
48 rfront(s) -ttot(s);
49 r(s) -ttot(s);
50 rluft(s) -ttot(s);
51 tinr(s)+luft(s) -ttot(s);
52 tinr(s) -ttot(s);
53 0 -ttot(s);
54 0 -ttot(s)+tc(s);
55 tinr(s) -ttot(s)+tc(s);
56 tinr(s)+luft(s) -ttot(s)+tc(s);
57 0 0;
58 0 Rinf(s);
59 0 Rinf2(s);
60 Rinf(s)*sign(theta(1))*sin(theta(1))
Rinf(s)*sign(theta(1))*cos(theta(1));
61 Rinf2(s)*sign(theta(1))*sin(theta(1))
Rinf2(s)*sign(theta(1))*cos(theta(1));
```

```
62 Rinf(s)*sign(theta(2))*sin(theta(2))
Rinf(s)*sign(theta(2))*cos(theta(2));
63 Rinf2(s)*sign(theta(2))*sin(theta(2))
Rinf2(s)*sign(theta(2))*cos(theta(2));
64 Rinf(s)*sign(theta(3))*sin(theta(3))
Rinf(s)*sign(theta(3))*cos(theta(3));
65 Rinf2(s)*sign(theta(3))*sin(theta(3))
Rinf2(s)*sign(theta(3))*cos(theta(3));
66 Rinf(s)*sign(theta(4))*sin(theta(4))
Rinf(s)*sign(theta(4))*cos(theta(4));
67 Rinf2(s)*sign(theta(4))*sin(theta(4))
Rinf2(s)*sign(theta(4))*cos(theta(4));
68 Rinf(s)*sign(theta(5))*sin(theta(5))
Rinf(s)*sign(theta(5))*cos(theta(5));
69 Rinf2(s)*sign(theta(5))*sin(theta(5))
Rinf2(s)*sign(theta(5))*cos(theta(5));
70 Rinf(s)*sign(theta(6))*sin(theta(6))
Rinf(s)*sign(theta(6))*cos(theta(6));
71 Rinf2(s)*sign(theta(6))*sin(theta(6))
Rinf2(s)*sign(theta(6))*cos(theta(6));
72 Rinf(s)*sign(theta(7))*sin(theta(7))
Rinf(s)*sign(theta(7))*cos(theta(7));
73 Rinf2(s)*sign(theta(7))*sin(theta(7))
Rinf2(s)*sign(theta(7))*cos(theta(7));
74 Rinf(s)*sign(theta(8))*sin(theta(8))
Rinf(s)*sign(theta(8))*cos(theta(8));
75 Rinf2(s)*sign(theta(8))*sin(theta(8))
Rinf2(s)*sign(theta(8))*cos(theta(8));
76 Rinf(s)*sign(theta(9))*sin(theta(9))
Rinf(s)*sign(theta(9))*cos(theta(9));
77 Rinf2(s)*sign(theta(9))*sin(theta(9))
Rinf2(s)*sign(theta(9))*cos(theta(9));
78 Rinf(s)*sign(theta(10))*sin(theta(10))
Rinf(s)*sign(theta(10))*cos(theta(10));
79 Rinf2(s)*sign(theta(10))*sin(theta(10))
Rinf2(s)*sign(theta(10))*cos(theta(10));
80 Rinf(s)*sign(theta(11))*sin(theta(11))
Rinf(s)*sign(theta(11))*cos(theta(11));
81 Rinf2(s)*sign(theta(11))*sin(theta(11))
Rinf2(s)*sign(theta(11))*cos(theta(11));
82 Rinf(s)*sign(theta(12))*sin(theta(12))
Rinf(s)*sign(theta(12))*cos(theta(12));
83 Rinf2(s)*sign(theta(12))*sin(theta(12))
Rinf2(s)*sign(theta(12))*cos(theta(12));
84 Rinf(s)*sign(theta(13))*sin(theta(13))
Rinf(s)*sign(theta(13))*cos(theta(13));
85 Rinf2(s)*sign(theta(13))*sin(theta(13))
Rinf2(s)*sign(theta(13))*cos(theta(13));
86 Rinf(s)*sign(theta(14))*sin(theta(14))
Rinf(s)*sign(theta(14))*cos(theta(14));
87 Rinf2(s)*sign(theta(14))*sin(theta(14))
Rinf2(s)*sign(theta(14))*cos(theta(14));
88 Rinf(s)*sign(theta(15))*sin(theta(15))
Rinf(s)*sign(theta(15))*cos(theta(15));
89 Rinf2(s)*sign(theta(15))*sin(theta(15))
Rinf2(s)*sign(theta(15))*cos(theta(15));
90 Rinf(s)*sign(theta(16))*sin(theta(16))
Rinf(s)*sign(theta(16))*cos(theta(16));
```

```
91 Rinf2(s)*sign(theta(16))*sin(theta(16))
Rinf2(s)*sign(theta(16))*cos(theta(16));
92 Rinf(s)*sign(theta(17))*sin(theta(17))
Rinf(s)*sign(theta(17))*cos(theta(17));
93 Rinf2(s)*sign(theta(17))*sin(theta(17))
Rinf2(s)*sign(theta(17))*cos(theta(17));
94 Rinf(s)*sign(theta(18))*sin(theta(18))
Rinf(s)*sign(theta(18))*cos(theta(18));
95 Rinf2(s)*sign(theta(18))*sin(theta(18))
Rinf2(s)*sign(theta(18))*cos(theta(18));
96 0 -Rinf(s);
97 0 -Rinf2(s);
98 t1(s) -ttot(s)+tc(s)+tair(s);
99 t1(s) -ttot(s)+tc(s)+tair(s)+tbak(s)-tin(s);
100 t1(s) -ttot(s)+tc(s)+tair(s)+tbak(s);
101 t1(s) -ttot(s)+tc(s)+tair(s)+tbak(s)+t(s);
102 t1(s) -ttot(s)+tc(s)+tair(s)+tbak(s)+t(s)+tlim(s);
103 t1(s) -ttot(s)+tc(s)+tair(s)+tbak(s)+t(s)+tlim(s)+tfront(s);
104 Rinf(s)*sign(theta(19))*sin(theta(19))
Rinf(s)*sign(theta(19))*cos(theta(19));
105 Rinf2(s)*sign(theta(19))*sin(theta(19))
Rinf2(s)*sign(theta(19))*cos(theta(19));
106 t2(s) -ttot(s)+tc(s)+tair(s);
107 t2(s) -ttot(s)+tc(s)+tair(s)+tbak(s)-tin(s);
108 t2(s) -ttot(s)+tc(s)+tair(s)+tbak(s);
109 t2(s) -ttot(s)+tc(s)+tair(s)+tbak(s)+t(s);
110 t2(s) -ttot(s)+tc(s)+tair(s)+tbak(s)+t(s)+tlim(s);
111 t2(s) -ttot(s)+tc(s)+tair(s)+tbak(s)+t(s)+tlim(s)+tfront(s);
112 Rinf(s)*sign(theta(20))*sin(theta(20))
Rinf(s)*sign(theta(20))*cos(theta(20));
113 Rinf2(s)*sign(theta(20))*sin(theta(20))
Rinf2(s)*sign(theta(20))*cos(theta(20));
114 t1(s) -ttot(s)+tc(s)+tair(s)-t3(s);
115 t2(s) -ttot(s)+tc(s)+tair(s)-t3(s);
116 rluft(s) -ttot(s)+tc(s)+tair(s)-t3(s);
117 r(s) -ttot(s)+tc(s)+tair(s)-t3(s);
118 rfront(s) -ttot(s)+tc(s)+tair(s)-t3(s);
119 rfront(s)+tc2(s) -ttot(s)+tc(s)+tair(s)-t3(s);
120 Rinf(s)*sign(theta(21))*sin(theta(21))
Rinf(s)*sign(theta(21))*cos(theta(21));
121 Rinf2(s)*sign(theta(21))*sin(theta(21))
Rinf2(s)*sign(theta(21))*cos(theta(21));
 122 t2(s) -ttot(s)+tc(s)+tair(s)-t4(s);
123 rluft(s) -ttot(s)+tc(s)+tair(s)-t4(s);
124 r(s) -ttot(s)+tc(s)+tair(s)-t4(s);
125 rfront(s) -ttot(s)+tc(s)+tair(s)-t4(s);
126 rfront(s)+tc2(s) -ttot(s)+tc(s)+tair(s)-t4(s);
127 Rinf(s)*sign(theta(22))*sin(theta(22))
Rinf(s)*sign(theta(22))*cos(theta(22));
128 Rinf2(s)*sign(theta(22))*sin(theta(22))
Rinf2(s)*sign(theta(22))*cos(theta(22));
129 t1(s) -ttot(s)+tc(s);
130 t2(s) -ttot(s)+tc(s);
131 t1(s) -ttot(s);
132 t2(s) -ttot(s);
133 Rinf(s)*sign(theta(23))*sin(theta(23))
Rinf(s)*sign(theta(23))*cos(theta(23));
134 Rinf2(s)*sign(theta(23))*sin(theta(23))
```

```
Rinf2(s)*sign(theta(23))*cos(theta(23));
135 Rinf(s)*sign(theta(24))*sin(theta(24))
Rinf(s)*sign(theta(24))*cos(theta(24));
136 Rinf2(s)*sign(theta(24))*sin(theta(24))
Rinf2(s)*sign(theta(24))*cos(theta(24));
137 tinr(s) -ttot(s)+tc(s)+tair(s)-t3(s);
138 tinr(s)+luft(s) -ttot(s)+tc(s)+tair(s)-t3(s)];

        read.areas(:,:,s)=[1 6 100 101 11 elr(s) elr(s) 0 0;
            1 100 7 12 101 elr(s) elr(s) 0 0;
            1 7 8 13 12 elr(s) elr(s) 0 0;
            1 8 108 109 13 elr(s) elr(s) 0 0;
            1 108 14 15 109 elr(s) elr(s) 0 0;
            1 14 9 16 15 elr(s) elr(s) 0 0;
            2 11 101 102 18 elr(s) elr(s) 0 0;
            2 12 13 20 19 elr(s) elr(s) 0 0;
            2 101 12 19 102 elr(s) elr(s) 0 0;
            2 13 109 110 20 elr(s) elr(s) 0 0;
            2 109 15 21 110 elr(s) elr(s) 0 0;
            2 15 16 22 21 elr(s) elr(s) 0 0;
            2 16 17 23 22 elr(s) elr(s) 0 0;
            3 18 102 103 24 elr(s) elr(s) 0 0;
            3 102 19 25 103 elr(s) elr(s) 0 0;
            3 19 20 26 25 elr(s) elr(s) 0 0;
            3 20 110 111 26 elr(s) elr(s) 0 0;
            3 110 21 27 111 elr(s) elr(s) 0 0;
            3 21 22 28 27 elr(s) elr(s) 0 0;
            3 22 23 29 28 elr(s) elr(s) 0 0;
            5 1 99 100 6 elr(s) elr(s) 0 0;%4
            5 99 2 7 100 elr(s) elr(s) 0 0;%4
            5 9 10 17 16 elr(s) elr(s) 0 0;
            5 2 3 8 7 elr(s) elr(s) 0 0;
            5 3 107 108 8 elr(s) elr(s) 0 0;
            5 107 39 14 108 elr(s) elr(s) 0 0;
            5 39 4 9 14 elr(s) elr(s) 0 0;
            5 4 5 10 9 elr(s) elr(s) 0 0;
            5 30 98 99 1 elr(s) elr(s) 0 0;
            5 98 31 2 99 elr(s) elr(s) 0 0;
            5 31 32 3 2 elr(s) elr(s) 0 0;
            5 32 106 107 3 elr(s) elr(s) 0 0;
            5 106 33 39 107 elr(s) elr(s) 0 0;
            5 33 34 4 39 elr(s) elr(s) 0 0;
            5 34 35 5 4 elr(s) elr(s) 0 0;
            5 114 137 31 98 elr(s) elr(s) 0 0;
            5 137 138 32 31 elr(s) elr(s) 0 0;
            5 138 115 106 32 elr(s) elr(s) 0 0;
            5 115 116 33 106 elr(s) elr(s) 0 0;
            5 116 117 34 33 elr(s) elr(s) 0 0;
            5 117 118 35 34 elr(s) elr(s) 0 0;
            5 122 123 116 115 elr(s) elr(s) 0 0;
            5 123 124 117 116 elr(s) elr(s) 0 0;
            5 124 125 118 117 elr(s) elr(s) 0 0;
            5 36 37 124 123 elr(s) elr(s) 0 0;
            5 37 38 125 124 elr(s) elr(s) 0 0;
            6 23 41 40 29 elr(s) elr(s) 0 0;
            6 17 42 41 23 elr(s) elr(s) 0 0;
            6 10 43 42 17 elr(s) elr(s) 0 0;
            6 5 44 43 10 elr(s) elr(s) 0 0;
```

```
6 35 45 44 5 elr(s) elr(s) 0 0;
6 118 119 45 35 elr(s) elr(s) 0 0;
6 125 126 119 118 elr(s) elr(s) 0 0;
6 38 46 126 125 elr(s) elr(s) 0 0;
6 48 47 46 38 elr(s) elr(s) 0 0;
6 49 48 38 37 elr(s) elr(s) 0 0;
6 50 49 37 36 elr(s) elr(s) 0 0;
6 132 50 36 130 elr(s) elr(s) 0 0;
6 51 132 130 56 elr(s) elr(s) 0 0;
6 52 51 56 55 elr(s) elr(s) 0 0;
6 131 52 55 129 elr(s) elr(s) 0 0;
6 53 131 129 54 elr(s) elr(s) 0 0;
7 24 103 104 58 elr(s) elr(s) 0 57;
7 103 25 60 104 elr(s) elr(s) 0 57;
7 25 26 62 60 elr(s) elr(s) 0 57;
7 26 111 112 62 elr(s) elr(s) 0 57;
7 111 27 64 112 elr(s) elr(s) 0 57;
7 27 28 66 64 elr(s) elr(s) 0 57;
7 28 29 68 66 elr(s) elr(s) 0 57;
7 29 40 70 68 elr(s) elr(s) 0 57;
7 40 41 72 70 elr(s) elr(s) 0 57;
7 41 42 74 72 elr(s) elr(s) 0 57;
7 42 43 76 74 elr(s) elr(s) 0 57;
7 43 44 78 76 elr(s) elr(s) 0 57;
7 44 45 80 78 elr(s) elr(s) 0 57;
7 45 119 120 80 elr(s) elr(s) 0 57;
7 119 126 127 120 elr(s) elr(s) 0 57;
7 126 46 82 127 elr(s) elr(s) 0 57;
7 46 47 84 82 elr(s) elr(s) 0 57;
7 47 48 86 84 elr(s) elr(s) 0 57;
7 48 49 88 86 elr(s) elr(s) 0 57;
7 49 50 90 88 elr(s) elr(s) 0 57;
7 50 132 133 90 elr(s) elr(s) 0 57;
7 132 51 92 133 elr(s) elr(s) 0 57;
7 51 52 94 92 elr(s) elr(s) 0 57;
7 52 131 135 94 elr(s) elr(s) 0 57;
7 131 53 96 135 elr(s) elr(s) 0 57;
8 58 104 105 59 1 1 57 57;
8 104 60 61 105 1 1 57 57;
8 60 62 63 61 1 1 57 57;
8 62 112 113 63 1 1 57 57;
8 112 64 65 113 1 1 57 57;
8 64 66 67 65 1 1 57 57;
8 66 68 69 67 1 1 57 57;
8 68 70 71 69 1 1 57 57;
8 70 72 73 71 1 1 57 57;
8 72 74 75 73 1 1 57 57;
8 74 76 77 75 1 1 57 57;
8 76 78 79 77 1 1 57 57;
8 78 80 81 79 1 1 57 57;
8 80 120 121 81 1 1 57 57;
8 120 127 128 121 1 1 57 57;
8 127 82 83 128 1 1 57 57;
8 82 84 85 83 1 1 57 57;
8 84 86 87 85 1 1 57 57;
8 86 88 89 87 1 1 57 57;
8 88 90 91 89 1 1 57 57;
8 90 133 134 91 1 1 57 57;
```

```
                8 133 92 93 134 1 1 57 57;
                8 92 94 95 93 1 1 57 57;
                8 94 135 136 95 1 1 57 57;
                8 135 96 97 136 1 1 57 57];

            read.materials(:,:,s)=[1 glob.globvariables.piezo matnum(s);
                2 glob.globvariables.mechanic matnumlim(s);
                3 glob.globvariables.mechanic matnumfront(s);
                4 glob.globvariables.mechanic matnumtin(s);
                5 glob.globvariables.mechanic matnumbak(s);
                6 glob.globvariables.mechanic matnumstaal(s);
                7 glob.globvariables.fluid matnumf(s);
                8 glob.globvariables.infinitefluid matnumf(s)];

    read.dof(:,:,s)=[-1e-9 r(s)+1e-9 -ttot(s)+tc(s)+tbak(s)+t(s)+tair(s)-
    1e-9 -ttot(s)+tc(s)+tbak(s)+t(s)+tair(s)+1e-9 glob.free.ep];
    read.restraints(:,:,s)=[-1e-9 r(s)+1e-9 -ttot(s)+tc(s)+tbak(s)
    +tair(s)-1e-9 -ttot(s)+tc(s)+tbak(s)+tair(s)+1e-9 glob.free.ep 1];
    glob.tfront(s)=-ttot(s)+tbak(s)+t(s)+tfront(s)+tlim(s)+tair(s)+tc(s);

        end
end
end
```

A.1.2 Material file

```
        51      piezo                   Hcp70
# mechanical terms
 7.73289e+08 3.63923e+08 3.63923e+08 0.00000e+00 0.00000e+00 0.00000e+00
 3.63923e+08 7.73289e+08 3.63923e+08 0.00000e+00 0.00000e+00 0.00000e+00
 3.63923e+08 3.63923e+08 7.73289e+08 0.00000e+00 0.00000e+00 0.00000e+00
 0.00000e+00 0.00000e+00 0.00000e+00 2.04683e+08 0.00000e+00 0.00000e+00
 0.00000e+00 0.00000e+00 0.00000e+00 0.00000e+00 2.04683e+08 0.00000e+00
 0.00000e+00 0.00000e+00 0.00000e+00 0.00000e+00 0.00000e+00 2.04683e+08
# coupling terms
 0.00000e+00 0.00000e+00 0.00000e+00 0.00000e+00 0.00000e+00 0.00000e+00
 0.00000e+00 0.00000e+00 0.00000e+00 0.00000e+00 0.00000e+00 0.00000e+00
 0.00000e+00 0.00000e+00 0.00000e+00 0.00000e+00 0.00000e+00 0.00000e+00
# dielectric terms
 0.00000e+00 0.00000e+00 0.00000e+00
 0.00000e+00 0.00000e+00 0.00000e+00
 0.00000e+00 0.00000e+00 0.00000e+00
# density and damping coefficients
 3.00000e+02 2.50000e+01 0.00000e+00
# end of material data
        70      piezo                   mf114
# mechanical terms
 1.44281e+10 8.72813e+09 8.72813e+09 0.00000e+00 0.00000e+00 0.00000e+00
 8.72813e+09 1.44281e+10 8.72813e+09 0.00000e+00 0.00000e+00 0.00000e+00
 8.72813e+09 8.72813e+09 1.44281e+10 0.00000e+00 0.00000e+00 0.00000e+00
 0.00000e+00 0.00000e+00 0.00000e+00 2.85000e+09 0.00000e+00 0.00000e+00
 0.00000e+00 0.00000e+00 0.00000e+00 0.00000e+00 2.85000e+09 0.00000e+00
 0.00000e+00 0.00000e+00 0.00000e+00 0.00000e+00 0.00000e+00 2.85000e+09
# coupling terms
 0.00000e+00 0.00000e+00 0.00000e+00 0.00000e+00 0.00000e+00 0.00000e+00
 0.00000e+00 0.00000e+00 0.00000e+00 0.00000e+00 0.00000e+00 0.00000e+00
 0.00000e+00 0.00000e+00 0.00000e+00 0.00000e+00 0.00000e+00 0.00000e+00
# dielectric terms
```

```
 0.00000e+00 0.00000e+00 0.00000e+00
 0.00000e+00 0.00000e+00 0.00000e+00
 0.00000e+00 0.00000e+00 0.00000e+00
# density and damping coefficients
 2.85000e+03 2.00000e+01 0.00000e+00
# end of material data
        80      piezo                   steel
# mechanical terms
 2.67267e+11 1.18427e+11 1.18427e+11 0.00000e+00 0.00000e+00 0.00000e+00
 1.18427e+11 2.67267e+11 1.18427e+11 0.00000e+00 0.00000e+00 0.00000e+00
 1.18427e+11 1.18427e+11 2.67267e+11 0.00000e+00 0.00000e+00 0.00000e+00
 0.00000e+00 0.00000e+00 0.00000e+00 7.44200e+10 0.00000e+00 0.00000e+00
 0.00000e+00 0.00000e+00 0.00000e+00 0.00000e+00 7.44200e+10 0.00000e+00
 0.00000e+00 0.00000e+00 0.00000e+00 0.00000e+00 0.00000e+00 7.44200e+10
# coupling terms
 0.00000e+00 0.00000e+00 0.00000e+00 0.00000e+00 0.00000e+00 0.00000e+00
 0.00000e+00 0.00000e+00 0.00000e+00 0.00000e+00 0.00000e+00 0.00000e+00
 0.00000e+00 0.00000e+00 0.00000e+00 0.00000e+00 0.00000e+00 0.00000e+00
# dielectric terms
 0.00000e+00 0.00000e+00 0.00000e+00
 0.00000e+00 0.00000e+00 0.00000e+00
 0.00000e+00 0.00000e+00 0.00000e+00
# density and damping coefficients
 8.00000e+03 1.00000e+03 0.00000e+00
# end of material data
         2      piezo                   aanes_piezoelectric_constants
# mechanical terms
 1.20250e+11 7.62000e+10 7.42000e+10 0.00000e+00 0.00000e+00 0.00000e+00
 7.62000e+10 1.20250e+11 7.42000e+10 0.00000e+00 0.00000e+00 0.00000e+00
 7.42000e+10 7.42000e+10 1.10050e+11 0.00000e+00 0.00000e+00 0.00000e+00
 0.00000e+00 0.00000e+00 0.00000e+00 2.11000e+10 0.00000e+00 0.00000e+00
 0.00000e+00 0.00000e+00 0.00000e+00 0.00000e+00 2.11000e+10 0.00000e+00
 0.00000e+00 0.00000e+00 0.00000e+00 0.00000e+00 0.00000e+00 2.22250e+10
# coupling terms
 0.00000e+00 0.00000e+00 0.00000e+00 0.00000e+00 1.12000e+01 0.00000e+00
 0.00000e+00 0.00000e+00 0.00000e+00 1.12000e+01 0.00000e+00 0.00000e+00
-5.40000e+00 -5.40000e+00 1.70000e+01 0.00000e+00 0.00000e+00 0.00000e+00
# dielectric terms
 8.11044e-09 0.00000e+00 0.00000e+00
 0.00000e+00 8.11044e-09 0.00000e+00
 0.00000e+00 0.00000e+00 8.14585e-09
# density and damping coefficients
 7.70000e+03 9.99000e+02 9.99000e+02
# mechanical Q-factors
 9.60000e+01 7.00000e+01 1.20000e+02 0.00000e+00 0.00000e+00 0.00000e+00
 7.00000e+01 9.60000e+01 1.20000e+02 0.00000e+00 0.00000e+00 0.00000e+00
 1.20000e+02 1.20000e+02 1.90000e+02 0.00000e+00 0.00000e+00 0.00000e+00
 0.00000e+00 0.00000e+00 0.00000e+00 7.50000e+01 0.00000e+00 0.00000e+00
 0.00000e+00 0.00000e+00 0.00000e+00 0.00000e+00 7.50000e+01 0.00000e+00
 0.00000e+00 0.00000e+00 0.00000e+00 0.00000e+00 0.00000e+00 2.25342e+02
# piezoelectric Q-factors
 0.00000e+00 0.00000e+00 0.00000e+00 0.00000e+00 -2.00000e+02 0.00000e+00
 0.00000e+00 0.00000e+00 0.00000e+00 -2.00000e+02 0.00000e+00 0.00000e+00
-1.66000e+02 -1.66000e+02 -3.24000e+02 0.00000e+00 0.00000e+00 0.00000e+00
# dielectric Q-factors
 5.00000e+01 0.00000e+00 0.00000e+00
 0.00000e+00 5.00000e+01 0.00000e+00
 0.00000e+00 0.00000e+00 1.30000e+02
```

```
# end of material data
        30      piezo                   conductive_adhesive
# mechanical terms
 6.76260e+09 2.08290e+09 2.08290e+09 0.00000e+00 0.00000e+00 0.00000e+00
 2.08290e+09 6.76260e+09 2.08290e+09 0.00000e+00 0.00000e+00 0.00000e+00
 2.08290e+09 2.08290e+09 6.76260e+09 0.00000e+00 0.00000e+00 0.00000e+00
 0.00000e+00 0.00000e+00 0.00000e+00 2.34000e+09 0.00000e+00 0.00000e+00
 0.00000e+00 0.00000e+00 0.00000e+00 0.00000e+00 2.34000e+09 0.00000e+00
 0.00000e+00 0.00000e+00 0.00000e+00 0.00000e+00 0.00000e+00 2.34000e+09
# coupling terms
 0.00000e+00 0.00000e+00 0.00000e+00 0.00000e+00 0.00000e+00 0.00000e+00
 0.00000e+00 0.00000e+00 0.00000e+00 0.00000e+00 0.00000e+00 0.00000e+00
 0.00000e+00 0.00000e+00 0.00000e+00 0.00000e+00 0.00000e+00 0.00000e+00
# dielectric terms
 0.00000e+00 0.00000e+00 0.00000e+00
 0.00000e+00 0.00000e+00 0.00000e+00
 0.00000e+00 0.00000e+00 0.00000e+00
# density and damping coefficients
 2.34000e+03 5.00000e+01 0.00000e+00
# end of material data
       100      fluid                   water
 1.00000e+03 2.20523e+09 0.00000e+00 0.00000e+00
# end of material data
        90      piezo                   tungstenepoxy11.9MRayl
# mechanical terms
 2.85805e+10 1.42903e+10 1.42903e+10 0.00000e+00 0.00000e+00 0.00000e+00
 1.42903e+10 2.85805e+10 1.42903e+10 0.00000e+00 0.00000e+00 0.00000e+00
 1.42903e+10 1.42903e+10 2.85805e+10 0.00000e+00 0.00000e+00 0.00000e+00
 0.00000e+00 0.00000e+00 0.00000e+00 7.14512e+09 0.00000e+00 0.00000e+00
 0.00000e+00 0.00000e+00 0.00000e+00 0.00000e+00 7.14512e+09 0.00000e+00
 0.00000e+00 0.00000e+00 0.00000e+00 0.00000e+00 0.00000e+00 7.14512e+09
# coupling terms
 0.00000e+00 0.00000e+00 0.00000e+00 0.00000e+00 0.00000e+00 0.00000e+00
 0.00000e+00 0.00000e+00 0.00000e+00 0.00000e+00 0.00000e+00 0.00000e+00
 0.00000e+00 0.00000e+00 0.00000e+00 0.00000e+00 0.00000e+00 0.00000e+00
# dielectric terms
 0.00000e+00 0.00000e+00 0.00000e+00
 0.00000e+00 0.00000e+00 0.00000e+00
 0.00000e+00 0.00000e+00 0.00000e+00
# density and damping coefficients
 9.82000e+03 1.10000e+01 0.00000e+00
# end of material data
        95      piezo               tungstenepoxy16.8MRayl
# mechanical terms
 1.91232e+10 9.56140e+09 9.56140e+09 0.00000e+00 0.00000e+00 0.00000e+00
 9.56140e+09 1.91232e+10 9.56140e+09 0.00000e+00 0.00000e+00 0.00000e+00
 9.56140e+09 9.56140e+09 1.91232e+10 0.00000e+00 0.00000e+00 0.00000e+00
 0.00000e+00 0.00000e+00 0.00000e+00 4.78090e+09 0.00000e+00 0.00000e+00
 0.00000e+00 0.00000e+00 0.00000e+00 0.00000e+00 4.78090e+09 0.00000e+00
 0.00000e+00 0.00000e+00 0.00000e+00 0.00000e+00 0.00000e+00 4.78090e+09
# coupling terms
 0.00000e+00 0.00000e+00 0.00000e+00 0.00000e+00 0.00000e+00 0.00000e+00
 0.00000e+00 0.00000e+00 0.00000e+00 0.00000e+00 0.00000e+00 0.00000e+00
 0.00000e+00 0.00000e+00 0.00000e+00 0.00000e+00 0.00000e+00 0.00000e+00
# dielectric terms
 0.00000e+00 0.00000e+00 0.00000e+00
 0.00000e+00 0.00000e+00 0.00000e+00
 0.00000e+00 0.00000e+00 0.00000e+00
```

```
# density and damping coefficients
 7.47000e+03 1.35000e+01 0.00000e+00
# end of material data
        91      piezo               tungstenepozy8.7MRayl
# mechanical terms
 1.39158e+10 6.14132e+09 6.14132e+09 0.00000e+00 0.00000e+00 0.00000e+00
 6.14132e+09 1.39158e+10 6.14132e+09 0.00000e+00 0.00000e+00 0.00000e+00
 6.14132e+09 6.14132e+09 1.39158e+10 0.00000e+00 0.00000e+00 0.00000e+00
 0.00000e+00 0.00000e+00 0.00000e+00 3.88725e+09 0.00000e+00 0.00000e+00
 0.00000e+00 0.00000e+00 0.00000e+00 0.00000e+00 3.88725e+09 0.00000e+00
 0.00000e+00 0.00000e+00 0.00000e+00 0.00000e+00 0.00000e+00 3.88725e+09
# coupling terms
 0.00000e+00 0.00000e+00 0.00000e+00 0.00000e+00 0.00000e+00 0.00000e+00
 0.00000e+00 0.00000e+00 0.00000e+00 0.00000e+00 0.00000e+00 0.00000e+00
 0.00000e+00 0.00000e+00 0.00000e+00 0.00000e+00 0.00000e+00 0.00000e+00
# dielectric terms
 0.00000e+00 0.00000e+00 0.00000e+00
 0.00000e+00 0.00000e+00 0.00000e+00
 0.00000e+00 0.00000e+00 0.00000e+00
# density and damping coefficients
 5.47000e+03 2.85000e+01 0.00000e+00
# end of material data
        92      piezo               tungstenepoxy10.1MRayl
# mechanical terms
 1.58184e+10 7.90920e+09 7.90920e+09 0.00000e+00 0.00000e+00 0.00000e+00
 7.90920e+09 1.58184e+10 7.90920e+09 0.00000e+00 0.00000e+00 0.00000e+00
 7.90920e+09 7.90920e+09 1.58184e+10 0.00000e+00 0.00000e+00 0.00000e+00
 0.00000e+00 0.00000e+00 0.00000e+00 3.95460e+09 0.00000e+00 0.00000e+00
 0.00000e+00 0.00000e+00 0.00000e+00 0.00000e+00 3.95460e+09 0.00000e+00
 0.00000e+00 0.00000e+00 0.00000e+00 0.00000e+00 0.00000e+00 3.95460e+09
# coupling terms
 0.00000e+00 0.00000e+00 0.00000e+00 0.00000e+00 0.00000e+00 0.00000e+00
 0.00000e+00 0.00000e+00 0.00000e+00 0.00000e+00 0.00000e+00 0.00000e+00
 0.00000e+00 0.00000e+00 0.00000e+00 0.00000e+00 0.00000e+00 0.00000e+00
# dielectric terms
 0.00000e+00 0.00000e+00 0.00000e+00
 0.00000e+00 0.00000e+00 0.00000e+00
 0.00000e+00 0.00000e+00 0.00000e+00
# density and damping coefficients
 6.50000e+03 1.50000e+01 0.00000e+00
# end of material data
        1       piezo               knappskog_piezoelectricconstants
# mechanical terms
 1.18750e+11 7.43000e+10 7.42500e+10 0.00000e+00 0.00000e+00 0.00000e+00
 7.43000e+10 1.18750e+11 7.42500e+10 0.00000e+00 0.00000e+00 0.00000e+00
 7.42500e+10 7.42500e+10 1.12050e+11 0.00000e+00 0.00000e+00 0.00000e+00
 0.00000e+00 0.00000e+00 0.00000e+00 2.11000e+10 0.00000e+00 0.00000e+00
 0.00000e+00 0.00000e+00 0.00000e+00 0.00000e+00 2.11000e+10 0.00000e+00
 0.00000e+00 0.00000e+00 0.00000e+00 0.00000e+00 0.00000e+00 2.16000e+10
# coupling terms
 0.00000e+00 0.00000e+00 0.00000e+00 0.00000e+00 1.12000e+01 0.00000e+00
 0.00000e+00 0.00000e+00 0.00000e+00 1.12000e+01 0.00000e+00 0.00000e+00
-5.40000e+00 -5.40000e+00 1.60389e+01 0.00000e+00 0.00000e+00 0.00000e+00
# dielectric terms
 8.11044e-09 0.00000e+00 0.00000e+00
 0.00000e+00 8.11044e-09 0.00000e+00
 0.00000e+00 0.00000e+00 8.14585e-09
# density and damping coefficients
```

```
 7.70000e+03 9.99000e+02 9.99000e+02
# mechanical Q-factors
 9.57500e+01 7.12400e+01 1.20190e+02 0.00000e+00 0.00000e+00 0.00000e+00
 7.12400e+01 9.57500e+01 1.20190e+02 0.00000e+00 0.00000e+00 0.00000e+00
 1.20190e+02 1.20190e+02 1.77990e+02 0.00000e+00 0.00000e+00 0.00000e+00
 0.00000e+00 0.00000e+00 0.00000e+00 7.50000e+01 0.00000e+00 0.00000e+00
 0.00000e+00 0.00000e+00 0.00000e+00 0.00000e+00 7.50000e+01 0.00000e+00
 0.00000e+00 0.00000e+00 0.00000e+00 0.00000e+00 0.00000e+00 3.15010e+02
# piezoelectric Q-factors
 0.00000e+00 0.00000e+00 0.00000e+00 0.00000e+00 -2.00000e+02 0.00000e+00
 0.00000e+00 0.00000e+00 0.00000e+00 -2.00000e+02 0.00000e+00 0.00000e+00
-1.66000e+02 -1.66000e+02 -3.23770e+02 0.00000e+00 0.00000e+00 0.00000e+00
# dielectric Q-factors
 5.00000e+01 0.00000e+00 0.00000e+00
 0.00000e+00 5.00000e+01 0.00000e+00
 0.00000e+00 0.00000e+00 8.62800e+01
# end of material data
        83      piezo                   solder
# mechanical terms
 7.31741e+10 4.22431e+10 4.22431e+10 0.00000e+00 0.00000e+00 0.00000e+00
 4.22431e+10 7.31741e+10 4.22431e+10 0.00000e+00 0.00000e+00 0.00000e+00
 4.22431e+10 4.22431e+10 7.31741e+10 0.00000e+00 0.00000e+00 0.00000e+00
 0.00000e+00 0.00000e+00 0.00000e+00 1.54655e+10 0.00000e+00 0.00000e+00
 0.00000e+00 0.00000e+00 0.00000e+00 0.00000e+00 1.54655e+10 0.00000e+00
 0.00000e+00 0.00000e+00 0.00000e+00 0.00000e+00 0.00000e+00 1.54655e+10
# coupling terms
 0.00000e+00 0.00000e+00 0.00000e+00 0.00000e+00 0.00000e+00 0.00000e+00
 0.00000e+00 0.00000e+00 0.00000e+00 0.00000e+00 0.00000e+00 0.00000e+00
 0.00000e+00 0.00000e+00 0.00000e+00 0.00000e+00 0.00000e+00 0.00000e+00
# dielectric terms
 0.00000e+00 0.00000e+00 0.00000e+00
 0.00000e+00 0.00000e+00 0.00000e+00
 0.00000e+00 0.00000e+00 0.00000e+00
# density and damping coefficients
 8.74300e+03 0.00000e+00 0.00000e+00
# end of material data
```

A.1.3 Inn-file

```
set
r,8.08537e-3
t,3.97299e-3
tfront,1.12315e-3
rfront,11.5157e-3
end

materialfile
34
end

piezodiskfrontlim
r,t,rfront,tfront,3,1,70,0.03561e-3,30,45.01e-3,95,83,0.03e-3,0.03e-3
end

meshingtype
elementsperwavelength,1e6
end
```

```
#viewmesh
#1
#end

#The order of the finite elements is 2 - i.e. 8 node isoparametric elements
#are applied
order
2
end

#The order of the infinite elements is set to 12.
infiniteorder
12
end

directharmonicanalysis
0,1e3,1e6,complex_loss
end

admittance
0,0,0
end

sensitivity
0,0,0,1
end

directivity
0,0,0,1
end

save
admittance,admittance_f,sensitivity,sensitivity_f,
directivity,directivity_f,directivity_theta
end
```

A.2 MATLAB Scripts used for electrical measurements

The electrical measurements were performed using the MATLAB script impanal.m, provided by the supervisors.

A.2.1 Impanal.m

```
clear all
clc
close all
instrreset
vinfo = instrhwinfo('visa','agilent');
%% vinfo = instrhwinfo('visa','agilent','gpib');
%% vinfo = instrhwinfo('gpib','ni');
%% vinfo = instrhwinfo('visa','ni'); Er ikke installert!
vinfo.ObjectConstructorName

% fff = instrfind;    %sterkere versjon av instrreset
% if ~isempty(fff);pause(0.1);fclose(fff);pause(0.1);delete(fff);end
% instrreset
% clear
```

```
% obj1 = visa('agilent','GPIB0::0::1::INSTR');
obj1 = visa('agilent','GPIB0::17::INSTR');
% obj1 = gpib('NI', 0, 17);
% obj1 = gpib('agilent', 0, 1);
% obj1 = gpib('NI', 1, 17);


% Connect to instrument object, obj1.
fopen(obj1);
fprintf(obj1, 'V1');

    %%%%%%%%%%%%%%%%%%%%%%%%%%%%%%%%%%%%%%%%%%%%%%%%%%%%%%%%%%%%%%%%%%%%%%%

     % Osc. level [V]
     amplitude = 0.3;


f = [1e3:100:1000e3]/1e3;
% f = [50e3:5e3:300e3]./5e3;


     %%%%%%%%%%%%%%%%%%%%%%%%%%%%%%%%%%%%%%%%%%%%%%%%%%%%%%%%%%%%%%%%%%%%%%%
     ol = sprintf('%3.3f',amplitude);
     % Sett analysator i mode for admittans-mÃ¥ling
     fprintf(obj1, ['A2C3F1OL',ol,'EN']);

     % Tids-streng pÃ¥ format yyyymmddHHMMSS
     time = datestr(now, 'yyyymmddHHMMSS');
     % Tittelen som mÃ¥lingen blir lagra under

     i = 1;
     ii = 1;
     antal = length(f);
     g = ones(1,antal);
     b = ones(1,antal);
     fr = ones(1,antal);
     disp([num2str(antal),' frekvensar.'])
     disp('Starter mÃ¥ling...')
     for freq = f
          percent = i/antal*100;
          if percent >= ii*10
               disp([num2str(ii*10),' %'])
               ii = ii + 1;
          end

          %disp(['Frekvens (',num2str(i),' av ',num2str(antal),'): '
          %, num2str(freq), ' kHz'])
          s = sprintf('%3.3f',freq);
          fprintf(obj1, ['FR',s,'ENEX']);
          pause(0.1)
          data1 = fscanf(obj1);
          d=sscanf(data1,'%4c%f,%4c%f,%2c%f');
          g(i)=d(5);b(i)=d(10);fr(i)=d(13);
          i = i + 1;
     end
     disp('MÃ¥ling ferdig.')
     disp('Lagrer data...')
     stoptime = datestr(now, 'yyyymmddHHMMSS');
```

```
save(stoptime,'g','b','fr')
disp('Ferdig!')
```

A.3 MATLAB Scripts used for acoustical measurements

The acoustical measurements, the source sensitivity and beam pattern were performed by using MATLAB scripts provided by the supervisors and scripts given in [1].

A.3.1 Main program for the source sensitivity measurements

```
addpath(genpath(pwd));
disp('Source sensitivity using hydrophone!');
disp('Commencing calculation of source sensitivity');
d = 0.885; % Avstand mellom lydkilde og hydrofon (i m)
amp_faktor = 45.74; % [dB] Forsterkning i HVA-10M-60-F
%delta_amp = 20.24; % [dB] delta mellom 40/60 dB. (mÃČÂělt ved 500kHz)
delta_amp = 0;
temperatur = 23; % Temperatur (i C)
% Steady-state omrÃČÂěde for spenning inn pÃČÂě sendertransduser (v1)
grense1 = 24000;
grense2 = 34000;
% Steady-state omrÃČÂěde for spenning ut fra forsterker (v2)
grense3 = 30000;
grense4 = 40000;
disp('Loading measurement data...');
%% PROGRAM
load elektrisk0802121001step.mat

resultatV1 = resultat;
fv1 = frekvens;
tidsskala1 = tidsskala;
load akustisk0802121001step.mat
resultatV2 = resultat;
fv2 = frekvens;
tidsskala2 = tidsskala;
disp('Done!');
disp('Method for calculating voltage amplitude:');
valg2 = input('[FFT = 1] [MAXMIN = 2]');
disp('Calculating voltage amplitudes...');
if valg2 == 1
% FFT-metode fra Halvor for ÃČÂě finne amplitude, modifisert
[v1,v2,serie1,serie2] = fftamplitude(resultatV1,fv1,resultatV2,fv2,grense1
,grense2,grense3,grense4,tidsskala1,tidsskala2);
disp('Done!');
else if valg2 == 2
% %%---MAKS PEAK-PEAK AV SPENNING UT OG INN---%%
[v1,v2] = maxmin(resultatV1,fv1,resultatV2,fv2,grense1,grense2,grense3,grense4);

end
disp('Done!');
end
if length(fv1)>length(fv2)
f = fv2;
else f = fv1;
end
disp('');
valg1 = input('End-of-cable free field loaded sensitivity by [1]-UiB or [2]-NPL: ');
```

```
% End-of-cable free field loaded sensitivity! DCC terminated with 50 ohm
% before high impedance amplifier.
if valg1 == 1
[M_ref] = frekresponsPA_MIN(f);
else if valg1 == 2
[M_ref] = frekresponsPA_NPL(f);
end
end
amp = 10^((amp_faktor+delta_amp)/20);
V = v2/amp; %v2 er i peak2peak
% Korrigerer for forsterkning i HK-filteret
V = V./frekresponsHK(f);
% Trykk ved hydrofon (peak2peak)
p = V./M_ref;
disp('Calculating␣source␣sensitivity␣at␣1␣m...');
absorb = absorbsjonvann(f,temperatur,0);
p_m=p./(exp(0.1151*absorb*d/1000));
% Trykk ved 1 m
d0 = 1;
p_1m = p*d/d0;
% KildefÃČ Ìğlsomhet Sv
Sv=p_1m./v1;
% KildefÃČ Ìğlsomheten gitt i dB re 1V/Pa
Svlg = 20*log10(abs(Sv));
save akustiskSVhyd.mat f Sv Svlg
disp('Done!');
%%%%%%%%%%%%%%%%%%%%%%%%%%%%%%%%%%%%%%%%%%%%%%%%%%%%%%%%%%%%%%%%%%%%%%%%%%%%%%%%
```

A.3.2 Calculation of the source sensitivity

```
%% Program for akustiske maalinger i vanntank
% Magne Aanes, juli 2011
% Programmet kjorer gjennom spesifisert frekvensomraade
% og henter ut data fra valgfritt skop
% Bruk 'instrreset' hvis programmet bryter for det avsluttes skikkelig
%%--------------------------------BRUKER---------------------------------%%
pw = pwd;
addpath(genpath(pw));
% Frekvensomraadet en onsker aa undersoke
fstart = 200e3;
fstep = 1e3;
fstop = 1000e3;
burst_rate = 50; % Tid(i Hz) mellom hver burst
voltinn = 10; % Spenning paa innsignal fra generatoren(pk)
samples = 100e3; % antall samples paa skop
ch=1; % Lese fra kanal 1 paa skop
average = 256; % antall midling paa skop
meas = 1; % Tid for midling
%%----------------------------------------------------------------------%%
%%----------------------------------------------------------------------%%

ud_signal = visa('ni', 'GPIB0::12::INSTR');
fopen(ud_signal);
ScopeOffset_par.OffsetMethod='ScopeZero'; %mode, mean, ScopeZero, Fourier
ScopeOffset_par.SampleMethod='sample'; %sample, time, periods, auto
ScopeOffset_par.StartStop=[1 100000];
% ScopeOffset_par.Freq= 500e3; %frequency
```

```
ud_skop = visa('keysight','USB0::0x0699::0x0410::C010246::0::INSTR'); % defekt?
ud_skop.InputBufferSize = samples;
ud_skop.OutputBufferSize = samples;

fopen(ud_skop);
fprintf(ud_signal,['BM:INT:RATE␣' num2str(burst_rate)]);
fprintf(ud_signal,['VOLT␣' num2str(voltinn)]);
fprintf(ud_skop,'ACQ:MOD␣AVE');
fprintf(ud_skop,['ACQ:NUMAV␣' num2str(average)]);
fprintf(ud_skop,['HOR:RECO␣' num2str(samples)]);
fprintf(ud_skop,'DAT:START␣1');
fprintf(ud_skop,['DAT:STOP␣' num2str(samples)]);
fprintf(ud_skop,'TRIG:A:TYP␣EDG;A:EDGE:AUX');
fprintf(ud_skop,'TRIG:A:TYP␣EDG');
resultat = {};
frekvens = [];
f = fstart;
i = 1;
% Avstand til forste kant paa PA hydrofon er 26 mm --> 18 pulser ved 500 kHz
%t = 30e-6;
% Avstand til stang - 170 mm --> 225ÃĆÎijs
%t = 225e-6;
% Pulslengde lang, 60 pulser ved 500 kHz
t = 130e-6;
disp('Commencing␣measurements')
%% Innhenting av data fra skop og sweeping av frekvensomraadet
while f <= fstop;
    disp(f)
    fprintf(ud_signal,['BM:NCYC␣', num2str(ceil(f*t))]);
    fprintf(ud_signal,['FREQ␣', num2str(f)]);
    pause(2);
    [tid{1},resultat{i},tidsskala] = adjustAmplitude(ch,ud_skop,meas,samples);
    frekvens(i) = f;
    ant_peri(i) = ceil(f*t);
    f = f + fstep;
    i = i + 1;
end
disp('Done!');
disp('Saving␣data␣to␣file...');
save 16-5.mat tid resultat frekvens tidsskala ant_peri
disp('Done!');
%%%%%%%%%%%%%%%%%%%%%%%%%%%%%%%%%%%%%%%%%%%%%%%%%%%%%%%%%%%%%%%%%%%%%%%%%%%%%%%%%%%%%%%%%%%%%%%%%%%%%%%%

%addpaths;
%% BRUKER
```

A.3.3 Directivity measurements

```
% %% Sletting og addpath
% instrreset    % sletter alle lagrede instrumentobjekt
% clear         % sletter data
% clear path
% addpath(genpath('../../../subRutines'))
pw = pwd;
addpath(genpath(pw));

%% Aktuelle input verdier
```

```
DPORead_par.Samples = 100e3; % antall samples pï£¡ skop
DPORead_par.Ch=1; % Lese fra kanal 2 pï£¡ skop
DPORead_par.Average = 256;
DPORead_par.burst_rate = 50;
DPORead_par.screenRows = 4;
DPORead_par.verticalScalings = [1e-3 10];

ScopeOffset_par.OffsetMethod='ScopeZero';  %mode,mean,ScopeZero,Fourier
ScopeOffset_par.SampleMethod='sample';  %sample, time, periods, auto
ScopeOffset_par.StartStop=[1 100000];
% ScopeOffset_par.Freq= 500e3;  %frequency


id_scope = visa('keysight','USB0::0x0699::0x0410::C010246::0::INSTR');
id_scope.InputBufferSize = DPORead_par.Samples;
id_scope.OutputBufferSize = DPORead_par.Samples;
id_sig = visa('agilent', 'GPIB0::12::INSTR');

freq = 520e3;
timeSig_gen = 130e-6;

vinkel_step = 0.1;     % grader
vinkel_ends = 45;
vinkler = -vinkel_ends:vinkel_step:vinkel_ends;

%% Program starts

fopen(id_sig);
    fprintf(id_sig,['FREQ ', num2str(freq)]);
    fprintf(id_sig,['BM:NCYC ', num2str(ceil(freq*timeSig_gen))]);
fclose(id_sig);

% First_step = vinkler(2)-vinkler(1);
Micosstep(vinkler(1),2,0)
for ii = 1:length(vinkler)
    ii
    read_tmp = adjustAmplitudeScope_rev02(id_scope,DPORead_par,
    ScopeOffset_par);
    wf_save{ii} = read_tmp{2};
    x_save{ii} = read_tmp{1};
    Micosstep(vinkel_step,2,0)
end

Back_to_start = (floor(length(vinkler)/2)+1)*vinkel_step;
Micosstep(-Back_to_start,2,0)

% samleRate = query(id_scope,'HORizontal:MAIn:SAMPLERate?');

%% saving parameters
save Directivity_save.mat wf_save x_save freq vinkler

clear
% addpath(genpath('../../subRutines'))
addpath(genpath(pwd));

%% load file
load('O:/Documents/Program_Students/Directivity_save.mat');
vinkler = vinkler;
x_wa = x_save;
```

```
wf_wa = wf_save;

%% other

 SampleInfoStruct.Both = 'Aanes';
 SampleInfoStruct.StartVal = 30e3;
 SampleInfoStruct.EndVal = 50e3;
 SigStruct.SigFreq = freq;


%% Program starts

for ii = 1:length(vinkler)
% ii= 71 ;

 SigStruct.x = x_wa{ii};
 SigStruct.y = wf_wa{ii};

CutOffIndxs = find_index_in_sig_advanced(SigStruct,SampleInfoStruct); % helt
%antall perioder starter pÃě
Sig_wa_reg = SigStruct.y(SampleInfoStruct.StartVal : CutOffIndxs(3));

Y_k_tmp = fourier_transform(SigStruct.x,Sig_wa_reg,1);
Y_k(ii) = max(abs(Y_k_tmp{2}(2:end)));


% SigStruct.periodFracJump =1/16;
% PeakInfo = findPeaksAndZeros(SigStruct.x,Sig_wa_reg,SigStruct.SigFreq,
 SigStruct.periodFracJump);
%  peak_peak(ii) = PeakInfo{12};
end
```

A.3.4 Micosstep.m

```
%%%%%%%%%%%%%%%%%%%%%%%%%%%%%%%%%%%%%%%%%%%%%%%%%%%%%%%%%%%%%%%%%%%%%%%%%%%
% Skript som styrer Micos-motorer.
% Fungerer pÃě Matlab/Windows.
% Espen Storheim, 08/07-2009
% Magne Aanes, 28.04.2011 - modifisert
% Mathias SÃęther, feb 2019 - modifisert
%%%%%%%%%%%%%%%%%%%%%%%%%%%%%%%%%%%%%%%%%%%%%%%%%%%%%%%%%%%%%%%%%%%%%%%%%%%

% g: antall grader eller posisjon i mm
% a:    1: mottaker transverselt,    2: sender rotasjon
% m:    bevegelse relativ m=0   bevegelse absolutt m=1
% g = 20;
% a = 1;
% m = 0;

function Micosstep(g,a,m)

% KORT FORKLARING:
% Dette skriptet styrar Micos DT-80 (2008/04) rotasjonsmotoren som finns
% pÃě akustikklaben. Argument som trengs er lista nedanfor.
%
% g er antal grader (positiv eller negativ), Mp vÃęre en streng + X.0 i mm
% a er aksen (1),0
% m = 0 -> relativ rÃÿyrsle,
```

```
% m = 1 -> absolutt rÃÿyrsle.

% Standardinnstillingar dersom ein berre oppgir vinkelen i argumentet til skriptet:
if (nargin < 3)
    a = 1;  % Akse 1 er default.
    m = 0;  % Relativ step (r) er default.
else
end

global s1   % Brukar handtaket frÃě Micosinitialisering.m.

% Setter bevegelsestype (absolutt eller relativ).
if (m==0)
    cmd = [num2str(g) ' ' num2str(a) ' nr'];
else (m==1)
    cmd = [num2str(g) ' ' num2str(a) ' nm'];
end

fprintf(s1,cmd);


%% SÃętther mars 2021 "beveger_seg"  transverselt!!!   kan kanskje variere??
ff = 0;
% go_tmp = 0;
test_cnt = 1;
while true
    pause(0.1)
    beveger_seg = MotorSend(s1,[num2str(a) ' nst']);
    ttt{test_cnt} = beveger_seg;
    number = str2num(beveger_seg);

    test_cnt = test_cnt+1;
    ff(test_cnt) = number;
    if (number ==32 || number ==36)
        return
    end
end


end
```

A.3.5 Parkerstep.m

```
%%%%%%%%%%%%%%%%%%%%%%%%%%%%%%%%%%%%%%%%%%%%%%%%%%%%%%%%%%%%%%%%%%%%%%%%%%%%%%%%
% Skript som kjÃÿrer motorane ein gitt distanse,
her konvertert til mm. Input i denne funksjonen er
%distanse og motor nummer. Dette forutset at skriptet
% Parkerinitiering.m er brukt i forkant slik at
%motorane er klar til bruk.
% Espen Storheim, 08/07-2009.
% Magne Aanes, 28.04.2011 - modifisert
% Mathias SÃętther, feb 2019 - modifisert
%%%%%%%%%%%%%%%%%%%%%%%%%%%%%%%%%%%%%%%%%%%%%%%%%%%%%%%%%%%%%%%%%%%%%%%%%%%%%%%%

% n = akse
% n = 1: langs tank
% n = 2: hÃÿyde
% d = avstand i mm
```

```
function Parkerstep(d,n)
global s2

% Konverterar distanse til antal step.

if (nargin ==1)
        n = 1;
else
end

% Konverterar distanse til antal step.
a1 = 1.250e-3;
a2 = 1.250e-3;

if (n == 1)
    d = d/a1;
else
    d = d/a2;
end
% Klargjer motoren.
cmd = [num2str(n) 'D' num2str(d)];
fprintf(s2,cmd);
fscanf(s2);

% KjÃ¿rar steget.
fprintf(s2,[num2str(n) 'G']);
fscanf(s2);

% Sjekker hvortid motor er ferdig med Ãě kjÃ¿re
beveger_seg = 1;
while beveger_seg == 1
    midlertidig = MotorSend(s2,[num2str(n) 'R(MV)']);
    midlertidig = fscanf(s2);
    beveger_seg = str2num(midlertidig(3:end));
    if beveger_seg == 0
        break;
    end
end
end
```

A.3.6 Frequency response of the hydrophone

```
function [M_ref] = frekresponsPA_MIN(f)
%##############
%
% Frequency response of a 1 mm PVDF needle hydrophone with submersible
% preamplifier and DC coupler from Percision Acoustics with NPL
% calibration.
%
% My own calibration of the hydrophone!
% This is the end-of-cable loaded sensitivity!
% DCC terminated with 50 ohm before high impedance amplifier!
%
% Hydrophone serial number 1820 (cone length = 100 mm)
% Preamplifier serial number PA110078
% DC coupler serial number DCPS223
%
% Date of calibration: 19.12.2011
```

```
%
% ##########
% @author, Magne Aanes (PhD candidate)

% Frequency range
fr = [100000,105000,110000,115000,120000,125000,130000
,135000,140000,145000,150000,155000,160000,165000,170000
,175000,180000,185000,190000,195000,200000,205000,210000
,215000,220000,225000,230000,235000,240000,245000,250000
,255000,260000,265000,270000,275000,280000,285000,290000
,295000,300000,305000,310000,315000,320000,325000,330000
,335000,340000,345000,350000,355000,360000,365000,370000
,375000,380000,385000,390000,395000,400000,405000,410000
,415000,420000,425000,430000,435000,440000,445000,450000
,455000,460000,465000,470000,475000,480000,485000,490000
,495000,500000,505000,510000,515000,520000,525000,530000
,535000,540000,545000,550000,555000,560000,565000,570000'
,575000,580000,585000,590000,595000,600000,605000,610000'
,615000,620000,625000,630000,635000,640000,645000,650000
,655000,660000,665000,670000,675000,680000,685000,690000
,695000,700000,705000,710000,715000,720000,725000,730000
,735000,740000,745000,750000,755000,760000,765000,770000
,775000,780000,785000,790000,795000,800000,805000,810000
,815000,820000,825000,830000,835000,840000,845000,850000
,855000,860000,865000,870000,875000,880000,885000,890000
,895000,900000,905000,910000,915000,920000,925000,930000
,935000,940000,945000,950000,955000,960000,965000,970000'
,975000,980000,985000,990000,995000,1000000,1005000
,1010000,1015000,1020000,1025000,1030000,1035000,1040000
,1045000,1050000,1055000,1060000,1065000,1070000,1075000
,1080000,1085000,1090000,1095000,1100000,1105000,1110000
,1115000,1120000,1125000,1130000,1135000,1140000,1145000
,1150000,1155000,1160000,1165000,1170000,1175000,1180000
,1185000,1190000,1195000,1200000,1205000,1210000,1215000
,1220000,1225000,1230000,1235000,1240000,1245000,1250000
,1255000,1260000,1265000,1270000,1275000,1280000,1285000
,1290000,1295000,1300000,1305000,1310000,1315000,1320000
,1325000,1330000,1335000,1340000,1345000,1350000,1355000
,1360000,1365000,1370000,1375000,1380000,1385000,1390000
,1395000,1400000,1405000,1410000,1415000,1420000,1425000
,1430000,1435000,1440000,1445000,1450000,1455000,1460000
,1465000,1470000,1475000,1480000,1485000,1490000,1495000
,1500000];

% End-of-cable free-field loaded sensitivity of the hydrophone with
% submersible preamplifier was measured using the 3-way transducer method.
% 2xV301 transducers used for this calibration.
Mr = [2.63730482477810e-07,2.63093051514725e-07,
3.02090605704314e-07,2.97550060791525e-07,2.90040911321805e-07,
3.00391457863272e-07,3.02592248294422e-07,2.98854764681035e-07,
3.04420833315268e-07,2.91899389756351e-07,3.48087121996044e-07,
3.64872658093246e-07,3.59871913686794e-07,3.55245076965871e-07,
3.51654364830467e-07,3.66429974314540e-07,3.85142129675431e-07,
3.85558382413347e-07,3.79965108608615e-07,3.81501383552803e-07,
3.81142829819464e-07,3.80002803931646e-07,3.81250245283209e-07,
3.82554091506685e-07,3.90438361817487e-07,3.92942240179533e-07,
3.97557078940451e-07,4.08304149524530e-07,4.12146379902778e-07,
4.16166120588611e-07,4.13377481178345e-07,4.19567107359845e-07,
```

4.37802354706025e-07,4.46454262314542e-07,4.51203829592438e-07,
4.61074978883106e-07,4.61960929650019e-07,4.58791342669926e-07,
4.56991011240665e-07,4.57060836012366e-07,4.64694031494169e-07,
4.68857062062937e-07,4.72046664036588e-07,4.79374526996212e-07,
4.83323757079751e-07,4.84683011576343e-07,4.88815987779093e-07,
4.94866809792246e-07,4.98865521650793e-07,5.02745327495700e-07,
5.03758839955449e-07,5.04474859146257e-07,5.03810276010221e-07,
5.08463299757748e-07,5.15619831582752e-07,5.22088503578282e-07,
5.27793250010068e-07,5.32262164942315e-07,5.36851642795524e-07,
5.39347356058686e-07,5.48052441377343e-07,5.53293837242447e-07,
5.58208654312356e-07,5.61644082738965e-07,5.64159798427035e-07,
5.68090668187908e-07,5.73335128133702e-07,5.77974136174695e-07,
5.80611385800364e-07,5.83454498723442e-07,5.89326847302909e-07,
5.92935716469476e-07,5.96938402811951e-07,6.02279976541762e-07,
6.06198600826615e-07,6.09261525592912e-07,6.12680019625702e-07,
6.17021463303224e-07,6.21222729510779e-07,6.26300744678821e-07,
6.30994013662505e-07,6.33890913731177e-07,6.37302828637980e-07,
6.39700559357453e-07,6.40134467987429e-07,6.42436976309690e-07,
6.47119374861928e-07,6.53485568078448e-07,6.57945433266761e-07,
6.60866074254660e-07,6.61753965147164e-07,6.61406611859574e-07,
6.63114494038948e-07,6.66667532023846e-07,6.70929216428134e-07,
6.74569561695719e-07,6.76436304076716e-07,6.79764322632717e-07,
6.83526024137935e-07,6.88785167010555e-07,6.94263697262023e-07,
7.00054873025296e-07,7.04910867603177e-07,7.06639102218591e-07,
7.07517892205511e-07,7.08949969331902e-07,7.11862049661856e-07,
7.15084525253522e-07,7.16895216473270e-07,7.17421949110846e-07,
7.07000007710153e-07,7.05739331097190e-07,7.02992204465461e-07,
7.01280834933501e-07,7.02280785100232e-07,7.01077281912985e-07,
6.97775069325476e-07,6.97265962662003e-07,6.98804080728228e-07,
6.99986297435509e-07,7.02086783478862e-07,7.05530077704941e-07,
7.08162892150589e-07,7.09388601692968e-07,7.08209060532280e-07,
7.04236620810677e-07,7.02982380765834e-07,7.04217819576647e-07,
7.07449981608850e-07,7.12891995827992e-07,7.15686805919126e-07,
7.14497576908881e-07,7.09978976630072e-07,7.05226883203120e-07,
7.01845699348250e-07,6.97726432047924e-07,6.93750528294035e-07,
6.88185642724295e-07,6.81231033414356e-07,6.73113041876864e-07,
6.66646957977208e-07,6.62059311395109e-07,6.63173462904852e-07,
6.65032408072855e-07,6.67845306392012e-07,6.70731322970406e-07,
6.72590106827523e-07,6.74153352009653e-07,6.76366316167965e-07,
6.83525863408066e-07,6.75015301098015e-07,6.84484408305396e-07,
7.00136250711587e-07,7.03469694707777e-07,7.08337888165872e-07,
7.14289998609265e-07,7.21886551203777e-07,7.31137710035840e-07,
7.41299087906205e-07,7.46441500630713e-07,7.41897673894252e-07,
7.46584290320912e-07,7.48917313198359e-07,7.49544545481249e-07,
7.50353346669775e-07,7.49235436967253e-07,7.48395344884634e-07,
7.46928336560267e-07,7.47806223078506e-07,7.50833270087365e-07,
7.56961539414815e-07,7.63554130237669e-07,7.68409127391359e-07,
7.71849319700413e-07,7.73550637945994e-07,7.75376737407802e-07,
7.77949960202384e-07,7.78942033279007e-07,7.79151858578309e-07,
7.78851574182922e-07,7.75016957253435e-07,7.74898727587659e-07,
7.76898204641387e-07,7.81618244962253e-07,7.83626817714080e-07,
7.87882055807977e-07,7.88617535409864e-07,7.90197908457892e-07,
7.97134888174549e-07,8.06952323578312e-07,8.19364508600073e-07,
8.21105434481859e-07,8.23933155982614e-07,8.25427187679209e-07,
8.29051748383838e-07,8.32378940561914e-07,8.32701294056175e-07,
8.38011466864199e-07,8.37896731861260e-07,8.38492307443015e-07,
8.40089381386900e-07,8.49169220971030e-07,7.96104783144397e-07,
7.51116667296437e-07,7.10601216418836e-07,6.71341899478451e-07,

```
6.41301373314291e-07,6.24092119983363e-07,6.14587382462978e-07,
6.17081710668588e-07,6.23398312066223e-07,6.36076114456850e-07,
6.53213586609853e-07,6.90114908351305e-07,7.19107132159433e-07,
7.73791992723962e-07,8.15834947601935e-07,8.57478614884809e-07,
8.51452317577960e-07,8.47903128475721e-07,8.48572456557980e-07,
8.41283137721422e-07,8.51748658162651e-07,8.53726240742883e-07,
8.55519180752256e-07,8.53144237925843e-07,8.53857909869496e-07,
8.55139769246399e-07,8.50610408457985e-07,8.51486853238843e-07,
8.35290184879967e-07,8.30058435304461e-07,8.23564615050077e-07,
8.20170970201227e-07,8.18330441803315e-07,8.18755448209199e-07,
8.20215348746920e-07,8.17253935821557e-07,8.11265620699893e-07,
8.06854042519187e-07,7.99999716532716e-07,7.96894192076756e-07,
8.01222126237408e-07,7.99170900695623e-07,7.99250116384126e-07,
7.97412995053446e-07,7.96883205421709e-07,7.96474025183344e-07,
7.96237644124659e-07,7.96743417321923e-07,8.03920452032970e-07,
8.05031816941231e-07,8.02902833913873e-07,8.00447123060901e-07,
8.00117474709902e-07,8.03907714135036e-07,8.09784931595715e-07,
8.14163779005428e-07,8.13853719868853e-07,8.09944206669957e-07,
7.89558465873485e-07,7.87655174788647e-07,7.89919480701787e-07,
7.95496034372034e-07,7.98594587743051e-07,7.98168195064847e-07,
7.94872671507924e-07,7.91340419266324e-07,7.88979909090006e-07,
7.88296654253152e-07,7.88297294657454e-07,7.89046534808200e-07,
7.86953304826121e-07,7.84310212666689e-07,7.81661136025576e-07,
7.80522840975320e-07,7.82354912616234e-07,7.82809449849273e-07,
7.81638437292252e-07,7.77716509380300e-07,7.73297625001981e-07];

% Interpolated using the frequency range specified by user!
M_ref = interp1(fr,Mr,f,'spline');
end
```